UNIVERSITÀ
DEGLI STUDI
FIRENZE

DOTTORATO DI RICERCA IN FISICA E ASTRONOMIA

CICLO XXX

COORDINATORE Prof. Raffaello D'Alessandro

Tracing our chemical origins: deuteration and complex organic molecules in Sun-like protostars

Settore Scientifico Disciplinare: FIS/05 Astronomia e Astrofisica

Dottoranda
Dott. Eleonora Bianchi

Tutori
Dott. Claudio Codella

Prof. Alessandro Marconi

Coordinatore
Prof. Raffaello D'Alessandro

Anni 2014 / 2017

Contents

The PhD project in a nutshell i

Refereed publications iii

1 Introduction 1
- 1.1 The formation of a Sun-like star and its planetary system 2
- 1.2 Molecules in star forming regions: our astrochemical origins . . . 7
  - 1.2.1 Deuterium fractionation 11
- 1.3 Previous observations and related limits 12

2 Methods 17
- 2.1 Radiative transfer 17
- 2.2 Spectral line fundamentals 19
- 2.3 Rotation diagram analysis 22
  - 2.3.1 Multiplets 25
  - 2.3.2 Large Velocity Gradient (LVG) approach 25
- 2.4 Molecular lines 26
  - 2.4.1 Spin statistic 28

3 Observations 29
- 3.1 Single-dish antennas: basic concepts 30
- 3.2 The IRAM-30m large program ASAI 35
- 3.3 Interferometers: basic concepts 38
- 3.4 ALMA Cycle 1 and Cycle 4 observations 41

4 Chemical complexity around Class 0 protostars **45**
4.1 The pristine jet-disk system in HH212 . . . 45
4.2 Deuteration on a solar system scale around HH212 . . . 49
4.2.1 Line spectra and maps . . . 49
4.2.2 Methanol deuteration . . . 52
4.2.3 Emitting region of deuterated methanol . . . 56
4.2.4 Single deuterated methanol CH_3OD . . . 59
4.2.5 Conclusions on HH212 deuteration . . . 60
4.3 iCOMs in HH212: accretion shocks and disk winds . . . 61
4.3.1 Line spectra and maps . . . 61
4.3.2 Physical properties . . . 63
4.3.3 Kinematics . . . 67
4.3.4 Discussion . . . 70
4.3.5 Conclusions on iCOMs . . . 73

5 Chemical complexity in a later Class I protostellar stage **75**
5.1 The SVS13-A Class I laboratory . . . 76
5.2 Decrease of deuteration in Class I objects . . . 82
5.2.1 Line identification . . . 85
5.2.2 Formaldehyde isotopologues . . . 87
5.2.3 Methanol isotopologues . . . 88
5.2.4 Wrap up . . . 90
5.2.5 LVG analysis . . . 95
5.2.6 Rotation Diagram analysis . . . 96
5.2.7 Methanol and formaldehyde deuteration . . . 98
5.2.8 The $[CH_2DOH]/[CH_3OD]$ ratio . . . 99
5.2.9 D/H of organics: from Class 0 to Class I . . . 101
5.2.10 Conclusions on deuteration . . . 106
5.3 From Class 0 to Class I: chemical heritage . . . 110
5.3.1 Ketene (H_2CCO) . . . 111
5.3.2 Acetaldehyde (CH_3CHO) . . . 115
5.3.3 Methyl Formate ($HCOOCH_3$) . . . 119
5.3.4 Dimethyl ether (CH_3OCH_3) . . . 127
5.3.5 Formamide (NH_2CHO) . . . 132

5.3.6 Constraints on other iCOMs 133
5.3.7 Conclusions on iCOMs 135

6 Conclusions **143**
6.1 Deuterium fractionation to shed light on the past 143
6.2 On the nature of a hot corino 144
6.3 How chemistry evolves from the Class 0 to the Class I phase . . . 145
6.4 iCOMs abundances: new constraints and related limits 146

7 Perspectives: the NOEMA-SOLIS revolution **149**

Bibliography **154**

The PhD project in a nutshell

Context

The PhD project aims to test the laboratory results and the theoretical models predictions on chemical differentation in Sun-like star forming regions. In particular, the project is focused on Interstellar Complex Organic Molecules (iCOMs) and deuterated species, which are considered our chemical heritage, namely the building blocks of the organic material observed in Solar System bodies. The jet/disk protostellar regions are thus perfect places to understand when and how the seeds of life form. Moreover iCOMs and deuterated species can be used as key tools to observe the fundamental processes (accretion, ejection) sculpting the cradle where a star (and its planetary system) is going to form. Our group is involved in a strong international observational effort to detect and analyse complex and rare molecular species in the interstellar space through emission due to their roto-vibrational transitions, using Large Programs based on both single dish (IRAM-30m) and high resolution interferometric data (IRAM-NOEMA, ALMA).

Data reduction and analysis

(1) IRAM 30m data in the framework of the ASAI IRAM Large Program;
(2) NOEMA data in the framework of the SOLIS IRAM Large Program;
(3) ALMA Cycle 1 and Cycle 4 data.

Roles within international synergies

(1) IRAM NOEMA Large Program SOLIS (Seed of Life In Space; PI: C. Ceccarelli and P. Caselli); Member of the WG on shocks;
(2) IRAM-30m Large Program ASAI (Astrochemical Surveys At IRAM; PI: B. Lefloch and R. Bachiller); Member of the WG on Class I/0 objects;
(3) iALMA Premiale-INAF (PI: L. Testi) Member of the WG on Complex organic molecules in star-forming regions;
(4) JEDI PRIN project (JEts and Disks@INAF) funded by PRIN-INAF 2013 Member of the WG on Complex organic molecules in star-forming regions;
(5) SOLIS-SNS synergy: Collaboration between the Arcetri astrochemical group involved in the SOLIS IRAM-NOEMA Large Program (led by C. Codella) and the the DREAM-SLab Center of the Scuola Normale Superiore led by Prof. V. Barone. Member of the WG on shocks and protostars;

(6) FAUST synergy: collaboration between EU, Japan and USA astrochemistry experts for the exploitation of ALMA and VLA data led by S. Yamamoto, N. Sakai, C. Ceccarelli, C. Codella, C. Chandler. Member of the WG on shocks and protostars.

Contributed talks

(1) *SVS13-A: Formaldehyde and methanol deuteration in a Class I hot corino.*
Contributed talk for the SOLIS meeting 2016, Cergy, France, 08-10/02/2017
(2) *How formaldehyde and methanol deuteration changes during the formation of a Sun-like star? The SVS13-A case.*
Contributed talk for the Workshop: Fractionation of isotopes in space: from the solar system to galaxies, Firenze, Italy, 10-13/10/2016
(3) *The first hot corino in a Class I object in Perseus as observed by ASAI.*
Contributed talk for the COST meeting: Complex Organic molecules in space, Scuola Normale Superiore, Pisa, Italy, 7-8/03/2016
(4) *Complex organic molecules towards SVS13-A.*
Contributed talk for the 3rd JEDI meeting, Firenze, Italy, 13-14/06/2016
(5) *The CH_3CHO/HDCO ratio as a tool to study the COMs formation.*
Contributed talk for the 2nd JEDI meeting, Osservatorio Astronomico Capodimonte, Napoli, Italy, 09/04/2015
(6) *Star forming regions: from single-dish to ALMA.*
Contributed talk for the iALMA workshop on mm/sub-mm interferometry, Bologna, Italy 20-21/01/2015

Main Conclusions

For the Class 0 protostars, deuterated molecules and iCOMs provide a brand new complementary picture with respect to standard molecular tracers such as CO and SiO. They sample the inner parts of the jet/disk system revealing on scales less than 30 au the chemically enriched region associated with accretion shocks and disk winds. These species are fundamental in understanding the energetic and angular momentum budget of the forming of a new Sun-like star. Regarding the more evolved Class I objects, the low deuterium fractionation as well as the change in the abundance ratios between different iCOMs indicate a modified chemical content in the evolutionary transition from the Class 0 phase to the Class I phase. On the other hand, [iCOMs]/[H_2] abundance ratios look the same moving from Class 0 to Class I paving the way for further investigations.

Refereed publications

10 among papers and letters; 2 as 1^{st} author, 2 as 3^{rd} author.

– **Bianchi, E.**, Codella, C., Ceccarelli, C., et al.
Decrease of the organic deuteration during the evolution of Sun-like protostars: the case of SVS13-A
MNRAS, 2017, 467, 3011

– **Bianchi, E.**, Codella, C., Ceccarelli, C., et al.
Deuterated methanol on solar system scale around the HH212 protostar,
A&A, 2017, 606, L7

– Ceccarelli, C., Caselli, P., Fontani, F., et al. (including **Bianchi, E.**)
Seeds Of Life In Space (SOLIS): the organic composition diversity at 300-1000 au scale in Solar-type star forming regions.
A&A, in press (arXiv:1710.10437)

– Codella, C., Ceccarelli, C., **Bianchi, E.**, et al.
Hot and dense water in the inner 25 au of SVS13-A
MNRAS, 2016, 462, L75

– Codella, C., Ceccarelli, C., Balucani, N., et al. (including **Bianchi, E.**)
Seeds Of Life In Space (SOLIS): II. Formamide in protostellar shocks:evidence for gas-phase formation.
A&A, 2017, 605L, 3C

– Codella, C., Viti, S., Lefloch, B., et al. (including **Bianchi, E.**)
Nitrogen oxide in protostellar envelopes and shocks: the ASAI survey
MNRAS, submitted

– Codella, C., **Bianchi, E.**, Cabrit, S., et al.
Water and interstellar complex organics associated with the HH212 protostellar disk
A&A, submitted

– Fontani, F., Ceccarelli, C., Favre, C., et al. (including **Bianchi, E.**)
Seeds Of Life In Space (SOLIS):I. Carbon-chain growth in the solar-type proto-cluster OMC2-FIR4
A&A, 2017, 605A, 57F

- Lefloch, B., Bachiller, R., Ceccarelli, C., et al. (including **Bianchi, E.**)
  Astrochemical evolution along star formation: Overview of the IRAM Large Program ASAI
  MNRAS, submitted

- Punanova, A., Caselli, P., Feng, S., et al. (including **Bianchi, E.**)
  Seeds of Life in Space (SOLIS). III. Zooming into the methanol peak of the prestellar core L1544
  ApJ, in press

- Tabone B., Cabrit S., **Bianchi E.**, Ferreira J., Pineau des Forêts G., Codella C., Gusdorf A., Gueth F., Podio L.
  ALMA discovery of a rotating SO/SO_2 flow in HH212. A possible MHD disk wind?
  A&A Letters, in press (arXiv:1710.01401)

1 Introduction

Understanding how our own Solar System, Earth and life, have come to be is one of the most important and exciting topics in science. The analysis of the small bodies like the Kuiper Belt Objects (KBOs), comets and meteorites revealed the presence of several organic compounds including amminoacids. Given these bodies are thought to be the most pristine objects of the Solar System, these findings suggest an interstellar chemical heritage. A surprising large number (about 200) of molecules have been observed so far in the interstellar medium (CDMS[1]). Among them about one third are Intestellar Complex Organic Molecules (iCOMs) namely molecular species with 6 or more atoms and based on carbon. The detection of this complex species is an evidence that the building blocks of the large organic compounds are ubiquitus in star forming regions. The study of the early protostellar stages is thus fundamental to understand how and when simple molecules form the large macromolecules and how they are inherited and/or reprocessed during the evolution from the protostellar stages to the planetary systems. Key reviews can be found in: Ehrenfreund & Charnley (2000), Herbst & van Dishoeck (2009), Caselli & Ceccarelli (2012), Ceccarelli et al. (2014), Yamamoto (2017).
This chapter gives an overview of the processes involved in the formation of a Sun-like star and its planetary system (see Fig. 1.1), providing the scientific context for the results presented further on. In Chap. 2 an overview of the physical processes and methods used to analyse the data are reported. In Chap. 3 the obser-

[1]The Cologne Database for Molecular Spectroscopy, Müller et al. 2001, 2005; www.astro.uni-koeln.de/cdms/molecules

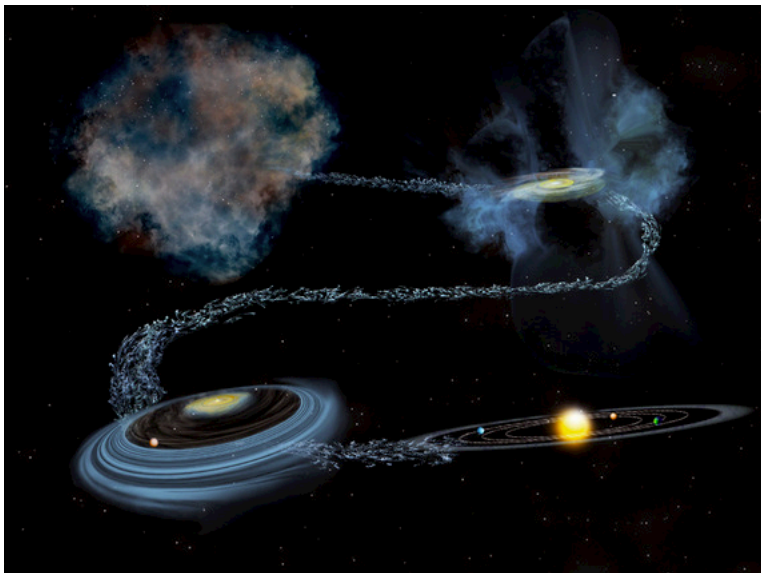

Figure 1.1: Sketch of the formation of a Sun-like star and its planetary system (Credit:ESO).

vational datasets and the relative instruments are described. Chapter 4 is dedicated to the analysis of the chemical complexity towards the Class 0 object HH212. In Chap. 5 the discovery and analysis of a hot corino in a more evolved Class I object, SVS13-A, is reported. The main results and discoveries related to this theses work are reported in Chap. 6 while in Chap. 7 the forthcoming observations and the related projects are described.

1.1 The formation of a Sun-like star and its planetary system

Stars like our Sun form in dark clouds invisible to optical observations. Only the development of infrared and (sub-)millimeter telescopes enables the direct studies of this complex process. Dense giant molecular clouds originated by the cooling of the diffuse medium and their extent is on scales of ~100 pc. The internal structure is complex because of the interplay of several phenomena such as gravitational collapse, magnetic fields and turbolence (Klessen & Glover 2016).

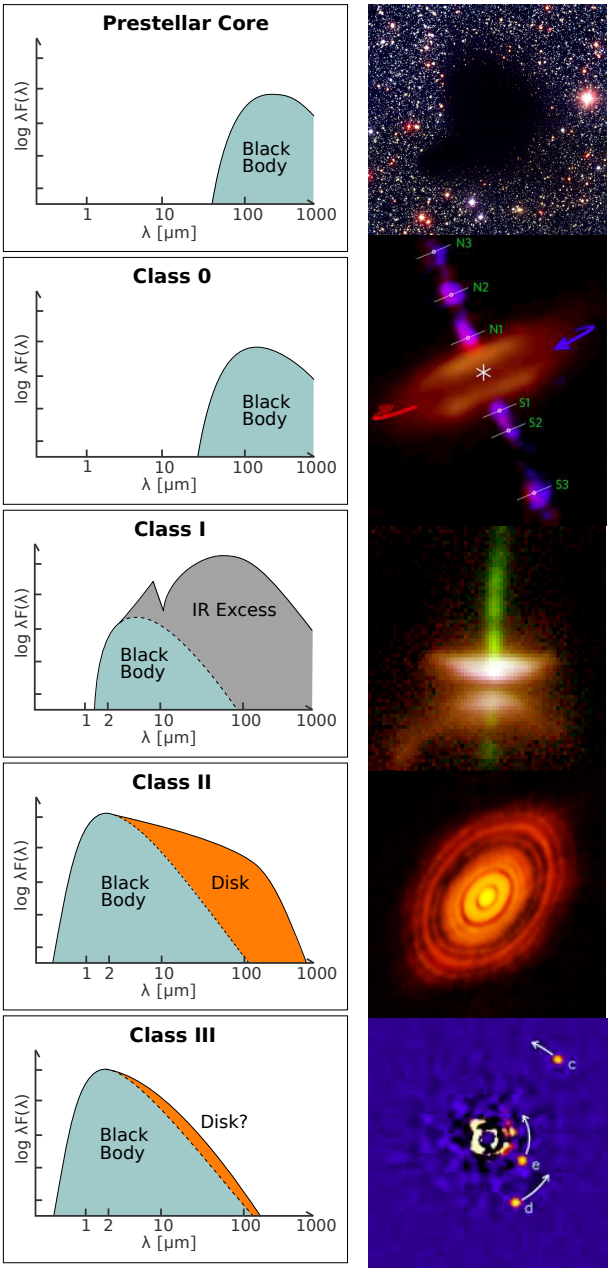

Figure 1.2: *Left panels*: Spectral energy distributions (SEDs) of the different formation stages of a Sun-like star (Adapted from Persson 2014). *Right panels*: Real observations of objects in the different evolutionary stages taken with different instruments. The prestellar core is the dark cloud B68 as obsrved by VLT/FORS1 (Credit:ESO). The Class 0 object is the HH212 protostar in Orion as observed by ALMA (Lee et al. 2017a). The Class I object is HH30 as observed by the Hubble Space Telescope (Credit: Chris Burrows (STScI), the WFPC2 Science Team and NASA/ESA). The Class II object is an ALMA view of the protoplanetary disc surrounding the young star HL Tauri (Credit: ALMA; ESO/NAOJ/NRAO). The Class III object is the image of the system HR 8799 with three orbiting planets. The image has been acquired at the Keck II telescope (Credit: Marois et al. 2010).

Observations performed by the ESA *Herschel* space telescope[2] revealed that molecular clouds have a filamentary structure (André et al. 2014). In the densest part of the filaments fragmentation due to gravitation instabilities can occurr forming dense ($n_{H_2} > 10^4$ cm^{-3}) prestellar cores ($\sim$ 0.1–0.01 pc). These objects are gravitationally bound clouds with low temperatures (around 10 K). During a process lasting fews Myr prestellar cores collapse under gravity forming one or more protostars (Shu 1977). In these cold objects are set the initial conditions of a complex process which end with a star and its planetary system formation. Young Stellar Objects (YSOs) have been empirely classified by Lada (1987) in a scheme based on the slope of their infrared spectral energy distribution (SED), which reflects their evolutionary stage. Other criteria have been introducted to classify objects too deeply embedded to be detected in the near-infrared as for example the ratio of submillimeter to bolometric luminosity (L_{submm}/L_{bol}; André et al. 1993) and the bolometric temperature (Myers & Ladd 1993), that is the temperature of a black body with the same mean frequency as the observed SED. Figure 1.2 extends the Lada's classification scheme to the current known evolutionary stages from the prestellar cores phase to the formation of a planetary system. On the right panels are reported observations in different wavelenghts of objects in the different stages. The first stage is the prestellar core, represented by the Hubble image of the Barnard object B68 which appears at visual wavelenght like a dark object on the stellar backgroung because of the large visual extinction. Once the collapse occurs, the material starts to accrete into a central object forming a protostar which enters in the Class 0 phase. In this stage the central object is still deeply embedded in a large scale envelope. The infalling meterial has to lose angular momentum in orded to be accreted from the protostar. The infalling material tends to conserve angular momentum, producing the so-called centrifugal barrier (see Fig. 1.3) which is this transition zone (a ring) from an infalling-rotating envelope to a rotationally (Keplerain) supported disc (Sakai et al. 2014b, 2017, Oya et al. 2016). At the centrifugal barrier, not only the gas motion is discontinuous, but also the chemical composition of the gas drastically changes, due to slow accretion shocks which drives the sputtering of the dust mantles and triggers warm gas chemistry. This prevents the material from falling directly onto the protostar surface and generate a disk-like structure. The angular momentum is removed

[2]http://sci.esa.int/herschel/

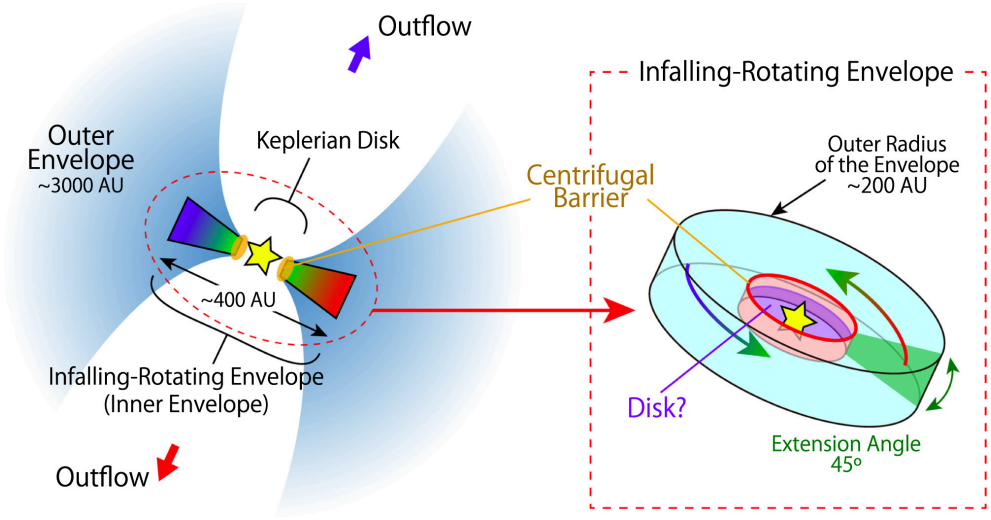

Figure 1.3: Figure from Oya et al. (2016) is a schematic illustration of the gas components around the Class 0 source IRAS 16293–2422. The sketch shows in the left panel the source large scale structure while the right panel is a zoom in of the central region (~ 400 au). The spherical outer envelope is represented by light blue regions. The small scales structure shows the rotation of the inner envelope, assumed to be cylindrical, and the disk around the protostar. In red the centrifugal barrier of the infalling-rotating envelope is indicated.

thanks to the ejection of gas through low-velocity and poorly collimated molecular outflows and high-velocity and highly collimated protostellar jets. While the outflows are very massive and and constituted by swept-up material, jets are denser and generated very close to the protostellar surface. Jets from young accreting stars remain one of the most spectacu- lar phenomena in astrophysics. Although their exact launch zone is still debated (in the inner 0.05 AU, according recent measurements by Lee et al. 2017b), it is currently accepted that they are powered by the rotation and accretion energy of the system, and are accelerated or collimated via a magneto-hydrodynamical (MHD) process (see e.g. Ferreira et al. 2006; Shang 2007; Frank et al. 2014, and references therein). The ejected material drives bow-shocks through the surrounding high-density medium and traced by H_2 ro-vibrational lines at excitation temperatures above 1000 K. Slower and cold (10–20 K) molecular outflows are in turn formed by swept-up material, usually traced by CO. Shocks heat the gas and trigger several processes such as endothermic chemical reactions and ice grain mantles sublimation or sputtering. A large number of molecular species undergo a dramatic enhancement in their abundances (see e.g. van Dishoeck & Blake 1998), as observed by observations at millimeter wavelengths towards a number of outflows (e.g. Bachiller et al. 2001). The Class 0 object reported in Fig. 1.2 is the HH212 protostar in the Orion star forming region, recently observed in the submillimeter (Lee et al. 2017b) where a bipolar jet and a forming dusty disk have been identified. After about 10^5 yr, the protostar reaches the Class I phase in which the large scale envelope is still present but the luminosity start to be dominated by the central object. The SED is characterized by an infrared excess due to the protostellar light absorbed and scattered by the disk and the dust envelope. The object reported in Fig. 1.2 is HH30 in Taurus as observed with the Hubble space telescope. The image show a jet and an edge-on disk illuminated by the protostellar light. After about 10^6 yr the protostar enter in the Class II phase when most of the envelope has dissipated and the young star is sorrounded by an accretion disk. In Fig. 1.2 is reported the spectacular ALMA image of the protoplanetary disk around the Class II protostar HL Tauri. Within the disk dust coagulation occurs ending up with the formation of a debris disk during the Class III phase and a planetary system. In Fig. 1.2 the direct imaging of three planets orbiting around the protostellar objects HH 8799 are shown.

1.2 Molecules in star forming regions: our astrochemical origins

During the low-mass star forming process, the interstellar medium evolves toward denser condensations and molecules can therefore be formed, destroyed or incorporated at the varius stages so that the chemical composition of the gas becomes increasingly more complex (see e.g. Caselli & Ceccarelli 2012, Ceccarelli et al. 2014, Yamamoto 2017). Molecular complexity builds up at each step of the Sun–like star formation process, starting from simple molecules and ending up in large polyatomic species (see Figure 1.4). While matter slowly accumulates toward the center of a molecular cloud, the central density increases and the temperature decrease. Atoms and molecules in the gas phase freeze-out onto the cold surfaces of the dust grains, forming the grain mantles. Hydrogenation of atoms and molecules takes place, forming molecules such as water (H_2O), and formaldehyde (H_2CO). In these regions the formation of new molecules in icy mantles is also caused by the effects of UV photons and low-energy cosmic rays. At this point the collapse starts, the gravitational energy is converted into radiation and the envelope around the central object warms up. The molecules frozen on the mantles acquire mobility and form new, more complex species. When the temperature reaches about 100 K the mantle sublimates, given origin to the so-called hot corino phase, which has a very small size (< 0.01 pc). Molecules in the mantle are injected in the gas forming the so-called "first generation" species. Successively they react in the gas-phase to form the "second generation" of more complex molecules. The abundance of iCOMs (such as methyl formate, $HCOOCH_3$ or dymethyl ether, CH_3OCH_3) dramatically increases. However recent works suggest that gas-phase chemistry could play an important role also in the formation of the first generation species (Balucani et al. 2015, Codella et al. 2017). A classical example of a chemically rich hot corino is provided by IRAS16293–2422 (e.g. Ceccarelli et al. 2007), where recently also glycolaldehyde ($HCOCH_2OH$), a crucial molecule for the formation of metabolic molecules, has been detected (Jørgensen et al. 2012). Simultaneously to the collapse, a newborn protostar generates a fast and well collimated jet, possibly surrounded by a wider angle wind. In turn, the ejected material drives shocks travelling through the surrounding high-density medium. Shocks heat the gas up to thousands of K and trigger several

processes such as endothermic chemical reactions and ice grain mantle sublimation or sputtering (e.g. van Dishoeck & Blake 1998). Several molecular species undergo significant enhancements in their abundances. The envelope dissipates with time and eventually only a circumstellar disk remains, which is also called protoplanetary disk. In the hot regions, close to the central forming star, new complex molecules are synthesized by reactions between the species formed in the protostellar phase. In the cold regions of the disk, where the vast majority of matter resides, the molecules formed in the protostellar phase freeze-out onto the grain mantles again. Dust grains then coagulate into larger planetesimals, the bricks of future planets, comets, and asteroids.

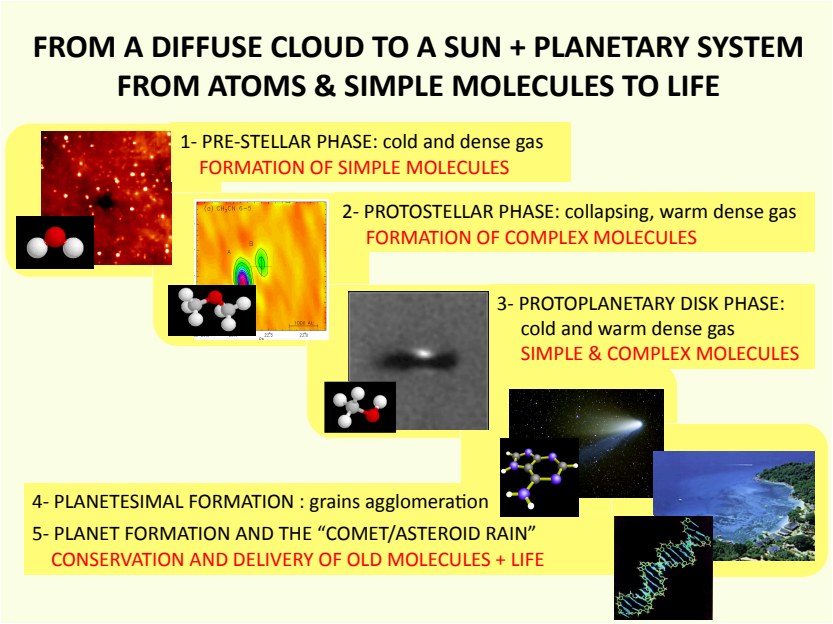

Figure 1.4: Star formation and chemical complexity. The formation of a star and a planetary system, like the Solar System, passes through fundamental phases, marked in the sketch (Caselli & Ceccarelli 2012)

iCOMs such as methyl formate, $HCOOCH_3$, dymethyl ether, CH_3OCH_3, or glycolaldehyde, $HCOCH_2OH$) have been found in all the components of the star formation recipe (prestellar cores, hot–corinos, shocks induced by fast jets). These

species are thought to be either formed in solid state chemistry of grain mantles and then released in the gas-phase due to ice grain mantle sublimation or sputtering (see Fig. 1.5), or produced in the gas phase using simpler species released by mantles (such as H_2CO or CH_3OH). This question is still hotly debated. In both the proposed mechanism for iCOMs formation (in the gas or onto mantles surface), the chemical complexity is related to the initial ice composition (Öberg et al. 2009, Sakai et al. 2010), confirming the importance of recovering the phisical conditions of the natal protostellar cloud. In particular, one of the key bricks for the iCOMs grain surface chemistry is CH_3OH, formed through CO hydrogenation (Sakai & Yamamoto 2013).

In the last years it has been discovered a new class of YSOs characterised by a composition as rich as that of hot-corinos but in different species. These objects are deficient in saturated iCOMs but rich in unsaturated species like carbon-chain molecules. The particular chemistry associated with these sources has been defined warm carbon-chain chemistry (WCCC; see Sakai et al. 2008, 2009). Even if the origin of this chemical diversity is yet unclear, it looks not related to a different evolutionary stage or to a particular star forming region. It has been proposed that the chemical diffences between hot-corinos and WCCC sources is related to the different duration of the prestellar core phase which reflects in a different chemical composition of the dust mantles (Sakai & Yamamoto 2011). For WCCC objects, the short prestellar stage ensures that carbon atoms deplete onto dust grains before being converted to CO. Indeed a recent paper by Oya et al. (2017) is proposing L483 as a WCCC source harbouring hot corino activity. Nevetheless only the analysis of a larger number of sources, both WCCC objects and hot-corinos, will allow us to build a unified model of low-mass star-formation. But it is clear that the key to undestrand the origin of the chemical differentiation is in the early prestellar and ptotostellar stages.

The last developements of astrochemistry demonstrates that complex species represent a powerful diagnostic tool to study the present and the past conditions of an astronomical source. However, extract the rich information provided by the observed spectra is a complex work which requires the collaboration and sinergy of different research fields. The starting point is the line identification process in which the observed lines are compared with the spectroscopic data collected

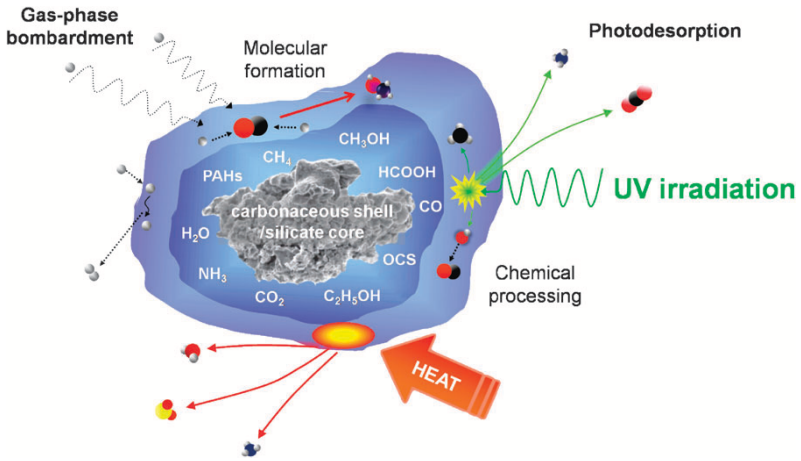

Figure 1.5: Schematic showing the main routes of interstellar ice processing that takes place in astrophysical environments (Burke & Brown 2010). The temperatures in interstellar dense clouds are low enough that most gas phase molecules freeze into ice mantles on dust grains. Organic material may be created in dense molecular clouds on the surface of icy dust grains by UV-driven chemistry. Heat generated by new born stars or shocks stimulates further surface chemistry prior to evaporation or sputtering of the icy mantles during cloud collapse. Once the molecules have been released into the gas phase, they drive a rich chemistry leading to the formation of larger organics.

in spectral databases. These contain the predicted lfrequency and spectroscopic parameters for rotational transitions of a particular species. The most used are the Jet Propulsor Laboratory (JPL[3], Pickett et al. 1998) and Cologne Database for Molecular Spectroscopy (CDMS[4]; Müller et al. 2001, Müller et al. 2005) molecular databases. Once identified a molecular species, the observed lines intensities need to be converted to molecular abundances. This is done with the help of radiative transfer codes, once the collisional coefficients are known. Finally, to derive the physical and chemical source structure the observed abundances have to be compared with abundances predicted by an astrochemical model which take into account the chemical reactions pathways and their rate coefficients. Current astrochemical models ar e far to reproduce the large abundances of iCOMs observed so far in the protostellar objects. This demonstrates the need of exploring new

[3]https://spec.jpl.nasa.gov/
[4]http://www.astro.uni-koeln.de/cdms/

chemical pathways and of obtaining more observational evidence to put stronger constraints on the models.

1.2.1 Deuterium fractionation

The deuterium fractionation is the process that enriches the amount of deuterium with respect to hydrogen in molecules. While the D/H elementary abundance ratio is $\sim 1.6 \times 10^{-5}$ (Linsky 2007), for molecules this ratio can be definitely higher and can be a precious tool to understand the chemical evolution of interstellar gas (see e.g. Ceccarelli et al. 2014, and references therein). In particular, during the process leading to the formation of a Sun-like star, large deuteration is observed in cold and dense prestellar cores (e.g. Bacmann et al. 2003, Caselli & Ceccarelli 2012, and references therein). The process start when cosmic rays ionizate H_2 and H, forming the ion H_3^+. Reactions with HD, which is the major deuterium reservoir in cold environments, produce H_2D^+ through the exothermic reaction $H_3^+ + HD \rightarrow H_2D^+ + H_2 + 230$ K (e.g. Caselli & Ceccarelli 2012, Ceccarelli et al. 2014 and references therein). In a similar way the ions D_2H^+ and D_3^+ are formed. In cold gas (where $T < 20$ K) the inverse reaction cannot proceed. The formation of all the other deuterated molecules thake place both in gas-phase or on the gain surfaces via reactions of the other species with H_2D^+, D_2H^+ and D_3^+. The enanchment of H_2D^+ which trigger all the deuteration process is due to the low temperature. Indeed in these conditions abundant neutral species as O and CO which are destruction partner of H_3^+ are deplited from the gas-phase and freeze-out onto grain mantles. Moreover the relative abundance of the ortho and para modifications of H_2 can have an effect on the deuterium fractionation. Normally the statistical ratio of the ortho/para is 3 but at low temperatures it is predicted to drop below 10^{-3} (Sipilä et al. 2013) enhancing the H_2D^+ abundance. In prestellar cores, deuterated and duble deuterated formaldehyde can be formed through gas phase chemistry and then the formaldehyde D/H ratio could reflect the gas phase chemistry (Roberts & Millar 2000). The picture is different for formaldehyde as well as for methanol around protostars which are mostly formed via active grain surface chemistry (e.g. Tielens 1983). For single deuterated methanol, the grain chemistry statistical models of Charnley et al. (1997) and Osamura et al. (2004), predict that the ratio of the isotopologues CH_2DOH and CH_3OD formed on the mantles

should be 3. Deuterated H_2CO and CH_3OH are then stored in the grain mantles to be eventually released into the gas phase once the protostar is formed and the grain mantles are heated and successively evaporated (e.g. Ceccarelli et al. 1998, Ceccarelli et al. 2007; Parise et al. 2002, Parise et al. 2004, Parise et al. 2006) or sputtered by protostellar shocks (Codella et al. 2012; Fontani et al. 2014). As a consequence, D/H can be used as fossil record of the physical conditions at the moment of the icy water and organics formation (e.g. Taquet et al. 2012b, Taquet et al. 2013, Taquet et al. 2014).

1.3 Previous observations and related limits

Low-mass star forming regions have been sparsely studied so far. Several observtions have been carried out with single-dish telescopes in the mm-spectral range (in particular with the IRAM-30m antenna) to detect iCOMs in Class 0/I protostars (see e.g. Bottinelli et al. 2004, Maret et al. 2005, Bottinelli et al. 2007, Öberg et al. 2011, 2014, Graninger et al. 2016). However, these studies are far to provide a comprehensive census of the chemical content towards these sources. The major problem is that to firmly identify iCOMs and, at the same time, to safely derive the physical conditions of the gas we need to detect a large number of lines. The project TIMASSS (The IRAS16293–2422 Millimeter And Submillimeter Spectral Survey: Caux et al. 2011), was a first pioneering project aimed to a comprehensive study of molecular complexity in a Class 0 protostar which demonstrates for the first time the need for systematic spectral surveys. Another example is the 3mm survey performed towards L1527 by Takano et al. (2011). In general terms, as different lines from transitions with different upper level energies are excited in a range of temperatures and densities, line surveys permit to probe various regions along the line-of-sight. Star-forming regions are particularly complex because of the chemical differentiation of the regions (dominant chemical species depend on the cloud zone) and because, for a given species, the excited lines depend on the conditions (such as temperature, density, velocity field), with sometimes complex kinematics, where infall and out flow motions are simultaneously present. Another limitation consists in the lack of observations in different evolutionary stages. The bulk of the observed objects are indeed in the Class 0 phase, while no clear results have been so far obtained for the later Class

I/II phases. Because of the paucity of dedicated surveys, there is no evidence of a change of the chemical content during the evolutionary transition from Class 0 to Class I. An instructive example is provided by the IRAM-30m survey performed with angular resolutions larger than 20″ by (Öberg et al. 2011, 2014, Bergner et al. 2017): some Class I objects are included but iCOMs are almost non-detected or detected through very low excitation lines possibly not originating in a hot corino.

This picture is valid not only for the iCOMs abundances but also for the level of deuterium fractionation. While deuterated molecules have been detected towards the early stages of the Sun-like star formation (i.e. prestellar cores and Class 0 objects) as well as in the Solar System (see e.g. Ceccarelli et al. 2014, and references therein), no clear result has been obtained for intermediate evolutionary phases (Class I and II objects). A handful of measurements of deuterium fractionation in Class I sources exists (i.e. Roberts & Millar 2007) but they refer only to few transitions sampling large regions (up to 58″) well beyond the protostellar system. Loinard et al. (2002) reported measurements of double deuterated formaldehyde in star-forming regions with both the SEST (Swedish ESO Submillimeter telescope) and IRAM single dishes suggesting a decrease with the evolutionary stage. In addition, Watanabe et al. (2012) reported the deuterium fractionation measurements toward R CrA IRS7B, a low-mass protostar in the Class 0/I transitional stage. They measured for H_2CO a D/H $\sim$ 0.05, lower with respect to deuteration measured in Class 0 objects. However, they argued a different origin for the altered chemical composition of the envelope of R CrA IRS7B. In their case the low deuterium fractionation ratios do not suggest only an evolutionary trend, because the protostar parent core was heated by the external UV radiation from the nearby Herbig Ae star R CrA that considerably affect the protostar chemical evolution. Systematic observations of D/H in Class I objects are therefore required to understand how the deuterium fractionation evolves from prestellar cores to protoplanetary disks (see Fig. 1.6).

In this context, the unbiased spectral survey ASAI (Astrochemical Survey At IRAM-30m; see Chap. 3), covering different evolutionary protostellar stages represents a major step ahead by observing with unprecedented sensitivity the emission of a large number of molecular rotational transitions in the millimeter domain.

The advent of new powerful interferometric facilities such as ALMA (Ata-

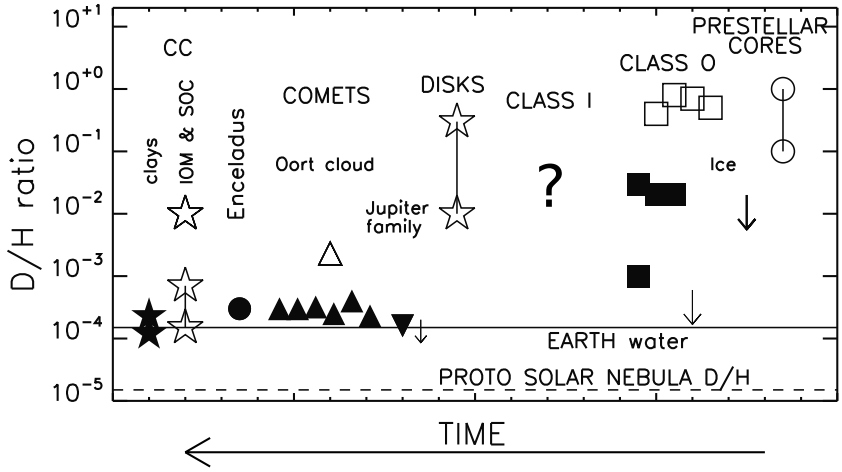

Figure 1.6: Figure adapted from Ceccarelli et al. (2014), reports the D/H ratio measured in organic matter in diferent sources: from the Solar System objects to the prestellar cores. The filled symbols refer to the D/H water measures whereas open symbols refer to organic matter.

cama Large Millimeter Array; see Chap. 3 and NOEMA (NOrthern Extended Millimeter Array[5]), has opened a new era of exploration of the chemical complexity in the very inner regions of the protostellar objects. Despite the protostars observed so far at high-angular resolution are fews (see e.g. Taquet et al. 2015, Sakai et al. 2014a, Jørgensen et al. 2016, Sakai et al. 2016, 2017, Oya et al. 2017) the obtained results are very promising. More specifically, interferometric observations enable to minimise or even eliminate the beam dilution affecting single-dish observations, providing the most reliable measuremets of molecular abundances. This is even more important for iCOMs given that we want to investigate the chemical heritage originated on spatial scales comparable to our Solar System (inner 100 au). In sources characterised by a complex physical and kinematical structure as young protostars, iCOMs demontrated to be powerful tracers of the different processes at work. In particular, iCOMs allow us to go beyond the classical definition of hot-corino, i.e. a generic roundish region of 100 au around the protostar, imaging regions previously unexplored as for example the shocks created by the rotating envelope infalling onto the extrernal layers of the

[5]http://iram-institute.org/EN/noema-project.php

self-gravitating disks, creating the high-temperature ring so-called the centrifugal barrier (Oya et al. 2016).

In this context, the main goals of the present PhD project can be summarized as follows:

1. Which is the spatial distribution of iCOMs and D-bearing species once observed at Solar System scales? In other words, which is the picture of a jet/disk protostellar system once we go beyond the classical 100 au frontier? Which is the inner structure and kinematics of a Class 0 protostar? In Chap. 4 we provide some answers by analysising emission due to methanol isotopologues, acetaldehyde and deuterated water towards the HH212 protostar. In particular, we report the first measurements of methanol deuteration in a Class 0 object on a Solar System scale (see also Bianchi et al. 2017b).

2. which is the the chemical content of a more evolved Class I source, in both iCOMs emission and deuterium fractionation? Is there any evolutionary trend in the comparison with earlier Class 0 protostars? In Chap. 5 we attack these topics by studying iCOMs emission as well as organics deuteration (Bianchi et al. 2017a). towards the Class I protostar SVS13-A.

3. Can we provide robust constraints for state-of-the-art chemical models aimed to follow the chemical content of a Sun-like star forming region, from cold cores to protoplanetary disks? We tackle these issues in Chap. 5, where we exploit in this context an IRAM-30m unbiased spectral survey.

2 Methods

2.1 Radiative transfer

The propagation of the radiation through a medium is described by the equation of transfer (see e.g. a classical book as Wilson et al. 2013):

$$\frac{dI_\nu}{ds} = -k_\nu I_\nu + \varepsilon_\nu \tag{2.1}$$

where I_ν is the source brightness for a given frequency, k_ν is the absorption coefficient and ε_ν is the emissivity. Under the hypothesis of Thermodynamic Equilibrium (TE), namely if the radiation is in equilibrium with its surroundings, the source brightness can be descibed by the Planck function:

$$B_\nu(T) = \frac{2h\nu^3}{c^2}\left(\frac{1}{e^{h\nu/kT} - 1}\right), \tag{2.2}$$

which describes the spectral distribution of the radiation of a black body in thermodynamic equilibrium and depends only on the temperature T; h and k are the Planck and Boltzmann constants respectively . Real systems are very different from ideal systems, for this reason is more convenient to define the Local Thermodynamic Equilibrium (LTE). It is a less strict condition than TE and it holds whenever the medium has a well-defined temperature on scales much greater then the free mean path of a photon. In this way all the real systems (which are not in full TE because the temperature varies in the different regions) can be described

as a collection of local regions each one characterised by a single temperature. In LTE conditions holds Kirchhoff's law:

$$\frac{\varepsilon_\nu}{k_\nu} = B_\nu(T) \tag{2.3}$$

Defining the optical depth $d\tau_\nu$ as

$$d\tau_\nu = -k_\nu ds \tag{2.4}$$

the transport equation (Eq. 2.1) can be written as follows:

$$-\frac{1}{k_\nu}\frac{dI_\nu}{ds} = \frac{dI_\nu}{d\tau_\nu} = I_\nu - B_\nu(T) \tag{2.5}$$

and integrated (see e.g. Wilson 2009)

$$I_\nu(s) = I_\nu(0)e^{-\tau_\nu(s)} + \int_0^{\tau_\nu(s)} B_\nu(T(\tau))e^{-\tau}d\tau\,. \tag{2.6}$$

If T is constant (LTE condition), the general solution is then:

$$I_\nu(s) = I_\nu(0)e^{-\tau_\nu(s)} + B_\nu(T)(1 - e^{-\tau(s)})\,. \tag{2.7}$$

Considering a source emitting as a black body; if $h\nu \ll kT$, then the Planck function become the Rayleigh-Jeans relation:

$$B_{RJ}(\nu, T) = \frac{2\nu^2}{c^2}kT\,. \tag{2.8}$$

We can also define a radiation temperature, $J(T)$ as

$$J(T) = \frac{c^2}{2k\nu^2}I = \frac{h\nu}{k}\frac{1}{e^{h\nu/kT} - 1} \tag{2.9}$$

Substituting the numerical constants k and h we obtain

$$\frac{\nu}{GHz} \ll 20.84\left(\frac{T}{K}\right)\,. \tag{2.10}$$

This relation shows that the source brightness distribution is proportional to

the temperature of the black body which is emitting the radiation. For this reason it is common to express the brightness of a source using the brightness temperature

$$T_b = \frac{c^2}{2k}\frac{1}{\nu^2}I_\nu = \frac{\lambda^2}{2k}I_\nu \,. \tag{2.11}$$

For every source T_b is defined as the temperature that would have a black body emitting the same source brightness. The source total flux is obtained by integrating the brightness I_ν over the solid angle Ω

$$S_\nu = \int_{\Omega_s} I_\nu(\theta,\varphi) cos\theta d\Omega \,. \tag{2.12}$$

For the small flux density of the astronomical sources the used unit is Jansky (Jy)

$$1\,\mathrm{Jy} = 10^{-26}\,\mathrm{W\,m^{-2}\,Hz^{-1}} = 10^{-23}\,\mathrm{erg\,s^{-1}\,cm^{-2}\,Hz^{-1}} \,. \tag{2.13}$$

Combining Eq. 2.11 and Eq. 2.12 we obtain

$$S_\nu = \frac{2k\nu^2}{c^2} T_b \Delta\Omega \tag{2.14}$$

which describes how it is possible to determine the true source brightness temperature T_b if the flux density S_ν and the source size are known.

2.2 Spectral line fundamentals

The interaction between radiation and matter can be described using the Einstain coefficients. If the intensity of the radiation field is I_ν then the average intensity is

$$\bar{I} = \int I_\nu \phi(\nu) d\nu \tag{2.15}$$

where $\phi(\nu)$ is the line profile function, normalize so that

$$\int \phi(\nu) d\nu = 1 \,. \tag{2.16}$$

Then the average energy density of the radiation field is

$$\overline{U} = \frac{4\pi\bar{I}}{c} \,. \tag{2.17}$$

Consider a system with a lower energy state E_l and an upper level energy E_u, as illustrated in Fig. 2.1. Three different processes can occurr: (i) spontaneous

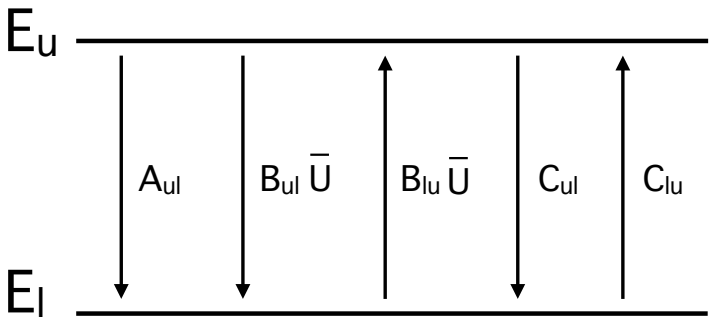

Figure 2.1: Sketch of two energy levels in a molecules. One photon, of energy $h\nu$, can be absorbed by an electron inducing a transition from a lower energy state E_l to an upper level with energy E_u. On the other hand the transition from E_u to E_l can occurr emitting a photon. In particular, A_{ul}, B_{ul} and B_{lu} represent the Einstein coefficents for spontaneous emission, absorption, and stimulated emission, respectively. C_{ul} and C_{lu} are the collisional coefficients (see text).

emission,

$$A_{ul} n_u = -\left(\frac{dn_u}{dt}\right)_{spon.emiss.} = \left(\frac{dn_l}{dt}\right)_{spon.emiss.} \tag{2.18}$$

(ii) absorption, and

$$B_{ul} n_u \overline{U} = -\left(\frac{dn_u}{dt}\right)_{stim.emiss.} = \left(\frac{dn_l}{dt}\right)_{stim.emiss.} \tag{2.19}$$

(iii) stimulated emission,

$$B_{lu} n_l \overline{U} = \left(\frac{dn_u}{dt}\right)_{abs.} = -\left(\frac{dn_l}{dt}\right)_{abs.} \,, \tag{2.20}$$

where n_l and n_l indicates the number density of particles in the lower and upper energy state, respectively. In LTE conditions the radiation follows the Planck function $B_\nu(T)$ and the Einstein coefficients (A_{ul}, B_{lu} and B_{ul}; [s^{-1}]) are not indipendent but related by the Kirchhoff's law (2.3)

$$\left(\frac{dn_u}{dt}\right)_{abs.} + \left(\frac{dn_u}{dt}\right)_{spon.emiss.} + \left(\frac{dn_u}{dt}\right)_{stim.emiss.} = 0\,, \tag{2.21}$$

which implies

$$B_{lu} = \frac{g_u}{g_l} B_{ul} \tag{2.22}$$

and

$$B_{ul} = \frac{c^2}{2h\nu_{ul}^3} A_{ul} \tag{2.23}$$

If some cases the LTE conditions are not verified. A more general treatment should include the role of the collisions. If we include (see Fig. 2.1) to the rate equation the terms for collisional excitation (C_{lu}; [$cm^3 s^{-1}$]) and de-excitation (C_{ul}; [$cm^3 s^{-1}$]) rates we have:

$$n_u(A_{ul} + B_{ul}\overline{U} + C_{ul}) = n_l(B_{lu}\overline{U} + C_{lu}) \tag{2.24}$$

where $\overline{U}$ is the average radiation field intensity:

$$\overline{U} = \frac{4\pi}{c} \times \bar{I} = \frac{8\pi h\nu^3}{c^3} \frac{1}{exp(h\nu/kT_{bg}) - 1} \tag{2.25}$$

with T_{bg} is the background temperature. The collision rate C_{ul} (or C_{lu}) for two general levels u and l depends on the number density of the collision partern n_{coll} as

$$C_{ul} = \gamma_{ul} \times n_{coll}\,, \tag{2.26}$$

where γ_{ul} [cm^3 s^{-1}] is the velocity-integrated collision cross section:

$$\gamma_{ul} = \int \sigma_{ul} V f(V) dV \tag{2.27}$$

with $f(V)$ being the velocity distribution function of the colliding particles.

In principle, collisions with any of the many different chemical species present in the ISM will contribute towards C_{ul}, but in practice, the main contributors are few key species like H_2, He, and free electrons. If collisions dominate then the collision rates are related by

$$\frac{C_{lu}}{C_{ul}} = \frac{n_u}{n_l} = \frac{g_u}{g_l} exp\left(-\frac{h\nu}{kT_k}\right) \tag{2.28}$$

where T_k is the kinetic temperature. The relation holds even when the system is not in LTE conditions. If we neglet the background radiation field ($h\nu \gg kT_{bg}$) we can use Eq. 2.24 to obtain:

$$\frac{n_u}{n_l} = \frac{(g_u/g_l)e^{E_{ul}/kT_k}}{1 + A_{ul}/C_{ul}} \,. \tag{2.29}$$

From Eq. 2.24, Eq. 2.25 and Eq. 2.28 we then obtain

$$T_{ex} = \frac{h\nu/k}{h\nu/kT_k + ln(1 + A_{ul}/C_{ul})} \,. \tag{2.30}$$

When collisions dominate over radiative decays we have $C_{ul} \gg A_{ul}$. Then the level populations approach their LTE values and $T_{ex} \rightarrow T_k$. In the other limit ($C_{ul} \ll A_{ul}$), collisional excitations are balanced by radiative de-excitations, and collisional de-excitations are negligible. We can therefore define a critical density which is the parameter that discriminate between the two regimes

$$n_{cr} = A_{ul}/\gamma_{ul} \tag{2.31}$$

When $n \gg n_{cr}$, collisions dominate and the level populations tend to LTE values. On the other hand when $n \ll n_{cr}$, radiative decay dominates and the bulk of the atoms are in the ground states.

2.3 Rotation diagram analysis

The equation of transfer, which relates the integrated area of the observed line to a u→l transition to the column density of the molecular species is

$$\int T_b dV = \Big[J_\nu(T_{ex}) - J_\nu(T_{bg})\Big](1 - e^{-\tau}) \tag{2.32}$$

where T_{ex} is the excitation temperature of the observed transition u→l, and T_{bg} is the background brightness temperature. Takin into account that

$$\int \tau dV = \frac{c}{\nu} \int \tau d\nu \,, \tag{2.33}$$

the opacity is then

$$\int \tau d\nu = \frac{c^2}{\nu^2} \frac{A_{ul}}{8\pi} \frac{g_u}{g_l} N_l \Big[1 - e^{h\nu/kT_{ul}}\Big] \,. \tag{2.34}$$

In the case of optically thin lines ($\tau \ll 1$) and $J_\nu(T_{bg}) \ll J_\nu(T_{ex})$ using Eq. 2.32 and Eq. 2.33, the upper level column density can be written as:

$$n_u = \frac{8\pi k \nu^2}{hc^3 A_{ul}} \int T_b dV \tag{2.35}$$

where k is the Boltzmann constant, ν is the frequency of the transition, h is the Planck constant, c is the light speed, Aul is the Einstein coefficient and the integral is the velocity integrated line intensity.

In LTE, the energy levels are populated according to the Boltzmann distribution for the temperature T.

$$n_u = \frac{g_u}{g_l} exp\,(-E_u - E_l/kT)\, n_l \tag{2.36}$$

with g_u and g_l the statistical weights of the u and l level.

If we consider all the energy levels then

$$\frac{n_u}{g_u} = \frac{n_{tot}}{Q(T)} e^{-E_u/kT} \,, \tag{2.37}$$

where

$$n_{tot} = \sum n_l \tag{2.38}$$

and $Q(T)$ is the partition fuction at a given temperature, defined as

$$Q(T) = \sum g_l exp\left(-\frac{E_l}{kT}\right). \tag{2.39}$$

If we consider an isothermal cloud, we can integrate along the line-of-sight so that

$$N_u = \int n_u ds \tag{2.40}$$

and

$$N_{tot} = \int n_{tot} ds \tag{2.41}$$

Taking the natural logarithm, we have:

$$ln\left(\frac{N_u}{g_u}\right) = ln\left(\frac{N_{tot}}{Q(T)}\right) - \frac{E_u}{kT} \tag{2.42}$$

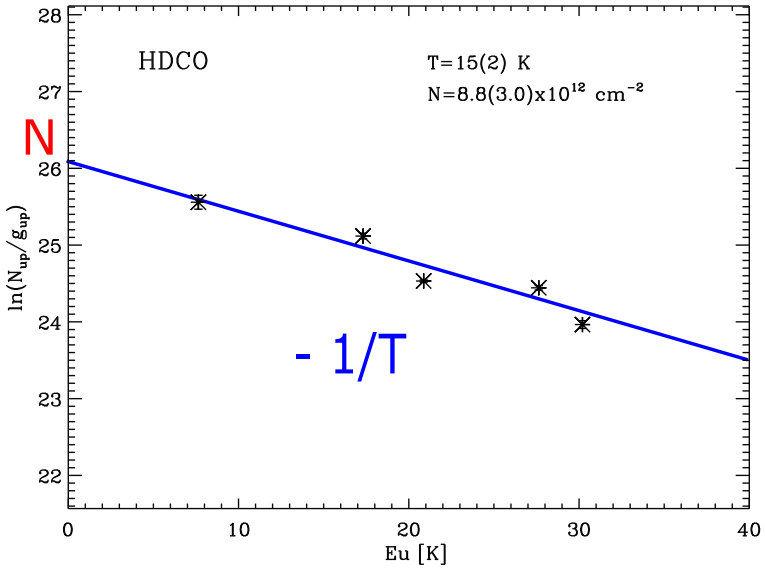

Figure 2.2: Schematic view of a rotation diagram: in the x-axis there are the upper level energies of the observed transitions, expressed in K. After fitting the data using a y = ax+b line, then a = –1/T and b = ln(N_{up}/g_{up}). In other words the slope of the best fit to the data points allow us to find the rotational temperature while the intercept, at E_{up}=0, is the total gas column density.

If we have several observed line transitions, we can plot

$$y = ln\left(\frac{N_u}{g_u}\right) \tag{2.43}$$

versus $x = E_u$, as shown schematically in Fig. 2.2 The best fit to the data points allow one to derive the rotational temperature while the intercept is the total gas column density.

2.3.1 Multiplets

In some cases the spectral resolution of the observation does not allow one to resolve the single transitions. We observe only one line which consists of several transitions i of the same molecule with very close frequencies and the same upper level energy E_u, but different Einstein coefficients $A_{ul}(i)$ and degeneracies $g_u(i)$. These unresolved multiplets require to be treated using the following method in the rotation diagram analysis. The observed intensity is the sum of the integrated intensity of the single i transitions, so that

$$I = \sum_i I(i) \tag{2.44}$$

Given that the transitions have the same E_u, Eq. 2.35 become

$$\frac{n_u(i)}{g_u(i)} = \frac{8\pi k\nu^2}{hc^3}\frac{\int T_b dV}{\sum_i (A_{ul}(i)g_u(i))} \tag{2.45}$$

This method has been applied to the analysis of molecular lines in Sec. 5.3.4.

2.3.2 Large Velocity Gradient (LVG) approach

So far we treated only the optically thin case. When the lines are not optically thin we can solve the radiative transfer takin into account high optical dephts with the Large Velocity Gradient (LVG) approximation. This model assumes that the cloud is spherically symmetric and that the systematic velocity is a function of distance from the center of the cloud $V = V_0(r/r_0)$. Under these assumptions, a photon emitted by a two level system at one position in the cloud can only interact

with those that are nearby, reducing the global problem of photons transport to local problem. More specifically, we can define a probability β that a photon emitted at a radius r will escape from the cloud. The β parameter can be expressed as a function of the optical depth τ:

$$\beta = \frac{1 - e^{-\tau}}{\tau} \tag{2.46}$$

for a radially expanding sphere. The excitation temperature can then be expressed as:

$$T_{ex} = \frac{h\nu}{h\nu/kT_k} + ln(1 + A_{ul}\beta/C_{ul}) \tag{2.47}$$

This method has been applied to the analysis performed in Sec. 4.3 and Sec. 5.2.

2.4 Molecular lines

The structure of molecules is more complex than that of atoms. In particular, transitions can be divided in three components, according to the different energies W:

$$W^{tot} = W^{el} + W^{vib} + W^{rot} \tag{2.48}$$

W^{el} are the energies corresponding to electronic transitions (typically few eV) which can be observed in the in the ultraviolet (UV) and visible. W^{vib} are typically between 0.1 eV and 0.01 eV corresponding to vibrational transitions caused by the oscillations of the relative positions of the nuclei. These lines are observable mainly in the infrared region of the spectum. W^{rot} (typical energies of $\cong 10^{-3}$ eV) are relative to rotational transitions responsible to the line emissions observed from the cm to the mm and submm range. More specifically, if we consider only the mm/submm wavelenght ranges, the only observable transitions are rotational or vibrational. For the simplest case of a diatomic molecules (like CO), the rotational energy levels can be obtained by resolving the Schrödinger equation in the rigid rotor approximation:

$$E(J) = BJ(J + 1) \tag{2.49}$$

where J is the quantum number for the total rotational angular momentum, and B

is the rotational constant, related to the moment of inertia I of the molecule

$$B = \frac{h}{8\pi^2 cI} \tag{2.50}$$

where

$$I = \mu r^2 \tag{2.51}$$

while μ is the reduced mass and r the bond lenght.

However for all the molecules with more than two atoms, this simple approximation is not valid and their treatment is more complex. More specifically, the rotation of any molecule with an arbitrary shape can be describe as the superposition of three free rotations about the three principal axes. All the iCOMs analysed in this work are *asymmetric top* molecules. In this case the molecule have three

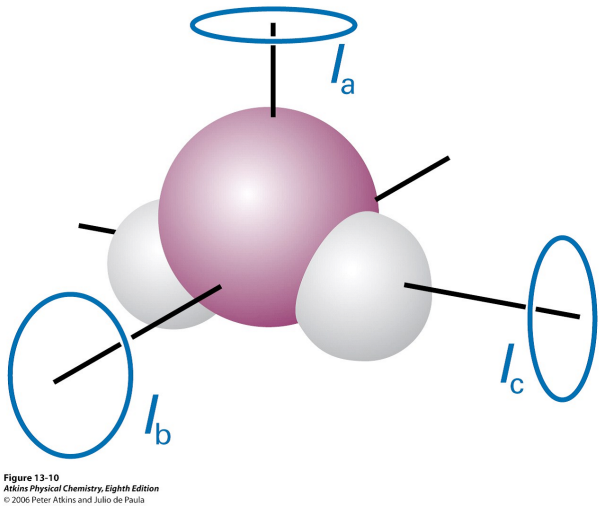

Figure 2.3: Schematic view of a water molecule showing its three distinct principal moment of inertia. Fig. from *Atkins Physical Chemistry*, 2006, Oxford University Press. Inc. New York, 2006, 8th Edition.

different moments of inertia I_a, I_b, and I_c associated with each axis (see Fig. 2.3) and corresponding to the rotational constants

$$A = \frac{h}{8\pi^2 cI_a} \tag{2.52}$$

$$B = \frac{h}{8\pi^2 c I_b} \tag{2.53}$$

$$C = \frac{h}{8\pi^2 c I_c} \tag{2.54}$$

with $I_a < I_b < I_c$. The energy levels are indicated by the quantum numbers J, K_a and K_c. K_a and K_c are in the case of symmetric top molecules, the projection of J on the assigned axis of symmetry. For asymmetric top molecules the two quantum numbers K_a and K_c have not the same simple meaning but are the projection of J for the limiting cases of oblate ($I_a = I_b < I_c$) and prolate ($I_a < I_b = I_c$) tops.

2.4.1 Spin statistic

The total wavefunction of a molecule is the product of the spin and the rotational wavefunctions. In the case of molecules containing identical nuclei, for example H_2, the symmetry of the spin wavefunction will depend on the relative orientations of the spins. If the spin wavefunction is symmetric, we have the *ortho*-modification of the molecule while if antisymmetric we have the *para*-modification. In the ISM, in conditions of thermal equilibrium, the exchange between the two modifications occur very slowly (on time scales $> 10^6$ years). The ortho and para modifications of a species can then be considered as different molecules.

3 Observations

As reported in Chap. 1, stars form in dark molecular clouds where the extinction is large and observations in the infrared or in the optical are limited. To observe these dense and deeply embedded regions the use of millimeter and submillimeter telescopes (both single-dish antennas and interferometers) is crucial. In addition, the (sub)mm domain is the spectral region where the bulk of the lines due to rotational and vibrational molecular transitions are falling. Nevertheless, (sub)mm bands are affected from atmospheric noise. In particular, there is a cut-off at about 300 GHz ($\lambda \sim 1$mm) due to the resonant absorption of the lower rotation bands of molecules in the troposphere. The main atmospheric noise components are due to water vapour H_2O, responsible of strong bands at 184 GHz (1.63 mm). Also O_2 contributes with absorption lines near 60 GHz (5 mm) and a single line near 119 GHz (2.52 mm). Moreover, the tropospheric events are characterized by various phenomena, such as turbolence and variation of the refraction index that contribute to add noise to the astrophysical signal. The only way to extend the observable frequency window is by doing the measurements from sites where air has a low water content. This is the reason for the choice of the telescope location at so elevate altitude and in dry climate places with a medium precipitable water vapour (pwv) value of about $\sim$ 1mm.

In this chapter I will give an overview of the basics concepts of single-dish and interferometric observations. A more comprehensive treatment is out of the scope of the present PhD thesis and it can be found in the classical texts, e.g. Kraus (1986, *Radio Astronomy*, Cygnus-Quasar Books) and Wilson et al. (2013). More

Figure 3.1: The IRAM-30m antenna at Pico Veleta, near Granada, Spain.

specifically, I will describe the observations with IRAM-30m antenna and ALMA interferometer (see Fig. 3.1 and Fig. 3.2), analysed in Chap. 5 and in Chap. 4, respectively.

3.1 Single-dish antennas: basic concepts

A single dish antenna is a parabolic reflector which collect the radiation and reflect it to a central focus. Consider an antenna pointing a source with brightness $I(\nu, \theta, \phi)$, where ν is the frequency and θ and ϕ are the angular coordinates (see Fig. 3.3). The power pattern of the antenna consist of a large main lobe (called main beam) in the forward direction and small sidelobes in the other directions.

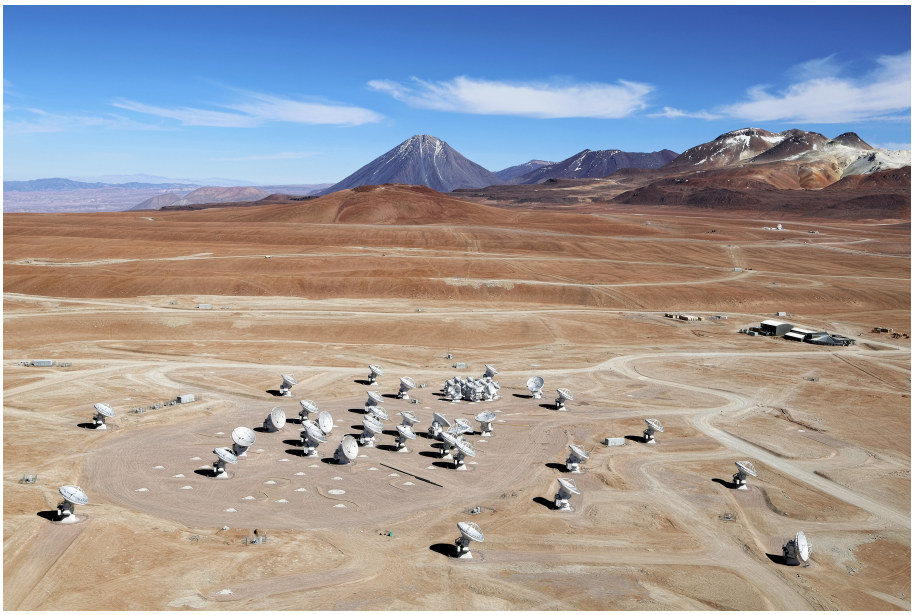

Figure 3.2: Aerial view of the ALMA array on the Chajnantor Plateau, Chile. Credit: Clem & Adri Bacri-Normier (wingsforscience.com)/ESO.

The width of the main lobe is usually indicated by the half power beam width (HPBW), which is the angle from where the recived radiation decrease by the 50% from the peak in the main beam.

The minimum angular distance that can be resolved in the observed image is indicated as the angular resolution. For a single telescopes this quantity scales as

$$\vartheta \approx \frac{\lambda}{d} \tag{3.1}$$

where λ is the wavelenght of the observations and d is the antenna diameter.

The power P received by the antenna from an element of solid angle $\Delta\Omega$ in the bandwidth $\Delta\nu$ is

$$P = I(\nu, \theta, \phi)A(\nu, \theta, \phi)\Delta\Omega\Delta\nu \tag{3.2}$$

where $A(\nu, \theta, \phi)$ is the antenna reception pattern, normalized to A_E (effective antenna aperture), the antenna response at the center of the main lobe.

If we consider $P_n(\theta, \phi)$ (the powern pattern normalized to its maximum) then

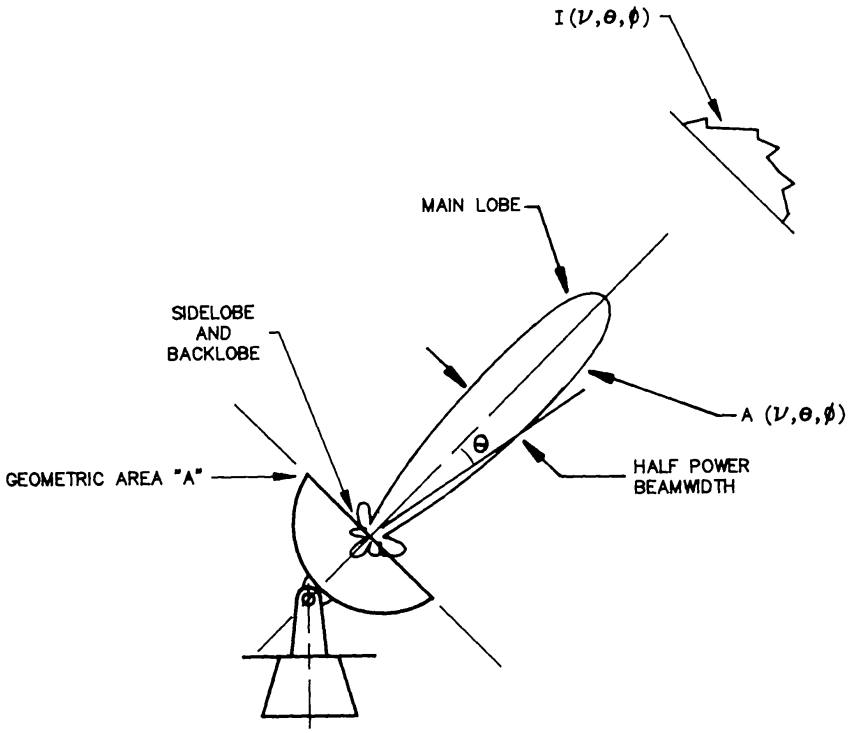

Figure 3.3: The reception pattern of an antenna (Napier 1999).

the total power per unit bandwidht is

$$P_\nu = mA_E \int\int I(\nu,\theta,\phi)P_n(\theta,\phi)d\Omega \tag{3.3}$$

where m=1/2 for a single dipole antenna which is sensitive to a single polarisation. The beam solid angle of the power pattern is:

$$\Omega_A = \int_{4\pi} P_n(\theta,\phi)d\Omega \tag{3.4}$$

while the main beam solid angle is given by

$$\Omega_{mb} = \int_{mb} P_n(\theta,\phi)d\Omega \tag{3.5}$$

The efficency is a parameter considering all the effects that can reduce the

antenna performaces. Two important parameters are the forward efficency:

$$\eta_F = \frac{\Omega_{2\pi}}{\Omega_A} \tag{3.6}$$

and the main-beam efficency:

$$\eta_{mb} = \frac{\Omega_{mb}}{\Omega_A} \tag{3.7}$$

which is a measure of how the power pattern is well concentrated in the main beam.

Using the Nyquist theorem we can introduce the antenna temperature T_A, which is the temperature of a resistance that would lead to a power equal to that of the antenna:

$$P_\nu = kT_A \tag{3.8}$$

with P_ν being the total power per unit bandwidth.

If a source has a constant brightness temperature T_b then

$$T'_A = \frac{\int_{source} P_n(\vartheta, \varphi d\Omega)}{\int_{4\pi} P_n(\vartheta, \varphi d\Omega)} T_b \tag{3.9}$$

where T'_A is the antenna temperature corrected for the atmospheric attenuation.

The Main-Beam temperature (T_{MB}) is the beam-averaged brightness temperature of a source over the solid angle of the main beam. This quantity is related to T_A:

$$T_{MB} = \left(\frac{\eta_F}{\eta_{mb}}\right) T^*_A \tag{3.10}$$

where η_F is the forward efficency, η_{mb} is the main-beam efficency, and T^*_A is the antenna temperature corrected not only for the atmospheric absorption but also for the rear-sidelobes. If the source is unresolved, the signal recived in the beam will be diluted, so that a further correction is needed (beam-filling factor). The relation is

$$T_{MB} = \left(\frac{\eta_F}{\eta_{mb}}\right)\frac{1}{\eta_{bf}}T_A^* \tag{3.11}$$

with

$$\eta_{bf} = \frac{\theta_s^2}{\theta_s^2 + \theta_b^2} \tag{3.12}$$

with θ_s and θ_b are the angular source and the beam sizes (assumed to be both a circular Gaussian).

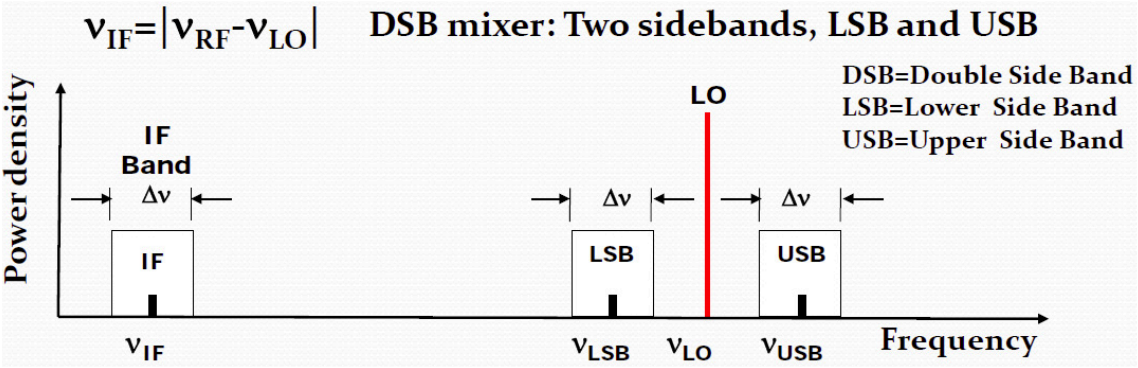

Figure 3.4: The sidebands of a heterodyne receivers (from C. Kramer, *Millimeter calibration*, 8th IRAM-30m Summer School, 2015).

The observed sky frequency need to be down-converted to a lower frequency to send the signals to the back hands as for istance an hetorodyne correlator. This process involves a Local Oscillators (LO) as shown in Fig. 3.3. The mixer produces a shift in frequency of an input sky signal by mixing it with the LO signal. In this way the observing frequency is down-converted into an Intermediate Frequency (IF) with no other effect on the signal properties. In Double Sideband (DSB) mixer operation, the mixing processes creates two sidebands, a lower sideband (LSB) and an upper sideband (USB), also called the signal and image bands. However in some cases is preferable to operate in sigle sideband (SSB). This is the case of single dish spectral line observations, where the line of interest is in only one of the sideband and the other sideband is a source of extra noise and lines confusion. The image sideband can be then eliminated and the mixer operates in SSB mode. For more details see e.g. Wilson (2009).

3.2 The IRAM-30m large program ASAI

The IRAM-30m telescope is a single-dish antenna located on Pico Veleta in the Spanish Sierra Nevada, at an altitude of 2850m. The telescope is equipped with the Eight MIxer Receiver (EMIR) to offer a bandwidth of up to 16 GHz in each of the two orthogonal linear polarisations for the 3, 2, 1.3 and 0.9mm atmospheric windows. The four EMIR bands are designated as E090, E150, E230, and E330 according to their approximate center frequencies in GHz. The telescopes efficencies are reported in the webpage[1]. The atmospheric trasmission at the IRAM-30m site and the EMIR bands are shown in Fig. 3.5.

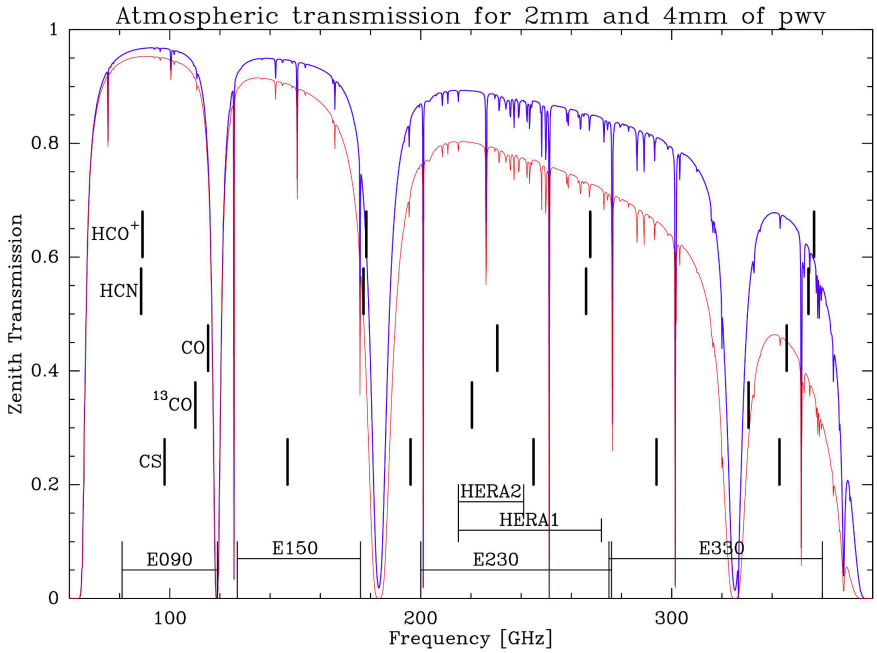

Figure 3.5: Atmospheric transmission for 2 mm and 4 mm of precipitable water vapour (pwv) at the site of the 30m telescope. The EMIR bands are marked together with the frequencies of a few important molecular transitions (Credits: IRAM website, www.iram-institute.org).

[1] http://www.iram.es/IRAMES/mainWiki/Iram30mEfficiencies

For IRAM-30m antenna the observed HPBWs can be well fitted by

$$HPBW['] = \frac{2460}{\nu[GHz]} \tag{3.13}$$

The observations of SVS13-A, analysed in Chap. 5 were carried out with IRAM-30m telescope, in the framework of the Astrochemical Surveys At IRAM[2] (ASAI) Large Program. The data consist of an unbiased spectral survey acquired during several runs between 2012 and 2014, using the broad-band EMIR receivers. Observations were carried out with very good to excellent, stable weather conditions. In particular the observed bands are at 3 mm (80–116 GHz), 2 mm (129–173 GHz), and 1.3 mm (200–276 GHz). The observations were acquired in wobbler switching mode in order to obtain high quality baselines. This procedure uses the wobbling secondary reflector to switch between the source (ON position) and a reference position located at a wobbler throw in azimuth from the source (OFF position). The maximum angular offset allowed by the wobbler mode is, in the present case, 180″. In some cases (see Chap. 5), such a value is not large enough to avoid the contaminations of line emission occurring in the OFF position. This could be avoided by using another observing mode, i.e. the position switching mode; in this case the OFF position is observed in any region of the sky, not necessarily nearby the source. However the baselines collected in the OFF position could be slightly different from that in the ON position, providing worse baselines than wobbler mode. In conclusion, the high quality baselines make the wobbler switching mode the best approach for a spectral survey with the goal to detect (also) weak lines (see Chap. 5).

For SVS13-A the wobbler throw was of 180″ towards the source coordinates, namely $\alpha_{J2000} = 03^h\ 29^m\ 10\overset{s}{.}42$, $\delta_{J2000} = +31^\circ\ 16'\ 0\overset{''}{.}3$. The pointing was checked by observing every our on the nearby continuum sources 0316+413 and 0333+321, and was found to be accurate to within 2″–3″. The telescope HPBWs range between $\simeq 9''$ at 276 GHz to $\simeq 30''$ at 80 GHz.

Because of the high sensitivity of the ASAI observations, the line contamination from the image band cannot be ignored. In order to permit an easier lines identification from the image band, the LO frequency was regularly shifted by a fixed amount of 50 MHz. As an example, Fig. 3.6 show the contamination of the

[2] www.oan.es/asai

bright ^{13}CO(1–0) line at 110201.354 MHz from the image band. Spurious features

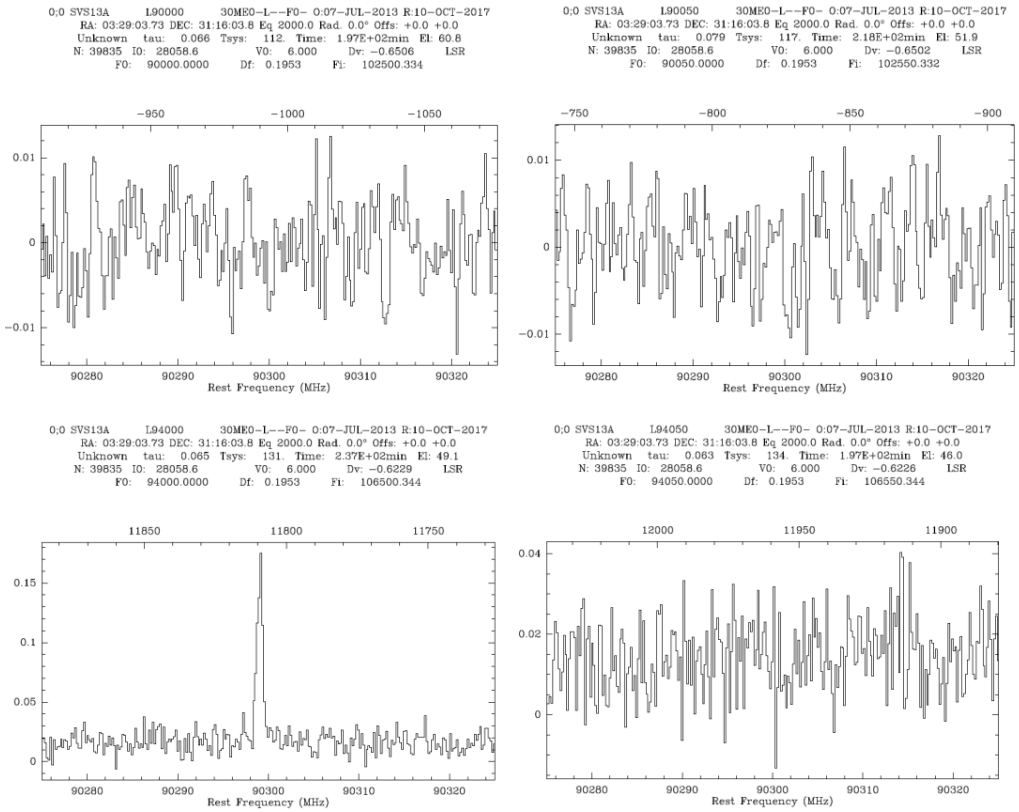

Figure 3.6: Examples of contamination from the image band: the bottom-left panel show the attenuated ghost of the bright ^{13}CO(1–0) line at 110201.354 MHz.

were corrected in close collaboration with the IRAM receiver engineers group (for details see Lefloch et al. 2017, in preparation). The data reduction was performed using the GILDAS–CLASS[3] package. Calibration uncertainties are stimated to be $\simeq$ 10% at 3 mm and $\sim$ 20% at lower wavelengths. Note that some lines (see Sect. 5.2.2) observed at 2 mm and 3 mm (i.e. with a HPBW $\geq$ 20″) are affected by emission at OFF position observed in wobbler mode. Line intensities have been converted from antenna temperature to main beam temperature ($T_{\rm MB}$), using the

[3]http://www.iram.fr/IRAMFR/GILDAS

main beam efficiencies reported in the IRAM-30m website[4]. The typical rms are 2.0–4.8 mK at 3mm, 4.2–5.1 mK at 2mm and 4.3–4.6 mK at 1.3 mm, respectively.

3.3 Interferometers: basic concepts

The angular resolution of a single telescope is given by (Eq. 3.1), being d the antenna diameter. The telescope capability to resolve very small regions would be thus limited because of the practical problems related to the increase of the antenna diameter. This problem can be overcome using array of antennas working togheter in interferometry. The telescope angular resolution (also called synthesized beam) then become $\vartheta \approx \lambda/D$ where D is the maximum distance between two antennas with an improvement of several orders of magnitude in the angular resolution.

Every interferometer composed by N>2 elements, can be described considering N(N-1)/2 pairs of radio antennas. The basic unit is the two-element interferometer, illustrated in Fig. 3.7. A pair of antennas observing the same source at the same frequency will recive a wavefront at different times because of the geometric delay (τ_g). The signal from the single antennas (V_1 and V_2 in Fig. 3.7) are then multiplied and coherently integrated in time by the correlator, taking into account this delay. The output voltage of the interferometer correlator (R) varies sinusoidally with the change of source direction in the interferometer frame, yielding the interferometer fringes. In particular, if the interferometer is observing a source with a brightness distribution I_ν, the telescope response is described by the visibility function:

$$V_\nu(u,v) = \int\int A(x,y) I_\nu(x,y) e^{-2\pi i(ux+vy)} dxdy \tag{3.14}$$

where V_ν is the Fourier transform of the sky brightness distribution $I_\nu(x,y)$ modified by the primary beam shape $A(x,y)$. Visibility is a complex function with amplitude depending only on the source strength and phase on its position. It can be inverted as:

$$A(x,y) I_\nu(x,y) = \int\int V_\nu(u,v) e^{2\pi i(ux+vy)} dudv \tag{3.15}$$

[4]http://www.iram.es/IRAMES/mainWiki/Iram30mEfficiencies

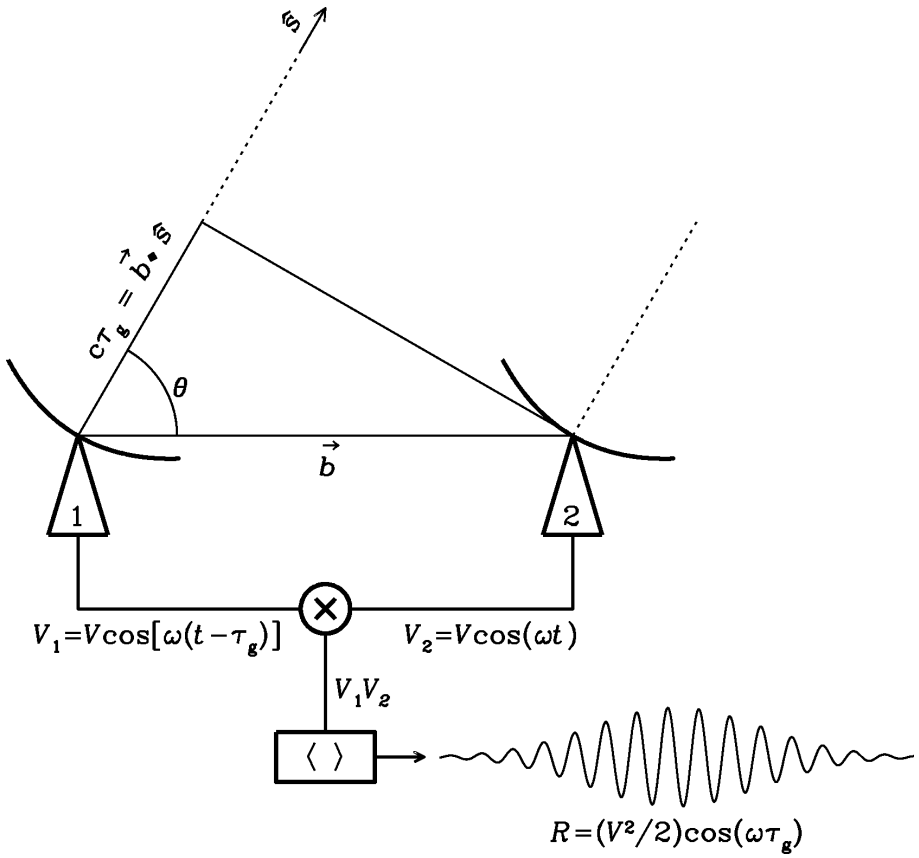

Figure 3.7: Cartoon showing a two-element interferometer. (From NRAO website: www.cv.nrao.edu).

The primary beam is the HPBW of the individual array elemet, which gives also the telescope field of view (FoV) $\sim \lambda/d$. The Fourier plane is called *uv*-plane and contains the coordinates in wavelenght of all the measured visibilities. One of the main differences between interferometric and single-dish observations is that while the latter is a filled-aperture antenna, in the case of an interferometer the visibility function V_ν is not sampled everywhere, but only at specific points of the *uv* plane. The telescope capability to reconstract the image of the real observed source improves with increasing *uv* coverage. Given that the *uv* coordinates describe the baselines projected in the plane perpendicular to the source direction, the *uv* coverage improves moving the antennas to obtain different baselines spac-

ing. This is done using the aperture synthesis tecnique which take advantage of the Earth rotation to sample the *uv* plane. Indeed the Earth's rotation make the baseline vector between two antennas, as seen from a distant source, continuously changing. Another important difference of an interferoment with respect to a single-dish is that the first acts as a spacial filter. More specifically, the sky emission with large angular sizes corresponding to Fourier components at spacing shorter than the smaller baseline are invisible for an interferometer. The smaller baseline is always limited to the smaller physical separation of two antennas, so that for extended sources there is always some missing flux which can be eventually recovered complementing the interferometer measumerements with single-dish observations. Finally, the point-source sensitivity σ_s of a standard array is given by:

$$\sigma_s = \frac{2kT_{sys}}{\eta A_{eff}\sqrt{N(N-1)n_p\Delta\nu t_{int}}} \tag{3.16}$$

where A_{eff} is the telescope effective area, η is the efficency, N is the number of antennas and n_p is the number of polarizations. $\Delta\nu$ is the widht of the spectral resolution element and t_{int} is the total on-source integration time. T_{sys} is the system temperature and is build up of a number of terms that contribute to the noise. The principal elements are the environment, sky and receiver temperatures and the fractional transmission of the atmosphere. The interferometer sensitivity can be substantially improved by increasing the number of the antennas, the bandwidth, and/or the integration time.

Once obtained the interferometer observed visibilies, it is necessary to perform a calibration process and finally a cleaning process to reconstract the source image. During the calibration, all the data with unexpected behaviours, resulting from instrumental errors or contaminated by atmospheric lines are flagged. Successively using the observations of the calibrators, the bandpass, flux density, and phase calibration are applied to the target data. The last step is the cleaning process which produce the final source image from the visibility data. More specifically, for spectral lines observations a first clean procedure in the multi-frequency synthesis mode is performed to generate the continuum image. The continuum flux density is then subtracted from the image to generate the continuum-free spectral line images. The next step is then performed in channel mode, selecting only chan-

nels containing the spectral lines of interest. The output of the imaging process is an image datacube, with a frequency (or velocity) channel axis in addition to the two sky coordinate axes. For a more detailed description of the procedures used to analysed interferometric data we refer again to a classical text such as Wilson et al. (2013).

3.4 ALMA Cycle 1 and Cycle 4 observations

The Atacama Large Millimeter/Submillimeter Array (ALMA) is an aperture syntesis telescope composed of 66 high-precision reconfigurable antennas that works in the millimeter/submillimeter band. The array is located on the Chajnantor plain of the Chilean Andes, a site that normally offers the exceptionally dry and clear sky conditions required to observe at millimeter and sub-millimeter wavelengths. The telescope is an international astronomy facility, it is a partnership of East Asia, Europe and North America in cooperation with the Republic of Chile. The Joint ALMA Observatory (JAO) is responsible for the overall leadership and management of construction, commissioning and operations of ALMA in Chile. The three ALMA regional partners (Executives) maintain ALMA Regional Centers (ARCs) within their respective regions. They are the East Asian ARC (EA ARC), based at the National Astronomical Observatory of Japan headquarters in Tokyo; the European ARC (EU ARC), organized as a coordinated network of scientific support nodes distributed across Europe, and the North American ALMA Science Center (NAASC), based at NRAO headquarters in Charlottesville, VA, USA. The ARCs provide the interface between the ALMA project and its user communities, mainly in the areas of proposal preparation, observation preparation, acquisition of data through the archive, data reduction, data analysis, delivery of data, and community formation and outreach.

Early Science Operations started in 2011 and the array was officially inaugurated in March 2013. The most recent ALMA operation cycle (Cycle 5) has started in October, 2017. The interferometer is composed of fifty antennas of 12 meter dishes in the 12-m Array, used for sensitive, high-resolution imaging. These are complemented by the Atacama Compact array (ACA), composed of twelve closely spaced 7 meter antennas (7-m Array), and four 12 meter antennas for single-dish (or Total Power) observations (TP Array), to enhance wide-field

imaging of extended structures. The antennas can be distributed in different configurations with baselines ranging from 15 m to ~ 16 km. Once completed, ALMA will accomodate up to 10 receiver bands covering most of the wavelength range from 10 to 0.3 mm (30-950 GHz). Each receiver band is designed to cover approximately all the atmospheric transmission windows (see Fig. 3.8). For Bands 3

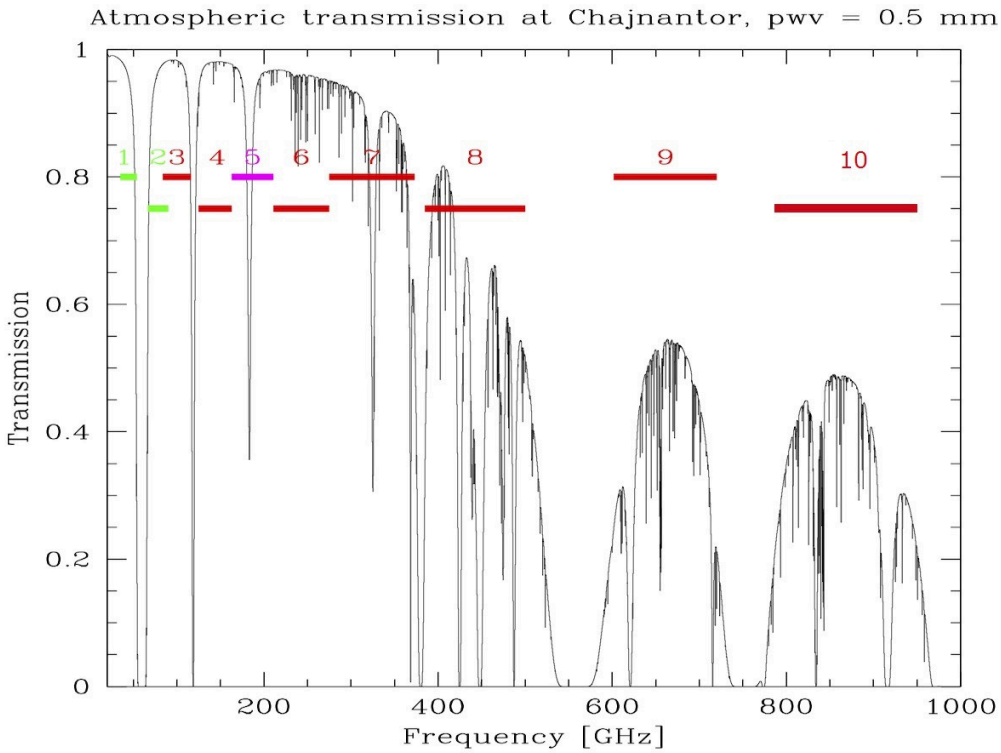

Figure 3.8: The figure from ALMA Cycle 5 Technical Handbook, shows the atmospheric transmission at the ALMA array operation site for 0.5 mm of precipitable water vapor (pwv). The 10 ALMA bands are superimposed, in red those available in Cycle 5 and in purple Band 5 which is the new band, introduced from Cycle 5.

to 8, the receivers are two-sideband (2SB), where both the upper and lower sidebands, with a bandwidth of 4 GHz, are provided separately and simultaneously for the two polarizations. On the other hand Bands 9 and 10 use double sideband (DSB) receivers, where the IF contains noise and signals from both sidebands.

In Chap. 4 we analysed ALMA Cycle 1 and Cycle 4 observations of the

HH212 protostellar system. In particular, the source was observed in Band 7 using 34 12-m antennas between 15 June and 19 July 2014 during the Cycle 1 phase. Further observations of HH212 were performed in Band 7 using 44 12-m antennas between 6 October and 26 November 2016 during the Cycle 4 phase. The maximum baselines for Cycle 1 and 4 were 650 m and 3 km, respectively while the maximum unfiltred scale is $\sim 3''$, i.e. about 1200 au at the HH212 distance of 405 pc. In Cycle 1 the spectral windows between 337.1–338.9 GHz and 348.4–350.7 GHz were observed using spectral channels of 488 kHz (0.42–0.43 km s^{-1}), subsequently smoothed to 1.0 km s^{-1} to increase sensitivity and obtain higher Signal-to-Noise (S/N). Calibration was carried out following standard procedures, using quasars J0607-0834, J0541–0541, J0423–013, and Ganymede. The continuum-subtracted images have clean-beam FWHMs from $0\farcs41 \times 0\farcs33$ to $0\farcs52 \times 0\farcs34$ (PA = $-63°$), and an rms noise level of 5–6 mJy beam^{-1} in 1.0 km s^{-1} channels. For Cycle 4 spectral units of 122 kHz (0.1 km s^{-1}) were used to observe the spectral windows between 335.0–337.4 GHz (used also to collect continuum emission). The spectral windows were also used to derive continuum from the line-free channels. Calibration was carried out following standard procedures, using quasars J0510+1800, J0552+0313, J0541–0211 and J0552–3627. The continuum-subtracted images have a typical clean-beam FWHM of $0\farcs15 \times 0\farcs12$ (PA = $-88°$), and an rms noise level of 4–5 mJy beam^{-1} in 0.1 km s^{-1} channels. Spectral line imaging was achieved with the CASA package, while data analysis was performed using the GILDAS[5] package. Positions are given with respect to the MM1 protostar continuum peak located at α(J2000) = $05^h\ 43^m\ 51\fs41$, δ(J2000) = –01° 02′ $53\farcs17$ (Lee et al. 2014). Lines were identified using spectroscopic parameters extracted from the Jet Propulsor Laboratory (JPL[6], Pickett et al. 1998) and Cologne Database for Molecular Spectroscopy (CDMS[7]; Müller et al. 2001, 2005) molecular databases.

[5]http://www.iram.fr/IRAMFR/GILDAS
[6]https://spec.jpl.nasa.gov/
[7]http://www.astro.uni-koeln.de/cdms/

4 Chemical complexity around Class 0 protostars

The deuterium fractionation and iCOMs abundances at the different evolutionary stages of a Sun-like protostar provides us a unique tool to investigate the origin and the evolution of our Solar System (Caselli & Ceccarelli 2012, Ceccarelli et al. 2014; see also Chap.1). As reported in Chap. 1, Class 0 sources are the youngest protostar, still deeply embedded and accreating matter from a collapsing envelope (André et al. 1993). Submm observations at high spatial resolution, on scales ≤100 au, are fundamental to understand the physical and chemical structure of this sources which will set up the initial conditions of the protostellar disk that may eventually form planets. In this Section we report interferometric ALMA observations (see Sec. 3) of the jet-disk system associated with the Class 0 protostar HH212-mm. The results presented in this Section are reported in Bianchi et al. (2017b).

4.1 The pristine jet-disk system in HH212

HH212 is a bright and symmetric bipolar jet driven by a low-luminosity Class 0 protostar, IRAS 05413–0104, deeply embedded in a compact molecular cloud core, L1630 in the Orion star forming region (d = 405 ± 15 pc, Kounkel et al. 2017; Kounkel, private communication). The systemic velocity (V_{sys}) of the object is +1.7 km s^{-1} (Lee et al. 2014). The jet was first revealed in H_2 imaging (Zinnecker et al. 1998) and then further observed through H_2O masers using VLBI. In particular, water masers observations revealed that the jet lies close to the plane

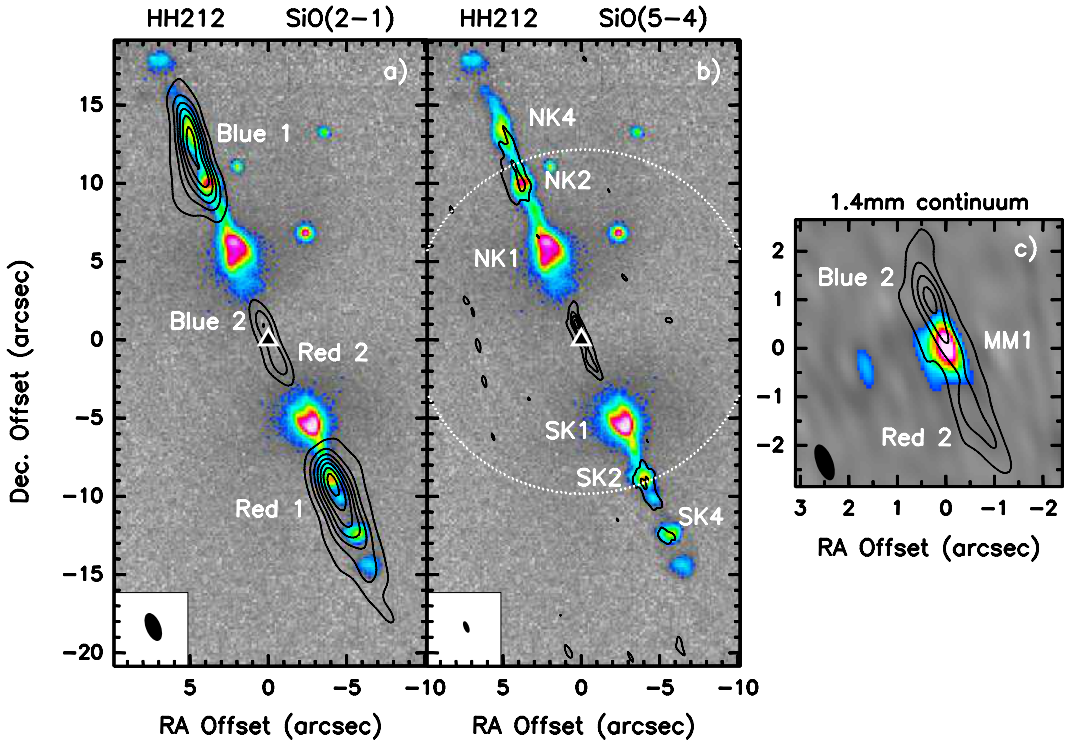

Figure 4.1: a) Contour map of integrated emission in SiO(2–1) superimposed on the H_2 image (Codella et al. 2007). The SiO emission regions are labelled in white. The filled triangle indicates the driving source MM1. Contour levels range from 3σ (0.22 Jy beam^{-1} km s^{-1}) to 39σ by steps of 6σ. The filled ellipse in the lower left corner shows the synthetised PdBI beam (HPBW): $1''.89 \times 0''.94$. b) Same as a) for the SiO(5–4) emission. The dotted circle indicates the primary beam of the PdBI antennae. H_2 knots are labelled in black. Contour levels range from 3σ (0.42 Jy beam^{-1} km s^{-1}) to 39σ by steps of 3σ. The beam is $0''.78 \times 0''.34$. c) Inner $5''$ of the SiO(5–4) map, superimposed onto the continuum image at 1.4 mm (gray scale and white contours). Continuum contour levels range from 3σ (1.9 mJy beam^{-1}) to 36σ by steps of 6σ.

of the sky (4°; Claussen et al. 1998). A large flattened rotating envelope in the equator perpendicular to the jet axis was observed in NH_3 with a radius of ~ 7000 au by Wiseman et al. (2001).

The innermost regions have been then extensively studied in CO(2–1), (3–2) and SiO(2–1), (5–4), (8–7) using IRAM-NOEMA, SMA, and ALMA (see Fig. 4.1 and 4.2) at scales ranging from ≃ 1″-2.5″ down to ≃ 0.1″-0.02″ (e.g. Lee et al. 2006, 2007, 2008, 2014, 2017a,c; Codella et al. 2007, 2014, 2016b, 2017;

Bianchi et al. 2017b; Cabrit et al. 2007, 2012).

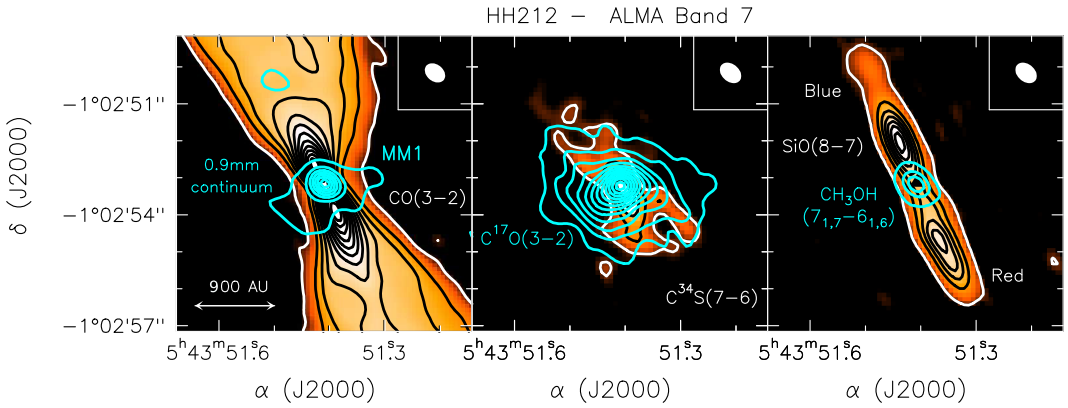

Figure 4.2: Protostellar system HH212 as observed by ALMA Cycle 0 in band 7 (Codella et al. 2014). *Left panel*: 850 μm continuum (turquoise contours) overlaid on SiO(8–7) integrated between -23 and +15 km s^{-1} (colour scale and black contours), compared with the systemic velocity V_{sys} (+1.7 km s^{-1}). First contours at 5σ (6 mJy beam^{-1} for continuum and 270 mJy beam^{-1} km s^{-1} for SiO) in steps of 20σ (continuum) and 5σ (SiO). The ellipse shows the synthesised continuum HPBW (0.″61 × 0.″45 at PA = 51°). The beam HPBW of the SiO map is 0.″63 × 0.″46 (PA = 49°). *Central panel*: contour plot of the C^{17}O(3–2) emission (turquoise) overaid on the of the C^{34}S(7–6) emission (colour and black), both integrated in the V_{sys} ± 6 km s^{-1} range. The HPBW is 0.″65 × 0.″47 (PA = 49°). First contours and steps correspond to 5σ (50 mJy beam^{-1} km s^{-1} for C^{34}S and 65 mJy beam^{-1} km s^{-1} for C^{17}O). *Right panel:* Contour plot of the CH$_3$OH($7_{1,7}$–$6_{1,6}$) emission (turquoise, integrated in the V_{sys}±6 km s^{-1} range) on top of the SiO(8–7) emission (colour and black, integrated between –23 and +15 km s^{-1} with respect to V_{sys}). The HPBW is 0.″65 × 0.″47 (PA = 49°) for CH$_3$OH and 0.″52 × 0.″47 (PA = 35°) for SiO. First contours and steps correspond to 5σ (65 mJy beam^{-1} km s^{-1} for CH$_3$OH and 270 mJy beam^{-1} km s^{-1} for SiO).

The high resolution NOEMA maps revealed a bright bipolar SiO microjet with inner peaks at ±1–2″ = 405–810 au of the protostar, invisible in H_2 due to high extinction (Codella et al. 2007; Lee et al. 2007). The SiO emission is confined to a highly-collimated bipolar jet (width ∼ 0.″35 close to the protostar) along the outflow axis. For the first time the jet is traced down to within 500 au of the protostar, in a region heavily obscured in H_2 images. Where both species are detected, SiO shows the same overall kinematics and structure as H_2 (see Fig. 4.1), indicating that both molecules trace shocked material. The SiO jet width ≃ 100 au is remarkably close to atomic jet widths in T Tauri stars, favouring a universal magnetohydrodynamical (MHD) collimation process (Cabrit et al. 2007). In this

way SiO filled in the gap between the jet larger scales proved by H_2 and the obscured innermost regions around the protostar, confirming to be a powerful tracer of molecular jets in Class 0 sources.

With the advent of ALMA, providing previously an unmatched combination of high angular resolution, high sensitivity, and spectral coverage, it has been possible to improve significantly the investigations on the complex kinematics of the innermost central regions of HH212. In particular, Fig. 4.2 (Codella et al. 2014, 2016b) shows the simultaneous identification, using the first ALMA cycles with angular resolutions of $\sim 0\farcs6$, of all the crucial ingredients known to be involved in the star formation recipe: (i) the fast, collimated bipolar SiO jet driven by the protostar; (ii) the large-scale swept-up CO outflow; (iii) the flattened rotating and infalling envelope, with bipolar cavities carved by the outflow, in $C^{17}O$(3–2); (iv) the hot-corino heated by the protostar and traced by iCOMs, e.g. $CH_3OH(7_{1,7}–6_{1,6})$; and (v) a rotating wide-angle flow that fills the cavities and surrounds the axial jet, in $C^{34}S$(7–6).

$C^{17}O$ observations, shown in Fig. 4.2, reveal for the first time velocity gradients (blue/red) in the compact high-velocity emission ($\pm$1.9–3.5 km s^{-1} from the systemic velocity). The gradients have been detected along the equatorial plane consistently with a rotating molecular disk around a 0.2-0.3 $M_\odot$ protostar (Lee et al. 2014, Codella et al. 2014, Podio et al. 2015). The emission centroid positions in each channel are obtained from elliptical Gaussian fits in the *uv* domain and plotted in Fig. 4.3 (right panel) along the disk plane. In the same figure, the centroid measurements are compared with Keplerian rotation curves and, as a reference, with a $\sim r^{-1}$ rotation curve that conserves specific angular momentum (pseudo-disk). In spite of the high spatial resolution, these ALMA observations does not allow the authors to distinguish between the different rotation curves, calling for further higher resolution observations. Finally, the molecular disk, which has a radius of $\sim$ 60 au has been recently imaged by Lee et al. (2017b) observing dust continuum emission at 850 μm with ALMA.

Interestingly, additional HDO and CH_3OH ALMA observations (Codella et al. 2016b, Leurini et al. 2016) suggest that the emission is likely associated with outflowing gas, and possibly with a disk wind. In addition, recent high angular resolution SiO maps have been used to prove the jet rotation (Lee et al. 2017a), previously suggested by one H_2 knot (Davis et al. 2000).

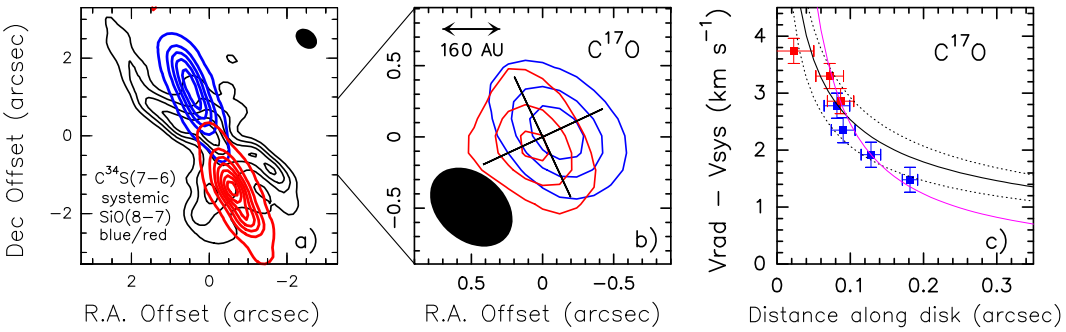

Figure 4.3: a) Figure from Codella et al. 2014 shows SiO(8–7) channel maps at V_{sys} ± 8 km s^{-1} (blue and red) overlaid on top of $C^{34}S$(7–6) close to systemic velocity (black). b) zoom in of the blue- and redshifted $C^{17}O$(3–2) emission in the velocity range (±1.9–3.5 km s^{-1} from V_{sys}) tracing the rotating inner disk. The tilted black cross indicates the SiO jet direction (PA = 22°) and the equatorial plane. First contour at 5σ (15 mJy beam^{-1} km s^{-1}), then steps of 7σ. c) Velocity shift from V_{sys} as a function of distance from the protostar along the equator (PA = 122°). Red and blue datapoints denote the $C^{17}O$(3–2) centroid positions (from fits in the *uv* domain with 1σ error bars) in the various velocity channels. Black solid and dotted curves show Keplerian rotation around a stellar mass of 0.3 ± 0.1 $M_\odot$. The r^{-1} curve for angular momentum conservation is plotted in magenta for comparison.

All these findings make HH212 the unique Class 0 protostellar region where a bright jet, a compact rotating disk, and signatures of a disk wind have been revealed. This source is thus an ideal laboratory to study the jet-disk system and the interplay of infall, outflow and rotation in the earliest stages of the low-mass star-forming process.

4.2 Deuteration on a solar system scale around HH212

In this Section we exploit ALMA Band 7 Cycle 1 and Cycle 4 observations with an angular resolution down to 0.″15 to obtain the first measurement of methanol deuteration in the disk formation region (see Sect. 3.4).

4.2.1 Line spectra and maps

In Cycle 1 data, we detected 5 lines of $^{13}CH_3OH$ and 12 lines of CH_2DOH covering excitation energies, E_{up}, from 17 to 438 K (see Tab. 4.1). In addition, in

Table 4.1: Methanol emission lines detected through both ALMA Cycle 1 and 4 towards HH212-mm.

Transition	ν^a (GHz)	E_{up}^a (K)	$S\mu^{2a}$ (D^2)	rms (K)	$T_{peak}{}^b$ (K)	$V_{peak}{}^b$ (km s^{-1})	$FWHM^b$ (km s^{-1})	$I_{int}{}^b$ (K km s^{-1})
Cycle 1								
$^{13}CH_3OH$ $13_{0,13}$–$12_{1,12}$E	338.75995	206	13	0.29	1.54 (0.19)	1.5 (0.3)	5.8 (0.8)	9.63 (1.12)
$^{13}CH_3OH$ $13_{4,9}$–$14_{3,11}$	347.78840	303	4	0.36	0.56 (0.09)	2.1 (1.2)	6.6 (2.6)	3.95 (1.39)
$^{13}CH_3OH$ $11_{0,11}$–$10_{1,9}$	348.10019	162	5	0.84	1.27 (0.08)	1.7 (1.1)	5.5 (2.6)	7.46 (2.98)
$^{13}CH_3OH$ $1_{1,1}$–$0_{0,0}$E	350.10312	17	2	1.16	1.49 (0.16)	1.7 (1.2)	4.7 (2.3)	7.44 (2.98)
$^{13}CH_3OH$ $8_{1,7}$–$7_{2,5}$	350.42158	103	2	0.93	1.49 (0.28)	1.2 (1.3)	5.5 (-)^e	8.72 (2.60)
CH_2DOH $9_{0,9}$–$8_{1,8}$ e0	337.34866	96	6	0.15	3.32 (0.10)	1.9 (0.1)	4.3 (0.2)	15.31 (0.49)
CH_2DOH $9_{1,8}$–$8_{2,6}$ o1^c	338.46254	120	2	0.26	1.94 (0.26)	2.0 (0.5)	5.2 (0.9)	10.74 (2.06)
CH_2DOH $13_{1,12}$–$12_{0,12}$ e0	338.86898	202	2	0.13	1.87 (0.13)	2.0 (0.1)	4.9 (0.2)	9.70 (0.43)
CH_2DOH $6_{1,6}$–$5_{0,5}$ e0	338.95711	48	5	0.29	3.65 (0.29)	1.8 (0.1)	4.3 (0.3)	16.67 (0.92)
CH_2DOH $18_{4,15}$–$18_{3,15}$ e1	347.76728	438	10	0.09	1.19 (0.09)	1.9 (0.1)	5.3 (0.3)	6.63 (0.31)
CH_2DOH $18_{4,14}$–$18_{3,16}$ e1	347.95281	438	10	0.18	1.16 (0.21)	1.3 (0.2)	5.2 (0.4)	66.44 (0.57)
CH_2DOH $4_{1,3}$–$4_{0,4}$ e1	348.16076	38	4	0.15	3.99 (0.25)	2.2 (0.1)	4.3 (0.1)	18.10 (0.49)
CH_2DOH $7_{4,4}$–$7_{3,4}$ e1	349.95168	132	3	0.16	5.28 (0.49)	1.7 (0.1)	4.5 (0.1)	25.26 (0.53)
CH_2DOH $7_{4,3}$–$7_{3,5}$ e1	349.95272	132	3					
CH_2DOH $6_{4,3}$–$6_{3,3}$ e1	350.02735	117	2	0.23	4.56 (0.32)	1.8 (0.1)	4.0 (0.2)	19.53 (0.72)
CH_2DOH $6_{4,2}$–$6_{3,4}$ e1	350.02777	117	2					
CH_2DOH $5_{4,2}$–$5_{3,2}$ e1	350.09024	104	2	0.63	3.85 (0.33)	1.7 (0.3)	4.9 (0.7)	20.03 (2.21)
CH_2DOH $5_{4,1}$–$5_{3,3}$ e1	350.09038	104	2					
CH_2DOH $6_{2,5}$–$5_{1,5}$ e1^c	350.45387	72	4	0.63	2.98 (0.20)	1.8 (0.5)	5.4 (1.5)	17.01 (3.92)
CH_2DOH $5_{1,4}$–$5_{0,5}$ e1	350.63207	49	5	0.60	4.50 (0.39)	2.3 (0.2)	4.4 (0.5)	21.04 (1.99)
Cycle 4								
$^{13}CH_3OH$ $12_{1,11}$–$12_{0,12}$ A	335.56021	193	23	9.14	10.60 (1.59)	2.6 (1.3)	4.7 (2.5)	53.70 (28.10)
CH_2DOH $16_{2,15}$–$16_{1,15}$ o1^d	334.68395	327	8	2.29	8.54 (1.72)	3.1 (0.5)	5.2 (1.3)	47.11 (9.23)

[a] Frequencies and spectroscopic parameters have been extracted from the Jet Propulsion Laboratory molecular database (Pickett et al. 1998) for all the transitions. Upper level energies refer to the ground state of each symmetry. [b] Gaussian fit. [c] The line transitions $9_{1,8}$–$8_{2,6}$ o1 is partially blended by the $7_{-5,2}$–$6_{-5,1}$ E1 CH_3OH transition. While the line $6_{2,5}$–$5_{1,5}$ e1 is partially blended by the $18_{1,17}$–$17_{1,16}$ E CH_3CHO transition. [d] The line transitions $16_{2,15}$–$16_{1,15}$ o with E_{up} = 327 K and $S_{ij}\mu^2$ = 8 D^2 is partially blended by the SO_2 (8 – 7) transition.

the Cycle 4 dataset we revealed one transition of $^{13}CH_3OH$ (E_{up}= 193 K), and one of CH_2DOH (E_{up}= 327 K).

Examples of the profiles of the detected lines are shown in Fig. 4.5: the emission peaks at velocities between $\simeq$ +1 km s^{-1} and +3 km s^{-1}, consistent with the systemic velocity of +1.7 km s^{-1} (Lee et al. 2014), when the spectral resolution of 1 km s^{-1} is considered. The profiles, fit using the GILDAS package, are Gaussian

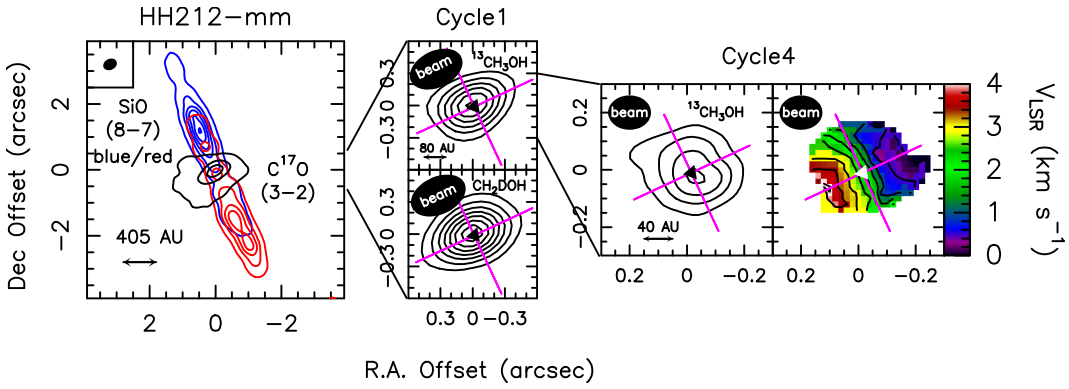

Figure 4.4: *Left Panel:* The HH212 protostellar system as observed by ALMA-Band 7 during Cycle 1 operations. Blue/red contours plot the blue/redshifted SiO(8–7) jet overlaid on the $C^{17}O$ (3–2) contours (in black). Positions are with respect to the MM1 protostar continuum peak located at α(J2000) = 05^h 43^m 51.^{s}41, δ(J2000) = –01° 02′ 53.″17 (Lee et al. 2014). The filled ellipse shows the synthesised beam (HPBW): 0.″43 × 0.″33. *Central Panels:* zoom-in of the central region (Bianchi et al. 2017a): $^{13}CH_3OH(13_{0,13}–12_{1,12})$E and $CH_2DOH(9_{0,9}–8_{1,8})$e0 integrated over ±4 km s^{-1} with respect to the v_{sys} = +1.7 km s^{-1}, (black contours and grey scale). First contours and steps are 5σ for $^{13}CH_3OH$ (15 mJy beam $^{-1}$ km s^{-1}) and CH_2DOH (35 mJy beam $^{-1}$ km s^{-1}). The HPBWs are: 0.″52 × 0.″34 (PA = -64°) for $^{13}CH_3OH$ and 0.″54 × 0.″35 (PA = -65°) for CH_2DOH. *Right Panel:* zoom-in of the central region, as observed by ALMA-Band 7 Cycle 4 (Bianchi et al. 2017a), showing the $^{13}CH_3OH(12_{1,11}–12_{0,12})$A emission integrated over 10 km s^{-1} around v_{sys} (black contours and grey scale). First contours and steps are 5σ (20 mJy beam $^{-1}$ km s^{-1}) and 3σ, respectively. The HPBW is 0.″15 × 0.″12 (PA = -88°). In addition we show the moment 1 map which is tracing in each pixel with emission larger than 5σ, the line profile peak of $^{13}CH_3OH$. Note the velocity gradient perpendicular to the jet axis.

with typical Full Width at Half Maximum (FWHM) ∼ 5 km s^{-1}. The spectral parameters of the detected lines are presented in Tab. 4.1. Figure 4.4 introduces the HH212 system: the $C^{17}O$(3–2) line traces the envelope hosting the protostar. The bipolar blue- and redshifted lobes are traced by SiO (Codella et al. 2007, Lee et al. 2014). The central panels, covering a zoom-in of the central protostellar region ($\lesssim$ 0.″5, i.e. 203 au), show the Cycle 1 data, specifically examples of the emission maps of $^{13}CH_3OH$ and CH_2DOH. The emission is spatially unresolved with a size smaller than the Cycle 1 beam (0.″5 × 0.″3) corresponding to a size of 203 ×122 au. However, the definitely higher angular resolution provided by the Cycle 4 dataset (0.″15 × 0.″12 corresponding to a radius of 30×24 au) provides spatially resolved images of both $^{13}CH_3OH$ and CH_2DOH emission lines. Note

that the CH_2DOH line is blended with the $SO_2(8_{2,6}–7_{1,7})$ line (Tab. 4.1). We use the $^{13}CH_3OH$ emission as revealed in the Cycle 4 image to show in the right panel of Fig. 4.4 a further zoom-in, sampling the inner 100 au of the system.

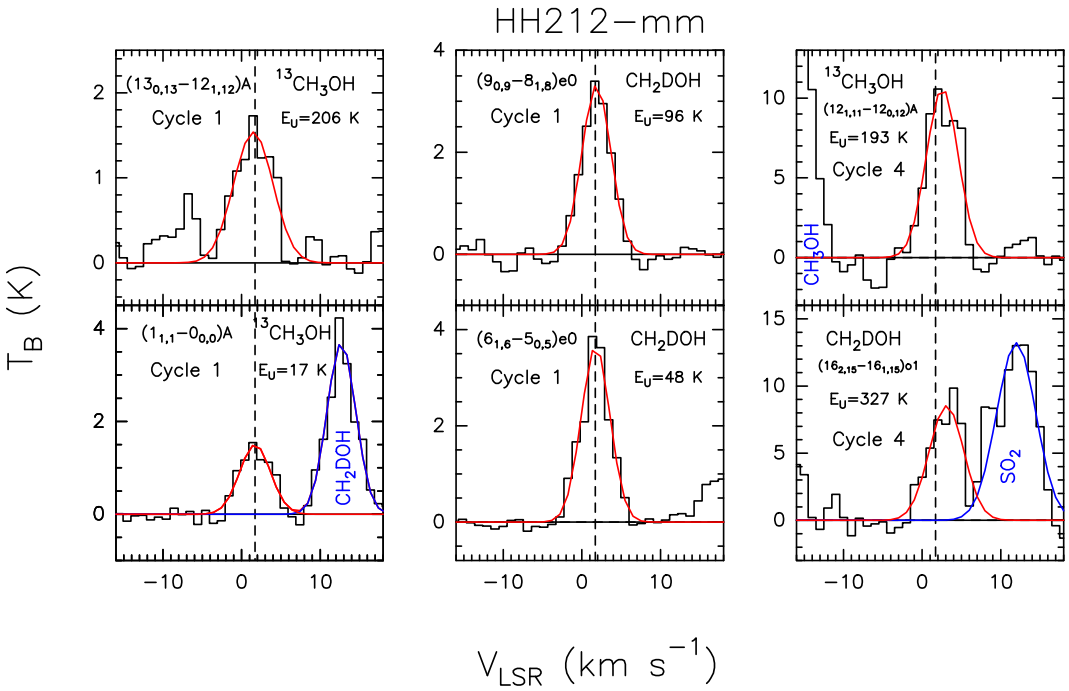

Figure 4.5: Examples of line profiles in T_B scale (not corrected for the beam dilution): species and transitions are reported. The vertical dashed line stands for the systemic V_{LSR} velocity (+ 1.7 km s^{-1}, Lee et al. 2014). Red and blue curves are for the Gaussian fit. In the spectrum of Cycle 1 $(1_{1,1}–0_{0,0})$A $^{13}CH_3OH$ transition, a CH_2DOH doublet containing the $(5_{4,2}–5_{3,2})$e1 and the $(5_{4,1}–5_{3,3})$e1 transitions is also shown (see Tab. 4.1). In Cycle 4 spectra the $(7_{1,7}–6_{1,6})$A CH_3OH and the $(8_{2,6}–7_{1,7})$ SO_2 transitions are also shown.

4.2.2 Methanol deuteration

We used the $^{13}CH_3OH$ lines detected in Cycle 1 to perform a rotation diagram analysis, assuming local thermal equilibrium (LTE) conditions and optically thin lines. In order to exclude opacity effects, we used the $^{13}CH_3OH$ lines to derive the CH_3OH column density because the main isotopologue lines observed by Leurini et al. (2016) are moderately optically thick ($\tau < 0.4$). We also verified that the

CH_2DOH transitions are indeed optically thin using a population diagram analysis (Goldsmith & Langer 1999) in which opacities are self-consistently computed. We used $^{13}CH_3OH$ and CH_2DOH lines extracted from the same ALMA dataset in order to have the same *uv* coverage and to minimise calibration effects. Moreover, the Cycle 0 (beam $\simeq$ 0.″6) observations of CH_3OH (Leurini et al. 2016) trace a much warmer component dominated by lines with E_{up} up to 747 K with respect to the emission lines analysed in this work. A source size of 0.″19 ± 0.″02 has been derived from the $^{13}CH_3OH$ Cycle 4 map integrated over the whole emission range and then used to correct the Cycle 1 observed values. This value is in good agreement with $\sim$ 0.″2, as derived from CH_3OH (Leurini et al. 2016). Figure 4.6 shows the derived rotational temperature and column density which are T_{rot} = (171 ± 52) K and $N_{tot} = (6.5 \pm 2.1) \times 10^{16}$ cm^{-2}, respectively. Conservatively, we used only Cycle 1 data to perform the fit; however, the $^{13}CH_3OH$ Cycle 4 line is in good agreement with Cycle 1 observations.

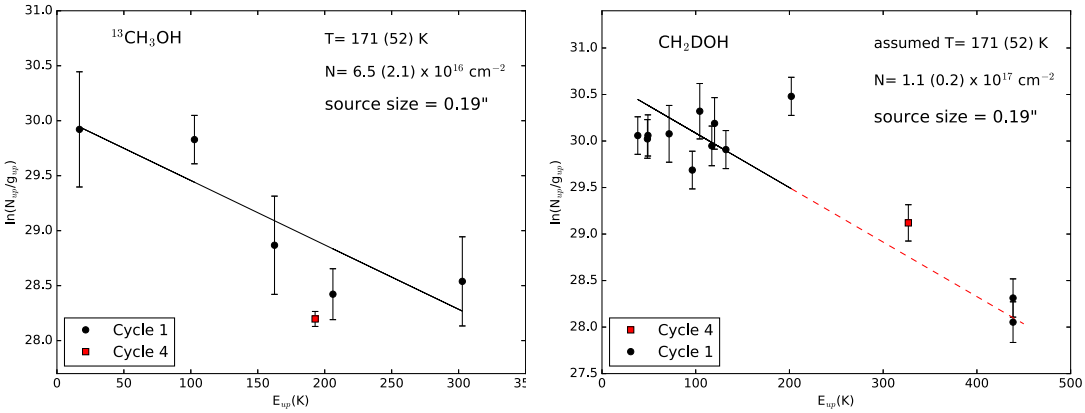

Figure 4.6: Rotation diagrams for $^{13}CH_3OH$ (left panel) and CH_2DOH (right panel). An emitting region size of 0.″19 is assumed (see text). The parameters N_u, g_u, and E_{up} are, respectively, the column density, the degeneracy and the energy of the upper level, respectively. The derived value of the rotational temperature is reported for $^{13}CH_3OH$. For CH_2DOH the T_{rot} derived from the ^{13}C-isotopologues is assumed to derive the column density. The two CH_2DOH transitions with excitation energies higher than 400 K as well as the Cycle 4 point are excluded from the fit, although they are in good agreement with it.

In the right panel of Fig. 4.6 we derive the column density of CH_2DOH, assuming the same rotational temperature and size derived for $^{13}CH_3OH$. We ex-

cluded from the fitting the two CH_2DOH transitions with $E_{up} > 300$ K to exclude any possible contamination from non-thermal excitation processes or the occurrence of a component with a different, higher, excitation condition. However the fitting obtained with the low-energies transitions (continuous line) is in agreement with the two excluded transitions, as well as with the Cycle 4 transition, as shown by the dotted line. The derived column density for CH_2DOH is then N_{tot} = (1.1 ± 0.2) × 10^{17} cm^{-2}. We note that an LVG analysis (see Ceccarelli et al. 2003 and Sec. 2.3.2 for further details) of the $^{13}CH_3OH$ emission indicates a source size of 0.″1-0.″2, T_{kin} larger than 100 K and densities larger than 10^6 cm^{-3} in agreement with the HDO results reported by Codella et al. (2016b).

The column densities derived from the rotation diagrams were used to derive the methanol D/H for the first time in the inner 100 au around a low-mass protostar. When we assume a $^{12}C/^{13}C$ ratio of 70 (Milam et al. 2005) at the galactocentric distance of HH212 (∼ 8.3 kpc), the D/H is consequently (2.4 ± 0.4) × 10^{-2}. This value is in agreement with the upper limit of 0.27 derived by Lee et al. (2017c) using CH_2DOH and three lines of CH_3OH. In addition, our measurement is lower than previous values of CH_2DOH in other Class 0 objects performed with the IRAM-30m single dish, which indicate D/H ≃ 40-60% (Parise et al. 2006). Taking into account that, as reported by Belloche et al. (2016), the column densities of CH_2DOH derived in Parise et al. (2006) were overestimated by a factor ∼2 because of a problem in the spectroscopic parameters, the HH212 deuteration is still one order of magnitude lower.

What are the reasons of this difference? To start with, the single-dish measurements by Parise et al. (2006) are sampling regions ≥ 2000 au: the D/H is calculated assuming that the main isotopologue and the deuterated species come from the same emitting source, but this cannot be verified with low angular resolutions. This issue is overcome with high angular resolution observations, like those presented here, which allow us to directly image the emitting region. Interestingly, Jørgensen et al. (2016) report a level of deuteration for glycolaldehyde of ∼5 % in IRAS16293 in Ophiuchus on 50 au scale. That said, a possible explanation for the lower methanol deuteration measured for HH212 mm could be related to different physical conditions during the formation of methanol on dust mantles during the prestellar phase. A higher gas temperature reduces the atomic gas D/H ratio landing on the grain surfaces, and in turn reduces the deuteration of methanol. All the

sources observed by Parise et al. (2006) are located in the Perseus star-forming region, which could have had experienced different conditions with respect to the Orion B region where HH212 lies.

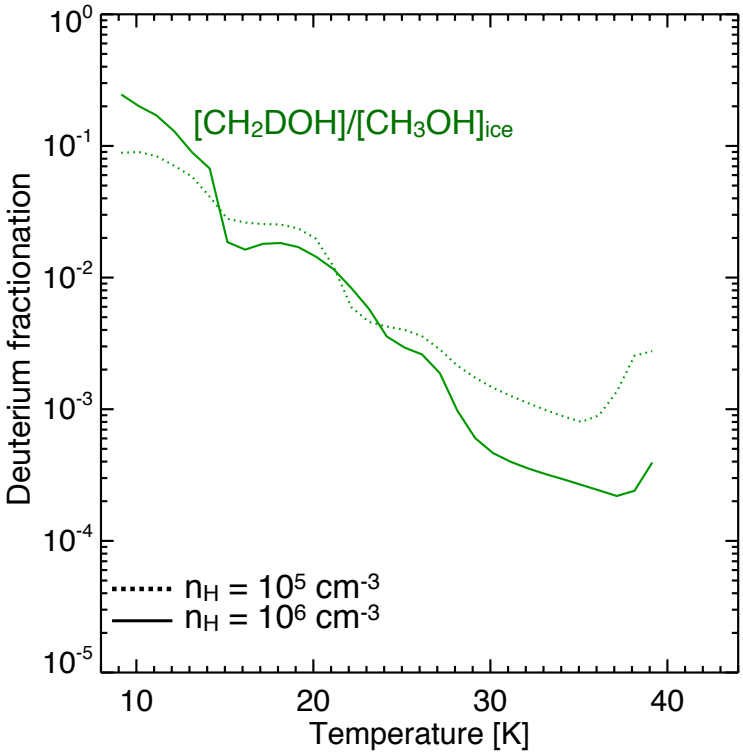

Figure 4.7: Final $[CH_2DOH]/[CH_3OH]$ abundance ratio in ices as a function of the temperature, as described by the Taquet et al. (2014) GRAINOBLE astrochemical model (V. Taquet, private communication). Two densities are considered here: $n_H = 10^5$ cm^{-3} (dashed) and $n_H = 10^6$ cm^{-3} (solid). In both cases the higher the temperature, the lower is the methanol deuteration.

Specifically, while in Perseus the dust temperature is about ∼12 K (Zari et al. 2016), HH212 is located about one degree north of the high-mass star forming region NGC 2024, and the dust temperature here is ≥16 K (Lombardi et al. 2014). To verify this possibility, the observed results are therefore compared with the prediction of methanol deuteration in interstellar ices obtained using the GRAINOBLE astrochemical model (Taquet et al. 2012b, 2013, 2014). The code follows the gas-ice interstellar chemistry through a 3-phase (gas, ice surface, ice bulk) rate equations approach initially developed by Hasegawa & Herbst (1993). Figure 4.7

shows the final [CH_2DOH]/[CH_3OH] abundance ratio in ices as a function of the temperature for two different densities: $n_H = 10^5$ cm^{-3} (dashed) and $n_H = 10^6$ cm^{-3} (solid). From Fig. 4.7 we note that the methanol deuteration is strongly dependent on the temperature (assuming that gas and dust have the same temperature). In particular the [CH_2DOH]/[CH_3OH] abundance ratio decrease up to one order of magnitude by increasing the temperature from 10 K to 20 K. For temperature ≥16 K, the expected [CH_2DOH]/[CH_3OH] abundance is fews 10^{-2}, perfectly consistent with the value measured in this work D/H= $(2.4 \pm 0.4) \times 10^{-2}$. This agreement confirms the diagnostic value of molecular deuteration to recover the physical conditions during the pre-collapse phase. Interestingly, we note that according to Fuente et al. (2014) the methanol deuteration in the hot core in the intermediate-mass star-forming regions NGC7129, FIRS 2 is ∼ 2 %, and in Orion massive hot cores the methanol D/H is between 0.8×10^{-3} and 1.3×10^{-3} (Peng et al. 2012).

4.2.3 Emitting region of deuterated methanol

Figure 4.8 shows the channel maps of the two transitions observed during ALMA Cycle 4, that is, at the highest spatial resolution presented here: $^{13}CH_3OH$ $(12_{1,11}–12_{0,12})$A and CH_2DOH $(16_{2,15}–16_{1,15})$o1 (see Tab. 4.1). For both lines the rightmost panels show the spatial distributions of the emission close to systemic velocity. The remaining panels are for the blue- and redshifted velocities, imaged up to ±4 km s^{-1}. We note that for CH_2DOH the redshifted emission is partially contaminated by the $SO_2(8_{2,6}–7_{1,7})$ emission (see Tab. 4.1 and Fig. 4.5).

The spatial distribution of the methanol isotopologues at the systemic velocity is elongated along the jet axis (PA = 22°). A fit in the image plane gives for $^{13}CH_3OH$ a beam-deconvolved FWHM size of 0.″18(0.″02)×0.″12(0.″02) at PA = 33°. For CH_2DOH we derived 0.″20(0.″02)×0.″10(0.″02) and PA = 19°. These values correspond to FWHM sizes of 73×49 au ($^{13}CH_3OH$) and 81×41 au (CH_2DOH). Closer to the blue- and redshifted emission, we resolve a clear velocity gradient parallel to the equatorial plane (see also Fig. 4.9) with shifts of ± 0.″1 = 41 au, in the same sense as the HH212 disk rotation. The typical (beam-deconvolved) size of the blue- and redshifted emission at ±2 km s^{-1} from the systemic velocity is 0.″22(0.″04)×0.″14(0.″04) and 0.″18(0.″02)×0.″10(0.″03), respectively, similar to the

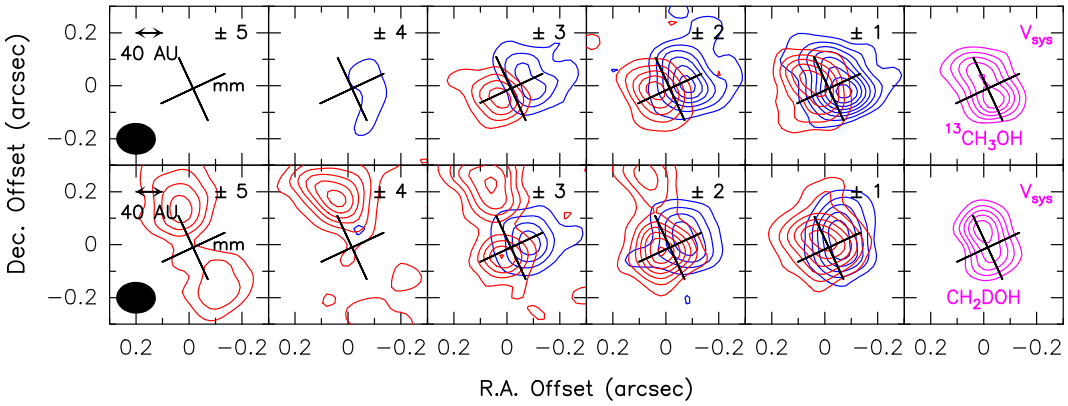

Figure 4.8: Channel maps of the $^{13}CH_3OH(12_{1,11}–12_{0,12})A$ (upper panels) and $CH_2DOH(16_{2,15}–16_{1,15})o1$ (lower panels) blue- and redshifted (continuum subtracted) emissions observed during ALMA-Cycle 4 towards the HH212 mm protostar. Each panel shows the emission integrated over a velocity interval of 1 km s^{-1} shifted with respect to the systemic velocity (see the magenta channel, sampling the velocity between +1.5 km s^{-1} and +2.5 km s^{-1}) by the value given in the upper-right corner. The black cross (inclined in order to point the SiO jet direction and consequently the equatorial plane, see Fig. 4.4) indicates the position of the protostar. The ellipse in the top left panel shows the ALMA synthesised beam (HPBW): 0.″15 × 0.″12 (PA = –88°). First contours and steps correspond to 3σ (2.7 mJy beam $^{-1}$ km s^{-1}). Note that for CH_2DOH at velocities higher than +1.0 km s^{-1} a further emission appears along the jet axes to the north and to the south with respect to the CH_2DOH emission. This is due to the $SO_2(8_{2,6}–7_{1,7})$ emission line (see Tab. 4.1 and Fig. 4.5). which has been confirmed to be a good tracer of outflowing matherial (Podio et al. 2015). Given that the velocity scale has been derived by first fixing the CH_2DOH frequency, the SO_2 emission looks artificially red, but it is clearly blueshifted (see Fig. 4.5)

size at V_{sys}. Rotation has previously been noted in CH_3OH by Leurini et al. (2016) from unresolved maps at lower resolution (≃ 0.″6). The authors further noted that emission centroids (fitted in *uv*-plane) moved away from the source, and eventually away from the mid plane, at higher velocity, speculating that the methanol emission is not dominated by a Keplerian disk or the rotating-infalling cavity, and possibly associated with a disk wind. With the present images we reach higher angular resolution, which allows us to refine the picture: the systemic velocity looks arising mainly from two peaks at ±0.″05 = 20 au above and below the disk plane (of which the centroids in Leurini et al. 2016 only traced the barycenter). In addition, channel maps at ±1 km s^{-1} suggest redshifted emission peaking in the north and blueshifted emission peaking in the south, which is not the sense we

would naively expect for a wind from HH212 mm. Since the jet axis is so close to the plane of the sky[1] this might perhaps still be explained by non-axisymmetric structure in a disk wind, but synthetic predictions would be needed to test this.

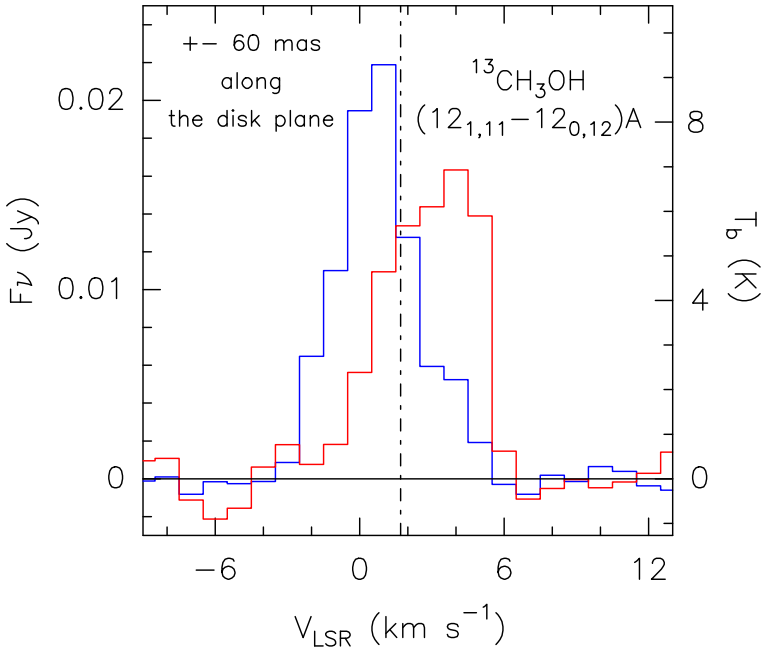

Figure 4.9: Comparison in flux density and in T_B scales (T_B/F_ν = 482.609 K Jy^{-1}) between the $^{13}CH_3OH(12_{1,11}-12_{0,12})A$ spectrum extracted at ± 0.″06 from the protostar (see Fig. 2: blue- and redshifted emission towards north-west and south-east, respectively) in the direction along the equatorial plane (i.e. disk plane; Lee et al. 2017b). The vertical dashed line stands for the systemic V_{LSR} velocity (+ 1.7 km s^{-1}, Lee et al. 2014).

Alternatively, our data suggest that the emission could arise from accretion shocks occurring at the centrifugal barrier associated with the accretion disk, and heating the gas at temperatures around 100 K (Sakai et al. 2014b,a; Oya et al. 2016). The radial extent ∼ 50 au of the observed red- and blueshifted emission is indeed consistent with the dust disk radius ∼ 60 au, recently resolved by Lee et al. (2017b) at 850 μm with ALMA. In this case, we would observe a thicker accretion shock near the centrifugal barrier in HH212, as recently seen in C_2H in L1527 (Sakai et al. 2017). We may also have a contribution from a warm disk atmosphere, emitting in the northern/southern portions of the accretion disk,

[1]The system inclination is 4° to the plane of sky, (Claussen et al. 1998; Lee et al. 2017b)

thicker than the dust atmosphere.

4.2.4 Single deuterated methanol CH_3OD

We detect the $CH_3OD(6_{2-}–6_{1+})$ line at 335.089660 GHz with upper level excitations energy E_u = 67 K with a S/N of ~44. In Figure 4.10 we show the spatial distribution of the CH_3OD emission integrated in velocity channels of 1 km s^{-1}, similarly to what reported in Fig. 4.8. The black contours show the emission close to the systemic velocity while the black cross indicates the position of the protostar. The latter is inclined in order to point the SiO jet direction and consequently the equatorial plane. In blue/red is shown the blue- and redshifted emission. Even if the line is weaker, the spatial distribution is in agreement with the observed $^{13}CH_3OH$ and CH_2DOH emission, see Fig. 4.8. We derive a value for the CH_3OD column density of $N_{tot} \sim 2 \times 10^{16}$ cm^{-2} , assuming a source size of 0.″19 and T_{rot} = 176 K as derived for $^{13}CH_3OH$, and using the rotational partition functions from Ratajczak et al. (2011).

We use the measure of the ratio between the two single deuterated methanol isotopologues to test the current theory of methanol deuteration. Basically, according to the grain chemistry statistical models of Charnley et al. (1997) and Osamura et al. (2004) the ratio of the isotopologues formed on the mantles, namely the ratio between CH_2DOH and CH_3OD should be 3. However, this is not always confirmed by the measurements in star forming regions (Ratajczak et al. 2011). We compare the CH_3OD column density with that of CH_2DOH, derived using a single line with an excitation energy close to that of the detected CH_3OD line. In particular we use the $CH_2DOH(6_{1,6}–5_{0,5})e0$ line observed in Cycle 1 (see Tab. 4.1) to derive a column density of $N_{tot} \sim 8 \times 10^{16}$ cm^{-2}, assuming again a source size of 0.″19 and T_{rot} = 176 K and correcting for the Cycle 1 beam dilution. The derived value of $[CH_2DOH]/[CH_3OD]$ is 3.5, in agreement with the statistical value suggested by the grain chemistry models. This values seems to indicate that the traced material is ejected from grain mantles and their abundances are still not affected by gas-phase processes, consistent with the fact that we are sampling the region around a Class 0 protostar in the earliest evolutionary phase. Note that to our knowledge this is the first $[CH_2DOH]/[CH_3OD]$ measurements at such small scales around a Class 0 protostar. Further observations are needed to confirm

these findings. For a more detailed discussion on the [CH_2DOH]/[CH_3OD] ratio, see Section 5.2.8.

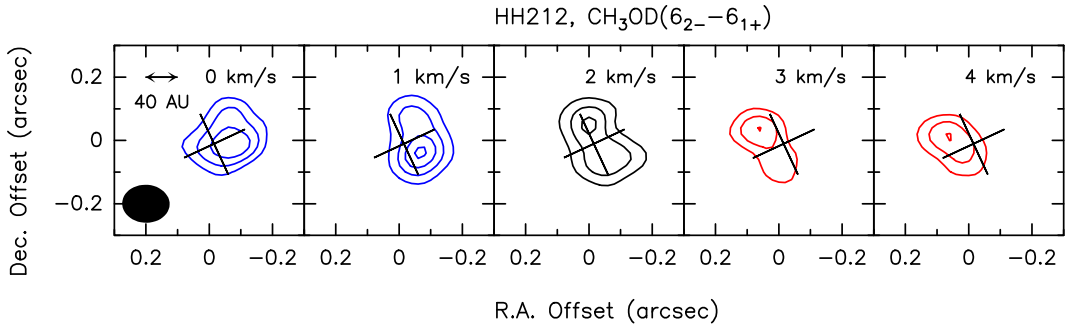

Figure 4.10: Channel maps of the $CH_3OD(6_{2-}–6_{1+})$ blue- and redshifted (continuum subtracted) emissions observed during ALMA-Cycle 4 towards the HH212 mm protostar. Each panel shows the emission integrated over a velocity interval of 1 km s^{-1} shifted with respect to the systemic velocity (see the black channel, sampling the velocity of +2 km s^{-1}) by the value given in the upper-right corner. The black cross indicates the position of the protostar. The ellipse in the top left panel shows the ALMA synthesised beam (HPBW): 0.″15 × 0.″13 (PA = –88°). First contours and steps correspond to 5σ (1.0 mJy beam $^{-1}$ km s^{-1}).

4.2.5 Conclusions on HH212 deuteration

The ALMA Cycle 1 and 4 observations allow us to measure methanol deuteration in the inner 50 au of the jet-disk system associated with the Class 0 protostar HH212, in Orion B. The deuteration is $\simeq 2 \times 10^{-2}$, a value lower than what previously measured using single-dish towards Class 0 protostars in Perseus. Although we cannot exclude that single-dish observations are mixing different gas components with different D/H values, our findings are consistent with a higher dust temperature in Orion B with respect to the Perseus cloud. This confirms the diagnostic value of molecular deuteration to recover the physical conditions during the pre-collapse phase. The emission is confined in a rotating structure which extends at ± 40 au from the equatorial plane and is elongated along the jet axis. Disk wind, disk atmosphere, and accretion shocks could explain the observed images. Higher spatial resolution maps will be necessary to distinguish between these possibilities.

4.3 iCOMs in HH212: accretion shocks and disk winds

The ALMA Cycle 1 and Cycle 4 datasets were further exploited to analyse the iCOMs emission in the HH212-mm system. In particular several transitions of CH_3CHO in Cycle 1 and Cycle 4 data and one transition of deuterated water (HDO) in Cycle 4 observations. The combination of water and iCOMs is obviously of paramount importance in the context of prebiotic chemistry. Note that in the following analysis HDO cannot be used to derive water deuteration, given the lack of the main isotopologue observation. We used HDO as a proxy to image water emission in protostellar systems on Solar-System scales. The spatial distribution and the kinematics of the observed lines have been analysed in order to determine the physical properties of the inner hot-corino region, emitting in water and iCOMs.

4.3.1 Line spectra and maps

We detected 14 CH_3CHO emission lines (12 in Cycle 1, 2 in Cycle 4) and one line of deuterated water (HDO) in the Cycle 4 dataset. Spectral line imaging was achieved with the CASA[2] package, while data analysis was performed using the GILDAS[3] package. Positions are given with respect to the MM1 protostar continuum peak located at α(J2000) = $05^h\ 43^m\ 51\overset{s}{.}41$, δ(J2000) = –01° 02′ 53″.17 (e.g. Lee et al. 2014). Emission HDO and CH_3CHO lines (see Tab. 4.2) were identified using spectroscopic parameters extracted from the Jet Propulsor Laboratory (JPL[4], Pickett et al. 1998) molecular database. We also used the Cycle 1 SiO(8–7) and $C^{43}S$ emission at 347330.63 GHz and 337396.69 MHz (also from JPL), respectively, as well as the continuum to show the direction of the jet, the shape of the asymmetric cavity, and point the protostar (Tabone et al. 2017).

Figure 4.11 shows the CH_3CHO spectra extracted from the protostellar position: the profiles, fit using the GILDAS package (see Tab. 4.2), are Gaussian-like and the S/N of the $T_{\rm peak}$ is always larger than 6. The line excitation is high, with

[2]http://casa.nrao.edu
[3]http://www.iram.fr/IRAMFR/GILDAS
[4]https://spec.jpl.nasa.gov/

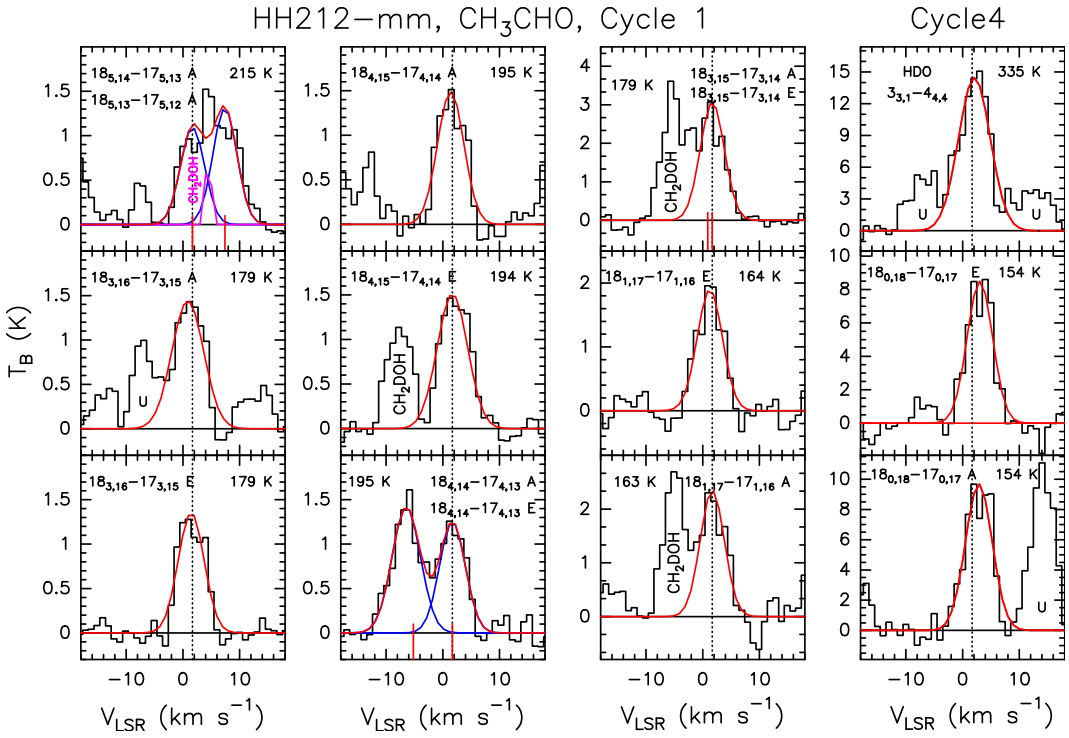

Figure 4.11: CH_3CHO and HDO line profiles in T_b scale observed during the ALMA Cycle 1 and 4 (right panels) operations. Species, transitions, and upper level excitations (E_u in K) are reported (see Table 1). The vertical dashed line stands for the systemic velocity v_{sys} = +1.7 km s^{-1} (e.g. Lee et al. 2014). Red curves are for the Gaussian fits, which results are reported in Table 1. In some panels, vertical red segments point out an additional CH_3CHO line close to that centred at v_{sys}. The CH_2DOH labels are for emission lines of the deuterated methanol, published by Bianchi et al. (2017b). Some unidentified lines are also reported.

E_u from 163 K to 215 K. In addition, we detected, in the Cycle 4 spectra the $3_{3,1}$–$4_{2,2}$ line of HDO, with E_u = 335 K (S/N ~ 12). All the emission lines peaks at velocities close to the systemic velocity and their Full Width Half Maximum (FWHM) linewidths are between +5.1 km s^{-1} and +6.6 km s^{-1} in agreement with the CH_3CHO and HDO lines detected at lower angular resolution by Codella et al. (2016b).

Figure 4.12 reports the spatial distribution of the $CH_3CHO(18_{1,17}–17_{1,16})$E and $CH_3CHO(18_{4,15}–17_{4,14})$A emission (observed in Cycle 1) integrated over ±5 km s^{-1} with respect to v_{sys}. These maps are representative of the spatial distributions of all the CH_3CHO lines detected in Cycle 1. The CH_3CHO images were not spatially resolved when observed by Codella et al. (2016b) using a beam of ~ 0.″6, and the present Cycle 1 maps (~ 0.″4) are still spatially unresolved. The higher spatial-resolution Cycle 4 images allows us to resolve the size of the emitting regions, which are quite roundish with the following diameters: 161±17 mas (HDO), 205±25 mas (CH_3CHO-E), and 213±34 mas (CH_3CHO-E).

4.3.2 Physical properties

The temperature and column density of CH_3CHO have been derived using the rotational diagram approach (Fig. 4.6), assuming Local Thermodinamic Equilibrium (LTE) conditions and optically thin emission. We used both Cycle 1 and Cycle 4 emission lines, assuming a source size of 0.″18, following the maps of Fig. 4.12, and consequently correcting the observed intensities. We derived a temperature of 78±14 K and column density of 7.6±3.2 × 10^{15} cm^{-2}. The temperature is in a perfect agreement with the Cycle 0 results reported by Codella et al. (2015), as well as consistent the temperatures of 165±85 K and 171±52 K derived from methanol observations by (Lee et al. 2017c) and (Bianchi et al. 2017b). On the other hand, the column density is higher by a factor 4 with respect to what reported by Codella et al. (2015), in agreement with the size of 0.″3 assumed using the unresolved Cycle 0 maps. The reliable measure of the CH_3CHO column density reflects in an improved estimate of the CH_3CHO abundance. As stressed in Codella et al. (2015) the continuum emission, being optically thick (see e.g. (Lee et al. 2017b), and references therein), cannot be used to derive a N(H_2) estimate. However, assuming H_2 column densities around 10^{24} cm^{-2}, which is a typical val-

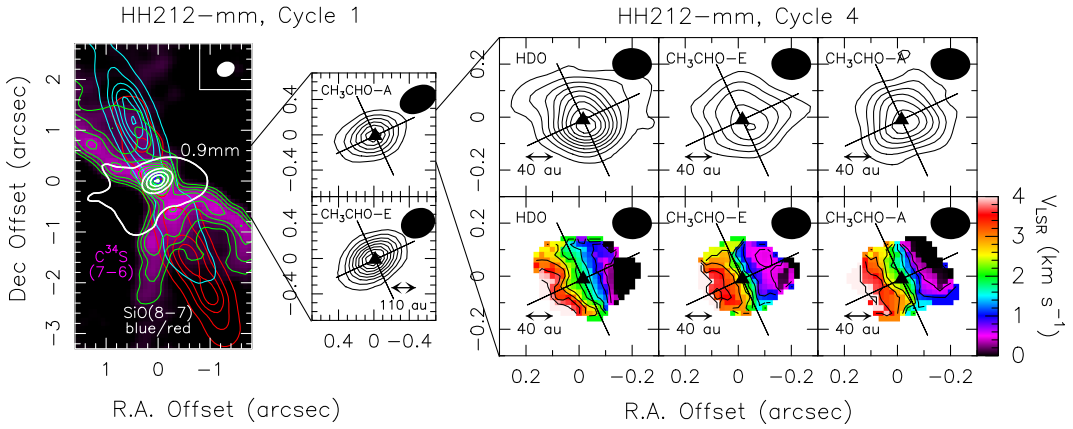

Figure 4.12: *Left panel:* The HH212 protostellar system as observed by ALMA-Band 7 during Cycle 1. Blue/red contours plot the blue/redshifted SiO(8–7) jet and the $C^{34}S$(7–6) asymmetric cavity (magenta and green contours) overlaid on the continuum at 0.9 mm (white contours). Positions are with respect to the coordinates of the MM1 protostar, reported in the text. The filled ellipse shows the synthesised beam (HPBW) for continuum: 0.″36 × 0.″28 (–62°). The beam for the SiO and $C^3$4S images is: 0.″43×0.″33 (–64°). First contours and steps for continuum are are 5σ (1.5 mJy beam $^{-1}$) and 60σ, respectively. For SiO first contours iand steps are 5σ and 25σ, respectively: the blue maps has been obtained by integrating down to –21 km s^{-1} (1σ = 29 mJy beam $^{-1}$ km s^{-1}), while the red map collects emission up to +12 km s^{-1} (1σ = 23 mJy beam $^{-1}$ km s^{-1}). The C^{34} map ihas been obtained by integrating the velocities from -1 km s^{-1} to +1 km s^{-1} with respect to the systemic velocity v_{sys} = +1.7 km s^{-1} (Lee et al. 2014): first contour and steps are 5σ (10 mJy beam $^{-1}$ km s^{-1}) and 3σ, respectively. *Central panels:* Zoom-in of the central region as observed by ALMA-Band 7 Cycle 1: $CH_3CHO(18_{1,17}–17_{1,16})$E and $CH_3CHO(18_{4,15}–17_{4,14})$A emission integrated over ±5 km s^{-1} with respect to v_{sys} (black contours). First contours and steps are 3σ (18 mJy beam $^{-1}$ km s^{-1}). The HPBWs are 0.″41×0.″33 (–64°) for $CH_3CHO(18_{1,17}–17_{1,16})$E, and 0.″44×0.″33 (–63°) for $CH_3CHO(18_{4,15}–17_{4,14})$A. The black triangle is for the MM1 coordinates, while the tilted cross indicated both the directions of the jet and of the equatorial plane. *Right panels:* Further zoom-in of the central region, as observed by ALMA-Band 7 Cycle 4, showing the $HDO(3_{3,1}–4_{2,2})$, $CH_3CHO(18_{0,18}–17_{0,17})$E, and $CH_3CHO(18_{0,18}–17_{0,17})$A. emission integrated over 10 km s^{-1} around v_{sys} (Upper panels; black contours). First contours and steps are 3σ (14 mJy beam $^{-1}$ km s^{-1}). The HPBW is 0.″15 × 0.″12 (PA = -88°). The corresponding first moment maps are reported in colour scale in the Lower panels. Contours are from 0 km s^{-1} to +4 km s^{-1} by step of 0.5 km s^{-1}.

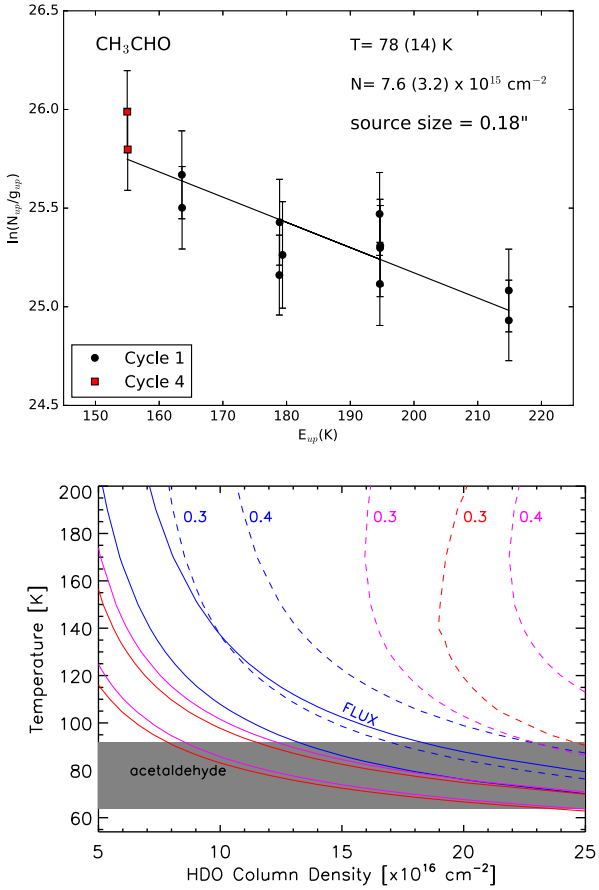

Figure 4.13: *Upper panel:* Rotation diagrams for CH_3COH, derived using both Cycle 1 (black points) and Cycle 4 (red) data. An emitting region size of 0.″18 is assumed (see text). The parameters N_u, g_u, and E_{up} are, respectively, the column density, the degeneracy and the energy of the upper level. The derived values of the rotational temperature and total column density are reported. *Lower panel:* LVG predictions of the temperature versus HDO column density required to reproduce the observed velocity-integrated emission (solid curves; see Tab. 4.2) densities of: 10^8 cm^{-3} (blue), 10^9 cm^{-3} (magenta), and 10^{10} cm^{-3} (red). Dashed lines are for the optical depth (τ = 0.3 and 0.4), increasing with column density. A source size of 0.″18 is assumed. The grey zone is for the temperature derived from CH_3CHO (see upper panel).

Table 4.2: CH_3CHO and HDO emission lines detected towards HH212-mm during Cycle 1 and Cycle 4 observations.

Transition[a]	ν_0 [a] (GHz)	E_u [a] (K)	$S_{ij}\mu^2$ [a] (D^2)	rms (K)	T_{peak} [b] (K)	V_{peak} [b] (km s^{-1})	FWHM [b] (km s^{-1})	I_{int} [b] (K km s^{-1})
Cycle 1								
CH_3CHO $18_{5,14}$–$17_{5,13}$ A	347.2883	215	210	0.2	1.3 (0.2)	+1.7 (–)[c]	5.0 (–)[c]	6.8 (0.4)
CH_3CHO $18_{5,13}$–$17_{5,12}$ A	347.2949	215	210	0.1	1.1 (0.2)	+1.7 (-)[c]	5.0 (–)[c]	5.8 (0.2)
CH_3CHO $18_{3,16}$–$17_{3,15}$ A	347.5192	179	221	0.2	1.4 (0.2)	+0.9 (0.3)	6.6 (0.7)	10.1 (0.9)
CH_3CHO $18_{3,16}$–$17_{3,15}$ E	347.5633	179	221	0.1	1.4 (0.2)	+1.5 (0.1)	5.1 (0.2)	7.7 (0.2)
CH_3CHO $18_{4,15}$–$17_{4,14}$ A	347.6504	195	216	0.4	1.5 (0.2)	+1.4 (0.4)	5.5 (0.8)	8.7 (1.3)
CH_3CHO $18_{4,15}$–$17_{4,14}$ E	347.7563	194	213	0.2	1.5 (0.2)	+1.7 (–)[c]	6.3 (0.5)	10.2 (0.7)
CH_3CHO $18_{4,14}$–$17_{4,13}$ E	347.8310	195	213	0.1	1.3 (0.1)	+1.7 (0.2)	5.3 (0.4)	7.1(0.5)
CH_3CHO $18_{4,14}$–$17_{4,13}$ A	347.8390	195	213	0.1	1.4 (0.1)	+0.5 (0.1)	5.9 (0.3)	8.8 (0.3)
CH_3CHO $18_{3,15}$–$17_{3,14}$ A	350.1334	179	221	1.1	3.1 (0.1)	+1.7 (–)[c]	5.0 (-)[c]	16.3 (2.3)
CH_3CHO $18_{3,15}$–$17_{3,14}$ E	350.1344	179	221					
CH_3CHO $18_{1,17}$–$17_{1,16}$ E	350.3628	164	226	0.2	1.9 (0.2)	+1.3 (0.2)	5.2 (0.3)	10.6 (0.6)
CH_3CHO $18_{1,17}$–$17_{1,16}$ A	350.4458	163	226	0.5	2.4 (0.4)	+1.7 (–)[c]	5.0 (–)[c]	12.5 (1.2)
Cycle 4								
HDO $3_{3,1}$–$4_{2,2}$	335.3955	335	0.4	0.5	16.2 (1.3)	+2.1 (0.1)	6.6 (0.2)	101.6 (1.9)
CH_3CHO $18_{0,18}$–$17_{0,17}$ E	335.3181	155	227	0.6	8.5 (1.3)	+3.0 (0.2)	5.3 (0.2)	47.8 (2.6)
CH_3CHO $18_{0,18}$–$17_{0,17}$ A	335.3587	155	227	1.1	9.6 (1.3)	+2.9 (0.2)	5.6 (0.5)	57.3 (4.5)

[a] *Frequencies and spectroscopic parameters have been extracted from the Jet Propulsion Laboratory molecular database (Pickett et al. 1998) for all the transitions. Upper level energies refer to the ground state of each symmetry.* [b] *Gaussian fit.* [c] *Assumed.*

ues for hot-corinos in Perseus and in B335 (Taquet et al. 2015, Imai et al. 2016), we can infer $X_{CH_3CHO} \simeq 8 \times 10^{-9}$. This is in good agreement with the CH_3CHO abundance found in a region within a few 10 au around the B335 protostar using ALMA (2×10^{-9}; Imai et al. 2016).

The HDO emission has been analysed using a non-LTE LVG model (see Ceccarelli et al. 2003 and Sec. 2.3.2), assuming collisional coefficients for the system HDO-H_2 computed by Faure et al. (2012). A Boltzmann distribution for the ortho-to-para H_2 ratio, in agreement with the Faure et al. (2012) computations, showing that para-H_2 and ortho-H_2 collisional coefficients are different only at temperatures $\ll$ 45 K. With respect to Codella et al. (2015), we can now use the measured size of 0.″18. Figure 4.6 (lower panel) shows the LVG predictions in the T_{kin}–N(HDO) plane for densities for 10^8 cm^{-3} (blue), 10^9 cm^{-3} (magenta), and 10^{10} cm^{-3} (red; representing the LTE regime). Assuming $N(HDO)/N(H_2O) \leq 0.1$, $X_{H_2O} = 3 \times 10^{-5}$; see Taquet et al. 2015), and the source size of 0.″18, then Fig. 4.6 shows that only densities of at least 10^8 cm^{-3} are possible, leading to $N(HDO) \leq 3 \times 10^{17}$ cm^{-2}. Indeed, densities of 10^7 cm^{-3} would imply $N(HDO) \leq 3 \times 10^{16}$ cm^{-2}, i.e. values ruled out by the LVG solutions in Fig. 4.6. With a density of 10^8 cm^{-3} the opacity of the HDO line is 0.3, while lower values are expected for higher densities. We note that the temperatures derived from CH_3CHO (grey region) are consistent with the solutions found with HDO.

In conclusion, the present dataset allow us to futher constrain (with respect to Codella et al. 2015) the physical properties associated with HDO and CH_3CHO: T_{kin} = 78±14 K and $n_{H_2} \geq 10^8$ cm^{-3}.

4.3.3 Kinematics

The study of kinematics is instructive: Fig. 4.12 (lower panels) reports the distribution of the 1st moment of the HDO and CH_3CHO Cycle 4 images. We detect a velocity gradient (± 2 km s^{-1} with respect to the systemic velocity) directed along the equatorial plane, consistent with both the gradients detected in the envelope and in the disk (e.g. Wiseman et al. 2001; Lee et al. 2014, 2017c; Codella et al. 2014, Leurini et al. 2016), i.e. blueshifted towards north-west and redshifted towards south-east. redshifted towards south-east. Additional information is coming from the channel maps (Fig. 4.14): the emission at v_{sys} looks elongated along

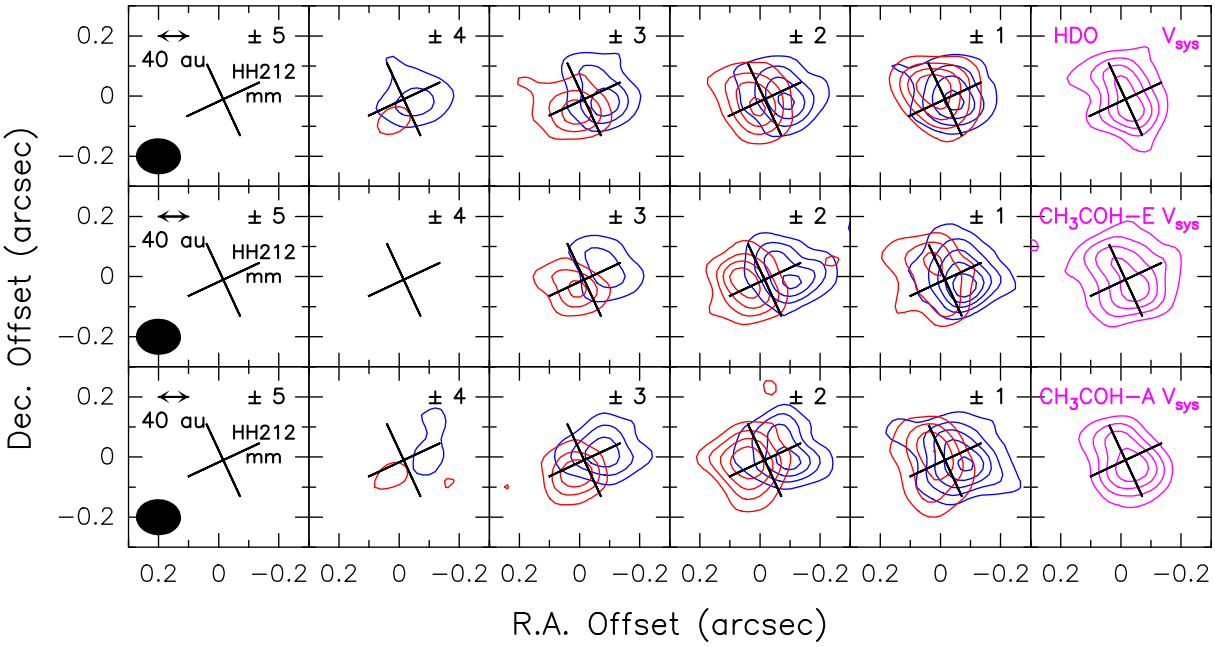

Figure 4.14: Channel maps of the HDO($3_{3,1}$–$4_{2,2}$) (upper panels) and CH_3CHO($18_{0,18}$–$17_{0,17}$) E&A (lower panels) blue- and redshifted (continuum subtracted) emissions observed during ALMA-Cycle 4 towards the HH212-mm protostar. Each panel shows the emission integrated over a velocity interval of 1 km s^{-1} shifted with respect to the systemic velocity (see the magenta channel, sampling the velocity between +1.5 km s^{-1} and +2.5 km s^{-1}) by the value given in the upper-right corner. The black cross (inclined in order to point the SiO jet direction and consequently the equatorial plane, see Fig. 4.12) indicates the position of the protostar. The ellipse in the top left panel shows the ALMA synthesised beam (HPBW): 0.″15 × 0.″12 (PA = –88°). First contours and steps correspond to 3σ (4.5 mJy beam $^{-1}$ km s^{-1} for HDO and 3.0 mJy beam $^{-1}$ km s^{-1} for CH_3CHO).

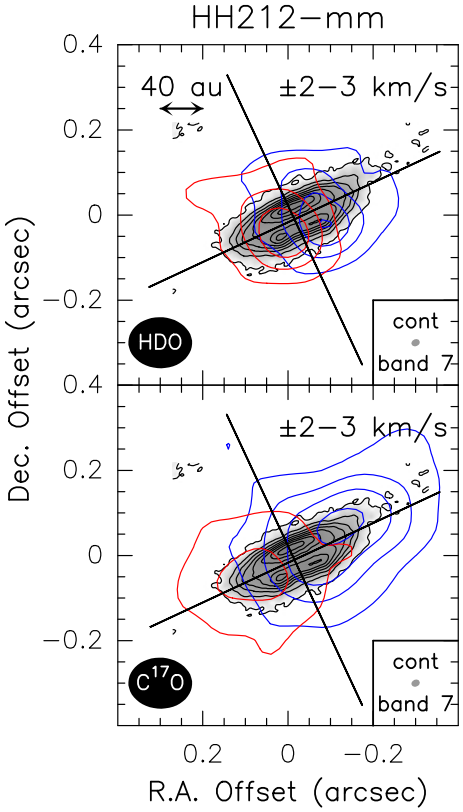

Figure 4.15: HDO($3_{3,1}$–$4_{2,2}$) (*Upper*) and $C^{17}O$(3–2) (*Lower*) channel maps emitting v_{sys}± 2–3 km s^{-1} (blue and red) overlaid on top of the disk traced by Lee et al. (2017b) using ALMA-Band 7 continuum observations (grey scale). $C^{17}O$(3–2) emission (a tracer of the HH212 disk at those velocities, se also Codella et al. (2014) has been also observed within the present Cycle 4 dataset (Tabone et al. 2017). First contours and steps correspond to 3σ (60 mJy beam^{-1} km s^{-1} for HDO and 73 mJy beam^{-1} km s^{-1} for $C^{17}O$) and 5σ, respectively.

the jet axis. The sizes of the emissing regions are, within the errors, consistent:

- 161(17)×103(18) mas (72×46 au; HDO);
- 213(34)×129(33) mas (99×58 au; CH_3CHO-A);
- 209(25)×98(26) mas (94×44 au; CH_3CHO-E).

At higher velocities we clearly spatially resolve both the red- and blueshifted regions, that have sizes similar to those derived at systemic velocity, and moves away from the jet axis revealing the velocity gradient. These spatial sizes well overlap with the disk, traced by Lee et al. (2017b) using ALMA continuum emission in Band 7 with a spatial resolution of 8 au (see Fig. 4.15). Although comparisons between images taken at different angular resolutions have to be taken with a pinch of salt, the present molecular suggest that HDO and CH_3CHO comes from a radius consistent to that (60 au) of the dusty disk around the protostar. However, the HDO and CH_3CHO channel maps do not show (within the present spatial resolution), a trend expected for inner envelopes ($v \sim r^{-1}$) or self-gravitating disks ($v \sim r^{-1/2}$), where higher velocities the positions of the blue- and redshifted clumps are getting closer. Such a trend was indeed observed using $C^{17}O$(3–2) and HCO^+(4–3) as observed at 0.″6 angular resolution by Codella et al. (2014) and Lee et al. (2014), respectively, revealing a rotating molecular disk. Figure 4.15 compares the spatial distribution of HDO at velocities[5] v_{sys} ± 2–3 km s^{-1} with that of $C^{17}O$(3–2) as observed in the same dataset presented here. Clearly, HDO is more compact that $C^{17}O$, that is more elongated along the equatorial plane confirming that are tracing different gas.

4.3.4 Discussion

After rounded up all the information: which is the origin of the hot, dense, chemically enriched, and rotating gas, and extended up to ± 40 au with respect to the HH212 disk plane? By the light of recent investigations on protostellar systems (Lee et al. 2017c, Sakai et al. 2017), different pictures can be discussed:

[5] These velocities are those that allow one to trace the disk given that, at velocities closer to v_{sys}, the emission is dominated by the molecular static cloud.

- we are observing the so-called disk atmosphere reported by Lee et al. (2017c), who imaged CH_3OH and NH_2CHO (among other species) with a spatial resolution of 8 au. The authors found that these iCOMs trace the outer layers (i.e. the atmosphere) of the disk rotating around HH212-mm within the centrifugal barrier of $\sim$ 44 au. The iCOMs emission detected by Lee et al. (2017c) shows no extended emission, but is rather imaging two thin ($\sim$ 50 mas) layers above and below the opaque mid-plane of the disk, at $\pm$ 50 mas. The maps here reported follow the iCOMs vertical distribution up to about $\pm$ 100 mas from the equatorial plane. A possible explanation is that they are tracing in HDO and CH_3CHO the same components, convolved at a larger beam, that makes us see a unique structure instead of two thin layers. However, we cannot exclude that HDO and CH_3CHO are complementing the CH_3OH and NH_2CHO images on spatial scales, larger than those by Lee et al. (2017c), tracing more extended emission. Note that Bianchi et al. (2017b), using the present ALMA dataset, found very similar images for $^{13}CH_3OH$. In both cases, we confirm that iCOMs around the HH212 protostar are either formed directly in the external layers of the disk itself and then injected into the gas-phase by thermal desorption, or formed in the gas-phase using simpler species released from grain mantles (e.g. Codella et al. 2017, and references therein, for a recent discussion on this question).

- we are observing the centrifugal barrier, i.e. the chemical enrichment in the ring where the infalling envelope meets the rotating disk. Indeed, the Position-Velocity (PV) diagrams obtained from the HDO and CH_3CHO images perpendicular to the jet axis and along the equatorial plane (Fig. 4.16) are well consistent with the classical shape expected from a ring around the protostar, i.e. with the projected velocity proportional to the position offset from the protostar (see e.g. Sakai et al. 2014b,a, 2016, 2017; Oya et al. 2016, Lee et al. 2017c, and references therein). Figure 4.16 suggests a radius for the centrifugal barrier of $\simeq$ 0.″15 (60 au) for CH_3CHO: considered the different angular resolution the present PVs are in agreement with the $\sim$ 0.″11–0.″12 derived by Lee et al. (2017c). Interestingly, the vertical size of the iCOMs structure is consistent with the results obtained for the L1527

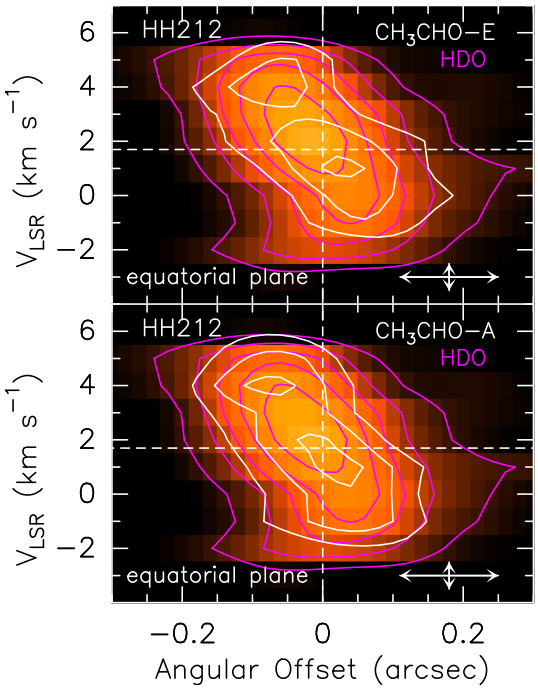

Figure 4.16: Position-velocity cut of HDO($3_{3,1}$–$4_{2,2}$) colour scale, magenta contours) along the equatorial plane (PA = 112°, see Fig. 1) overlap with that of the $CH_3CHO(18_{0,18}–17_{0,17})$-E (upper panel) and $CH_3CHO(18_{0,18}–17_{0,17})$-A (lower panel), drawn in white contours. First Contours and steps correspond to 3σ (3.1 K km s^{-1}). Dashed lines mark the position of HH212-mm protostar and the cloud V_{LSR} (+1.7 km s^{-1}; Lee et al. 2014). The error bars are drawn In the bottom-right corners.

protostar by Sakai et al. (2017): a fraction of the gas moves away slowly[6] from the mid-plane of the centrifugal barrier towards vertical directions. Figure 4.16 suggests that this effect could be more important for HDO, that is showing a sligthly wider distribution (± 0.″2) with respect the CH_3CHO one. Indeed, the possibility for HDO to be associated with outflowing motion has been already proposed by Codella et al. (2016b) by analysing the line profiles of ALMA data at lower (∼ 0.″6) spatial resolution.

[6]projected velocities around ± 1 km s^{-1}, being the L1527 system edge-on, as HH212.

4.3.5 Conclusions on iCOMs

The results of the present paper confirms that astrochemistry is a powerful tool that can be used to image kinematical components ocurring the inner 50 au from the newly born protostar. In particular, we show that water (in its deuterated form) and acetaldehyde are formed in regions associated with the disk, tracing a ring-like structure wich extends up to ± 60 au, in agreement with what previously found by Lee et al. (2017c) for formamide. The gas associated with HDO and CH_3CHO is hot, $T_{\rm kin}$ = 78±14 K, and dense, $n_{H_2} \geq 10^8$ cm^{-3}.

The present images shows iCOMs emission up to 40 au above and below the disk plane. Are these iCOMs ouflowing, thus leaving the protostellar system? Interstingly, both the HDO and CH_3OH peaks of the emission at low blue- and redshifted velocities, ± 1 km s^{-1} from $v_{\rm sys}$, are significantly offset from the equatorial plane. The red emission lies at north-east while the blue one mainly emits at south-west. This is found also in the $^{13}CH_3OH$ images reported by Bianchi et al. (2017b). This effect is clealy inconsistent with the jet, and it cannot be a signature of a disk wind, recently modeled in HH212 using SO and SO_2 emission by Tabone et al. (2017). Indeed a disk wind should show a kinematical pattern coherent with both the jet and the outflow which have northern/southern blue-/redshifted lobes. Detailed models of MHD disk winds are required to further analyse this aspect.

On the other hand, by inspecting the asymmetric cavity opened by the jet and well traced by $C^{34}S$ in Fig. 4.12 (see also Codella et al. 2014), we clearly note that the emission at ± 1 km s^{-1} from $v_{\rm sys}$ is brighter exactly in the north-east and south-west portions of the arms close tothe protostar. By the light of this, it is tempting to speculate that the HDO and CH_3OH peaks at $v_{\rm sys}$ ± 1 km s^{-1} are due to slow shocks releasing material outwards as suggested by Sakai et al. (2017). If so, this would imply that (i) the enriched gas could contribute to extract angular momentum from the protostellar system, and (ii) iCOMs, i.e. potential bricks to be used for a prebiotic chemistry would leave the region where a planetary system is expected to form. Clearly, further interferometric high resolution observations are needed to verify this possibility (see Chap. 7).

5 Chemical complexity in a later Class I protostellar stage

As reported in Sec. 4, the emission of iCOMs and deuterated molecules can provide precious information on the chemical and physical properties of Class 0 sources and they can be used as a sort of Ariadne thread to reach the later evolutionary stages, i.e. the craddle of Solar System analogs (Ceccarelli et al. 2014). However, while deuterated molecules have been detected towards the early stages of the Sun-like star formation (i.e. prestellar cores and Class 0 objects) as well as in the Solar System, no clear result has been obtained for intermediate evolutionary phases (Class I and II objects). In the same way, iCOMs have been detected towards the early stages (prestellar cores, Class 0) and the Solar System, demonstrating the existence of efficient pathways to chemical complexity. Nevertheless, the iCOMs observations in the intermediate stages (Class I / Class II) are still far to be comprehensively investigated.

In this Section, we present the observation of deuterated formaldehyde and methanol as well as several iCOMs (e.g. ketene, acetaldehyde, methyl formate and dimethyl ether) in the Class I object, SVS13-A. The results presented in this Section are reported in Bianchi et al. (2017a) and Bianchi et al. (in preparation). The source was observed between 2012 and 2014 in the context of the ASAI IRAM-30m large program (see Sec. 3.2).

5.1 The SVS13-A Class I laboratory

SVS13-A is a Class I protostar located in the SVS13 cluster of the NGC1333 cloud in Perseus. Since the discovery of the first dark clouds by Barnard (1913), the Perseus region has received increasing attention and has been extensively investigated at many wavelengths at a variety of resolutions. In particular, the young cluster NGC 1333, is one of the best studied and the most active region of star formation in the Perseus cloud. The region is rich in sub-mm cores, embedded YSOs, radio continuum sources, masers, IRAS sources, SiO molecular jets, H_2 and Herbig-Haro shocks, molecular outflows, and the lobes of extinct outflows (see e. g. Walawender et al. 2008, Tobin et al. 2016 and references therein). The eastern portion of the cloud contains the star forming cloud B5, a young (2 – 4 Myr) cluster IC 348 and a diffuse H II region (G159.6-18.5). The western portion of the Perseus cloud is associated with the most active sites of current star formation, including the NGC 1333 cluster, the small stellar aggregates associated with Barnard 1 (B1), L1448, L1455, and additional cloud cores which are producing smaller groups of young stars. Figure 5.1 (left panel, from Bally et al. 2008) shows an overview of the Perseus star forming region in which is indicated the NGC 1333 cluster. Submillimeter observations of its southern region revealed many bright Class 0/I objects, including SVS13, IRAS 2, IRAS 4 and their individual components (see Figure 5.1 from Plunkett et al. 2013, right panel). Early surveys were performed using single-dish telescopes to explore the dust envelopes of the IRAS objects and in some cases resolve them into multiple sources, for example for IRAS 4 which was first resolved into two objects 4A and 4B (Sandell et al. 1991). Further observations of the region pointed toward the importance of outflows for the distribution of the matter in NGC 1333. For example, Lefloch et al. (1998a) mapped the southern region of NGC 1333 at 1.3 mm using the IRAM-30 m telescope revealing two cavities in the region, related to the action of the outflows from the newly formed stars (see Figure 5.2.)

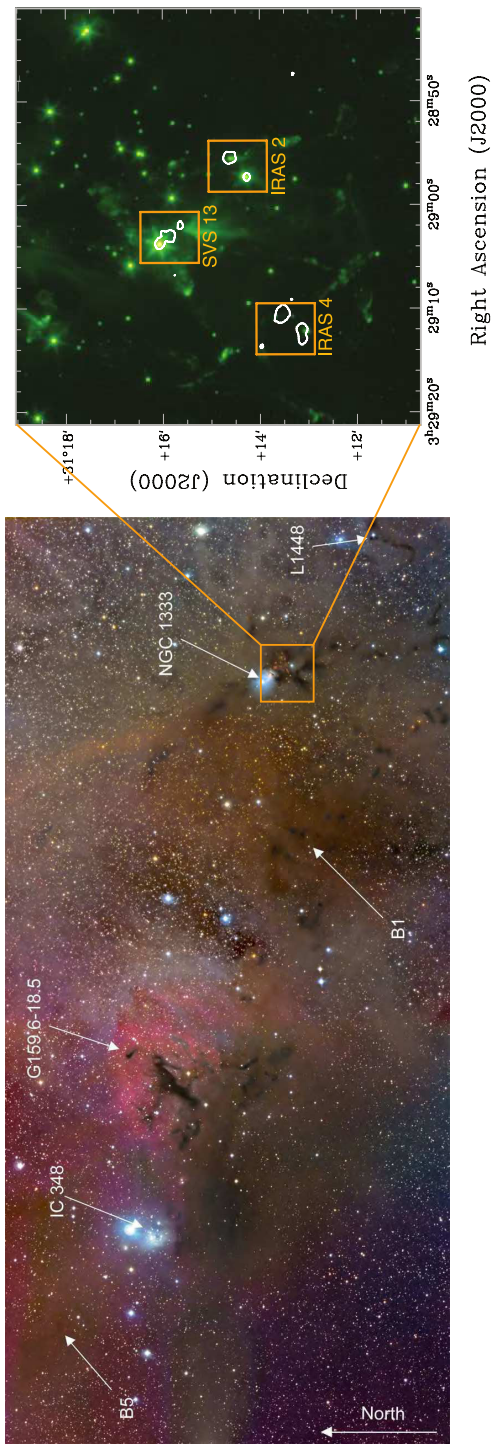

Figure 5.1: *Left panel:* Visual wavelength image of the Perseus molecular cloud lying at ~ 230 pc from the Sun (adapted from Bally et al. 2008). The region and its surroundings contain several regions of active star formation. With a total mass of about $10^4 M_\odot$, the Perseus cloud is the closest such object actively forming large numbers of low to intermediate-mass stars. Labels indicate the individual regions Barnard 1 (B1), Barnard 5 (B5), IC 348, NGC 1333, L1448 and the G159.6-18.5 regions. *Right panel:* Zoom-in of the NGC 1333 star forming region observed with the Spitzer telescope Infrared Array Camera (IRAC) at 4.5 μm (Gutermuth et al. 2008) (green). Orange boxes indicate the regions of IRAS 2, IRAS 4 and SVS13. The white contours refer to 2.7 mm continuum observations performed using the CARMA interferometer (Plunkett et al. 2013).

More specifically, SVS13-A is associated with an extended outflow (> 0.07 pc, Lefloch et al. 1998a, Codella et al. 1999) as well as with the well-known chain of Herbig-Haro (HH) objects 7–11 (Reipurth et al. 1993). The accurate distance of the SVS13 region (235 ± 18 pc) has been derived using VLBI parallax measurements of masers associated with this object (Hirota et al. 2008). IRAM-30m observations revealed that the SVS13 star forming region itself is associated with a Young Stellar Objects (YSOs) cluster dominated in the millimeter by two objects labelled A, and B, respectively, separated by ∼ 15″. SVS13-B has been first tentatively detected by Grossman et al. (1987) and then confirmed by Chini et al. (1997) with the discovery of a third source SVS13-C, at a distance of 20″ from A. The embedded objects in NGC 1333 identified in single-dish maps have been successively observed at higher resolution using various interferometers to improve understanding of their small scale structure and to look for further multiplicity. Aa an example, a significant number of the deeply embedded objects in NGC 1333 including the SVS13 region were targeted by Looney et al. (2000) with the BIMA array survey (see Figure 5.4). The region was found to be even more complex with the detection of additional nearby sources thanks to further radio observations. In particular the source SVS13-A has been resolved itself into a close binary system, separated by 0.″3 using the Very Large Array (Rodríguez et al. 1999; Anglada et al. 2000).

Interestingly, SVS13-A and SVS13-B are associated with two different evolutionary stages. On the one hand, SVS13-B is a Class 0 protostar with $L_{\rm bol} \simeq 1.0$ $L_{\rm sun}$ (e.g. Chen et al. 2009; Tobin et al. 2016) driving a well collimated SiO jet shown in Fig. (Bachiller et al. 1998; Lefloch et al. 1998b).

On the other hand, SVS13-A is definitely more luminous ($\simeq 32.5$ $L_{\rm sun}$, Tobin et al. 2016) and has a low $L_{\rm submm}/L_{\rm bol}$ ratio (∼ 0.8%) and a high bolometric temperature ($T_{\rm bol} \sim 188$ K, Tobin et al. 2016). Thus, although still deeply embedded in a large scale envelope (Lefloch et al. 1998a), SVS13-A is considered a more evolved protostar, already entered in the Class I stage. Recently a systematic study of SVS13-A has revealed the presence of a hot corino region with the detection of HDO (Codella et al. 2016a) lines originating in a very compact and hot region around the protostar. Indeed De Simone et al. (2017) imaged glycolaldehyde emission around SVS13-A using IRAM-NOEMA interferometer, obtaining a size of 0.″3 corresponding to ∼ 70 au. For all these reasons, SVS13-A is an almost

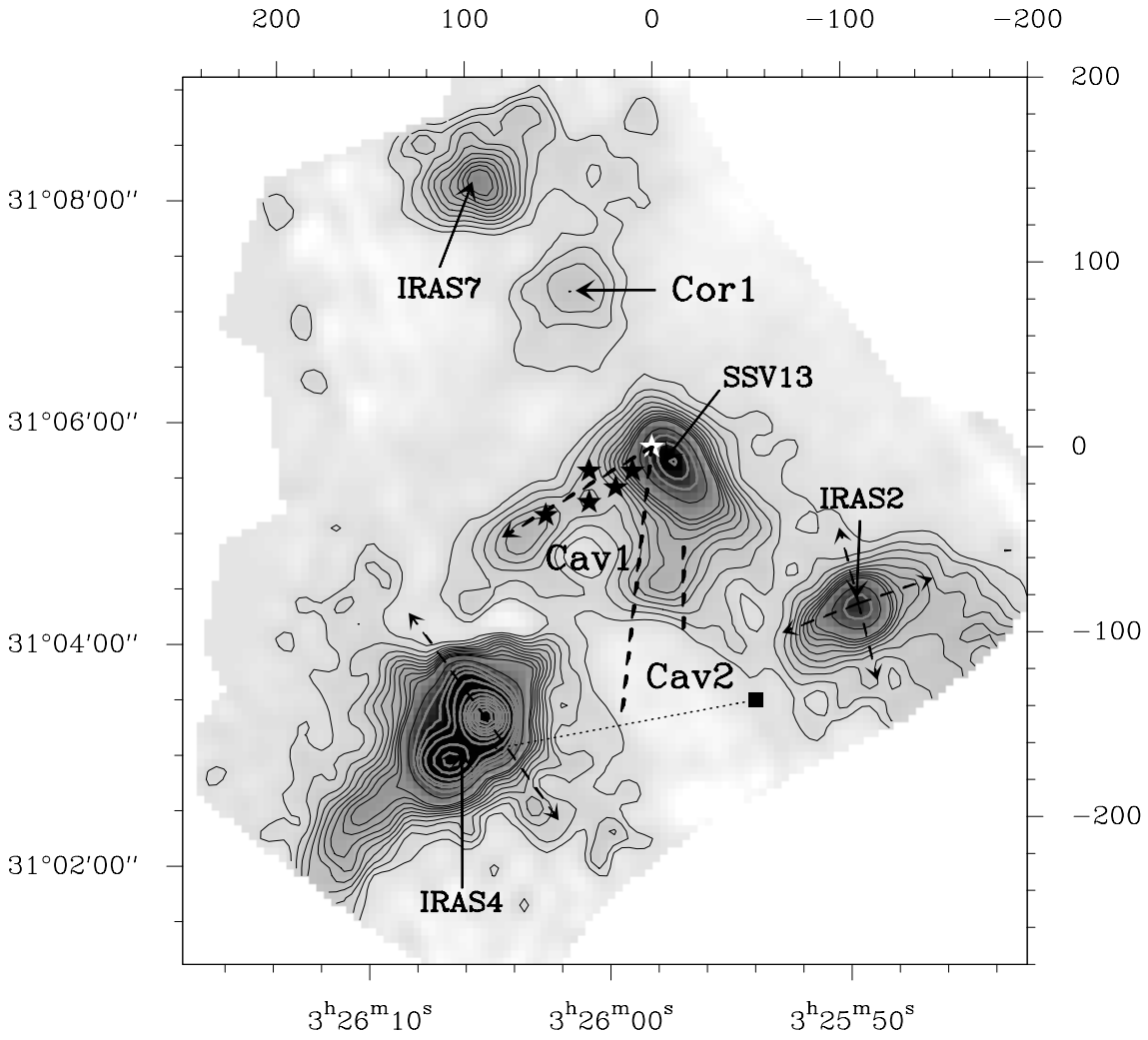

Figure 5.2: Continuum emission at 1.25mm of the NGC1333 star forming region obtained with the IRAM-30m radiotelescope (Lefloch et al. 1998a). The map is centered on the (here unresolved) SVS13 object, indicated by the star and it has an angular resolution of 15″. The continuum emission reveals not only conspicuous dust envelopes and cores associated with the protostars IRAS4A-B, IRAS2 and SVS13 but also the presence of material associated with the protostars outflows. Cav1 indicates the cavity opened to the southeast of SVS13 and situated between the HH 7–11 chain of objects (marked by black stars) and the SVS13 southern elongation. Cor1, and Cav2 indicate the positions of the core and cavity also present in the region. The molecular outflows and the H_2 filaments are indicated by dashed lines (see Lefloch et al. 1998a for details). Note that right ascension and declination refer to the B1950 coordinates.

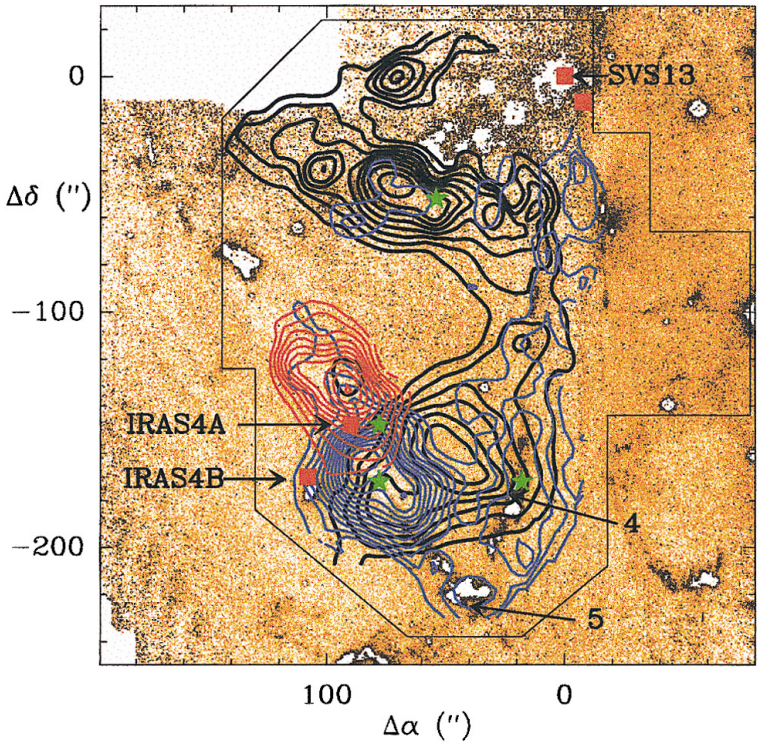

Figure 5.3: SiO (2–1) emission observed with the IRAM-30m telescope superposed upon an H_2 2.12 mm map of the region around the SVS13, IRAS 2, and IRAS 4 protostars in NGC 1333 (Lefloch et al. 1998b). The angular offsets are derived with respect to the position of the SVS13 system. Red squares indicate the position of the protostars while blue and red contours are tracing the velocity integrated emission of the blueshifted/redshifted high-velocity gas. The high-velocity SiO emission traces the bipolar outflow emanating from IRAS 4A and the SVS13-B outflow, which propagated from the south of the SVS13 core to the southwest of IRAS 4. The brightness emission of the quiescent SiO component is traced in thick black contours, widespread around the HH 7–11 objects and coincident with the SVS13-B outflow.

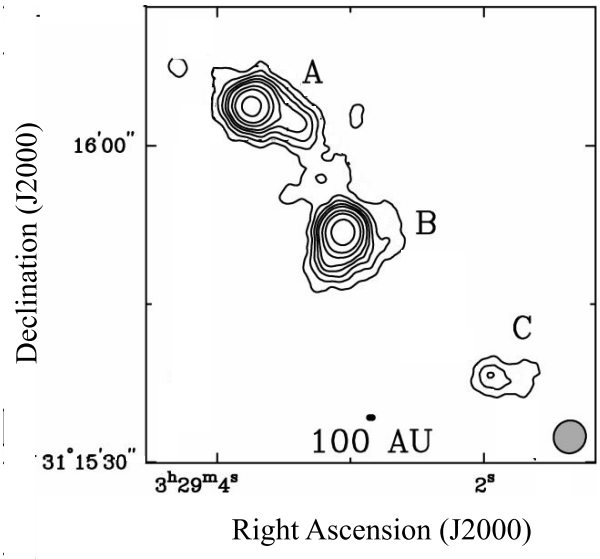

Figure 5.4: Continuum interferometric observations at 2.7 mm of the SVS13 region, performed with the BIMA array (Looney et al. 2000). In the map are indicated the two objects labelled A, and B, respectively, separated by ~ 15″ and the third fainter object SVS13-C, at a distance of 20″ from A.

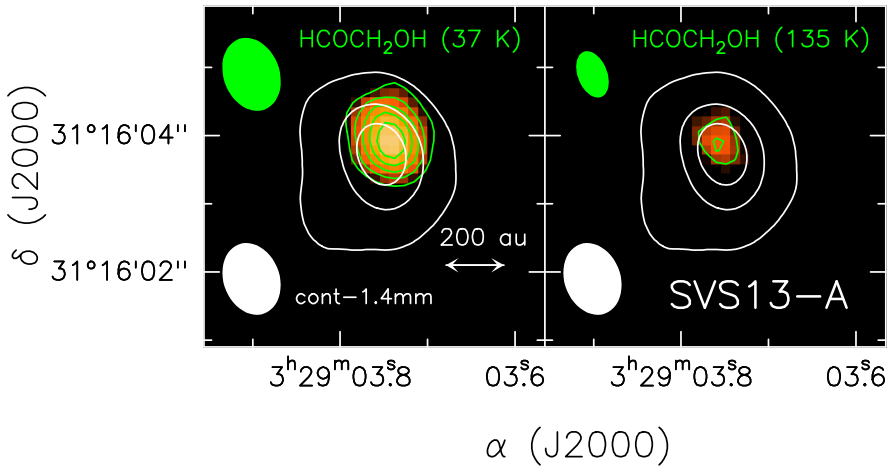

Figure 5.5: Glycolaldehyde maps of the source SVS13-A obtained with the IRAM-Plateau de Bure (PdB) interferometer in the framework of the CALYPSO IRAM large program (De Simone et al. 2017). In particular the maps show the comparison between the 1.4 mm continuum (white contours) and the glycolaldehyde spatial distributions (colour scale and green contours). On the left panel the glycolaldehyde distribution refers to the sum of the $7_{6,2}$–$6_{5,1}$ and $7_{6,1}$–$6_{5,2}$ with E_{up} = 37 K. On the right panel to the $22_{2,21}$–$21_{1,20}$ emission with E_{up} = 135 K. The detection of glycolaldehyde is an evidence of the presence of a hot-corino region n (i.e. 100 K in the inner 100 au) in SVS13-A.

unique laboratory to investigate how deuteration change from the Class 0 to the Class I phases.

5.2 Decrease of deuteration in Class I objects

In this Section we present the results of formaldehyde and methanol deuteration measurements towards the Class I low-mass protostar SVS13-A. This section is based on the work presented in (Bianchi et al. 2017a). SVS13-A has been observed with the IRAM-30m telescope near Pico Veleta (Spain), in the framework of the Astrochemical Surveys At IRAM (ASAI) Large Program.

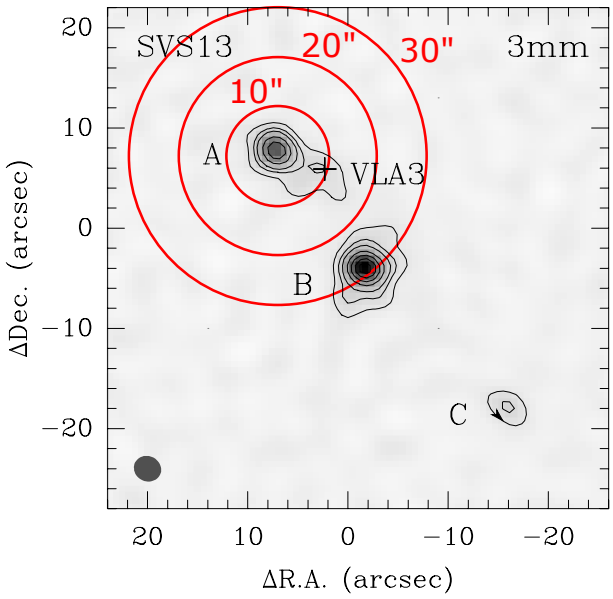

Figure 5.6: SVS13 region as observed with IRAM-PdBI at 3mm in dust continuum, from Chen et al. (2009). Cross in the images marks the position of the radio source VLA 3 (Rodríguez et al. 1997). The synthesized PdBI beam is shown as grey oval in the image. The superposed red circles show the IRAM-30m telescope HPBWs referring to the ASAI observations at 1, 2 and 3mm and corresponding to a size of 10″, 20″ and 30″, respectively.

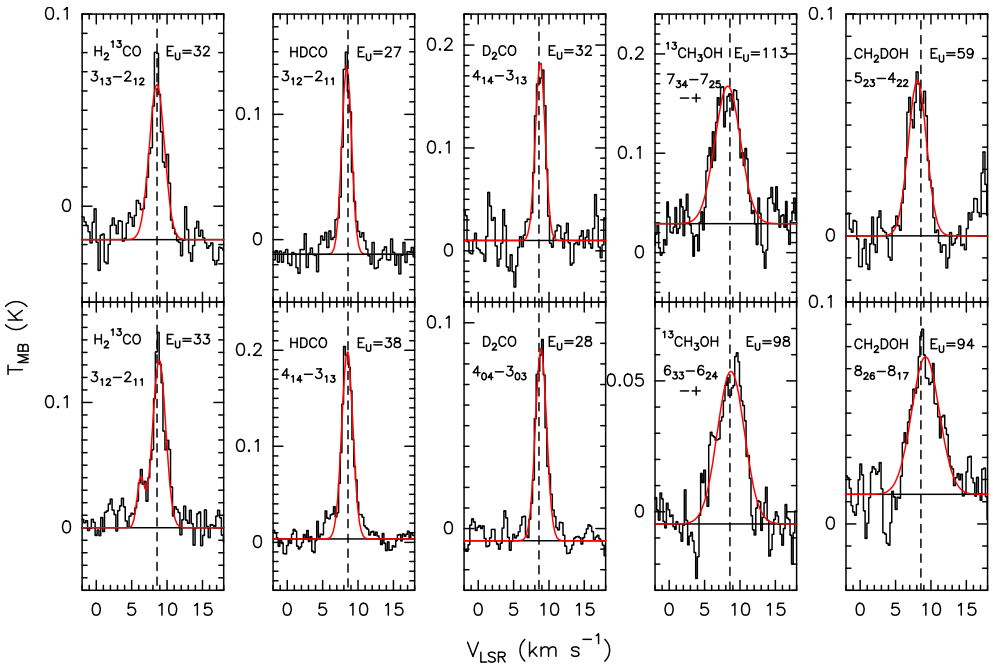

Figure 5.7: Figure from Bianchi et al. (2017a). Examples of line profiles in T_{MB} scale (not corrected for the beam dilution): species and transitions are reported. The vertical dashed line stands for the ambient LSR velocity (+ 8.6 Km s^{-1}, Chen et al. 2009)

5.2.1 Line identification

Line identification has been performed using a package developed at IPAG wich allows to identify lines in the collected ASAI spectral survey using the Jet Propulsor Laboratory (JPL[1], Pickett et al. 1998) and Cologne Database for Molecular Spectroscopy (CDMS[2]; Müller et al. 2001, Müller et al. 2005) molecular databases. We double checked the line identifications with the GILDAS Weeds package (Maret et al. 2011). We detected several lines of $H_2^{13}CO$, HDCO, D_2CO, $^{13}CH_3OH$ and CH_2DOH (see Tables 5.1 and 5.2). $^{13}CH_3OH$ is a species with internal rotation, divided in two *A*-type and *E*-type forms because of the presence of a methil group (CH_3). The total statistical weight of the *A* and *E* type levels is the same (Turner 1991 and references therein). For CH_2DOH the fundamental torsional level is further divided into three sub-levels indicated with *e0* (0 K), *e1* (13.4 K) and *o1* (18.3 K) (Parise 2004). On the other hand, $H_2^{13}CO$ and D_2CO exist in two isomers, ortho and para, that have different nuclear spin states. The statistical o/p ratio is 3:1 for $H_2^{13}CO$ and 2:1 for D_2CO. These values are expected beyond the so called *high-temperature limit*, which can be analytically approximated by hA << kT for asymmetric-top molecules as formaldehyde, where A (Hz) is the largest rotational constant of the molecule.

Examples of the detected line profiles in T_{MB} scale are shown in Figure 5.7. The peak velocities of the detected lines are between +8 km s^{-1} and +9 km s^{-1}, being consistent, once considered the fit uncertainties, with the systemic velocity of both A and B component of §(+8.6 km s^{-1}, Chen et al. 2009; López-Sepulcre et al. 2015). We fitted the lines with a Gaussian function, and excluded from the analysis those lines with $|v_{peak} - v_{sys}|$ >0.6 km/s plausibly affected by line blending. We select for the analysis only the lines with a signal to noise (S/N) higher than 4σ. The spectral parameters of the detected lines, as well as the results from the Gaussian fits, are presented in Tables 5.1 and 5.2, where we report the frequency of each transition (GHz), the telescope HPBW (″), the excitation energies of the upper level E_{up} (K), the $S\mu^2$ product (D^2), the line rms (mK), the peak temperature (mK), the peak velocities (km s^{-1}), the line full width at half maximum (FWHM) (km s^{-1}) and the velocity integrated line intensity I_{int} (mK km s^{-1}).

[1]https://spec.jpl.nasa.gov/
[2]http://www.astro.uni-koeln.de/cdms/

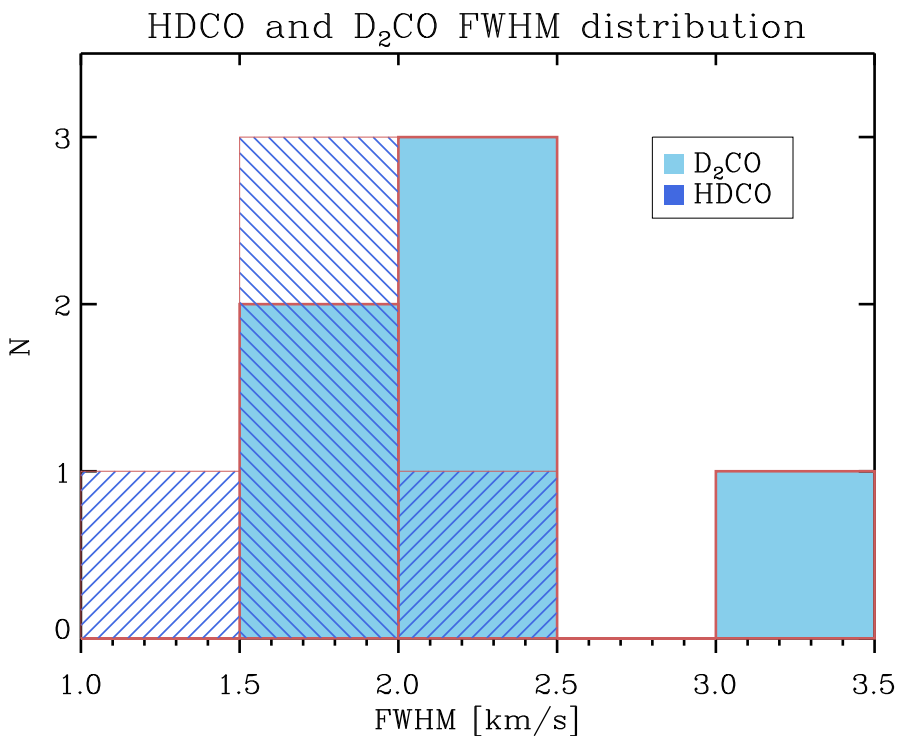

Figure 5.8: Figure from Bianchi et al. (2017a). Distribution of the linewidth (FWHM) of the observed HDCO and D_2CO lines. Cyano is for D_2CO and blue hatched is for HDCO.

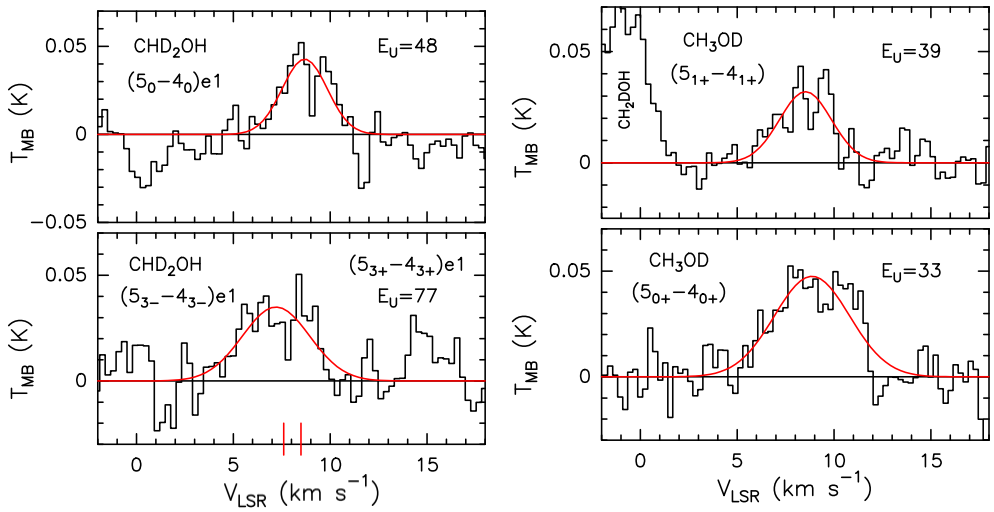

Figure 5.9: Figure from Bianchi et al. (2017a). Tentative detections of emission due to CHD_2OH (left panel) and CH_3OD (right panel) transitions. Transitions and upper level energies are reported. Red curves are for the Gaussian fit. Note that the middle-upper panel reports emission due to two different transitions (see the red vertical bars).

5.2.2 Formaldehyde isotopologues

We report the detection of several lines of H_2CO and its isotopologues $H_2^{13}CO$, HDCO and D_2CO. The measured intensity ratio between the low energy transitions of H_2CO and $H_2^{13}CO$ (as e.g. the $3_{1,3}$–$2_{1,2}$ at E_{up} = 32 K), is $\sim$ 25, a value well below the median value for the interstellar medium of $^{12}C/^{13}C \sim 68$ (Milam et al. 2005). This indicates that the observed H_2CO are optically thick. Therefore we use $H_2^{13}CO$ to derive the formaldehyde deuteration.

We detected 7 lines of $H_2^{13}CO$, 5 lines of HDCO and 5 lines of D_2CO, with excitation energies, E_{up}, in the 10–45 K range. Examples of the detected line profiles are shown in Figure 5.7; the detected transitions and the observational parameters are displayed in Table 5.1 and Table 5.2. The lines profiles are close to a gaussian shape and the peak velocities are close to the systemic source velocity with values between +7.8 km s^{-1} and +9.0 km s^{-1} while the FWHM is between 0.9 and 2.5 km s^{-1}. Three lines of $H_2^{13}CO$ (with frequencies 137.45 GHz, 141.98 GHz, and 146.64 GHz) and one line of HDCO (with frequency 134.2848) are detected in the 2 mm band and they are affected by contamination of emission in the off positions (see

Sec. 3.2 for details on the observing techniques), consistently with the analysis reported by López-Sepulcre et al. (2015), using ASAI spectra. The contaminated lines correspond to a size of the telescope HPBW > 16″. In these cases the measured intensities will be treated as lower limits in the rotational diagram analysis (see Sec. 5.2.6). For the D_2CO, only one line is detected at 2 mm but it does not show any absorption feature due to the wobbler contamination (see Chap. 3). This can be an indication of a more compact region emitting in D_2CO with respect to that of HDCO emission. A similar behaviour has been observed in a different context by Fuente et al. (2014) towards the intermediate-mass Class 0 protostar NGC 7129–FIRS 2. They detected, using interferometric observations, an intense and compact D_2CO component associated with the hot core. On the other hand Ceccarelli et al. (2001) detected in the low-mass Class 0 protostar IRAS16293-2422, an extended D_2CO emission (up to ~5000 au), associated with the external envelope. The present data do not allow us to draw reliable conclusions on the relative size of the two deuterated formaldehyde isotopologues. However, in the case of SVS13-A a more compact size is suggested by the broader line profiles of D_2CO with respect to HDCO (see Figure 5.8). In Figure 5.8 we show the distribution of the linewidths of the detected HDCO lines in hatched blue and D_2CO lines in cyano. The bulk of the HDCO lines has a FWHM between 1.5 and 2.0 km s^{-1} while for the D_2CO the peak of the distribution is in the 2.0–2.5 km s^{-1} range. Interestingly, three lines of low excitation (E_{up} < 35 K) of $H_2^{13}CO$ (with frequencies 212.81 GHz, 206.13 GHz and 219.91 GHz) and all the HDCO lines (except for the line in the 2 mm band) show weak (~ 30 mK) wings clearly indicating emission due to outflows that we analyse separately from the main line component.

5.2.3 Methanol isotopologues

Similarly to formaldehyde, the detected lines of CH_3OH are optically thick. We verified it through the measured ratio between the insensities of CH_3OH and $^{13}CH_3OH$ (as e.g. the $5_{1,5}$–$4_{1,4}$ + + at E_{up} = 49 K) that is ~ 2. For this reason also in this case, we use $^{13}CH_3OH$ to calculate methanol column density. In the case of methanol, the process of line identification was more complex than formaldheyde. This is due to the very rich spectra observed with ASAI towards SVS13-A

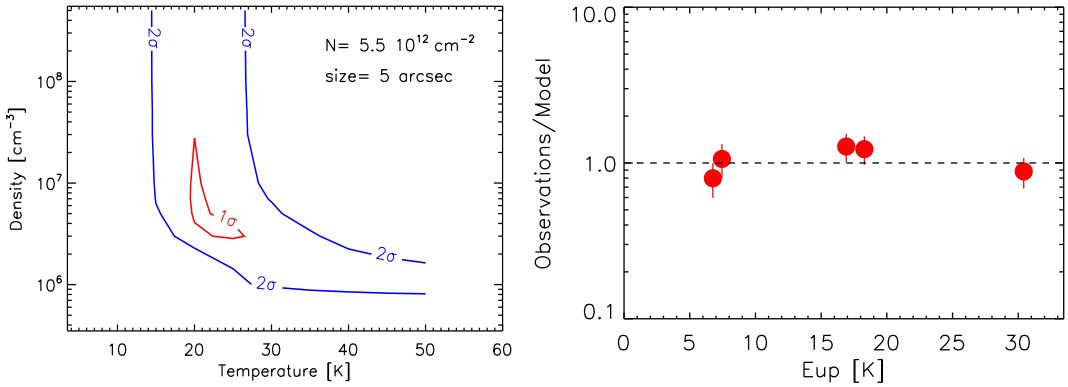

Figure 5.10: Figure from Bianchi et al. (2017a). *Upper panel:* The 1σ and 2σ contour plot of χ^2 obtained considering the non-LTE model predicted and observed intensities of all the detcted ortho $^{13}H_2CO$ lines. The best fit is obtained with $N(^{13}H_2CO) = 5.5 \times 10^{12}$ cm^{-2}, $\theta_s = 5''$, $T_{kin} = 20$ K and $n_{H_2} \geq 7 \times 10^6$ cm^{-3}. *Lower panel:* Ratio between the observed line intensities with those predicted by the best fit model as a function of line upper level energy E_{up}.

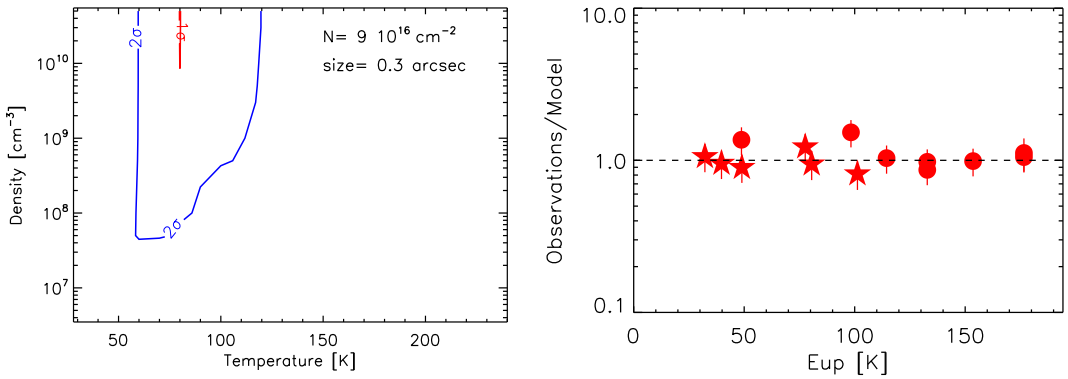

Figure 5.11: Figure from Bianchi et al. (2017a). *Left panel:* The 1σ (in red) and 2σ (in blue) contour plot of χ^2 obtained considering the non-LTE model predicted and observed intensities the detcted $^{13}CH_3CO$ lines with $E_{up} > 40$ K. The best fit is obtained with $N(^{13}CH_3OH) = 9 \times 10^{16}$ cm^{-2}, $\theta_s = 0''.3$, $T_{kin} = 80$ K and $n_{H_2} \geq 3 \times 10^{10}$ cm^{-3}. *Right panel:* Ratio between the observed line intensities with those predicted by the best fit model as a function of line upper level energy E_{up}. Circles refer to $^{13}CH_3CO$ A transitions while stars refer to E transitions.

with a consequent challenging lines identification for a complex molecule such as CH_3OH. In addition to the criteria summarized in Sec. 5.2.1, we further require FWHM > 2 km s^{-1} to discard any possible false identification. We report the detection of 18 transitions of $^{13}CH_3OH$ and 27 lines of CH_2DOH with excitation energies in the 20–276 K range. Examples of the detected line profiles for methanol isotopologues are shown in Figure 5.7. The spectral parameters and the results of the gaussian fit are shown in Tables 5.1 and 5.2. The line profiles are broader than for formaldehyde isotopologues, with a FWHM up to 5.4 km s^{-1}. None of the observed profiles show absorption features due to the wobbler contamination, pointing to an emitting region smaller than formaldehyde.

Interestingly, we detect two different transitions of both CHD_2OH and CH_3OD with E_{up} between 33 K and 77 K (see Table 5.1 and Figure 5.9). The peak velocities are consistent with the systemic source velocity and the FWHMs are in agreement with those of the lines from the other methanol isotopologues.

5.2.4 Wrap up

In summary, the bulk of methanol and formaldehyde isotopologues lines are detected in the 1 mm band. For this reason, the temperature estimate from the rotational diagram analysis (see Sec. 5.2.6) is not affected by the beam dilution. The 30m HPBW is ∼10″ at 1 mm, which ensures that the emission is coming from SVS13-A with no contamination from SVS13-B (the separation between SVS13-A and the companion protostar is ∼ 15″). The lines colllected in the 2 and 3 mm bands could be in principle contaminated from the emission from SVS13-B, because the HPBW is larger, but as we will see in the following discussion they are in agreement with the 1mm lines, confirming the origin of the emission is SVS13-A.

Interestingly, the formaldehyde profiles show line wings that suggest outflow emission, in agreement with the origin of the detected emission from the SVS13-A, that is associated with an extended outflow (> 0.07 pc, Lefloch et al. 1998a, Codella et al. 1999).

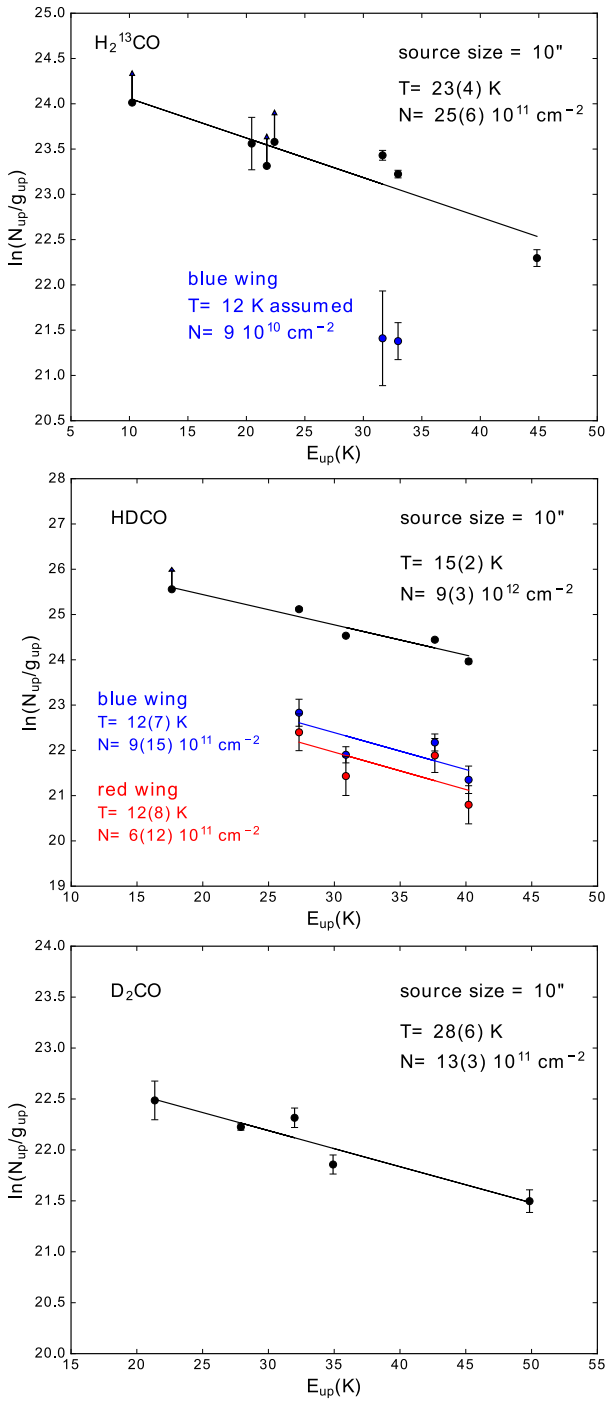

Figure 5.12: Figure from Bianchi et al. (2017a). Rotation diagrams for $H_2^{13}CO$ (upper panel), HDCO (middle panel) and D_2CO (lower panel). An emitting region size of 10″ is assumed (see text). The parameters N_u, g_u, and E_{up} are, respectively, the column density, the degeneracy and the energy (with respect to the ground state of each symmetry) of the upper level. The derived values of the rotational temperature are reported. Arrows are for the lines affected by wobbler contamination (see Sec. 5.2.2) and thus considered as lower limits.

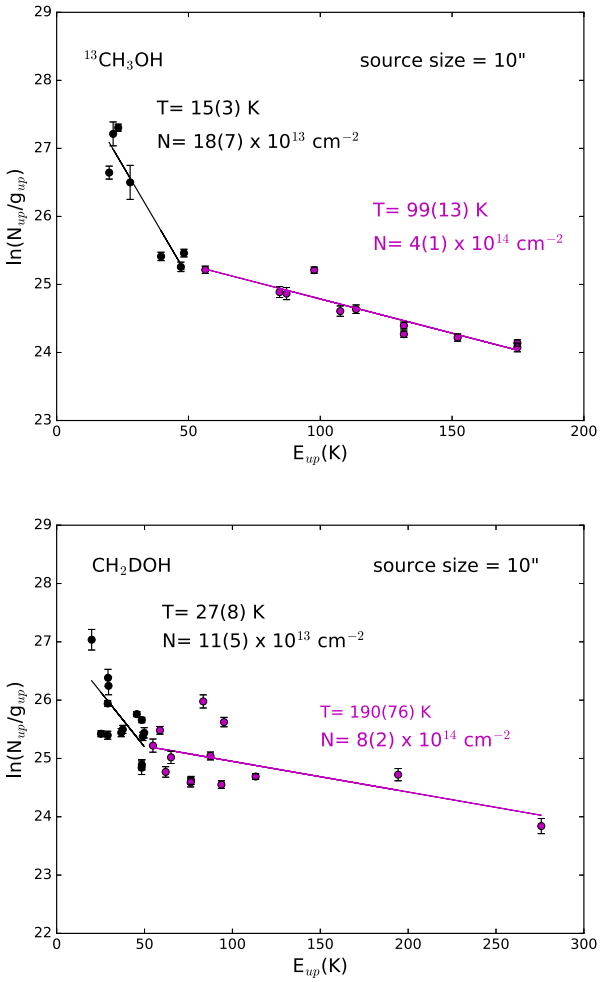

Figure 5.13: Figure from Bianchi et al. (2017a). Rotation diagrams for $^{13}CH_3OH$ (upper panel) and CH_2DOH (lower panel) assuming two emitting components. An emitting region size of 10″ is assumed (see text). The parameters N_u, g_u, and E_{up} are, respectively, the column density, the degeneracy and the energy (with respect to the ground state of each symmetry) of the upper level. The derived values of the rotational temperature are reported.

Table 5.1: List of transitions and line properties (in T_{MB} scale) of the HDCO, D_2CO and CH_2DOH emission detected towards SVS13-A

Transition	ν^a (GHz)	*HPBW* (″)	$E_{up}{}^a$ (K)	$S\mu^{2a}$ (D^2)	rms (mK)	$T_{peak}{}^b$ (mK)	$V_{peak}{}^b$ (km s^{-1})	$FWHM^b$ (km s^{-1})	$I_{int}{}^b$ (mK km s^{-1})
Deuterated species									
HDCO $2_{1,1}$–$1_{1,0}$	134.2848	18	18	8	17	158(5)	+8.31(0.05)	1.1(0.1)	188(17)
HDCO $3_{1,2}$–$2_{1,1}$	201.3414	12	27	14	19	334(22)	+8.43(0.03)	1.6(0.1)	561(21)
HDCO $4_{1,4}$–$3_{1,3}$	246.9246	10	38	20	17	312(22)	+8.50(0.03)	1.9(0.1)	619(18)
HDCO $4_{0,4}$–$3_{0,3}$	256.5854	10	31	22	10	376(20)	+8.54(0.01)	1.9(0.0)	777(11)
HDCO $4_{1,3}$–$3_{1,2}$	268.2920	9	40	20	21	207(21)	+8.55(0.05)	2.0(0.1)	451(23)
p-D_2CO $3_{1,3}$–$2_{1,2}$	166.1028	15	21	14	11	33(9)	+8.79(0.21)	2.2(0.5)	79(15)
p-D_2CO $4_{1,4}$–$3_{1,3}$	221.1918	11	32	20	16	92(7)	+8.74(0.09)	1.8(0.2)	178(17)
o-D_2CO $4_{0,4}$–$3_{0,3}$	231.4103	11	28	43	11	194(12)	+8.88(0.03)	1.9(0.1)	381(12)
o-D_2CO $4_{2,2}$–$3_{2,1}$	236.1024	10	50	33	13	56(7)	+8.95(0.13)	2.4(0.3)	144(16)
p-D_2CO $4_{1,3}$–$3_{1,2}$	245.5329	10	35	20	11	55(7)	+8.85(0.11)	2.4(0.3)	139(13)
CH_2DOH $2_{0,2}$–$1_{0,1}$ e1	89.2753	28	20	1	3	12(2)	+8.65(0.37)	4.2(1.1)	51(9)
CH_2DOH $6_{1,5}$–$6_{0,6}$ e0	99.6721	25	50	7	2	15(2)	+8.09(0.17)	4.1(0.5)	68(6)
CH_2DOH $7_{1,6}$–$7_{0,7}$ e0	105.0370	23	65	8	3	17(3)	+8.66(0.18)	3.1(0.4)	57(6)
CH_2DOH $3_{1,2}$–$2_{1,1}$ e1	135.4529	18	29	2	8	30(6)	+8.48(0.22)	3.0(0.5)	98(15)
CH_2DOH $3_{1,3}$–$4_{0,4}$ e1	161.6025	15	29	1	9	36(7)	+8.71(0.19)	2.7(0.4)	103(15)
CH_2DOH $5_{1,5}$–$4_{1,4}$ o1	221.2730	11	55	4	17	57(7)	+8.31(0.19)	3.2(0.4)	195(22)
CH_2DOH $5_{0,5}$–$4_{0,4}$ e1	222.7415	11	46	4	10	75(8)	+8.45(0.10)	4.3(0.2)	342(15)
CH_2DOH $5_{2,3}$–$4_{1,4}$ e0	223.0711	11	48	3	8	59(9)	+7.98(0.11)	4.5(0.2)	284(13)
CH_2DOH $5_{3,3}$–$4_{3,2}$ o1[c] CH_2DOH $5_{3,2}$–$4_{3,1}$ o1[c]	223.1535 223.1536	11	87	2	10	56(7)	+8.34(0.13)	3.8(0.3)	223(15)
CH_2DOH $5_{2,3}$–$4_{2,2}$ e1	223.3155	11	59	3	12	70(8)	+8.12(0.10)	3.0(0.2)	228(15)
CH_2DOH $5_{4,2}$–$4_{1,1}$ e0 [c] CH_2DOH $5_{4,1}$–$4_{0,0}$ e0 [c]	223.6162 223.6162	11	95	1	10	47(11)	+8.25(0.14)	3.5(0.3)	174(14)
CH_2DOH $5_{1,4}$–$4_{1,3}$ e1	225.6677	11	49	4	11	56(11)	+8.18(0.15)	4.0(0.3)	237(17)
CH_2DOH $5_{1,4}$–$4_{1,3}$ e0	226.8183	11	37	3	10	51(10)	+8.08(0.14)	3.8(0.3)	203(14)
CH_2DOH $15_{2,13}$–$15_{1,14}$ e0	228.2461	11	276	20	29	89(12)	+7.84(0.20)	3.0(0.4)	285(37)
CH_2DOH $9_{2,7}$–$9_{1,8}$ e0	231.9692	11	113	11	14	99(8)	+8.72(0.09)	3.7(0.2)	390(19)
CH_2DOH $8_{2,6}$–$8_{1,7}$ e0	234.4710	10	94	10	13	67(8)	+9.17(0.14)	4.1(0.3)	293(19)
CH_2DOH $7_{2,5}$–$7_{1,6}$ e0	237.2499	10	76	8	12	64(12)	+8.31(0.13)	3.9(0.3)	266(18)
CH_2DOH $7_{1,6}$–$6_{2,4}$ o1	244.5884	10	83	2	16	61(10)	+8.09(0.18)	3.6(0.6)	231(26)
CH_2DOH $3_{2,1}$–$3_{1,2}$ e0	247.6258	10	29	2	9	48(8)	+8.26(0.13)	3.7(0.3)	189(13)
CH_2DOH $3_{2,2}$–$3_{1,3}$ e0	255.6478	10	29	2	9	58(8)	+8.61(0.12)	5.3(0.4)	331(16)
CH_2DOH $4_{1,4}$–$3_{0,3}$ e0	256.7316	10	25	3	9	61(8)	+8.32(0.11)	4.3(0.2)	278(14)
CH_2DOH $4_{2,3}$–$4_{1,4}$ e0	258.3371	10	38	3	14	60(6)	+8.33(0.16)	4.7(0.4)	302(21)
CH_2DOH $5_{2,4}$–$5_{1,5}$ e0	261.6874	9	48	4	17	45(9)	+8.09(0.26)	4.3(0.5)	205(24)
CH_2DOH $13_{0,13}$–$12_{1,12}$ e0	262.5969	9	194	5	17	54(12)	+8.51(0.21)	3.8(0.4)	219(23)
CH_2DOH $6_{1,6}$–$5_{1,5}$ e0	264.0177	9	48	4	14	64(7)	+8.40(0.12)	2.8(0.3)	192(17)
CH_2DOH $7_{2,6}$–$7_{1,7}$ e0	270.2999	9	76	6	14	55(13)	+8.35(0.17)	4.2(0.4)	243(19)
CH_2DOH $6_{1,5}$–$5_{1,4}$ e1	270.7346	9	62	4	16	60(10)	+8.21(0.16)	3.5(0.3)	222(20)
CHD_2OH 5_0–4_0 e1	207.771	11	48	4	14	43(9)	+8.69(0.20)	2.7(0.4)	125(17)
CHD_2OH 5_{3-}–4_{3-} e1[c] CHD_2OH 5_{3-}–4_{3-} e1[c]	207.868 207.869	11	77	2	11	35(10)	+7.21(0.24)	4.1(0.5)	153(17)
CH_3OD 5_{1+}–4_{1+}	223.3086	11	39	3	20	32(10)	+8.53(0.41)	3.2(0.9)	108(27)
CH_3OD 5_{0+}–4_{0+}	226.5387	11	33	4	18	48(10)	+8.87(0.28)	4.6(0.6)	232(28)

[a] Frequencies and spectroscopic parameters of HDCO and D_2CO have been extracted from the Cologne Database for Molecular Spectroscopy (Müller et al. 2005). Those of CH_2DOH are extracted from the Jet Propulsion Laboratory database (Pickett et al. 1998). [b] The errors in brackets are the gaussian fit uncertainties. [c] The lines cannot be distinguished with the present spectral resolution.

Table 5.2: List of transitions and line properties (in $T_{\rm MB}$ scale) of the $H_2^{13}CO$ and $^{13}CH_3OH$ emission towards SVS13-A

Transition	ν^a (GHz)	$HPBW$ ($''$)	$E_{\rm up}{}^a$ (K)	$S\mu^{2a}$ (D^2)	rms (mK)	$T_{\rm peak}{}^b$ (mK)	$V_{\rm peak}{}^b$ (km s^{-1})	$FWHM^b$ (km s^{-1})	$I_{\rm int}{}^b$ (mK km s^{-1})
Isotopologues									
o-$H_2^{13}CO$ $2_{1,2}$–$1_{1,1}$	137.4500	18	22	24	10	63(4)	+8.50(0.08)	1.0(0.2)	64 (10)
p-$H_2^{13}CO$ $2_{0,2}$–$1_{0,1}$	141.9837	17	10	11	10	54 (10)	+8.46(0.10)	1.1(0.2)	62(10)
o-$H_2^{13}CO$ $2_{1,1}$–$1_{1,0}$	146.6357	17	22	24	14	105(4)	+8.39(0.06)	0.9(0.1)	98(13)
o-$H_2^{13}CO$ $3_{1,3}$–$2_{1,2}$	206.1316	12	32	44	13	124(15)	+8.58(0.06)	2.5(0.2)	332(18)
p-$H_2^{13}CO$ $3_{0,3}$–$2_{0,2}$	212.8112	12	20	16	10	70(6)	+7.76(0.14)	2.0(0.3)	235(65)
o-$H_2^{13}CO$ $3_{1,2}$–$2_{1,1}$	219.9085	11	33	43	10	134(12)	+8.90(0.04)	2.2(0.1)	359(17)
o-$H_2^{13}CO$ $4_{1,4}$–$3_{1,3}$	274.7621	10	45	31	21	102(16)	+8.34(0.11)	2.5(0.3)	270(25)
$^{13}CH_3OH$ $2_{0,2}$–$1_{0,1}$	94.4110	26	20	2	2	10(2)	+8.61(0.21)	3.9 (0.4)	42(4)
$^{13}CH_3OH$ $2_{1,1}$–$1_{1,0}$	94.4205	26	28	1	2	11(1)	+9.19(0.16)	2.4(0.4)	27(4)
$^{13}CH_3OH$ $2_{1,1}$–$1_{1,0}$- -	95.2087	26	21	1	2	17(2)	+7.56(0.10)	3.5(0.3)	65(4)
$^{13}CH_3OH$ $1_{1,0}$–$1_{0,1}$	165.5661	15	23	1	8	76(8)	+8.58(0.09)	3.6(0.2)	289(15)
$^{13}CH_3OH$ $7_{1,6}$–$7_{0,7}$	166.5695	15	84	6	5	34(5)	+8.64(0.13)	3.5(0.4)	125(10)
$^{13}CH_3OH$ $8_{-1,8}$–$7_{0,7}$	221.2852	11	87	5	11	49(11)	+8.05(0.16)	3.5(0.3)	180(16)
$^{13}CH_3OH$ $5_{1,5}$–$4_{1,4}$+ +	234.0116	11	48	4	10	66(13)	+8.87(0.11)	4.1(0.3)	284(16)
$^{13}CH_3OH$ $5_{0,5}$–$4_{0,4}$	235.8812	10	47	4	13	70(8)	+9.11(0.12)	3.3(0.3)	245(17)
$^{13}CH_3OH$ $5_{-1,5}$–$4_{-1,4}$	235.9382	10	40	4	10	52(10)	+8.84(0.15)	5.0(0.3)	275(17)
$^{13}CH_3OH$ $10_{3,7}$–$10_{2,8}$- +	254.5094	10	175	9	8	54(7)	+8.31(0.09)	3.7(0.2)	215(10)
$^{13}CH_3OH$ $8_{3,5}$–$8_{2,6}$- +	254.8418	10	132	7	7	52(7)	+8.29(0.09)	4.0(0.2)	218(11)
$^{13}CH_3OH$ $7_{3,4}$–$7_{2,5}$- +	254.9594	10	113	6	11	52(7)	+8.25(0.14)	4.3(0.3)	238(15)
$^{13}CH_3OH$ $6_{3,3}$–$6_{2,4}$- +	255.0510	10	98	5	10	71(11)	+8.63(0.11)	4.7(0.2)	353(16)
$^{13}CH_3OH$ $8_{3,6}$–$8_{2,7}$+ -	255.2656	10	132	7	6	47(6)	+8.30(0.09)	3.9(0.2)	193(9)
$^{13}CH_3OH$ $9_{3,7}$–$9_{2,8}$+ -	255.3559	10	152	8	7	51(7)	+8.52(0.09)	3.8(0.2)	208(11)
$^{13}CH_3OH$ $10_{3,8}$–$10_{2,9}$+ -	255.4970	10	175	9	9	46(9)	+8.43(0.14)	4.1(0.3)	202(13)
$^{13}CH_3OH$ $5_{2,3}$–$4_{1,3}$	263.1133	9	56	4	10	60(10)	+8.31(0.12)	4.4(0.3)	278(15)
$^{13}CH_3OH$ $9_{-1,9}$–$8_{0,8}$	268.6354	9	107	6	13	55(13)	+7.99(0.16)	4.1(0.4)	236(18)

[a] Frequencies and spectroscopic parameters of $H_2^{13}CO$ and $^{13}CH_3OH$ have been extracted from the Cologne Database for Molecular Spectroscopy (Müller et al. 2005). Upper level energies refer to the corresponding ground state of each symmetry. [b] The errors in brackets are the gaussian fit uncertainties.

5.2.5 LVG analysis

We analysed the $H_2{}^{13}CO$ and $^{13}CH_3OH$ observed lines with the non-LTE Large Velocity Gradient (LVG) approach using the model described in Ceccarelli et al. (2003) and in Sec. 2.3.2. For methanol we used the CH_3OH-H_2 collisional coefficients provided by the BASECOL database (Dubernet et al. 2013). In the case of formaldehyde, we considered only the ortho form, for which the H_2CO-H_2 collisional coefficients (Troscompt et al. 2009b) are available. We assumed a Boltzmann distribution for the H_2, using for the methanol analysis the statistical ortho-to-para ratio of 3. In the case of formaldehyde we assumed a ortho-to-para ratio close to zero following Troscompt et al. (2009a). We ran grids of models varying the kinetic temperature, $T_{\rm kin}$, (from 10 to 200 K), the H_2 density, $n_{\rm H_2}$, (from 10^4 to 10^{10} cm^{-3}), the $H_2{}^{13}CO$ column density, $N(^{13}H_2CO)$, (from 10^{11} to 10^{13} cm^{-2}), and the $^{13}CH_3OH$ column density, $N(^{13}CH_3OH)$, (from 10^{16} to 10^{18} cm^{-2}), while the emitting size, θ_s, was left as free parameter.

In the case of formaldehyde, the best fit was obtained with $N(^{13}H_2CO) = 5.5 \times 10^{12}$ cm^{-2} and $\theta_s = 5'' \pm 1''$: Figure 5.10 (upper panel) shows the χ^2_r contour plot as a function of the temperature and H_2 density using these values. The temperatures corresponding to the best fit solution are $T_{\rm kin}$ = 20-25 K and the density are quite high $n_{\rm H_2} \simeq 0.2$–2×10^7 cm^{-3}, suggesting to be close to LTE. Figure 5.10 (lower panel) shows, for the best fit solution, the ratio between the measured lines intensities and the LVG model predictions, as a function of the line upper level energy. The detected transitions are predicted to be optically thin (opacities between 0.03 and 0.06). The LVG analysis clearly supports the association of formaldehyde with the protostellar envelope with a size of $\sim$ 1200 au.

Different is the case of $^{13}CH_3OH$ for which the LVG model does not converge towards a solution suggesting we are mixing emission from different regions, possibly due to different HPBWs. In the light of this suggestion, we considered separately the lines with higher excitations ($E_{\rm up} > 40$ K) observed with similar HPBWs (between 9″ and 15″). The solution with the lowest χ^2_r corresponds to $N(^{13}CH_3OH) = 9 \times 10^{16}$ cm^{-2} and an emitting size of $\theta_s = 0\farcs3 \pm 0\farcs1$, i.e. a radius of 35 au (see Figure 5.11). The best fit solution corresponds to a temperature of T_{kin} = 80 K and very high-densities, $n_{\rm H_2} \geq 10^8$ cm^{-3}. The line opacities vary from 0.8 to 2.5, being thus moderately optically thin. All these values suggest that the

emission detected at high excitations is dominated by a hot-corino, an environment which is typically very abundant in methanol, due to thermal evaporation of the dust mantles (e.g. Caselli & Ceccarelli 2012). Interestingly, the occurrence of a hot-corino around SVS13-A has been recently suggested by high-excitation HDO lines, also observed in the ASAI context and indicating a T_{kin} larger than 150 K on smaller spatial scales (a radius $\sim$ 25 au; Codella et al. 2016b).

The analysis of the remaining 4 lines (observed with HPBWs larger than 15″) is not straightforward given the 4 transitions have almost the same E_{up} (20 – 28 K). The LVG approach suggests typical solutions with column densities of $N(^{13}CH_3OH) \sim 10^{15}$ cm^{-2}, temperatures $\leq$ 70 K, densities at least 10^6 cm^{-3}, and sizes $\simeq 2'' - 4''$. The line opacities in this case range from 0.007 to 0.02, being thus optically thin. The lower densities and the more extended emitting size suggest that we are sampling a more extended region (a radius $\sim$ 350 au) around the protostar where the temperature is still high enough to allow the methanol molecules to be released from grain mantles.

5.2.6 Rotation Diagram analysis

In order to derive the D/H values we determined the temperature and the column density of formaldehyde and methanol isotopologues through the rotational diagram analysis. The two main assumptions are that the lines are optically thin and they are in LTE. The LVG analysis previously described suggests that these conditions are plausible. Under these assumptions, for a given molecule, the relative population distribution of all the energy levels, is described by a Boltzmann temperature, that is the rotational temperature T_{rot} (for further details see Sec. 2.3).

As a first step we assumed a size filling the smaller IRAM-30m beam, i.e. 10″, a value consistent with the continuum emission at 1.25 mm observed with IRAM-30m radiotelescope by Lefloch et al. (1998a). Note however that the T_{rot} estimate does not depend on the source size assumption because almost all the lines have been observed with a beam of $\sim$ 10″ and then suffer the same beam dilution. The rotational diagram analysis shows low values of T_{rot}, around 20 K, consistent with the LVG results and consistent with an association with the extended molecular envelope around the protostar. We obtained $T_{rot} = 23 \pm 4$ K and column density $N_{tot} = 25 \pm 6 \times 10^{11}$ cm^{-2} ($H_2^{13}CO$), $T_{rot} = 15 \pm 2$ K and $N_{tot} = 9 \pm 3 \times 10^{12}$

cm^{-2} (HDCO), and $T_{\rm rot}$ = 28 ± 6 K and column density $N_{\rm tot}$ = 13 ± 3 × 10^{11} cm^{-2} (D_2CO), see Figure 5.12.

For HDCO we detected line wings with velocities up to ∼ ±3 km s^{-1} with respect to the systemic source velocity. This low velocity emission is likely probing ambient material swept-up by the outflow associated with SVS13-A Lefloch et al. (1998a). We derived the temperature and column density of this outflow component using the residual intensities after subtracting the gaussian fit of the ambient component and then we analysed them separately. From the rotational diagram analysis we obtained for both the blue- and the redshifted emission, a $T_{\rm rot}$ ∼ 12 K. Also in this case, the $T_{\rm rot}$ value is not affected by beam dilution because the lines come from the 1.3 mm band. The low $T_{\rm rot}$ value is again an indication of an extended emission, in agreement with the well-studied extended outflow driven by SVS13-A (Lefloch et al. 1998a). We assumed also in this case an arbitrary source size of 10″, obtaining $T_{\rm rot}$ = 12± 7 K and $N_{\rm tot}$ = 9± 15 × 10^{11}cm^{-2} (HDCO blue wing), $T_{\rm rot}$ = 12± 8 K and $N_{\rm tot}$ = 6± 12 × 10^{11}cm^{-2} (HDCO red wing). In the case of $H_2^{13}CO$, due to line contamination, we detected blue wings only for two lines; by assuming the same rotational temperature of the HDCO wings, we obtained a column density of $N_{\rm tot}$ ∼ 9 × 10^{10}cm^{-2}.

For $H_2^{13}CO$ and HDCO we detect both para and ortho transitions (see Tables 5.1 and 5.2). Once considered both species in a single rotation diagram, the distribution does not show any significant scatter from the linear fit. Considered the poor statistic (2 para and 5 ortho transitions for $H_2^{13}CO$; 3 para and 2 ortho transitions for HDCO) and the uncertainties of the line intensities, this is consistent with the o/p statistical values at the high-temperature limit (3:1 for $H_2^{13}CO$ and 2:1 for D_2CO). This is in agreement with the rotational temperatures for both $H_2^{13}CO$ and D_2CO which are above the expected high-temperature limit of ∼ 14 K and ∼ 7 K for $H_2^{13}CO$ and D_2CO, respectively.

For the methanol analysis one rotational temperature is not able to fit the rotational diagrams of $^{13}CH_3OH$ and CH_2DOH, supporting the occurrence of two emitting components associated with different excitation conditions, as already suggested by the LVG analysis.

A better fit is obtained using two slopes (see Figure 5.13; again as a first step assuming a source size of 10″):

1. one with a low $T_{\rm rot}$ (15 ± 3 K for $^{13}CH_3OH$ and 27 ± 8 K for CH_2DOH)

for the lines with $E_{up} < 50$ K. The column densities are $N_{tot} = 18 \pm 7 \times 10^{13}$cm^{-2} for $^{13}CH_3OH$ and $N_{tot} = 11 \pm 5 \times 10^{13}$cm^{-2} for CH_2DOH;

2. one with a higher T_{rot} (99 ± 13 K for $^{13}CH_3OH$ and 190 ± 76 K for CH_2DOH) for the lines with $E_{up} > 50$ K. The column densities are $N_{tot} = 4 \pm 1 \times 10^{14}$cm^{-2} for $^{13}CH_3OH$ and $N_{tot} = 8 \pm 2 \times 10^{14}$cm^{-2} for CH_2DOH.

These two excitation regimes are in agreement with what found with the LVG approach: a hot corino and a more extended region associated with a lower temperature. The higher T_{rot} values obtained for both $^{13}CH_3OH$ and CH_2DOH with respect to the formaldehyde isotopologues suggest again that the origin of the emission is not the extended envelope but the hot corino.

5.2.7 Methanol and formaldehyde deuteration

We use the column densities derived from the rotation diagrams to derive the D/H ratio for formaldehyde and methanol. In order to properly measure the D/H, the column densities are derived assuming for each specie, the source size suggested by the LVG analysis: $5''$ for formaldehyde isotopologues, $\sim 3''$ for methanol lines with $E_{up} < 50$ K and $0\farcs3$ for methanol lines with $E_{up} > 50$ K. As already discuss in Sec. 5.2.2 and 5.2.3, it was not possible to directy measure the column density of the main isotopologue of H_2CO and CH_3OH because the lines are optically thick. For this reason we derived the formaldehyde and methanol column densities from the $H_2^{13}CO$ and $^{13}CH_3OH$ column densities, assuming a $^{12}C/^{13}C$ ratio of 86 (Milam et al. 2005) at the galactocentric distance of SVS13-A.

We report the obtained D/H ratios in Table 5.3. To be consistent, we assumed for the D-species the T_{rot} derived from the ^{13}C-isotopologues. In any case the following conclusions do not change if we assume for all the molecules the corresponding T_{rot}.

For H_2CO we measured a D/H of $9 \pm 4 \times 10^{-2}$. We can compare this value with measurements of deuterated formaldehyde in Class 0 sources performed by Parise et al. (2006), using data obtained with the same antenna (IRAM-30m) and a consistent beam sampling. The value measured towards SVS13-A is close to the average value reported for the Class 0 sources, which is D/H ~ 0.12.

For the double deuterated formaldehyde we obtained a D/H value of $4 \pm 1 \times 10^{-3}$. If we compare this value with that reported by Parise et al. (2006), we can note that it is definitely lower, by at least one order of magnitude, suggesting that the D/H is indeed lower in the more evolved Class I objects, like SVS13-A, with respect to the Class 0 sources.

The D/H value for the D_2CO respect to the HDCO, is $\sim 5 \times 10^{-3}$, a value again lower of at least one order of magnitude that those reported by Parise et al. (2006) for the Class 0 sources. This estimate is even more reliable because it is indipendent from $H_2^{13}CO$.

Finally, we derived the D/H ratio also for the outflowing gas. In this case, we assumed an extended component with a source size of 10″, obtaining a value of $4 \pm 6 \times 10^{-3}$ for the HDCO in the blue wing and $3 \pm 6 \times 10^{-3}$ for the HDCO in the red wing. These measurements are in agreement with that measured in the shocked region associated with the L1157 protostellar outflow by Codella et al. (2012), that reported a value of 5–8 $\times 10^{-3}$ using IRAM-30m data.

The derived D/H ratio for CH_2DOH with respect to CH_3OH is indicated in Table 5.3. To calculate this ratio, we derived the CH_2DOH column density assuming the same T_{rot} of $^{13}CH_3OH$, obtaining D/H $\sim 2 \times 10^{-3}$, for the lines with excitation energies $E_{up} < 50$ K, and D/H $\sim 7 \pm 1 \times 10^{-3}$ for the lines with $E_{up} > 50$ K. These values are two orders of magnitude below the D/H reported in Parise et al. (2006), supporting that also the methanol deuteration for the Class I object SVS13-A is dramatically decreased with respect to Class 0 objects.

We give an estimate of the CHD_2OH and CH_3OD column densities using the tentative detected two lines, which can be used as lower limits for the following analysis. We derived a value of $N_{tot} \sim 1 \times 10^{16}$ cm^{-2} for CHD_2OH and $N_{tot} \sim 6 \times 10^{14}$ cm^{-2} for CH_3OD, assuming the same source size and T_{rot} of the $^{13}CH_3OH$ low energy transitions (size $\sim 3''$ and $T_{rot} = 12$ K) and using the rotational partition functions from Ratajczak et al. (2011).

5.2.8 The [CH_2DOH]/[CH_3OD] ratio

Finally, we derived a measure of the [CH_2DOH]/[CH_3OD] ratio, and thus test the predictions of the current theory of methanol deuteration. Basically, according to the grain chemistry statistical models of Charnley et al. (1997) and Osamura

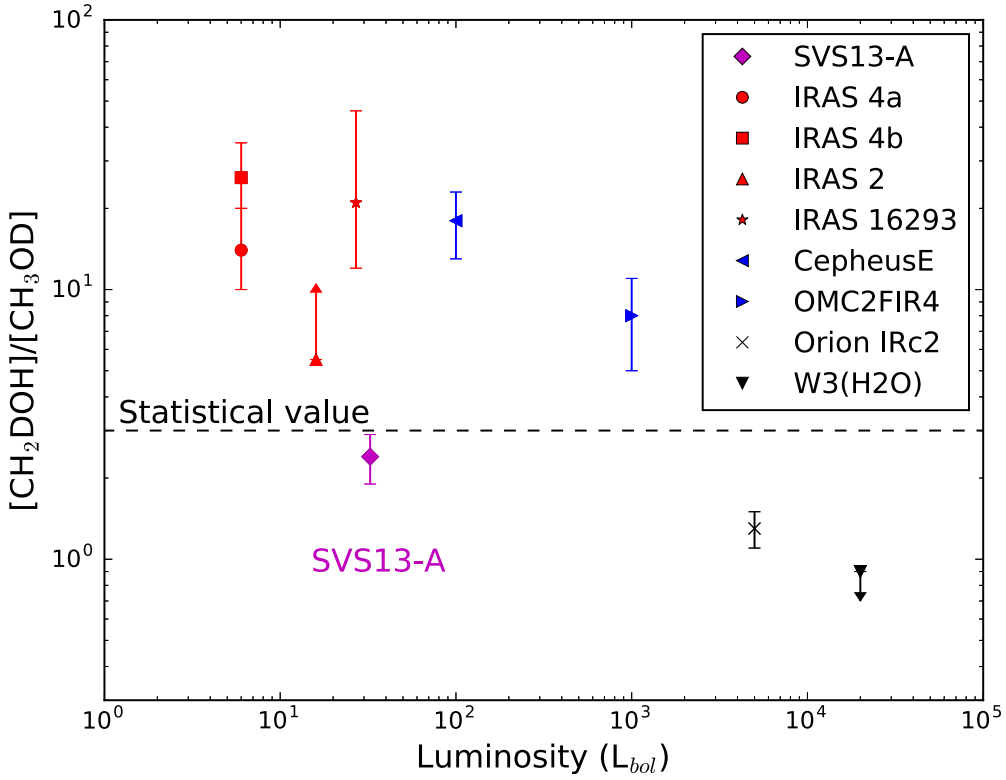

Figure 5.14: Figure from Bianchi et al. (2017a); adapted from Ratajczak et al. (2011). The figure show the $[CH_2DOH]/[CH_3OD]$ ratio as a function of the protostar luminosity. The horizontal dashed line refers to the value predicted by grain chemistry models (Charnley et al. 1997).

et al. (2004) the ratio of the singly deutereted isotopologues CH_2DOH and CH_3OD formed on the mantles should be 3. However, this is not confirmed by the few measurements in star forming regions.

Figure 5.14 (adapted from Ratajczak et al. 2011 and reference therein) reports the so far measured ratios as a function of the bolometric luminosity, including both low- and high-mass star forming regions. The $[CH_2DOH]/[CH_3OD]$ ratio always differs from the statistical value, and in particular, a weak trend have been proposed with the abundance ratio is substantially lower in massive hot cores than in (low-mass) hot- corinos (as well as in intermediate-mass protostars), by typically one order of magnitude. In particular, in low mass protostars, CH_3OD is found to be less abundant than CH_2DOH, by more than a factor 10 (Ratajczak et al. 2011). Unless the prediction for the methanol formation on dust grains has to be revised, these measurements are suggesting that the ratio is altered by gas-phase reactions at work once the deuterated methanol molecules are released by the dust mantles.

The present work allows us to provide a little piece of information to this general context. For SVS13-A we obtained $[CH_2DOH]/[CH_3OD]$ in the 2.0 – 2.5 range (see the magenta point in Figure 5.15), comparing the column density estimated from the CH_3OD 5_{1+}–4_{1+} line and the column density from a CH_2DOH line with similar energy ($4_{2,3}$–$4_{1,4}$ e0). Our measurement seems to question the previous conclusions on a change of the $[CH_2DOH]/[CH_3OD]$ ratio as a function of the protostellar luminosity. On the other hand, it suggests an evolution with time going from Class 0 to Class I, with CH_2DOH more efficiently destroyed than CH_3OD. To conclude, it is clear that we need further measurements to properly investigare any possible dependence on time and/or luminosity.

5.2.9 D/H of organics: from Class 0 to Class I

The present results strongly support that both H_2CO and CH_3OH deuteration decreases when a protostar leaves the Class 0 stage to enter in the Class I phase. Figure 5.15 shows the D/H ratio measured for organic molecules at different stages of the Sun-like star forming process, from prestellar cores to protoplanetary disks (the time increases from the left to the right along the x-axis). The present observation for SVS13-A can be properly compared with that of Class 0 objects,

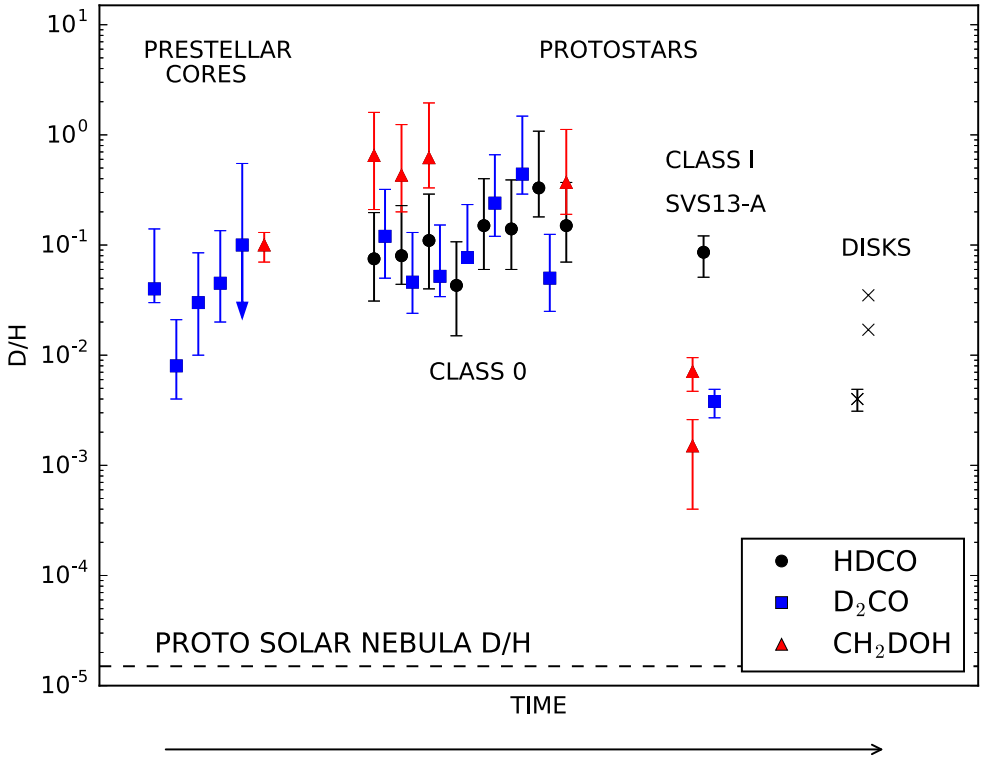

Figure 5.15: Figure from Bianchi et al. (2017a). D/H ratio measured in organic matter in different astronomical sources. Prestellar cores measurements of D_2CO and CH_2DOH are from respectively Bacmann et al. (2003) and Bizzocchi et al. (2014). Class 0 data are taken from Parise et al. (2006). SVS13-A data refer to the D/H inferred in the present paper for HDCO (8.6×10^{-2}), D_2CO (3.8×10^{-3}) and CH_2DOH (7.1×10^{-3} for the hot corino and 1.5×10^{-3} for a larger region, i.e. a radius $\leq$ 350 au). Protoplanetary disks data refer to measurements of DCN/HCN (Öberg et al. 2012) and DCO^+/HCO^+ (van Dishoeck et al. 2003) in TW Hya and of DCO^+/HCO^+ (Guilloteau et al. 2006) in DM Tau. Note that the prestellar cores and the Class 0 protostars are not ordered in age thus any trend within the classes is not significant (as in the plot reported by Ceccarelli et al. 2014.

derived by sampling similar spatial scales around the protostar. The methanol and formaldehyde deuteration measurements of SVS13-A, fill in the gap between Class 0 objects and protoplanetary disks, associated with Class II-III objects.

For HDCO, the average value measured in Class 0 sources (Parise et al. 2006) is D/H ~ 0.12, consistent with the value measured in SVS13-A, which is D/H ~ 8.6 ± 3.5 × 10^{-2}. Completely different is the case of D_2CO, which shows an increase going from prestellar cores (average value D/H ~ 0.045, Bacmann et al. 2003) to Class 0 sources (D/H ~ 0.15, Parise et al. 2006 and then a strong decrease in SVS13-A (D/H = 3.8 ± 1.1 × 10^{-3}. A similar behaviour is observed for the methanol deuteration that increase from a value of D/H ~ 0.1 in prestellar cores (Bizzocchi et al. 2014) to D/H ~ 0.52 in Class 0 (Parise et al. 2006) and then significantly decrease in SVS13-A to D/H = (1.5 – 7.1) × 10^{-3}.

In conclusion, the overall comparison shows a clear trend going from the prestellar cores to the Class 0 objects and to the Class I source. The deuterium fractionation of organics increase going from prestellar cores to Class 0 sources and then decreases up to two orders of magnitude going from Class 0 protostars to the more evolved phases. In protoplanetary disks the few available organics measurements refer to DCN/HCN (Öberg et al. 2012) and DCO^+/HCO^+ (van Dishoeck et al. 2003, Guilloteau et al. 2006) and are in agreement with the decreasing trend with values between 0.035 and 0.004. Note that the prestellar cores and the Class 0 protostars are not ordered in age thus any trend whithin the classes is not significant (as in Ceccarelli et al. 2014).

Why does D/H decrease from Class 0 to Class I protostars? Formaldehyde and methanol observed around embedded protostars have been mostly formed at the surface of interstellar grains and have been then evaporated thermally when the temperature exceeds their temperature of sublimation. Two possibilities can therefore be suggested. The decrease of D/H from Class 0 to Class I could be due to (1) warm gas phase chemistry after the evaporation of formaldehyde or methanol; (2) a lower deuteration of icy formaldehyde and methanol in Class I than in Class 0.

Case 1: Warm gas phase chemistry can decrease the deuterium fractionation of formaldehyde and methanol through ion-neutral reactions. Charnley et al. (1997) showed that the CH_2DOH/CH_3OH decreases dramatically by two orders of magnitude at times longer than 3 × 10^5 yr, because of electronic recombinations that

Table 5.3: Results from the rotational diagram analysis: derived rotational temperatures, $T_{\rm rot}$, derived column densities, $N_{\rm tot}$, and resulting deuteration ratios. The latter are calculated assuming for each deuterated specie, the same $T_{\rm rot}$ of the correspondent 13-isotopologue.

Transition	Lines	Energy range	Boltzmann Plots			D/H^b
			Size[a]	$T_{\rm rot}$	$N_{\rm tot}$	
		(K)	(")	(K)	(cm^{-2})	
whole emission						
D_2CO	5	21–50	5	25(5)	$3(1) \times 10^{12}$	$3.8(1.1) \times 10^{-3}$
HDCO	5	18–40	5	12(2)	$3(1) \times 10^{13}$	$8.6(3.5) \times 10^{-2}$
$H_2^{13}CO$	7	10–45	5	19(3)	$7(2) \times 10^{12}$	–
CH_2DOH ($E_{\rm up} < 50$ K)	14	20–50	~ 3	24(9)	$7(5) \times 10^{14}$	$1.5(1.1) \times 10^{-3}$
$^{13}CH_3OH$ ($E_{\rm up} < 50$ K)	7	20–48	~ 3	12(2)	$16(7) \times 10^{14}$	–
CH_2DOH ($E_{\rm up} > 50$ K)	13	54–194	0.3	177(71)	$4(1) \times 10^{17}$	$7.1(2.4) \times 10^{-3}$
$^{13}CH_3OH$ ($E_{\rm up} > 50$ K)	11	56–175	0.3	91(13)	$20(4) \times 10^{16}$	–
outflow						
$H_2^{13}CO$ Blue wing[c]	3	20–33	10	12[c]	$15(5) \times 10^{11}$	–
HDCO Blue wing[c]	4	27–40	10	12(7)	$9(15) \times 10^{11}$	$4.0(6.3) \times 10^{-3}$
HDCO Red wing[c]	4	27–40	10	12(8)	$6(12) \times 10^{11}$	$2.6(5.2) \times 10^{-3}$

[a] *Assumed from LVG analysis results; for the outflow component we arbitrarily assumed an extended (10″) size.*

[b] *To calculate the D/H ratio we assumed for HDCO and D_2CO the same rotational temperature of $H_2^{13}CO$ ($T_{\rm rot}$ = 19 K). For CH_2DOH we assumed the same rotational temperature of $^{13}CH_3OH$ ($T_{\rm rot}$ = 12 K and 91 K).*

[c] *Derived using the residual intensities after subtracting the gaussian fit of the ambient component. For the $H_2{}^{13}CO$ wings we assumed the same $T_{\rm rot}$ of the HDCO wings (see text).*

destroy more efficiently CH_2DOH than CH_3OH. The timescale of 3×10^5 yr is consistent with the typical lifetime of Class I protostars (0.2-0.5 Myr; Evans et al. 2009). However, there are two problems with this picture: (i) revised models by Osamura et al. (2004) suggests longer timescales (up to 10^6 yr), and (ii) the dynamical timescale of the material in the hot corino envelope inside the centrifugal radius could be lower (1×10^4–1×10^5 yr; Visser et al. 2009). In addition, the decrease of methanol deuteration occurs when most of the methanol is already destroyed with abundances lower than 1×10^{-8}. Although formaldehyde spends more time in the warm gas due its lower binding energy, it does not show any significant decrease of its deuteration (Charnley et al. 1997, Roberts & Millar 2007).

Case 2: A second possibility is that the decrease of deuteration is due to the gradual collapse of the external shells of the protostellar envelope. The deuterium chemistry is very sensitive to physical (density, temperature) and chemical (CO abundance, H_2 ortho/para ratio) parameters (see Flower et al. 2006). Icy formaldehyde and methanol deuterations increase with the density and with the decreasing temperature during the formation of prestellar cores (see Taquet et al. 2012a, Taquet et al. 2013). Taquet et al. (2014) showed that the deuteration of formaldehyde and methanol ices can decrease by two orders of magnitude from the centre to the external part of prestellar cores, the exact values depending on the structure of the core and its history. In the subsequent protostellar phase, the shells are then gradually accreted from the center to the outer part in an inside-out fashion during the core collapse. The methanol deuteration observed in the early Class 0 phase would reflect the material at the center of the prestellar core whereas the older Class I phase reflects the material coming from the external core shells. An instructive view has been reported by Codella et al. (2012), who analysed the H_2CO and CH_3OH deuteration in the shocked region L1157-B1, located relatively far (0.08 pc) from the protostar driving the shocks in the outflow, and thus sampling an outer region probably associated with a (pre-stellar) density lower than that where the protostar is successively born. The D/H derived for L1157-B1 are indeed lower than what found for the standard hot corino IRAS16293-2422, i.e. the inner 100 au of the protostellar core. In other words, H_2CO and CH_3OH deuteration can be used to measure the density at the moment of the ices formation, before the start of the star forming process: the higher is the D/H, the higher was the density. In the case of SVS13-A the D/H for formaldehyde in the outflow, sam-

pling a region definitely more extended than the protostellar high density cocoon, is indeed supporting this scenario (see Figure 5.16). The decrease by two orders of magnitude from Class 0 to Class I protostars observed for the D_2CO/H_2CO and CH_2DOH/CH_3OH ratios is in good agreement with the model predictions by Taquet et al. (2014) although the models still tend to underpredict the absolute ratios by one order of magnitude. It should be noted that the decrease of formaldehyde and methanol deuterations with the evolutionary stage of the protostar are not necessarily accompanied by a decrease of water deuteration. As water ice is mostly formed in molecular clouds before the formation of prestellar cores, its deuteration only weakly varies within prestellar cores. This scenario can therefore simultaneously explain the decrease of deuteration of formaldehyde and methanol observed in this work and, in addition, the constant deuteration of water observed towards SVS13-A by Codella et al. (2016b).

5.2.10 Conclusions on deuteration

We studied the formaldehyde and metanol deuteration in the Class I object SVS13-A with the IRAM-30m antenna in the framework of the ASAI large program consisting of an unbiased spectral survey at 1.3, 2 and 3 mm towards the source. The aim of this project was to understand how the deuterium fractionation of organics like H_2CO and CH_3OH change in a Class I object, SVS13-A, with respect to the Class 0 sources. The bulk of the detected lines are in the 1.3 mm band corresponding to a telescope HPBW $\sim 10''$. This ensures than the signal is coming from SVS13-A and it is not contaminated by the SVS13-B Class 0 object, offset by $15''$. The main results are reported as follows:

1. We detected 7 lines of $H_2{}^{13}CO$, 5 transitions of HDCO and 5 lines of D_2CO with excitation energies E_{up} in the 10–45 K range. The LVG analysis of $H_2{}^{13}CO$ indicates low values of T_{kin} ($\sim$ 20 K), densities larger than 10^6 cm^{-3}, and an emitting size of about $5''$ ($\sim$ 1200 au). The low temperature is confirmed by the rotational diagram performed for the all formaldehyde isotopologues, suggesting the association with the molecular envelope surrounding the protostar.

2. Both $H_2{}^{13}CO$ and HDCO lines show wings indicating emission from outflowing gas. For both the blue- and the redshifted emission we obtained

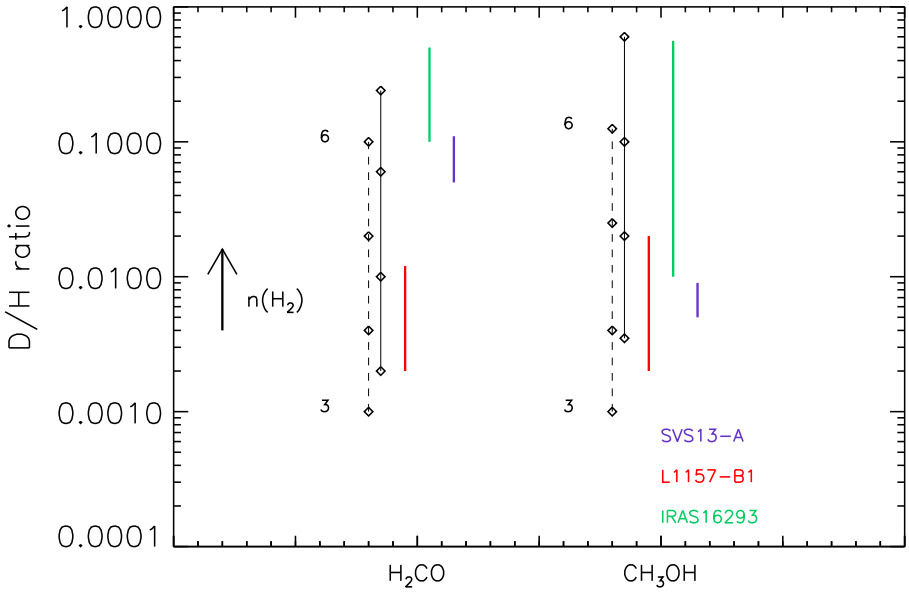

Figure 5.16: Figure from Bianchi et al. (2017a). Deuterium fractionation of H_2CO and CH_3OH as found toward SVS13-A (blue), L1157-B1 (red) and IRAS16293–2422 (green; from Loinard et al. 2001; Parise et al. 2002, Parise et al. 2004). Black diamonds stand for the prediction of Taquet et al. (2012a) for pre-shock gas densities of 10^3, 10^4, 10^5, and 10^6 cm^{-3} (see labels) and temperatures of 10 (dashed line) and 20 K (solid).

a low $T_{\rm rot}$ ($\sim$ 12 K), in agreement with the association with the extended outflow driven by SVS13-A.

3. We detected 18 lines of $^{13}CH_3OH$ and 27 transitions of CH_2DOH with $E_{\rm up}$ in the 20-276 K range. We report the detection of CHD_2OH and CH_3OD through 2 different transition for each species. The LVG analysis of $^{13}CH_3OH$ suggests the occurrence of of two components, with different excitation conditions: (1) a compact region ($\theta_s \simeq 0\farcs3$, 70 au) corresponding to high temperatures ($T_{\rm kin} \sim 80$ K) and very high densities ($> 10^8$ cm^{-3}), clearly being the hot-corino (recently discovered by HDO observations; Codella et al. 2016b). (2) a colder ($T_{\rm kin} \leq 70$ K), more extended ($\theta_s \simeq 2'' - 4''$) region associated with densities $> 10^6$ cm^{-3}. The rotation diagram analysis confirms for the deuterated methanol the presence of a hot corino component associated to high densities and temperatures and a second component due to colder gas emission.

4. We measured for formaldehyde D/H $\sim 9 \times 10^{-2}$, a value consistent with the average value reported from Class 0 sources (D/H $\sim$ 0.12, Parise et al. 2006). The deuterium fractionation derived for the outflowing component is D/H $\sim 4 \times 10^{-3}$, in agreement with that measured in the shocked region associated with the L1157 protostellar outflow by Codella et al. (2012). On the opposite, for D_2CO we obtained D/H $\sim 4 \times 10^{-3}$, lower by one order of magnitude respect to Class 0 objects. This trend is even stronger for the measured methanol deuteration, which is 4×10^{-3}, two orders of magnitude lower than the values reported by Parise et al. (2006) for Class 0 objects.

5. The [CH_2DOH]/[CH_3OD] ratio that is in the 2.0 – 2.5 range. Previous measurements by Ratajczak et al. (2011), including both low- and high-mass star forming regions, indicate a weak trend with a lower abundance ratio observed in massive hot cores with respect to (low-mass) hot- corinos (as well as in intermediate-mass protostars), by typically one order of magnitude. According to these indications, in SVS13-A CH_3OD was expected to be less abundant than CH_2DOH, by more than a factor 10 (Ratajczak et al. 2011) However, our [CH_2DOH]/[CH_3OD] measurement questions the previous indication on a change of the ratio as a function of the protostellar luminosity.

6. The low deuterium fractionation measured towards SVS13-A could be an indication of the modified chemical content in the evolutionary transition from the Class 0 phase to the Class I phase. Alternatively, the decrease of D/H in a more evolved phase could be due to the gradual collapse of the external shells of the protostellar evelope, less deuterated because composed of ices formed in a less dense region. Only high resolution interferometric observations, able to sample the inner region of the protostar ($< 1''$ corresponding to ~ 235 au at the source distance) and to disentangle the emission coming from the different protostar components, will properly answer these open questions.

5.3 From Class 0 to Class I: chemical heritage

So far, only NH_2CHO was analysed towards SVS13-A using the ASAI database (López-Sepulcre et al. 2015). We complement the analysis taking inventory of all the other iCOMs towards the source. In particular we identify 4 iCOMs: H_2CCO, CH_3CHO, $HCOOCH_3$ and CH_3OCH_3. We put also constraints on the abundance of a large number of iCOMs.

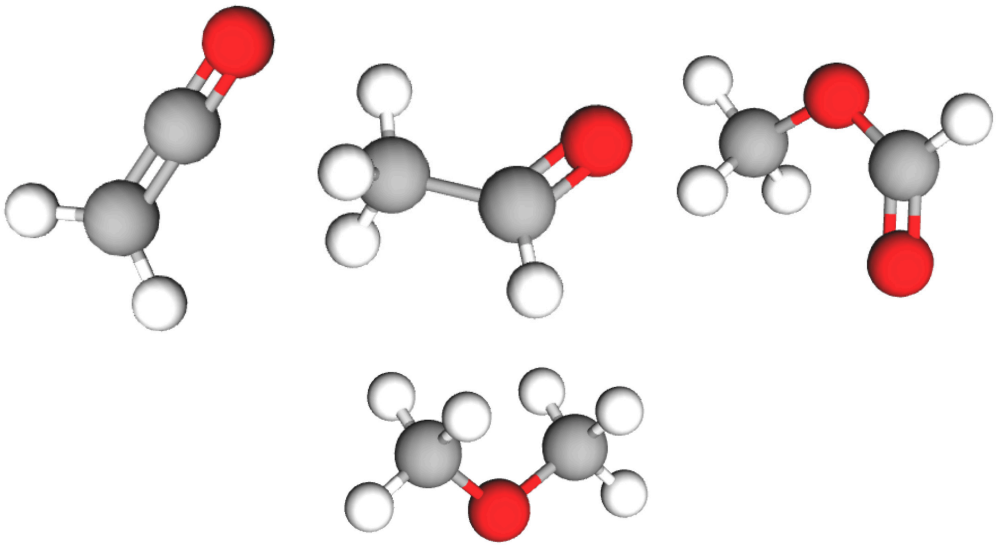

Figure 5.17: Sketch of the 3D structure of ketene (H_2CCO, upper left), acetaldehyde (CH_3CHO, upper right), methyl formate ($HCOOCH_3$, lower left), dimethyl ether (CH_3OCH_3, lower right).

The line identification process has been performed with the same procedure described in Sec. 5.2.1. We used in particular the Jet Propulsor Laboratory (JPL[3], Pickett et al. 1998) and Cologne Database for Molecular Spectroscopy (CDMS[4]; Müller et al. 2001, Müller et al. 2005) molecular databases.

[3]https://spec.jpl.nasa.gov/
[4]http://www.astro.uni-koeln.de/cdms/

5.3.1 Ketene (H_2CCO)

Table 5.4: List of transitions and line properties (in T_{MB} scale) of the H_2CCO emission detected towards SVS13-A

Transition	ν^a (GHz)	$HPBW$ ($''$)	$E_{up}{}^a$ (K)	$S\mu^{2a}$ (D^2)	rms (mK)	$T_{peak}{}^b$ (mK)	$V_{peak}{}^b$ (km s^{-1})	$FWHM^b$ (km s^{-1})	$I_{int}{}^b$ (mK km s^{-1})
o-H_2CCO $7_{1,6}$–$6_{1,5}$	142.7690	17	40	41	10	39 (4)	+8.61 (0.17)	2.0 (0.5)	82 (15)
o-H_2CCO $8_{1,8}$–$7_{1,7}$	160.1422	15	48	48	9	39 (9)	+8.35 (0.19)	3.7 (0.5)	153 (16)
o-H_2CCO $8_{3,5}$–$7_{3,4}$ [c]	161.6022	15	152	42	10	36 (7)	+8.19 (0.19)	2.6 (0.4)	98 (15)
o-H_2CCO $8_{3,6}$–$7_{3,5}$ [c]	161.6022								
o-H_2CCO $8_{1,7}$–$7_{1,6}$	163.1609	15	48	48	8	45 (12)	+8.47 (0.11)	2.1 (0.3)	99 (11)
p-H_2CCO $10_{0,10}$–$9_{0,9}$	202.0143	12	53	20	18	45 (13)	+8.23 (0.19)	1.4 (0.4)	68 (17)
o-H_2CCO $11_{1,11}$–$10_{1,10}$	220.1776	11	76	66	21	68 (7)	+8.76 (0.21)	3.3 (0.6)	241 (32)
p-H_2CCO $11_{2,10}$–$10_{2,9}$	222.2286	11	116	21	9	31 (4)	+8.94 (0.12)	1.3 (0.3)	41 (8)
p-H_2CCO $11_{2,9}$–$10_{2,8}$	222.3144	11	116	21	5	27 (5)	+8.27 (0.01)	2.0 (0.3)	56 (6)
o-H_2CCO $11_{1,10}$–$10_{1,9}$	224.3273	11	78	66	14	73 (10)	+7.91 (0.13)	3.7 (0.3)	283 (20)
o-H_2CCO $12_{1,12}$–$11_{1,11}$	240.1858	10	88	72	11	99 (9)	+7.56 (0.08)	4.1 (0.2)	432 (16)
p-H_2CCO $12_{2,10}$–$11_{2,9}$	242.5362	10	128	24	7	25 (7)	+7.76 (0.13)	1.5 (0.5)	40 (8)
o-H_2CCO $12_{1,11}$–$11_{1,10}$	244.7123	10	89	72	11	66 (6)	+8.37 (0.08)	2.2 (0.2)	153 (12)
o-H_2CCO $13_{3,10}$–$12_{3,9}$ [c]	262.5974	9	206	74	10	53 (12)	+8.09 (0.19)	3.7 (0.4)	207 (21)
o-H_2CCO $13_{3,11}$–$12_{3,10}$ [c]	262.5966								
p-H_2CCO $13_{2,12}$–$12_{2,11}$	262.6190	9	140	26	9	51 (9)	+8.75 (0.06)	0.9 (0.1)	51 (6)
p-H_2CCO $13_{2,11}$–$12_{2,10}$	262.7609	9	140	26	8	37 (8)	+8.11 (0.11)	2.4 (0.3)	95 (9)

[a] *Frequencies and spectroscopic parameters are extracted from the Cologne Database for Molecular Spectroscopy (CDMS[5];Müller et al. 2001,Müller et al. 2005).* [b] *The errors in brackets are the gaussian fit uncertainties.* [c] *The lines cannot be distinguished with the present spectral resolution.*

Ketene is one of the numerous carbon-chain molecules that have been observed in the interstellar medium, it was discovered for the first time in 1977 in Sgr B2 (Turner 1977) and subsequently found in many astronomical sources. Although it is not an iCOM in the strict sense (only 5 atoms), it is tought to be be involved in grain-surface reactions to form many iCOMs such as formic acid, ethanol and acetaldehyde (Charnley et al. 1997; Hudson & Loeffler 2013 and references therein). Ketene is a near-prolate asymmetric top rotor, a sketch of the 3D structure is illustrated in Fig. 5.17. Moreover, H_2CCO exist in two isomers, ortho (transition with K odd) and para (transitions with K even), that have different nuclear spin states. For kinetical temperature much larger than 15 K, as in typical hot corinos (T_{kin} ≥100 K), the ortho-to-para ratio is expected to be close to the statistical value of 3 (e.g. Ohishi et al. 1991).

We detcted 11 lines of the para and 6 of the ortho form of H_2CCO in the ASAI observed spectral bands. In particular only 4 of the detected transitions are in the 2mm band, observed with a HPBW of ∼15″ , while the rest of the lines are detected in the 1mm band (HPBW of ∼10″). The line upper level energies (E_{up}) are in the 40–206 K range. The observed spectra are shown in Fig. 5.18 while the spectral line parameters are reported in Tab. 5.4.

Note that the intensity of the para transitions is systematically lower than the intensity of the para transitions, in agreement with the o/p statistical values of 3 at the high-temperature limit. The line profiles are close to a gaussian shape with FWHM between 0.9 and 4.1 km s^{-1}. The peak velocities are close to the systemic source velocity (+8.6 km s^{-1}, Chen et al. 2009; López-Sepulcre et al. 2015) with values between +7.6 km s^{-1} and +8.8 km s^{-1}. The two transitions $8_{3,5}$–$7_{3,4}$ and $8_{3,6}$–$7_{3,5}$ with E_{up} = 152 K, as well as the two transitions $13_{3,10}$–$12_{3,9}$ and $13_{3,11}$–$12_{3,10}$ with E_{up} = 206 K, are not spectrally resolved whithin the present frequency resolution, forming a unique profile (see Tab. 5.4). These lines are then excluded from the further analysis.

We perform a rotation diagram analysis assuming LTE conditions and an the hot corino as the emitting source, consequently we assume a size of 1″. Once considered both ortho and para transitions in a single rotation diagram, the distribution does not show any significant scatter from the linear fit. Considering the uncertainties of the line intensities and the calibration errors, this is consistent with the o/p statistical values of 3 at the high-temperature limit. We found a rotational temperature T_{rot} = 64 ± 11 K and a column density N_{tot} = 11.4 ± 2.9 × 10^{14} cm^{-2}, see Fig. 5.19 and Tab. 5.10.

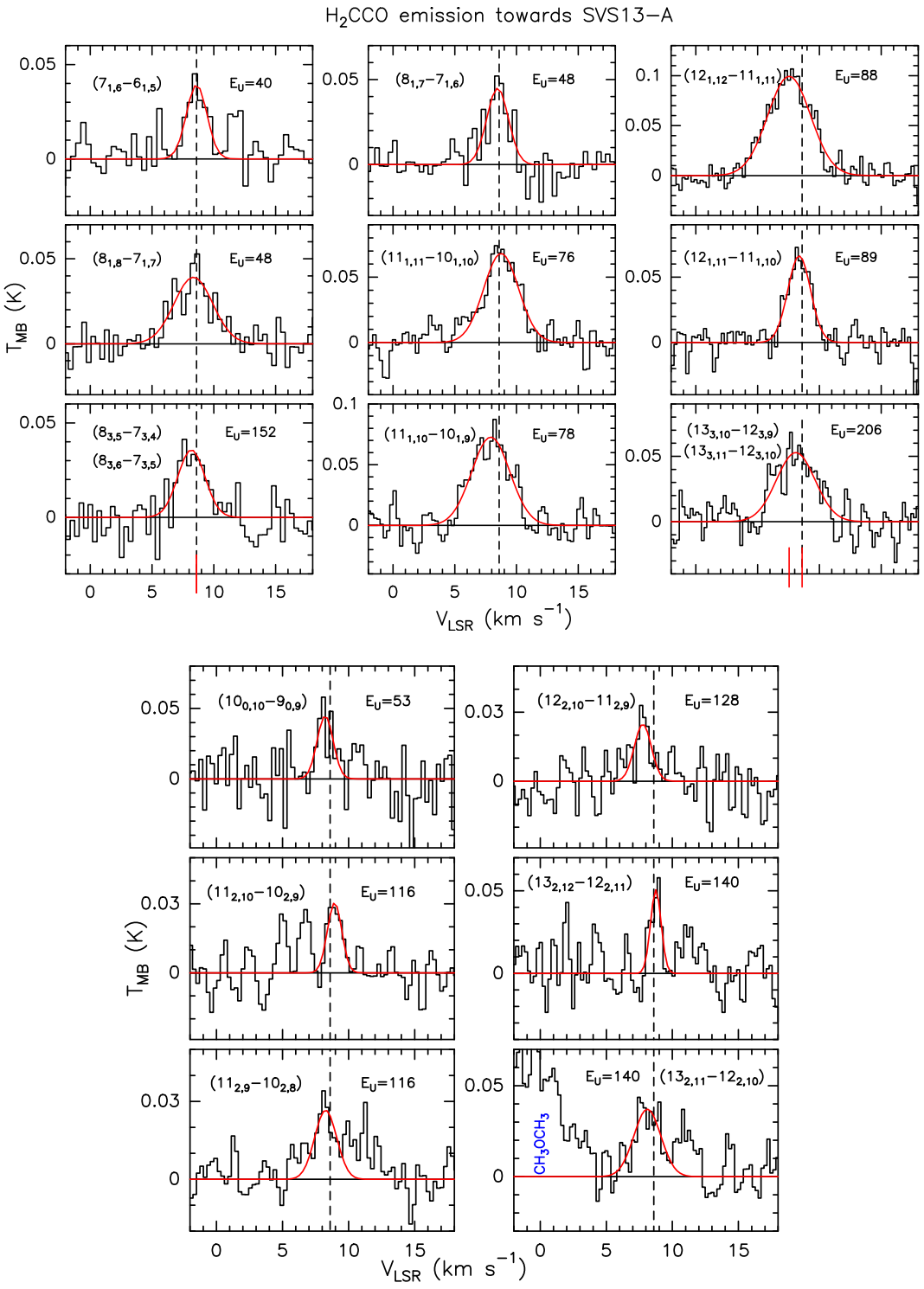

Figure 5.18: H_2CCO line profiles in T_{MB} scale (not corrected for the beam dilution); transitions are reported. The vertical dashed line stands for the ambient LSR velocity (+ 8.6 Km s^{-1}, Chen et al. 2009). In the upper and lower panel are reported the ortho and it para transitions respectively. Note that the intensity of the para transitions is lower than the ortho ones, consistently with the ratio 1:3 of the statistical weights in the high temperature limit (T $\gg$15 K).

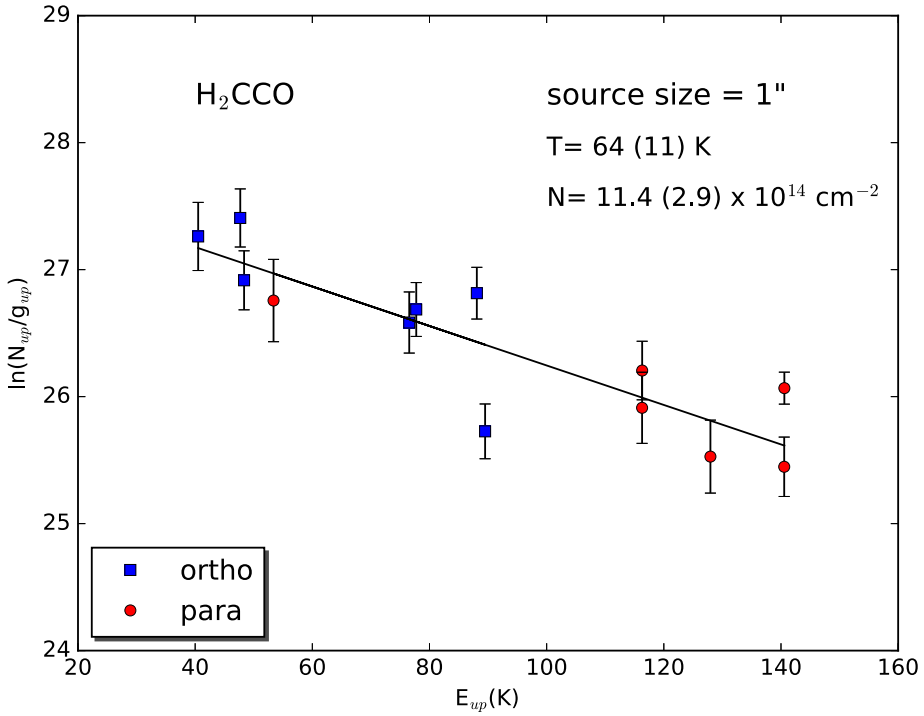

Figure 5.19: Rotation diagram for H_2CCO. An emitting region size of 1″ is assumed (see text). The parameters N_u, g_u, and E_{up} are, respectively, the column density, the degeneracy and the energy (with respect to the ground state of each symmetry) of the upper level. Blue squares and red dots indicate ortho and para transitions, respectively. The derived values of the rotational temperature and the column density are reported.

5.3.2 Acetaldehyde (CH_3CHO)

Table 5.5: List of transitions and line properties (in T_{MB} scale) of the CH_3CHO emission detected towards SVS13-A.

Transition	ν^a (GHz)	$HPBW$ ($''$)	$E_{up}{}^a$ (K)	$S\mu^{2a}$ (D^2)	rms (mK)	$T_{peak}{}^b$ (mK)	$V_{peak}{}^b$ (km s^{-1})	$FWHM^b$ (km s^{-1})	$I_{int}{}^b$ (mK km s^{-1})
CH_3CHO $5_{1,5}$–$4_{1,4}$ E [c]	93.5953	26	16	61	1	13 (1)	+8.74 (0.39)	2.37 (0.11)	32 (1)
CH_3CHO $11_{1,11}$–$10_{1,10}$ A	205.1707	12	61	138	7	43 (7)	+8.62 (0.08)	1.60 (0.22)	74 (8)
CH_3CHO $11_{2,10}$–$10_{2,9}$ A	211.2430	12	70	134	5	42 (5)	+8.42 (0.09)	2.25 (0.28)	101 (10)
CH_3CHO $11_{2,10}$–$10_{2,9}$ E	211.2738	12	70	134	6	38 (6)	+8.86 (0.99)	2.23 (0.36)	91 (11)
CH_3CHO $11_{4,8}$–$10_{4,7}$ A	212.1284	12	97	121	5	25 (5)	+8.89 (0.12)	2.15 (0.26)	57 (6)
CH_3CHO $11_{1,10}$–$10_{1,9}$ E	216.5819	11	65	138	11	53 (8)	+7.99 (0.09)	2.45 (0.21)	139 (10)
CH_3CHO $11_{1,10}$–$10_{1,9}$ A	216.6302	11	65	138	8	45 (11)	+7.81 (0.16)	3.44 (0.39)	166 (16)
CH_3CHO $12_{0,12}$–$11_{0,11}$ A	226.5927	11	71	151	8	41 (8)	+8.38 (0.15)	4.05 (0.45)	176 (15)
CH_3CHO $12_{2,11}$–$11_{2,10}$ A	230.3019	11	81	147	11	33 (6)	+8.60 (0.15)	1.47 (0.30)	52 (10)
CH_3CHO $12_{4,8}$–$11_{4,7}$ E [c]	231.4844	11	108	135	6	39 (6)	+ 8.48 (0.17)	3.08 (0.39)	129 (15)
CH_3CHO $12_{3,9}$–$11_{3,8}$ A [d]	231.9684	11	93	142	7	98 (7)	+8.09 (0.12)	2.84 (0.25)	296 (26)
CH_3CHO $12_{2,10}$–$11_{2,9}$ E	234.7955	10	82	147	7	49 (7)	+8.51 (0.09)	3.64 (0.24)	191 (10)
CH_3CHO $13_{1,13}$–$12_{1,12}$ E	242.1060	10	84	163	9	44 (9)	+8.14 (0.11)	2.53 (0.30)	120 (11)
CH_3CHO $13_{0,13}$–$12_{0,12}$ A	244.8322	10	83	164	7	44 (7)	+8.36 (0.07)	1.89 (0.19)	88 (7)
CH_3CHO $13_{3,10}$–$12_{3,9}$ A	251.4893	10	105	156	5	32 (5)	+8.16 (0.08)	1.71 (0.21)	59 (6)
CH_3CHO $13_{2,11}$–$12_{2,10}$ A	254.8505	10	94	161	7	34 (7)	+7.90 (0.13)	2.87 (0.33)	103 (10)

[a] *Frequencies and spectroscopic parameters are extracted from the Jet Propulsion Laboratory database (Pickett et al. 1998).* [b] *The errors in brackets are the gaussian fit uncertainties.* [c] *Irregular profile probably due to contamination by unidentified lines: excluded from the further analysis.* [d] *The transition CH_3CHO $12_{3,9}$–$11_{3,8}$ A at frequency 231.9684 GHz is observed but excluded from the analysis because contaminated by the CH_2DOH $9_{2,7}$–$9_{1,8}$ e0 transition (see Bianchi et al. 2017a)*

Acetaldehyde is a common interstellar molecule which has been detected in almost all the star-formation environment, from cold dark cores (e.g. Bacmann et al. 2012, Vastel et al. 2014, Jiménez-Serra et al. 2016) to hot corinos (e.g. Cazaux et al. 2003, Codella et al. 2016b) and protostellar shocks (e.g. Codella et al. 2015). CH_3CHO is an asymmetric top molecule; a sketch of the 3D structure is illustrated in Fig. 5.17. As in the case of methanol, because of the presence of a methil group (CH_3), acetaldehyde is a species with internal rotation. Having one rotor, CH_3CHO is divided in two *A*-type and *E*-type forms. The total statistical weight of the *A* and *E* type levels is the same (Turner 1991, and references therein). Despite the several detections in a large range of interstellar conditions, it is not yet clear if acetaldehyde is synthesized directly on the grain surfaces (e.g. Garrod & Herbst 2006) or via gas-phase reactions (e.g. Charnley et al. 1992). In particular the first route has been recently questioned by observations in protostellar shocks

(Codella et al. 2015) and quantum chemical calculations (Enrique-Romero et al. 2016). However the picture is still far from being clear.

We detected 6 transitions of CH_3CHO in the E form and 10 transitions in the A form. Almost all the lines are detected in the 1mm ASAI spectrum, observed with a telescope HPBW $\sim 10''$, except for the $5_{1,5}$–$4_{1,4}$ E which is detected in the 3mm band but excluded from the analysis because contaminated by an unidentified emission line. The line upper level energies (E_{up}) range from 16 K to 108 K while the peak velocities are consistent with the systemic velocity (+8.6 km s^{-1}, Chen et al. 2009; López-Sepulcre et al. 2015) with values between +7.8 km s^{-1} and +8.9 km s^{-1}. The line shape is nearly gaussian with typical FWHMs of ∼2–4 km s^{-1}. The spectral parameters and the gaussian fit results are reported in Tab. 5.5 while the specra of the detected lines are in Fig. 5.20. The CH_3CHO $12_{3,9}$–$11_{3,8}$ A transition is observed but excluded from the analysis being contaminated by the CH_2DOH $9_{2,7}$–$9_{1,8}$ e0 transition (see Bianchi et al. 2017a and Sec. 5.2.3). We analysed the detected lines using the rotation diagram technique, assuming LTE conditions and the hot corino region as the origin of the CH_3CHO emission, with a source size of $1''$. The results, shown in Fig. 5.21, indicate a rotational temperature $T_{rot} = 36 \pm 10$ K and a column density $N_{tot} = 10.7 \pm 6.6 \times 10^{15}$ cm^{-2}. Note that in Fig. 5.21 the red arrows indicate the upper limits derived from the two transitions $5_{1,5}$–$4_{1,4}$ E and $12_{4,9}$–$11_{4,7}$ E (see Tab. 5.5) which are contaminated by other emission lines and consequently excluded from the fit.

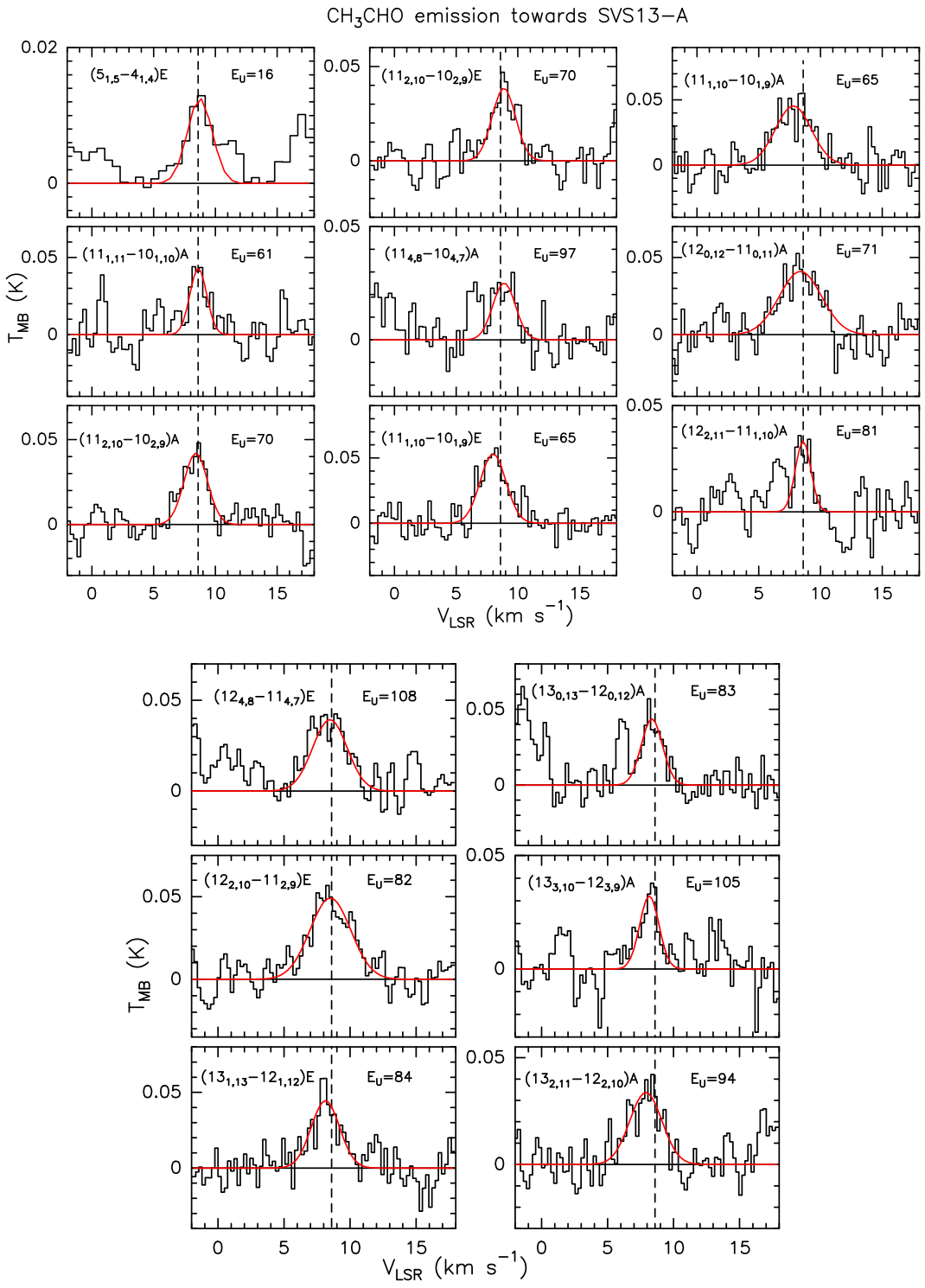

Figure 5.20: CH_3CHO line profiles in T_{MB} scale (not corrected for the beam dilution); transitions are reported. The vertical dashed line stands for the ambient LSR velocity (+ 8.6 Km s^{-1}, Chen et al. 2009). The $5_{1,5}$–$4_{1,4}$ E transition at frequency 93.5953 GHz and the $12_{4,8}$–$11_{4,7}$ E transition at 231.4844 GHz are contaminated by unidentified lines and thus excluded from the further analysis.

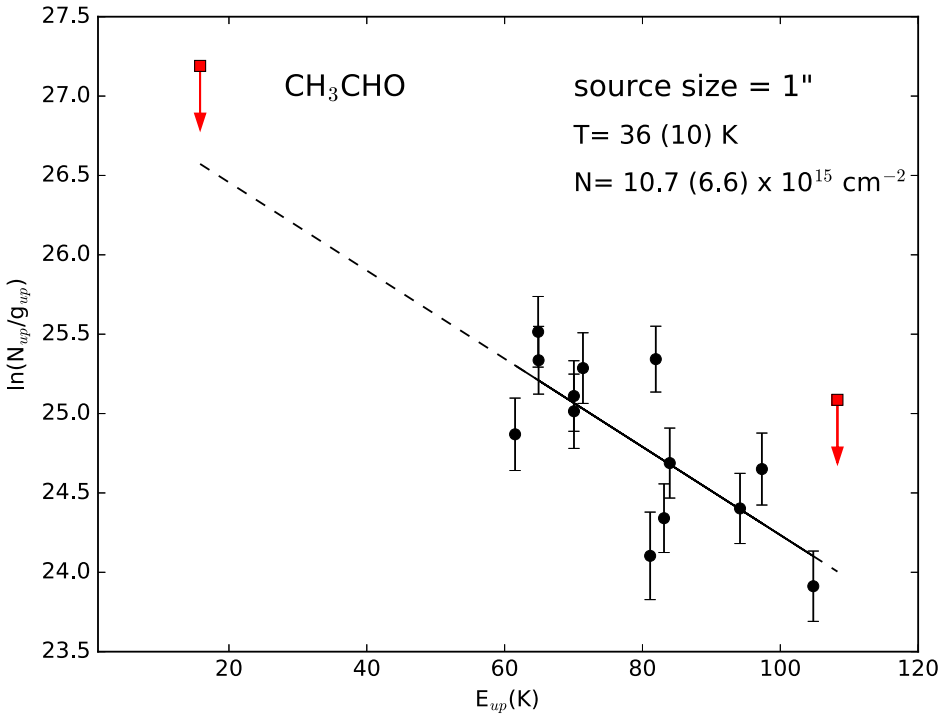

Figure 5.21: Rotation diagram for CH_3CHO. An emitting region size of 1″ is assumed (see text). The parameters N_u, g_u, and E_{up} are, respectively, the column density, the degeneracy and the energy (with respect to the ground state of each symmetry) of the upper level. The derived values of the rotational temperature are reported. Red arrows indicate the $5_{1,5}$–$4_{1,4}$ E and $12_{4,8}$–$11_{4,7}$ E transitions, not used to perform the fit because contaminated but reported as upper limits.

5.3.3 Methyl Formate ($HCOOCH_3$)

Another important iCOM which appears to be ubiquitous in the star forming regions is Methyl Formate. It was observed for the first time in 1975 towards the molecular cloud Sgr B2 by Brown et al. (1975) and then detected in both cold environments (e.g. Jiménez-Serra et al. 2016, Taquet et al. 2017 and references therein) as well as in the hot-corino phase (e.g. Cazaux et al. 2003, Bottinelli et al. 2004) and in protostellar shocks (Arce et al. 2008, Lefloch et al. 2017). As the previous species, $HCOOCH_3$ is an asymmetric top molecule, as illustrated in Fig. 5.17.

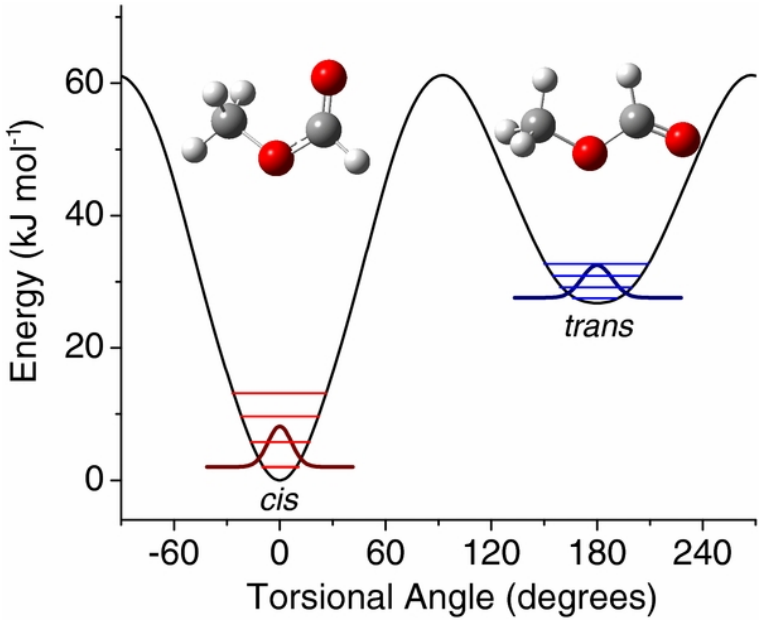

Figure 5.22: Potential energy surface of the *cis* and *trans* methyl formate ($HCOOCH_3$) molecule, from (Neill et al. 2012). The *cis* form is the most stable and in LTE conditions the population ratio of *cis* over *trans* is $\sim 10^{13}$:1 at a typical temperature of 100 K.

The presence of the methil group (CH_3) is responsible of the molecule internal rotation which reflects in the $HCOOCH_3$ *A* and *E* forms. As in the case of acetaldehyde, the total statistical weight of the *A* and *E* type levels is the same (Turner 1991 and references therein). Moreover $HCOOCH_3$ can exsist in two different geometrical configurations or isomerism: the *cis* configuration, if the

Table 5.6: List of transitions and line properties (in T_{MB} scale) of the CH_3CHO emission detected towards SVS13-A at 1 mm.

Transition	ν^a (GHz)	$HPBW$ ($''$)	$E_{up}{}^a$ (K)	$S\mu^{2a}$ (D^2)	rms (mK)	$T_{peak}{}^b$ (mK)	$V_{peak}{}^b$ (km s^{-1})	$FWHM^b$ (km s^{-1})	$I_{int}{}^b$ (mK km s^{-1})
$HCOOCH_3$ $18_{2,17}$–$17_{2,16}$ E	205.4957	12	99	47	7	43 (7)	+8.48 (0.15)	4.84 (0.40)	222 (15)
$HCOOCH_3$ $18_{2,17}$–$17_{2,16}$ A	205.5016	12	99	47	7	46 (7)	+8.02 (0.12)	4.07 (0.29)	199 (12)
$HCOOCH_3$ $16_{3,13}$–$15_{3,12}$ E	206.6012	12	89	41	11	47 (11)	+8.47 (0.18)	4.32 (0.37)	214 (17)
$HCOOCH_3$ $16_{3,13}$–$15_{3,12}$ A	206.6195	12	89	41	10	42 (11)	+8.34 (0.18)	3.83 (0.41)	171 (16)
$HCOOCH_3$ $17_{2,15}$–$16_{2,14}$ E	206.7109	12	95	43	4	43 (7)	+8.70 (0.06)	2.91 (0.14)	134 (59)
$HCOOCH_3$ $17_{4,14}$–$16_{4,13}$ E	209.9185	12	101	43	5	39 (5)	+8.90 (0.07)	2.63 (0.18)	110 (6)
$HCOOCH_3$ $17_{6,12}$–$16_{6,11}$ A	211.2550	12	115	40	6	28 (6)	+8.67 (0.12)	2.77 (0.26)	83 (7)
$HCOOCH_3$ $17_{6,12}$–$16_{6,11}$ E	211.2661	12	115	39	8	40 (8)	+8.21 (0.12)	2.45 (0.26)	104 (10)
$HCOOCH_3$ $17_{6,11}$–$16_{6,10}$ E	211.5372	12	115	39	6	29 (6)	+8.35 (0.17)	3.86 (0.46)	117 (11)
$HCOOCH_3$ $17_{6,11}$–$16_{6,10}$ A	211.5751	12	115	39	5	28 (5)	+8.43 (0.26)	3.73 (0.64)	111 (17)
$HCOOCH_3$ $17_{5,12}$–$16_{5,11}$ E	214.6317	11	108	41	9	39 (6)	+7.80 (0.14)	2.72 (0.29)	113 (11)
$HCOOCH_3$ $17_{5,12}$–$16_{5,11}$ A	214.6526	11	108	41	12	39 (12)	+7.93 (0.22)	3.81 (0.47)	159 (18)
$HCOOCH_3$ $18_{3,16}$–$17_{3,15}$ E	214.7824	11	106	46	9	53 (9)	+7.76 (0.11)	2.95 (0.23)	167 (12)
$HCOOCH_3$ $18_{3,16}$–$17_{3,15}$ A	214.7925	11	106	46	8	41 (8)	+7.87 (0.15)	4.23 (0.43)	185 (15)
$HCOOCH_3$ $19_{3,17}$–$18_{3,16}$ E [c,d]	216.2109	11	109	49	11	52 (11)	+8.05 (0.17)	4.06 (0.41)	224 (19)
$HCOOCH_3$ $19_{1,18}$–$18_{1,17}$ E [c,d]	216.2110								
$HCOOCH_3$ $19_{1,18}$–$18_{1,17}$ A	216.2165	11	109	49	6	30 (6)	+8.33 (0.15)	3.94 (0.40)	127 (10)
$HCOOCH_3$ $18_{2,16}$–$17_{2,15}$ E	216.8302	11	106	46	8	46 (8)	+8.15 (0.13)	3.75 (0.37)	183 (14)
$HCOOCH_3$ $18_{2,16}$–$17_{2,15}$ A	216.8389	11	106	46	8	39 (8)	+8.31 (0.14)	3.75 (0.37)	156 (13)
$HCOOCH_3$ $20_{1,20}$–$19_{1,19}$ E [c,d]	216.9648								
$HCOOCH_3$ $20_{1,20}$–$19_{1,19}$ A [c,d]	216.9659								
$HCOOCH_3$ $20_{0,20}$–$19_{0,19}$ E [c,d]	216.9663	11	111	53	9	99 (9)	+7.93 (0.13)	6.80 (0.48)	716 (40)
$HCOOCH_3$ $20_{2,19}$–$19_{0,19}$ E [c,d]	216.9663								
$HCOOCH_3$ $20_{0,20}$–$19_{0,19}$ A [c,d]	216.9673								
$HCOOCH_3$ $17_{1,16}$–$16_{1,15}$ E [c,d]	218.2808	11	100	44	7	51 (7)	+8.49 (0.08)	3.04 (0.20)	167 (9)
$HCOOCH_3$ $17_{3,14}$–$16_{3,13}$ E [c,d]	218.2809								
$HCOOCH_3$ $17_{3,14}$–$16_{3,13}$ A	218.2979	11	100	44	7	51 (7)	+8.07 (0.10)	3.41 (0.24)	184 (11)
$HCOOCH_3$ $17_{4,13}$–$16_{4,12}$ E	220.1669	11	103	43	10	46 (10)	+8.86 (0.14)	3.36 (0.40)	164 (15)
$HCOOCH_3$ $17_{4,13}$–$16_{4,12}$ A	220.1903	11	103	43	8	46 (8)	+8.89 (0.11)	2.94 (0.22)	144 (10)
$HCOOCH_3$ $18_{4,15}$–$17_{4,14}$ E [c,d]	221.6605	11	112	45					
$HCOOCH_3$ $18_{10,9}$–$17_{10,8}$ A [c,d]	221.6611	11	167	33	8	65 (8)	+8.10 (0.08)	3.69 (0.20)	257 (12)
$HCOOCH_3$ $18_{10,8}$–$17_{10,7}$ A [c,d]	221.6611	11	167	33					
$HCOOCH_3$ $18_{8,10}$–$17_{8,9}$ E	222.4214	11	144	38	11	43 (7)	+8.38 (0.15)	2.47 (0.37)	113 (13)
$HCOOCH_3$ $19_{3,16}$–$18_{3,15}$ E [c,d]	225.6088	11	117	49	8	44 (8)	+8.08 (0.13)	3.73 (0.26)	173 (11)
$HCOOCH_3$ $19_{3,17}$–$18_{3,16}$ E [c,d]	225.6088								
$HCOOCH_3$ $21_{1,21}$–$20_{1,20}$ E [c,d]	227.5609								
$HCOOCH_3$ $21_{0,21}$–$20_{0,20}$ E [c,d]	227.5617								
$HCOOCH_3$ $21_{2,20}$–$20_{2,19}$ E [c,d]	227.5618	11	112	55	12	93 (12)	+8.50 (0.10)	4.80 (0.25)	473 (21)
$HCOOCH_3$ $21_{1,21}$–$20_{1,20}$ A [c,d]	227.5620								
$HCOOCH_3$ $21_{0,21}$–$20_{0,20}$ A [c,d]	227.5628								
$HCOOCH_3$ $18_{5,13}$–$17_{5,12}$ E	228.6289	11	119	44	14	46 (6)	+8.61 (0.20)	3.33 (0.52)	162 (20)
$HCOOCH_3$ $18_{5,13}$–$17_{5,12}$ A	228.6514	11	119	44	9	38 (8)	+7.98 (0.14)	2.84 (0.29)	114 (11)
$HCOOCH_3$ $19_{4,16}$–$18_{4,15}$ A	233.2268	11	123	48	7	46 (7)	+8.65 (0.10)	3.60 (0.23)	178 (10)
$HCOOCH_3$ $20_{6,14}$–$19_{6,13}$ E	251.2645	10	149	48	10	35 (7)	+9.16 (0.17)	3.51 (0.34)	132 (13)
$HCOOCH_3$ $20_{6,14}$–$19_{6,13}$ A	251.2857	10	149	48	9	42 (9)	+8.56 (0.14)	3.44 (0.29)	155 (12)
$HCOOCH_3$ $21_{10,12}$–$20_{10,11}$ E	259.1379	9	203	43	15	16 (4)	+8.65 (0.55)	2.85 (1.09)	48 (18)
$HCOOCH_3$ $24_{1,24}$–$23_{1,23}$ E [c,d]	259.3420	9	158	64	8	79 (8)	+7.81 (0.07)	4.11 (0.16)	345 (11)
$HCOOCH_3$ $24_{0,24}$–$23_{0,23}$ E [c,d]	259.3421								
$HCOOCH_3$ $24_{1,24}$–$23_{1,23}$ A [c,d]	259.3429								
$HCOOCH_3$ $24_{0,24}$–$23_{0,23}$ A [c,d]	259.3430								
$HCOOCH_3$ $20_{4,16}$–$19_{4,15}$ A	259.5217	9	139	51	8	39 (7)	+8.69 (0.15)	3.86 (0.40)	159 (12)

[a] *Frequencies and spectroscopic parameters are extracted from the Jet Propulsion Laboratory database (Pickett et al. 1998).* [b] *The errors in brackets are the gaussian fit uncertainties.* [c] *The lines cannot be distinguished with the present spectral resolution.* [d] *The line is excluded from the further analysis because blended by other transitions with different upper level energies (see text).*

Table 5.7: List of transitions and line properties (in T_{MB} scale) of the $HCOOCH_3$ emission detected towards SVS13-A at 2 and 3 mm.

Transition	ν^a (GHz)	$HPBW$ ($''$)	$E_{up}{}^a$ (K)	$S\mu^{2a}$ (D^2)	rms (mK)	$T_{peak}{}^b$ (mK)	$V_{peak}{}^b$ (km s^{-1})	$FWHM^b$ (km s^{-1})	$I_{int}{}^b$ (mK km s^{-1})
$HCOOCH_3$ $7_{2,5}$–$6_{2,4}$ E	90.1457	27	20	17	3	8 (1)	+9.01 (0.37)	2.41 (0.73)	20 (6)
$HCOOCH_3$ $12_{2,11}$–$11_{2,10}$ A	141.0443	17	47	31	2	29 (2)	+9.05 (0.05)	1.58 (0.12)	48 (3)
$HCOOCH_3$ $13_{3,11}$–$12_{3,10}$ E	158.6937	16	60	33	3	19 (3)	+8.39 (0.11)	3.65 (0.27)	74 (5)
$HCOOCH_3$ $13_{3,11}$–$12_{3,10}$ A	158.7044	16	60	33	6	20 (6)	+8.28 (0.28)	4.61 (0.67)	98 (12)
$HCOOCH_3$ $14_{2,13}$–$13_{2,12}$ E	162.7689	15	63	36	6	26 (6)	+8.03 (0.20)	4.78 (0.48)	134 (11)
$HCOOCH_3$ $14_{2,13}$–$13_{2,12}$ A	162.7753	15	63	36	8	23 (8)	+7.47 (0.28)	4.01 (0.63)	98 (14)
$HCOOCH_3$ $14_{1,13}$–$13_{1,12}$ E	163.8297	15	62	36	5	31 (5)	+8.34 (0.15)	4.29 (0.38)	140 (10)
$HCOOCH_3$ $14_{1,13}$–$13_{1,12}$ A	163.8355	15	62	36	6	21 (6)	+8.65 (0.18)	2.52 (0.36)	57 (8)
$HCOOCH_3$ $15_{1,15}$–$14_{1,14}$ E [c] $HCOOCH_3$ $15_{1,15}$–$14_{1,14}$ A [c]	163.9604 163.9619	15	65	39	6	38 (6)	+7.54 (0.26)	4.69 (0.62)	187 (21)
$HCOOCH_3$ $15_{0,15}$–$14_{0,14}$ E [c] $HCOOCH_3$ $15_{0,15}$–$14_{0,14}$ A [c]	163.9875 163.9889	15	65	39	8	33 (8)	+6.84 (0.35)	5.92 (0.96)	209 (28)

[a] *Frequencies and spectroscopic parameters are extracted from the Jet Propulsion Laboratory database (Pickett et al. 1998).* [b] *The errors in brackets are the gaussian fit uncertainties.* [c] *The lines cannot be distinguished with the present spectral resolution.* [d] *The line is excluded from the further analysis because blended by other transitions with different upper level energies (see text).*

methyl group (CH_3) is on the same side of the carbon chain; the *trans* configuration if the methyl group is on opposing sides of the carbon chain (see Fig. 5.22). However the *trans* form is less stable than the *cis* form and at typical temperatures of 100 K, the population ratio of *cis* over *trans* is $\sim 10^{13}$:1 (Neill et al. 2012). Furthermore the energy barriers make unlikely the interconversion between *cis* and *trans* forms in interstellar environments, so only the *cis* has been detected (Laas et al. 2011).

Methyl formate is the most abundant among its isomers acetic acid (CH_3COOH) and glycolaldehyde ($HCOCH_2OH$). In the Sgr B2 complex, a relative abundance of $\sim$ 0.5:1:26 (glycolaldehyde : acetic acid : methyl formate) has been measured by Hollis et al. (2001). The reason of this abundances differentiation is still unclear but it is tought to be related to the respectively formation processes (e.g. Bennett & Kaiser 2007).

We detected in total 49 lines of $HCOOCH_3$ in the ASAI spectra. Among them, only one line has been detected in the 3mm ASAI band, with a HPBW $\sim$27$''$ while 11 lines are detected in the 2mm band and 37 in the 1mm band, observed with HPBWs of $\sim$15$''$ and $\sim$10$''$, respectively. The lines cover a large range of upper

level energies E_{up} , from 20 K to 203 K, the line profiles are close to gaussian shape with typical FWHM~2–4 km s^{-1} and the peak velocities are close to the systemic source velocity (+8.6 km s^{-1}, Chen et al. 2009; López-Sepulcre et al. 2015) with values between +7.5 km s^{-1} and +9.2 km s^{-1}. The spectral line parameters and the results of the gaussian fit are reported in Tab. 5.7 and in Tab. 5.6 while the emission line spectra are shown in Fig. 5.23.

Assuming LTE conditions and the hot corino region as the emitting source with a size of 1″, we performed a rotational diagram analysis. The results are a rotation temperature T_{rot} = 66 ± 5 K and a column density N_{tot} = 11.6 ± 1.3 × 10^{15} cm^{-2}, as illustrated in Fig. 5.24 and reported in Tab. 5.10. Note that in some cases, because of the limited spectral resolution, we observe only one line but it consists of different transitions with the same upper level energy E_{up}. These unresolved multiplets are treated in the rotation diagram analysis using the method illustrated in Section 2.3.1. On the contrary, the lines containing several transitions with different upper level energies and different quantum numbers are excluded from the analysis.

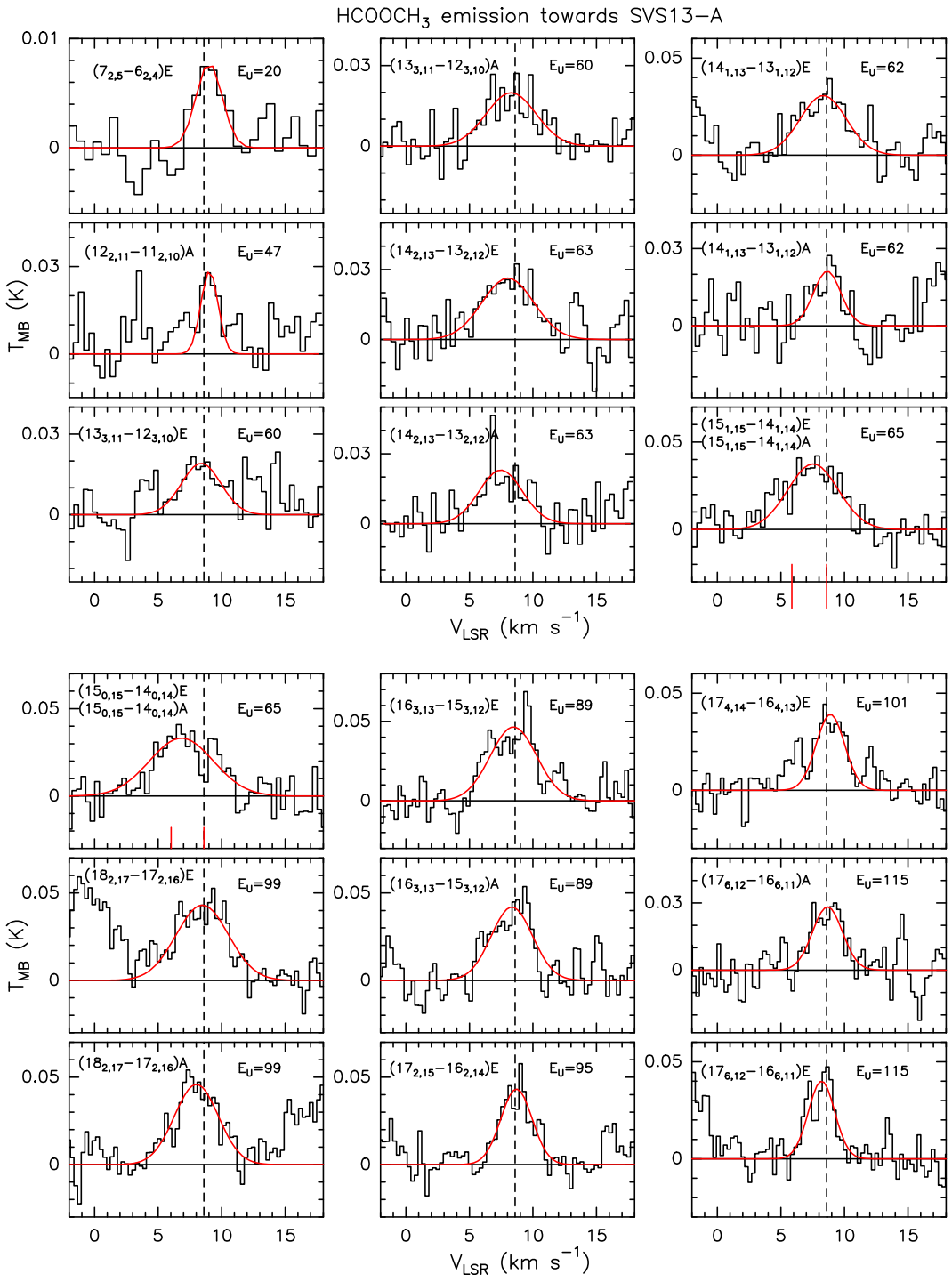

Figure 5.23: $HCOOCH_3$ line profiles in T_{MB} scale (not corrected for the beam dilution); transitions are reported. The vertical dashed line stands for the ambient LSR velocity (+ 8.6 Km s^{-1}, Chen et al. 2009). All the line profiles due to several transitions with different upper level energies are excluded from the analysis (see text).

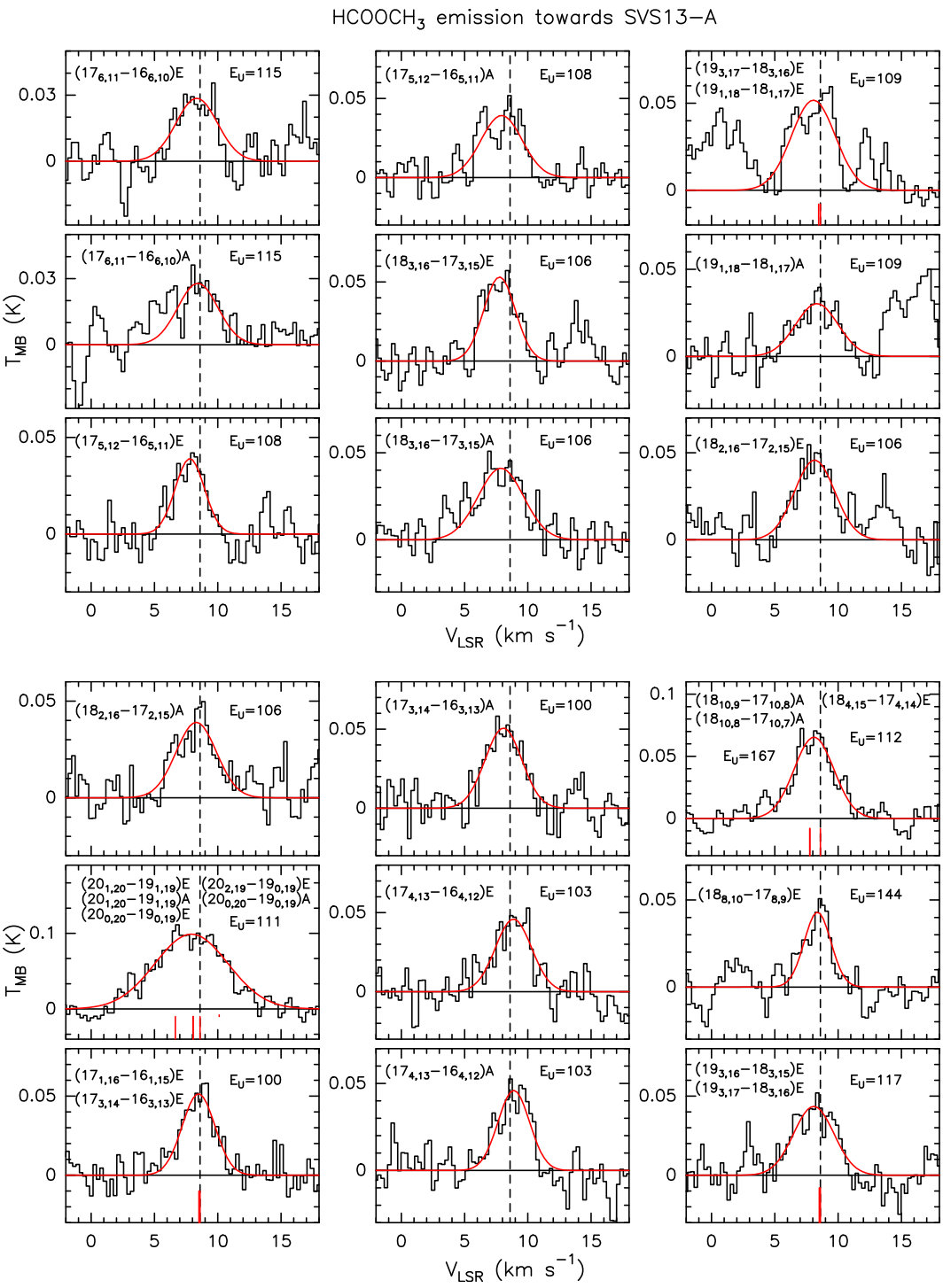

Figure 5.23: *Continued.*

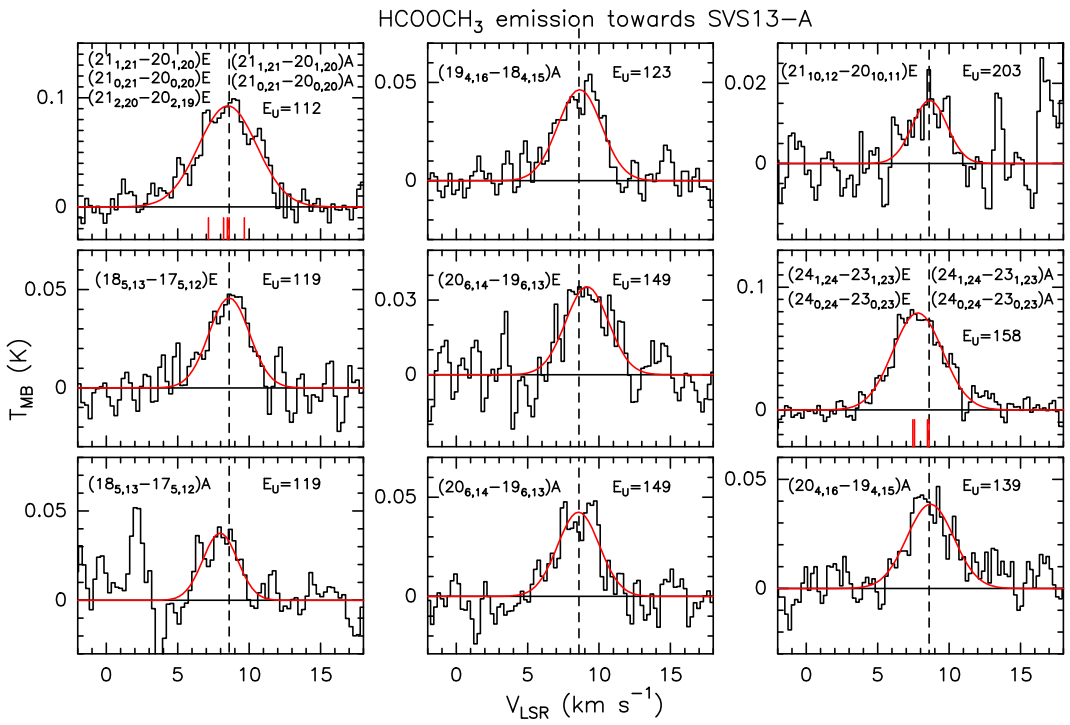

Figure 5.23: *Continued.*

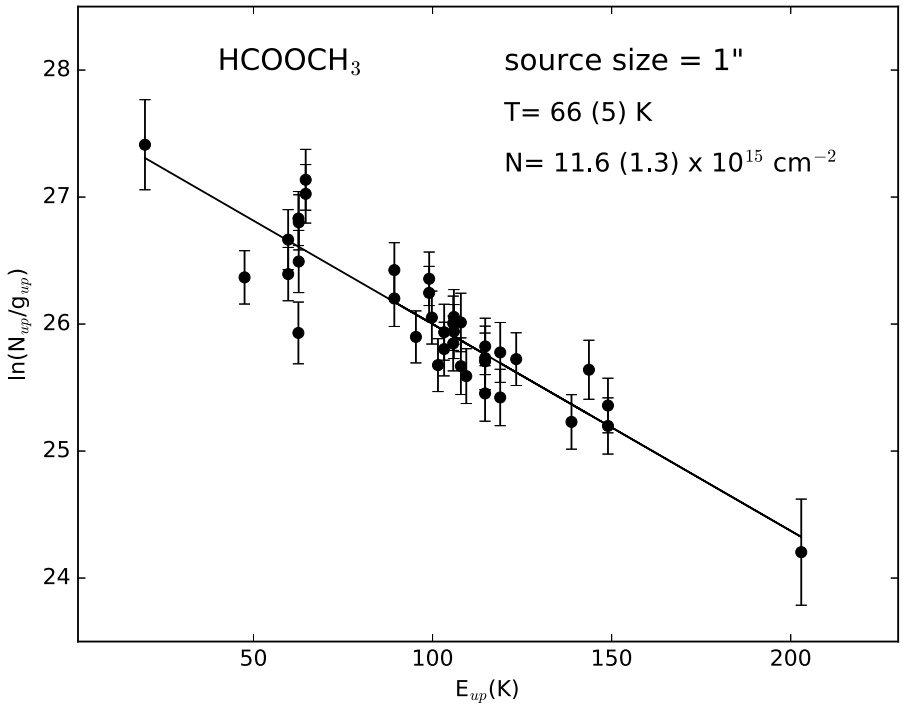

Figure 5.24: Rotation diagram for $HCOOCH_3$. An emitting region size of 1″ is assumed (see text). The parameters N_u, g_u, and E_{up} are, respectively, the column density, the degeneracy and the energy (with respect to the ground state of each symmetry) of the upper level. The derived values of the rotational temperature are reported.

Table 5.8: List of transitions and line properties (in T_{MB} scale) of the CH_3OCH_3 emission detected in the 2mm and 3mm ASAI bands towards SVS13-A.

Transition	ν^a (GHz)	$HPBW$ ($''$)	$E_{up}{}^a$ (K)	$S\mu^{2a}$ (D^2)	rms (mK)	$T_{peak}{}^b$ (mK)	$V_{peak}{}^b$ (km s^{-1})	$FWHM^b$ (km s^{-1})	$I_{int}{}^b$ (mK km s^{-1})
CH_3OCH_3 $7_{1,7}$–$6_{0,6}$ EA	147.0242	17	26	31	15	–	–	–	63 (39)
CH_3OCH_3 $7_{1,7}$–$6_{0,6}$ AE	147.0242			15					
CH_3OCH_3 $7_{1,7}$–$6_{0,6}$ EE	147.0249			124					
CH_3OCH_3 $7_{1,7}$–$6_{0,6}$ AA	147.0256			46					
CH_3OCH_3 $9_{0,9}$–$8_{1,8}$ AA	153.0545	16	40	100	8	–	–	–	116 (12)
CH_3OCH_3 $9_{0,9}$–$8_{1,8}$ EE	153.0548			160					
CH_3OCH_3 $9_{0,9}$–$8_{1,8}$ AE	153.0552			60					
CH_3OCH_3 $9_{0,9}$–$8_{1,8}$ EA	153.0552			40					
CH_3OCH_3 $22_{4,18}$–$22_{3,19}$ AE	162.4095	15	254	51	7	–	–	–	74 (13)
CH_3OCH_3 $22_{4,18}$–$22_{3,19}$ EA	162.4095			102					
CH_3OCH_3 $22_{4,18}$–$22_{3,19}$ EE	162.4107			407					
CH_3OCH_3 $22_{4,18}$–$22_{3,19}$ AA	162.4120			153					
CH_3OCH_3 $8_{1,8}$–$7_{0,7}$ EA	162.5290	15	33	36	8	–	–	–	142 (11)
CH_3OCH_3 $8_{1,8}$–$7_{0,7}$ AE	162.5290			55					
CH_3OCH_3 $8_{1,8}$–$7_{0,7}$ EE	162.5296			145					
CH_3OCH_3 $8_{1,8}$–$7_{0,7}$ AA	162.5302			91					

[a] Frequencies and spectroscopic parameters are extracted from the Cologne Database for Molecular Spectroscopy (CDMS[6];Müller et al. 2001,Müller et al. 2005) molecular database. [b] Gaussian fit is not performed given the asymmetric line profiles. [c]The transition is not used for the further analysis.

5.3.4 Dimethyl ether (CH_3OCH_3)

Dimethyl ether is one of the largest iCOM detected in the interstellar medium and similarly to the other species it seems to be present in all the stages of the star forming process. Dimethyl ether is an asymmetric top molecules with two equivalent methil groups, as illustrated in Fig. 5.17. The torsional movements along the CO-bond of the two CH_3 rotors, cause the splitting of each rotational level into four substates AA, EE, EA, and AE. The spin statistical weights were derived by Myers & Bright Wilson (1960) as 6(AA), 16(EE), 2(AE), 4(EA) and 10(AA), 16(EE), 6(AE), 4(EA) for ee-oo[7] and eo-oe rotational transitions, respectively. CH_3OCH_3 has been detected for the first time by (Snyder et al. 1974) in the Orion nebula and successively, in the context of Sun-like star forming regions, in different hot corinos (e.g. Cazaux et al. 2003, Bottinelli et al. 2004) as well

[7]e (even) and o (odd) refer to the K_a, K_c labels of the energy states of an asymmetric rotor.

as in cold prestellar cores (e.g. Jiménez-Serra et al. 2016). We detcted up to 15 lines of dimethyl ether in the three ASAI bands, with upper level energies ranging from 26 to 254 K. All the detected lines consist of several emission lines not spectrally resolved (at the present velocity resolution, are multiplets, see Tab. 5.8 and Tab. 5.9). As a consequence, the line profiles does not show a gaussian shape depending on the shift of the frequencies between the multiplet components. For this reason we do not perform a gaussian fit, as reported in Tab. 5.8 and Tab. 5.9. We perform a rotation diagram analysis treating the multiplets with the method illustated in Sec. 2.3.1. To be consistent we use for the analysis only the lines composed by the 4 forms (AA, AE, EE, EA) of the same transition.

The derived values for rotation temperature and column density are $T_{\rm rot}$ = 107 ± 26 K and $N_{\rm tot}$ = 5.5 ± 1.5 × 10^{15} cm^{-2}, respectively (see Fig. 5.26 and Tab. 5.10).

Table 5.9: List of transitions and line properties (in T_{MB} scale) of the CH_3OCH_3 emission detected in the 1mm ASAI band towards SVS13-A.

Transition	ν^a (GHz)	$HPBW$ ($''$)	$E_{up}{}^a$ (K)	$S\mu^{2a}$ (D^2)	rms (mK)	$T_{peak}{}^b$ (mK)	$V_{peak}{}^b$ (km s^{-1})	$FWHM^b$ (km s^{-1})	$I_{int}{}^b$ (mK km s^{-1})
CH_3OCH_3 $13_{1,12}$–$12_{2,11}$ AA	202.4906			77					
CH_3OCH_3 $13_{1,12}$–$12_{2,11}$ EE	202.4916	12	86	123	18	–	–	–	181 (24)
CH_3OCH_3 $13_{1,12}$–$12_{2,11}$ AE	202.4926			46					
CH_3OCH_3 $13_{1,12}$–$12_{2,11}$ EA	202.4926			31					
CH_3OCH_3 $8_{4,4}$–$8_{3,5}$ EE [c]	204.5520		55	75					
CH_3OCH_3 $8_{4,5}$–$8_{3,5}$ EA [c]	204.5525	12	55	17	18	–	–	–	146 (21)
CH_3OCH_3 $11_{4,8}$–$11_{3,9}$ EE [c]	204.5526		83	151					
CH_3OCH_3 $12_{0,12}$–$11_{1,11}$ AA	212.7559			91					
CH_3OCH_3 $12_{0,12}$–$11_{1,11}$ AA	212.7561	12	70	243	11	–	–	–	209 (15)
CH_3OCH_3 $12_{0,12}$–$11_{1,11}$ AA	212.7562			61					
CH_3OCH_3 $12_{0,12}$–$11_{1,11}$ AA	212.7562			30					
CH_3OCH_3 $12_{1,12}$–$11_{0,11}$ EA	225.5988			62					
CH_3OCH_3 $12_{1,12}$–$11_{0,11}$ AE	225.5988	11	70	93	18	–	–	–	324 (23)
CH_3OCH_3 $12_{1,12}$–$11_{0,11}$ EE	225.5991			247					
CH_3OCH_3 $12_{1,12}$–$11_{0,11}$ AA	225.5995			154					
CH_3OCH_3 $9_{2,8}$–$8_{1,7}$ EA	237.6188			23					
CH_3OCH_3 $9_{2,8}$–$8_{1,7}$ AE	237.6188	10	46	12	9	–	–	–	368 (16)
CH_3OCH_3 $9_{2,8}$–$8_{1,7}$ EE	237.6209			93					
CH_3OCH_3 $9_{2,8}$–$8_{1,7}$ AA	237.6230			35					
CH_3OCH_3 $13_{1,13}$–$12_{0,12}$ AE	241.9462			34					
CH_3OCH_3 $13_{1,13}$–$12_{0,12}$ EA	241.9462	10	81	69	12	–	–	–	329 (17)
CH_3OCH_3 $13_{1,13}$–$12_{0,12}$ EE	241.9465			274					
CH_3OCH_3 $13_{1,13}$–$12_{0,12}$ AA	241.9468			103					
CH_3OCH_3 $15_{1,14}$–$14_{2,13}$ AA	249.9238			105					
CH_3OCH_3 $15_{1,14}$–$14_{2,13}$ EE	249.9245	10	113	168	11	–	–	–	100 (12)
CH_3OCH_3 $15_{1,14}$–$14_{2,13}$ AE	249.9251			63					
CH_3OCH_3 $15_{1,14}$–$14_{2,13}$ EA	249.9251			42					
CH_3OCH_3 $21_{5,16}$–$21_{4,17}$ AE	251.1408			118					
CH_3OCH_3 $21_{5,16}$–$21_{4,17}$ EA	251.1408	10	246	79	13	–	–	–	95 (19)
CH_3OCH_3 $21_{5,16}$–$21_{4,17}$ EE	251.1424			316					
CH_3OCH_3 $21_{5,16}$–$21_{4,17}$ AA	251.1441			197					
CH_3OCH_3 $12_{5,8}$–$12_{4,9}$ AE	262.8893			58					
CH_3OCH_3 $12_{5,8}$–$12_{4,9}$ EE	262.8902	9	106	112	15	–	–	–	107 (15)
CH_3OCH_3 $12_{5,8}$–$12_{4,9}$ AA	262.8954			97					
CH_3OCH_3 $15_{0,15}$–$14_{1,14}$ EA [c]	269.6088			82					
CH_3OCH_3 $15_{0,15}$–$14_{1,14}$ AE [c]	269.6088		106	123					
CH_3OCH_3 $15_{0,15}$–$14_{1,14}$ EE [c]	269.6088	9		329	15	–	–	–	218 (18)
CH_3OCH_3 $15_{0,15}$–$14_{1,14}$ AA [c]	269.6088			205					
CH_3OCH_3 $22_{3,19}$–$21_{4,18}$ EE [c]	269.6096		246	106					
CH_3OCH_3 $15_{1,15}$–$14_{0,14}$ AE	275.3817			41					
CH_3OCH_3 $15_{1,15}$–$14_{0,14}$ EA	275.3817	9	106	82	18	–	–	–	224 (21)
CH_3OCH_3 $15_{1,15}$–$14_{0,14}$ EE	275.3819			330					
CH_3OCH_3 $15_{1,15}$–$14_{0,14}$ AA	275.3821			124					

[a] *Frequencies and spectroscopic parameters are extracted from the Cologne Database for Molecular Spectroscopy (CDMS[8];Müller et al. 2001,Müller et al. 2005) molecular database.* [b] *Gaussian fit is not performed given the asymmetric line profiles.* [c] *The transition is not used for the further analysis.*

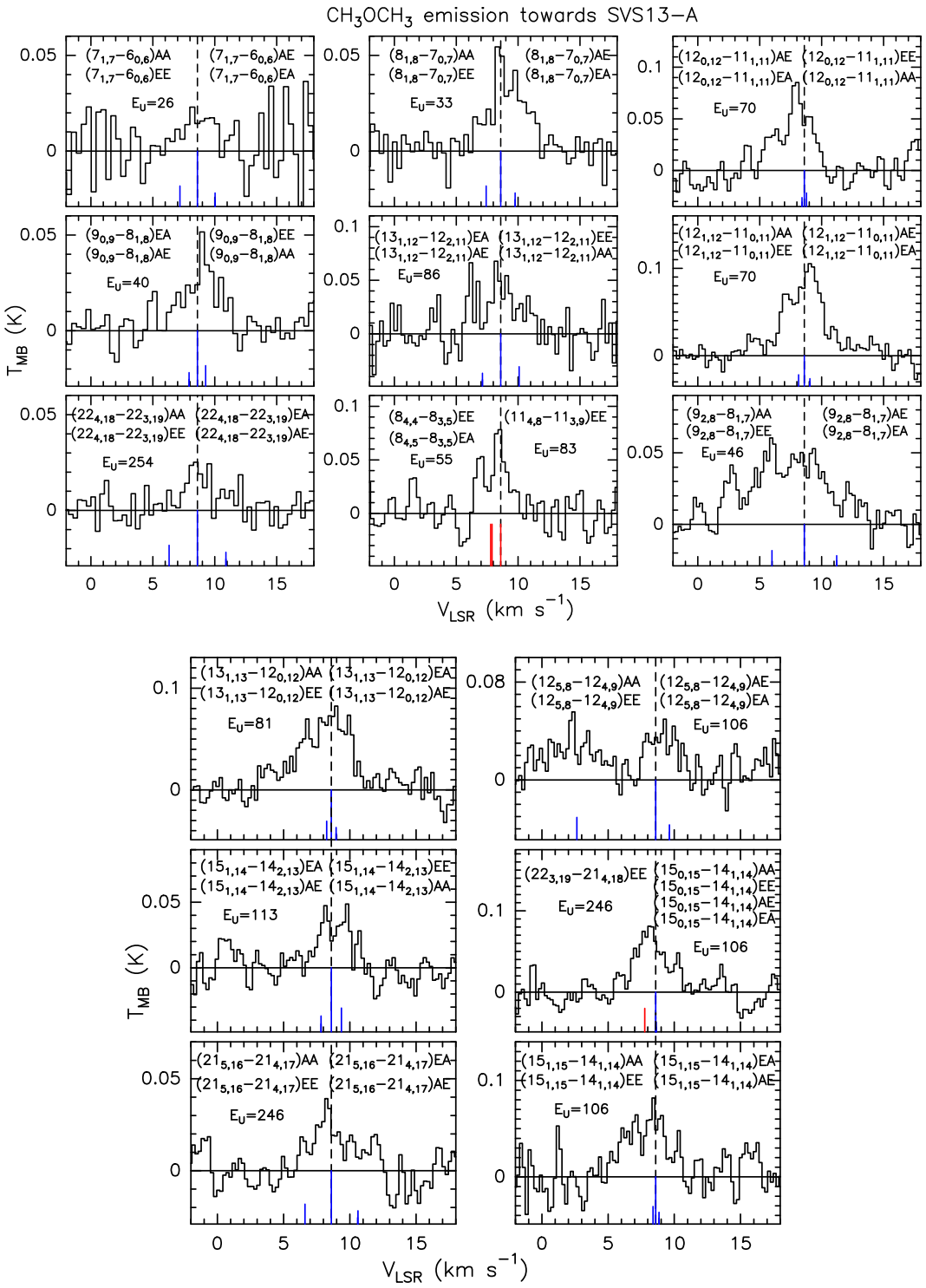

Figure 5.25: CH_3OCH_3 line profiles in T_{MB} scale (not corrected for the beam dilution); transitions are reported. The vertical dashed line stands for the ambient LSR velocity (+ 8.6 Km s^{-1}, Chen et al. 2009). The blue lines indicate transitions with the same upper level energies and quantum numbers, while the red lines indicate transitions with different upper level energies and quantum numbers.

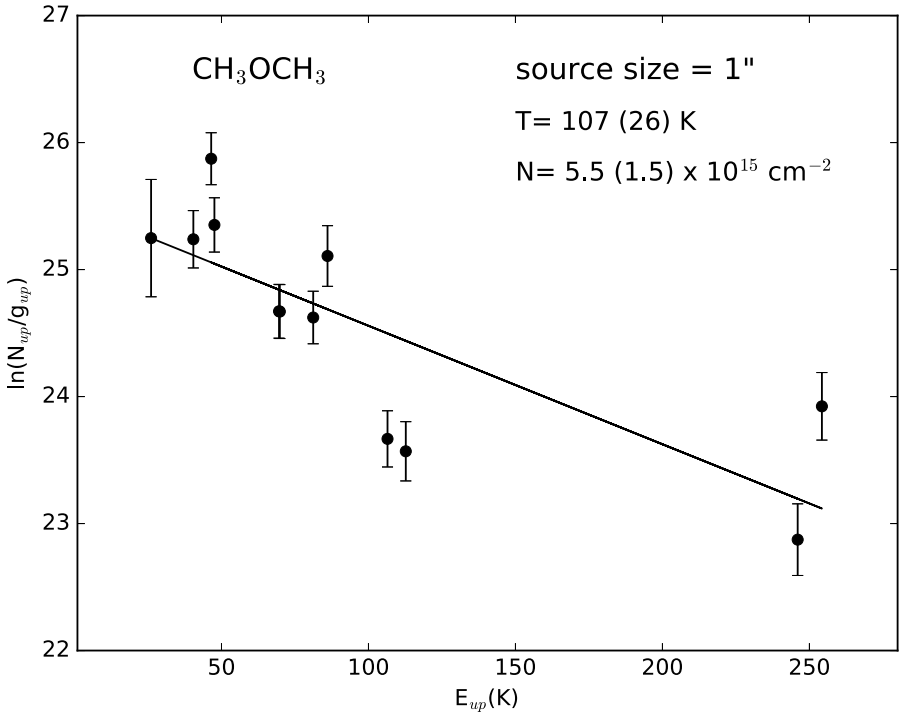

Figure 5.26: Rotation diagram for CH_3OCH_3. An emitting region size of 1″ is assumed (see text). The parameters N_u, g_u, and E_{up} are, respectively, the column density, the degeneracy and the energy (with respect to the ground state of each symmetry) of the upper level. The derived values of the rotational temperature are reported.

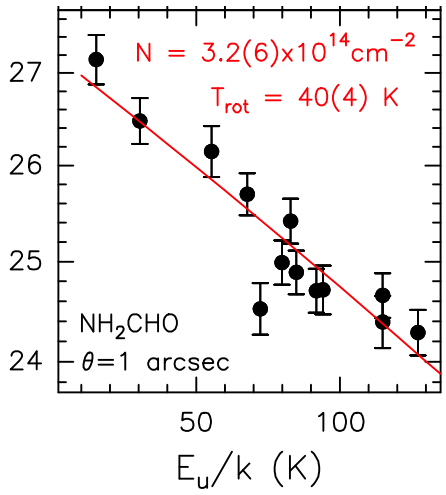

Figure 5.27: Rotation diagram for NH_2CHO from López-Sepulcre et al. (2015). An emitting region size of 1″ is assumed (see text). The parameters N_u, g_u, and E_{up} are, respectively, the column density, the degeneracy and the energy (with respect to the ground state of each symmetry) of the upper level. The derived values of the rotational temperature are reported.

5.3.5 Formamide (NH_2CHO)

Formamide is an interstellar molecule of great interest because it has been proposed as a pre-biotic precursor genetic material (e.g. Saladino et al. 2012, and references therein). Formamide was detected for the first time in space by Rubin et al. (1971) towards Sgr B2. Recently, Yamaguchi et al. (2012) and Mendoza et al. (2014) reported for the first time NH_2CHO emission towards the protostellar shocks L1157-B1 and B2. In addition Kahane et al. (2013), detected formamide towards the hot corino IRAS 16293–2422. The abundance of NH_2CHO was previously measured in all the ASAI targets, by López-Sepulcre et al. (2015). In particular, 13 formamide lines has been detected towards SVS13-A and analysed using the rotation diagram analysis, assuming the hot corino as the origin of the emission with a typical size of 1″. The derived values of rotation temperature and column density (see Fig. 5.27 and Tab. 5.10) are T_{rot} = 40 ± 4 K and N_{tot} = 3.2 ± 6 × 10^{14} cm^{-2}, respectively. We will use these values for the overall analysis of the iCOMs abundances around SVS13-A.

Table 5.10: List of the detected iCOMs towards SVS13-A.

Specie	E_{up} range (K)	T_{rot} [a] (K)	N_{tot} [a] (cm^{-2})	X_{H_2} [c]
H_2CCO	40–206	64 (11)	$11.4\ (2.9) \times 10^{14}$	2.3×10^{-9}
CH_3CHO	16–108	36 (10)	$10.7\ (6.6) \times 10^{15}$	2.1×10^{-8}
$HCOOCH_3$	20–203	66 (5)	$11.6\ (1.3) \times 10^{15}$	6.4×10^{-10}
CH_3OCH_3	46–246	107 (26)	$5.5\ (1.5) \times 10^{15}$	2.3×10^{-8}
NH_2CHO[b]	15–127	40 (4)	$3.2\ (0.6) \times 10^{14}$	1.1×10^{-8}

[a] *Parameters refer to an assumed source size of 1″.* [b] *From López-Sepulcre et al. (2015).* [c] *Assuming for a typical hot corino* $N(H_2) \sim 5 \times 10^{23}\ cm^{-2}$.

A summary of the measured iCOMs abundances towards SVS13-A is given in Tab. 5.10.

5.3.6 Constraints on other iCOMs

Beside the detected iCOMs we also put constraints on the column densities of non detected iCOMs which have been previously detected towards hot-corinos (e.g. Bottinelli et al. 2004, Jaber et al. 2014).

In particular we assumed (i) a temperature of 80 K, based on the rotational temperatures (T_{rot}) derived for the detected iCOMs, and (ii) a typical size of 1″ for the hot corino region. Under LTE conditions, we derived upper limits for the column densities of HCOOH, HCCCOH, $HCOCH_2OH$, CH_3NH_2, CH_3COCH_3 and CH_3O. The derived values are reported in Tab. 5.11. Note that $HCOCH_2OH$ has been recently imaged towards SVS13-A by De Simone et al. (2017) using the IRAM-NOEMA interferometer. The derived column density derived is N_{tot} = 1.2 ± 0.6 × 10^{15} cm^{-2}, well consistent with the upper limit derived here. In Chap. 6 we will discuss how upper limits on iCOMs can be fruitfully used to put firm contraints on chemical models.

Table 5.11: List of upper limits for non-detected iCOMs towards SVS13-A.

Specie	$T_{\rm rot}$ [a] (K)	$N_{\rm tot}$ [a] ($\rm cm^{-2}$)
HCOOH	80	$\lesssim 8 \times 10^{14}$
HCCCOH	80	$\lesssim 2 \times 10^{15}$
$HCOCH_2OH$[b]	80	$\lesssim 3 \times 10^{14}$
CH_3NH_2	80	$\lesssim 3 \times 10^{15}$
CH_3COCH_3	80	$\lesssim 2 \times 10^{15}$
CH_3O	80	$\lesssim 5 \times 10^{14}$

[a] *Parameters refer to an assumed source size of 1″. The temperature has been assumed based on the $T_{\rm rot}$ values derived for the iCOMs detected towards SVS13-A. The column densities upper limits refer to 1σ.* [b] *In agreement with the NOEMA CALYPSO measurements from De Simone et al. (2017) (see text).*

5.3.7 Conclusions on iCOMs

How can we estimate the abundances of the detected iCOMs ? The classical approach to quantify the iCOMs abundances in a source is to derive the fractional abundance of each species with respect to H_2, the most abundant molecular gas constituent. However, the determination of the molecular hydrogen column density in star forming regions may hide relevant difficulties. For instance, the homonuclear H_2 molecule has not a permanent dipole moment and it is consequently impossible to reveal using rotational transitions. Even carbon monoxide (CO) which is the second-most abundant interstellar molecule, with a fractional abundance $[CO]/[H_2] \simeq 10^{-4}$ (in particle numbers), is not easy easily exploitable for abundances determination. Carbon monoxide is ubiquitus in star forming regions, and it has a strong dipole moment; however, it is detected in all the components of the star forming recipe, from the static molecular cores to fast jets, thus it is difficult to determine from CO observations the origin of the emitting region, probably different from that emitting in iCOMs. Being back to H_2, its column density is normally estimated using continuum observations of the dust component. In particular, assuming optically thin emission, the envelope mass can be calcolated using:

$$M = \frac{S_\nu d^2}{K_\nu B_\nu(T_d) R_d} \tag{5.1}$$

where S_ν is the continuum integrated flux, d is the source distance, K_ν is the opacity for dust mass (see e.g. Ossenkopf & Henning 1994), $B_\nu(T_d)$ is the Plank function for a given dust temperature (T_d) and R_d is the dust-to-gas ratio (see Taquet et al. 2015). Then the H_2 column density can be derived from M using:

$$N(H_2) = \frac{M}{\mu m_H \Omega d^2} \tag{5.2}$$

with M being the mass of the envelope, μ the mean molecular mass in units of hydrogen molecular mass, m_H the hydrogen atom mass, Ω the solid angle subtended by the source and d its distance (see Taquet et al. 2015). The large uncertainty on the determination of some of these parameters, like for example the opacity or the gas-to-dust ratio makes the estimate of H_2 column density still challenging for the most of the sources.

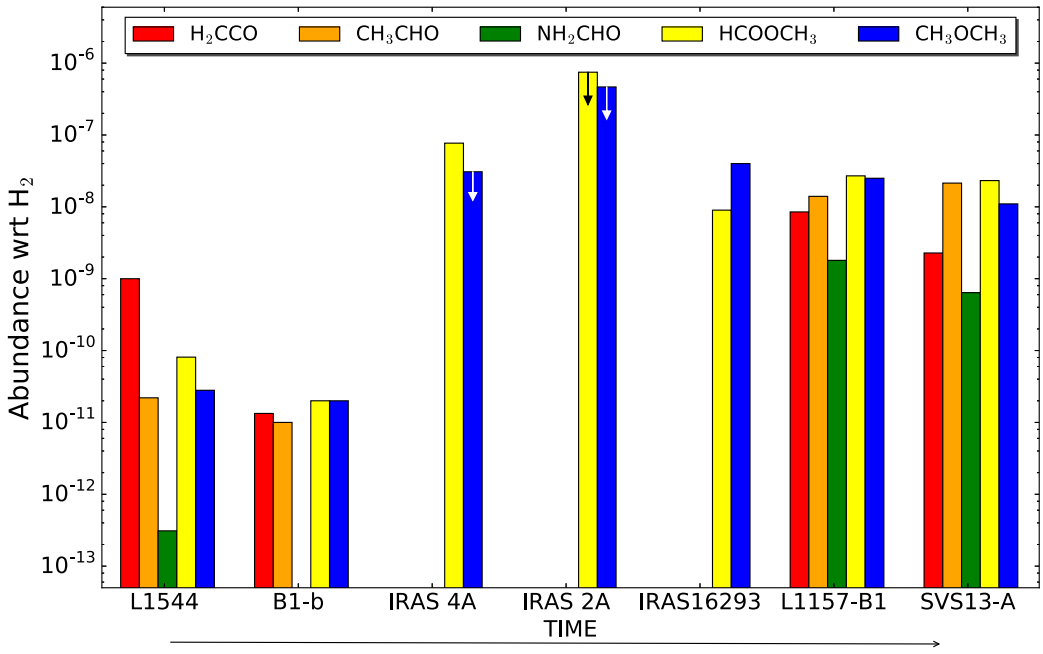

Figure 5.28: Abundances of the five iCOMs analysed in SVS13-A normalized to the H2 abundance for different objects: the prestellar core L1544 (Bizzocchi et al. 2014, Jiménez-Serra et al. 2016), the pre-protostar hydrostatic core B1-a (Pezzuto et al. 2012, Gerin et al. 2015), the Class 0 sources IRAS 4A, IRAS 2A and IRAS16293-2422 (e.g. Taquet et al. 2015, Jaber et al. 2014), the protostellar shock L1157-B1 (Codella et al. 2010, Lefloch et al. 2017) and the Class I source SVS13-A (this work). The iCOMs abundances with respect to H_2 in IRAS 4A, IRAS 2A and IRAS16293-2422 are from Taquet et al. (2015) while B1-a is from Cernicharo et al. (2012). Arrows indicate upper limits measurements. Note that all the sources are observed with the IRAM-30m telescope. The horizontal black arrow indicates the evolutionary stage (out of scale).

The iCOMs abundances with respect to H_2 in SVS13-A are reported in Tab. 5.10. We assumed typical values of H_2 column density of $\times\ 10^{23}$–10^{24} cm^{-2}, expected in the inner 100 au of hot-corinos (e.g. Maret et al. 2005 and references therein). In order to put the SVS13-A measuremets in the context of iCOMs abundances of low-mass star forming regions, Fig. 5.28 compares the present findings with those derived in prototypical objects (*observed with the same telescope, i.e. the IRAM-30m single dish*) such as:

- **L1544** is the prestellar core prototype located in the Taurus star forming region at a distance of 140 pc (see Caselli et al. 1999, 2002, and references within). It is a well studied source characterised by high density ($\geq 2 \times 10^6$ cm^{-3}) and low temperature ($\sim$ 7 K). Despite the high molecular depletion, in the core several iCOMs have been detected, produced possibly by reactive desorption or cosmic-ray irradiation of the external portion of the cloud (Vastel et al. 2014, Jiménez-Serra et al. 2016).

- **B1-b** is an intermediate stage between prestellar cores and Class 0 ($\geq 10^4$ yr) protostars. This source is located in the Barnard 1 dark cloud, in Perseus (d = 235 pc, see e.g. Bachiller & Cernicharo 1986). B1-b is composed of two different objects, B1-b N and B1-b S which are tought to be in the first hydrostatic core phase because of their spectral energy distribution (Pezzuto et al. 2012) and their association with small low-velocity outflows (Gerin et al. 2015). This indicate a more evolved stage with respect to starless cores but younger than a Class 0.

- **IRAS 4A, IRAS 2A and IRAS16293-2422** are classified as Class 0 solar-type protostars. In particular IRAS 4A and IRAS 2A are located in the NGC 1333 star forming region in Perseus (d = 235 pc) while IRAS16293-2422 is in the ρ Ophiuchi star-forming region (d = 120 pc, Loinard et al. 2008). All the sources are well studied and associated with iCOMs emission (e.g. Taquet et al. 2015, Jaber et al. 2014).

- **L1157-B1** is the prototype of a chemically rich protostellar shock. This bow shock originates at the apex of the cavity carved by the outflow associated to the Class 0 protostar L1157 (d = 250 pc, Looney et al. 2007). It has been extensively studied because it is one of the best laboratories to investigate

the interaction between shocks and molecular gas, having a kinematical age of only 2000 yr (Gueth et al. 1996). Several iCOMs have been detected towards the shock using both sigle-dishes and interferometric surveys (e.g. Codella et al. 2010, Lefloch et al. 2017).

Figure 5.28 compares the iCOMs abundances with respect to H_2: ketene is reported in red, acetaldehyde in orange, formamide in red, methyl formate in yellow, and dimethyl ether in blue. On the x-axes the sources are ordered following the evolutionary stage of the process leading to the formation of a Sun-like star: from the younger prestellar core L1544 to Class 0 and Class I protostars. In addition, we added the L1157-B1 prototypical shock, which is induced by the jet driven by the L1157-mm Class 0 protostar.

Even if some of the Class 0 measurements are only upper limit, we can discuss some general trends:

- The most abundant molecule in the prestellar core L1544 appears to be H_2CCO. However the abundances of CH_3OH, $HCOOCH_3$ and CH_3OCH_3 are not negligible ($\sim 10^{-11}$), and NH_2CHO is also present but with a definitively lower abundance (3×10^{-13}). The available measurements for the hydrostatic core B1-b (Cernicharo et al. 2012) are substantially in agreement with what found in L1544. Indeed the abundance of CH_3CHO, $HCOOCH_3$ and CH_3OCH_3 are $\sim 10^{-11}$. The only difference with respect to L1544 is in the H_2CCO abundance which is similar to the other iCOMs in B1-b, while it is higher by one order of magnitude in L1544.

- The main differences are observed if the cold sources (L1544, B1-b) are compared to the other stages. For Class 0 we observe a dramatic enanchement of the $HCOOCH_3$ and CH_3OCH_3 abundance: from 2 orders of magnitude, for IRAS16293-2422, to 4 orders of magnitude for IRAS 2A. Even if we consider that some measurements in Class 0 are upper limits (indicated by arrows in Fig. 5.28), it is clear that the outburst of the chemical complexity looks related to the hot-corino phase, when the grain mantles are sublimated by the increase of kinetic temperature due to stellar winds.

- The iCOMs abundances measured towards SVS13-A appears to be comparable with respect to the Class 0 abundances within an order of magnitude.

Indeed the abundances of $HCOOCH_3$ and CH_3OCH_3 in the three sources SVS13-A, IRAS 4A and IRAS 16293-2422, range between 9×10^{-9} and 8×10^{-8}. This behaviour seems to indicate that the more evolved Class I stage is as much chemically rich as the Class 0 phase. In other words, the iCOMs abundances observed in the early hot-corino stage looks to be preserved till the Class I phase. Furthermore, the protostellar shock L1157-B1 shows a chemical enrichment similar to the Class 0 sources and to SVS13-A with iCOMs abundances ranging between 2×10^{-9} for NH_2CHO to 3×10^{-8} for $HCOOCH_3$ and CH_3OCH_3. This is an indication that jets driven by Class 0 protostars, such as L1157-mm, can largely contribute to the chemical enrinchement in the protostellar surroundings. In this case, the process is related to the dust erosion in shocks (e.g. Pineau des Forets et al. 1993, Guillet et al. 2011 and references therein) due to gas-grain (sputtering) or grain-grain collisions (shattering).

Beside the abundances with respect to H_2, it is instructive to compare the abundance of iCOMs with respect to methanol (CH_3OH) which is assumed to be the unique iCOM which is formed only on dust mantles and not in the gas phase. In other words, methanol can be used, once assumed that the composition of dust mantles is the same, as a sort of proxy to measure the amount of material injected into the gas phase.

Figure 5.29 shows the abundance ratio of [iCOMs]/[CH_3OH] for selected sources, trying again to find evolutionary trends: the prestellar core L1544, the Class 0 IRAS16293-2422, and the Class I SVS13-A. The [iCOMs]/[CH_3OH] ratios for SVS13-A are definitely lower than those measured in the other sources. In particular we observe for H_2CCO a variation of three orders of magnitude between L1544 and SVS13-A. According to KIDA[9] ketene is not directly produced from methanol thus this could explain the large variation between the sources. However the lack of reliable measurements in IRAS16293-2422 prevent us to derive any trend. Also the NH_2CHO trend is not clear because the measument toward L1544 is an upper limit but we observe a decrease of two orders of magnitude from IRAS16293-2422 to the SVS13-A abundance. Again, this is not surprising given that for formamide it has been proposed a different chemistry with respect to

[9]KInetic database for Astrochemistry (KIDA), see Wakelam et al. 2012

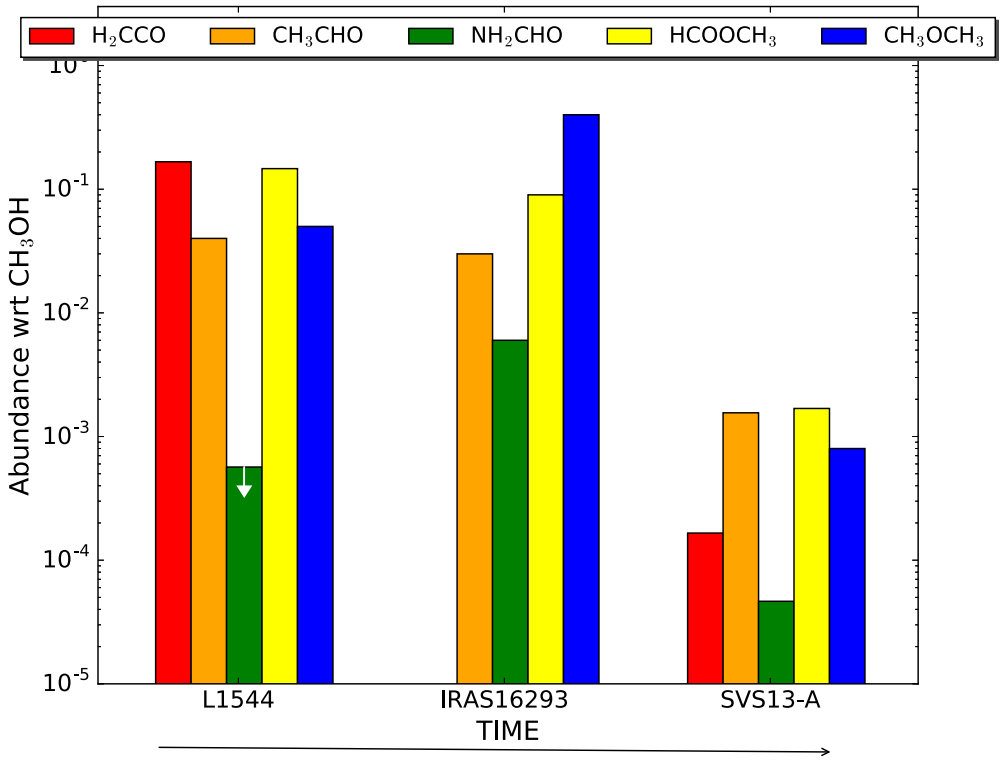

Figure 5.29: Abundances of different iCOMs normalized to the methanol abundance. The measurements towards SVS13-A (this work) are compared to the prestellar core L1544 (Bizzocchi et al. 2014, Jiménez-Serra et al. 2016) and to the Class 0 source IRAS16293-2422 (e.g. Taquet et al. 2015, Jaber et al. 2014). Arrows indicate upper limits measurements. The horizontal black arrow indicates the evolutionary stage (out of scale).

that of CH_3OH. In particular, recent observations suggest that the main precursor of formamide are H_2CO and NH_2 reacting in the gas phase (Codella et al. 2017, Barone et al. 2015 and references therein). On the other hand, the correlation existing between $HCOOCH_3$ and CH_3OCH_3 looks more intriguing: the abundances of the two species are similar within a factor 5, suggesting that they have to be related in both cold and warm environments. This is a strong evidence that methyl formate and dimethyl ether have a common precursor or one of the two is the precursor of the other, as alredy proposed in other works (Jaber et al. 2014, Brouillet et al. 2013, and references therein). For CH_3CHO and $HCOOCH_3$ we observe a decrease of a factor $\sim$ 20 and $\sim$ 70, respectively going from the early pre-stellar and protostaller stages to SVS13-A. On the other hand CH_3OCH_3 range from 0.05 in L1544, to 0.4 in IRAS16293-2422 and 8×10^{-4} in SVS13-A. These results seems to support the presence of gas-phase reactions at work on time scales of $\sim 10^4$–10^5 yr. Indeed, if all the iCOMs would be simply produced by desorption of grain mantles, we should observe roughly constant ratios relative to CH_3OH, presuming that the dust mantles composition is similar in the different sources.

We enphasise that all the comparisons between the sources have to be taken with a pinch of salt given we compare different works. These preliminary results have to be confirmed increasing the statistics with systematic observations of the chemical content of both Class 0 and (in particular) Class I objects.

6 Conclusions

The work of the thesis contributes to the overall effort to increase the observational studies of the chemical content in Solar-type protostars. As discussed in Chap. 1, molecular deuteration and iCOMs are of great importance in the study of protostellar regions. On the one hand deuterated species give the opportunity to recover the physical gas conditions in the pre-collapse phase. On the other hand, iCOMs are interesting because they constitute the smallest bricks to build up biotic matherial and they might have had a role in the emergence of life on Earth. Nevetheless, observations performed with single-dish antennas exist for very few sources and only a handful are at higher angular resolution (see e.g. Taquet et al. 2015). This prevents the elaboration of a firm and coherent picture. In this work (i) we improved the observational scenario with the analysis of deuterated species and iCOMs in the Class 0 source HH212, and (ii) we opened new laboratories to study how the chemical-physical properties evolves with time, as in the case of the Class I protostar SVS13-A.

6.1 Deuterium fractionation to shed light on the past

ALMA high angular resolution observations of the Class 0 source HH212 allow us to obtain the first measurements of methanol D/H on a Solar System scale. The comparison between the temperatures in Orion B and Perseus suggests that the derived D/H is related to the differences in the ambient gas temperature at the ices formation epoch. Interestingly the observed results are in good agreement

with the predictions on methanol deuteration in interstellar ices obtained using the GRAINOBLE astrochemical model (Taquet et al. 2012a, 2013, 2014). Our findings confirmed, once more, the power of deuterium fractionation in recovering the pre-stellar gas conditions; in addition we show the need to observe star forming regions in the different molecular clouds (such as Perseus, Taurus, Ophiucus, and Orion) to understand what is the role of the environment in the chemical differentiation.

6.2 On the nature of a hot corino

We detect and analyse deuterated water and iCOMs at high angular resolution (up to 0.″15) in the Class 0 HH212. Our work demonstrates that these tracers are more efficent than the classical molecular tracers (such as CO and SiO) for the imaging and kinematics of the very inner protostellar regions (below 100 au). One of the hypotesis is that the observed emission is originated by a disk wind or by slow shocks occurring at the centrifugal barrier (Sakai et al. 2017). In any case the recent observations with increasing angular resolution showed that the structure of the disk-outflow systems is far more complex than initially thought. The hot corinos, defined as the regions where the temperature is high enough (T $\geq$ 100 K) to trigger a rich chemistry, have been so far observed with a typical angular resolution of $\sim 1''$ (i.e. $\sim$ 230 au in Perseus). Here we indeed go beyond this frontier, tracing Solar System scales. One interesting point of the iCOMs images obtained using emission due to $^{13}CH_3OH$, CH_2DOH, HDO, and CH_3CHO, is the origin of the tilt of the red/blueshifted emission at low velocities ($\pm$ 1 km s^{-1} with respect to the systemic source velocity) in direction NE-SW. As we suggested in Chap. 4 it may be due to the interaction of a wind with the asymmetric cavity. An importante piece of the puzzle is provided by the inclination of the disk with respect to the line-of-sight ($\sim 4^\circ$). Considering this orientation, a further intriguing possibility could be infall motion toward the disk. In this case, the infalling material would present redshifted emission above the disk and blueshifted emission below the disk. When the infall motion is considered togheter with the rotation of the system/cloud, the redshifted emission of the infall would tend to be cancelled on the NW side above the disk plane that is blueshifted for the rotation. On the other hand, the blueshifted emission of the infall would tend to be cancelled

on the SE side below the disk plane that is redshifted for the rotation, giving in total the observed tilt. However, since we are observing the system so close to edge-on, any infalling velocity component is going to be projected at very small values ($\pm$ 0.2 km s^{-1}), maybe too small to produce a projected velocity shift of $\pm$ 1 km s^{-1} between the red and blue lobes. Whatever the answer is, we need a slow shock to produce the molecules we observe. A detailed modelling would be required to understand the complex kinematics observed towards the source. We are indeed working in synergy with the modelers of the LERMA-Paris node to start investigating these so far unexplored regimes of very high density and very low velocities.

To conclude our project shows that the chemical richness can also be used as unique tracer of kinematical components at work in the factory producing a Sun-like star, opening at the same time new questions on which are the dominating processes. Only future forthcoming ALMA and NOEMA data will possibly provide a final answer.

6.3 How chemistry evolves from the Class 0 to the Class I phase

The analysis of the Class I object SVS13-A provides us the opportunity to characterise the chemical content of a more evolved source, trying to determine a possible evolutionary trend in the comparison with Class 0 protostars. Even if the angular resolution of single-dish data is not enough to disentangle the protostellar components, the large number of lines provided by unbiased spectral surveys (such as ASAI) allows us to analyse the global chemical complexity in a source previously unexplored. More specifically, we detected several lines of deuterated formaldehyde and (for the first time) methanol obtaining reliable measurements of the organics D/H in a Class I object. This contributed to fill the gap between Class 0 objects and protoplanetary disks, associated with Class II-III objects, in the context of deuteration measurements (see Chap. 1). In SVS13-A the D/H is up to two orders of magnitude lower than the values measured in Class 0 sources located in the same star-forming region and observed using the same telescope. This is a first indication of a modified chemical content possibly due to the different evolution-

ary stages. Thanks to the wide observed bandwidth, we analysed several iCOMs such as H_2CCO, CH_3CHO, $HCOOCH_3$ and CH_3OCH_3, revealing for the first time a rich hot corino towards the source (see also López-Sepulcre et al. 2015, Codella et al. 2016a). Comparing the iCOMs abundances to H_2, SVS13-A appears to be as chemically rich as the observed Class 0 protostars. However, the ratio between iCOMs and methanol shows a different behaviour. [iCOMs]/[CH_3OH] decreases significantly (at least a factor 20) going from Class 0 to SVS13-A. Given methanol is a proxy of the material ejected in the gas-phase from dust grain mantles, a lower ratio indicates again a modified chemical content during the Class 0 $\rightarrow$ Class I evolutionary transition, plausibly due to gas-phase reactions. If confirmed, this would give us a further piece of information on how the protostellar chemical richness is inherited by a forming planetary system.

6.4 iCOMs abundances: new constraints and related limits

The low number of sources where iCOMs have been detected hampers our understanding on how these species are formed in the ISM. As reported in Chap. 1 two major theoretical routes of iCOMs formation are possible: on the grain surfaces or in the gas-phase. More likely, a combination of the two is at work, but their respective roles and the timescales involved are still hotly debated. The bulding of a solid and comprehensive theory requires: (1) the observations of a large number of lines to identify and properly derive the iCOMs abundances in each source; (2) the combination of single-dish and interferometer to obtain a complete picture, from the large envelope to the smallest scales comparable with the Solar System, and (3) a statistical approach obtained through the observations of several star-forming regions at the same angular scales.

1. The unprecedented results provided by ASAI, i.e. a large number of iCOMs detected through a large number of emission lines put severe constraints on the iCOMs relative abundances. A particular case is represented by methoxy (CH_3O) which, interestingly, is not detected in SVS13-A. More specifically, the derived CH_3O column density is $N_{\rm tot} \lesssim 5 \times 10^{14}$ cm^{-2}. This molecule has been recently proposed as a possible precursor of methyl

formate and dimethyl ether in gas-phase processes (Balucani et al. 2015). Given the high abundances of $HCOOCH_3$ ($N_{tot} \sim 12 \times 10^{15}$ cm^{-2}) and CH_3OCH_3 ($N_{tot} \sim 6 \times 10^{15}$ cm^{-2}), the present CH_3O non detection is indeed challenging the proposed gas formation routes (see 5.3.7). Chemical models should take into account that $[CH_3O]/[HCOOCH_3]<0.04$ and $[CH_3O]/[CH_3OCH_3]<0.09$. These values are not consistent with those predicted by Balucani et al. (2015) who reported $[CH_3O]/[HCOOCH_3]$ and $[CH_3O]/[CH_3OCH_3]$ larger than 1. However these models have been optimized for cold objects such as L1544 where indeed methoxy has been detected (Vastel et al. 2014, Jiménez-Serra et al. 2016). Clearly, the present observations imply a yet incomplete reaction network which need to be updated, especially for higher temperature as those probed in hot corinos. We are working in a close collaboration with the chemistry department of the Bologna and Perugia Universities as well as with Scuola Normale Superiore di Pisa to tackle this question.

2. In general, the measurements derived using single-dishes appears to be very different from that provided by high resolution interferometry. An instructive example is given by the recent ALMA project PILS (Protostellar Interferometric Line Survey: Jørgensen et al. 2016) which is providing a new census of iCOMs towards the Class 0 IRAS16293- 2422, improving the old one by TIMASSS (The IRAS16293-2422 millimeter and submillimeter spectral survey: Caux et al. 2011). These new observations at angular spatial resolution of 0.″5 (60 au at the source distance), shows $[CH_3CHO/CH_3OH]$ and $[HCOOCH_3]/[CH_3OH]$, lower down to one order of magnitude than what found with single-dish measurements. Moreover, recent observations revealed the presence of several iCOMs in comets Lovejoy and Hale-Bopp (e.g. Despois et al. 2005, Biver et al. 2015). The $HCOOCH_3$ and CH_3CHO abundance ratios are found to be fews $\times 10^{-2}$ (Biver et al. 2015), not so far from the abundances derived using ALMA in IRAS16293-2422 (Jørgensen et al. 2016), suggesting that the materials synthesized in the early stages of the Solar System formation has been preserved until nowadays. A further step ahead will be done with interferometric observations of a sample of sources in different evolutionary stages of the low-mass star forming process. This is needed to check the trends

found using single-dish data, verifying that the emission due to different iCOMs is really tracing the same gas within every source. Indeed it is not excluded that in a region like a hot corino where there is a huge temperature gradient, iCOMs can trace different regions. In conclusion, these findings definitely support a comparison based on interferometric observations which will minimise the uncertainties on the emitting source sizes of all the molecules involved in the analysis.

3. A final remark is dedicated to the fundamental need of a statistical approach. Data obtained so far are sparse and related to few objects. To properly compare the different environments and the different evolutionary stages we need systematic observations of a significant number of sources. Indeed, several large programs using interferometers have been carried out with this purpose, like SOLIS[1], a Large Project at IRAM-NOEMA aimed to image the iCOMs emission in a sample of Solar-type star forming regions in different evolutionary stages. In Chap. 7 the work in progress and the forthcoming projects related to this topic will be discussed.

[1] Seeds Of Life In Space (SOLIS), Codella et al. 2017, Fontani et al. 2017 and Chap. 7

7 Perspectives: the NOEMA-SOLIS revolution

The results of this thesis demonstrate not only the efficacy of interferometric observation in mapping the very inner regions of protostars using iCOMs (see Chap. 4), but also the utility of using single-dish observations to disclose the chemical complexity in sources chemically unexplored (see Chap. 5). Single-dishes are indeed powerful tools to unveil the chemical richness of young stellar objects thanks to the possibility of performing broad spectral line surveys of star forming regions. However, these observations are performed with typical beam sizes of 10″–30″, large enough to include several chemical/physical components around the protostellar objects. More specifically, whenever the source presents strong temperature and density gradients, like in the envelope and in the hot-corino regions of a young protostars, the filling factor of the emission becomes smaller with increasing exitation conditions. This effect can be taken into account tring to fit separately multiple components in the rotation diagram analysis, as we explained in Sec. 5.2.6. Nevetheless interferometric follow-ups are fundamental to disentagle all the different components of the emitting sources and to determine exactly their size. This will be necessary not only to dermine more accurately the abundances of the detected iCOMs and the deuterated species but also to map their spatial distribution in order to put strong constraints on their formation and destruction routes.

In order to answer some of these open questions our group, in Arcetri, is deeply involved in the SOLIS (*Seeds Of Life In Space*) Large Program at the IRAM-NOEMA interferometer, with P.I. C. Ceccarelli (IPAG-France) & P. Caselli

(MPE-Germany). The fundamental goal of this long-term project, started in 2016, is to obtain 1mm and 3mm observations of five key iCOMs in 7 targets representatives of all the different evolutionary stages of a Sun-like system, going from the prestellar cores, to Class 0 and Class I sources in addition to a protostellar shocked region. Typical angular resolution are $\leq 1''$ (1mm) and $\sim 4''$–$5''$ (3mm). The selected iCOMs are: methoxy (CH_3O), methanol (CH_3OH), dimethyl ether (CH_3OCH_3), methyl formate ($HCOOCH_3$) and formamide (NH_2HCO). These species have the advantage of being abundant in both cold and warm environments and/or they will allow us to discriminate between the different formation pathways, such as grain-surface versus gas-phase chemistry. In addition, the diversity of the source sample will enable to analyse for the first time methodically how the chemical content arises and evolves in the different stages of the star-formation process. Indeed the biggest limitation of the existing observations is that they are sparse and difficult to compare. On the other hand SOLIS will provide a homogeneous dataset for all the sources which will be properly compared. A number of papers exploiting the SOLIS datasets for single targets have been recently published or submitted (see Fontani et al. 2017, Codella et al. 2017, Ceccarelli et al. 2017, in preparation, and Punanova et al. 2017, in preparation).

An example of the potential of the SOLIS observations is presented by Codella et al. (2017) which exploited the dataset of the protostellar shocked region L1157-B1. The source has been extensively studied, being a unique laboratory to investigate the chemistry associated to the interaction of a jet-induced shock with the surrounding gas. More specifically, L1157-mm is a Class 0 protostar (d = 250 pc) driven a precessing, episodic jet (Gueth et al. 1996, Podio et al. 2016). The jet has excavated two main cavities, with apices called B1 and B2 (see Fig. 7.1). B1 itself consists of a series of shocks caused by different episodes of ejection impacting against the cavity wall (Podio et al. 2016), the oldest of which (kinematical age $\simeq$ 1100 yr) is also the farthest away from the source. The study of the L1157-B1 region is strategic because the protostar is 0.08 pc away, so that the heating is produced only by the shock and we can study the species injected into the gas phase straight after the sputtering of the icy dust mantles (Bachiller et al. 2001).

As part of my involment in SOLIS I reduced the L1157-B1 data at the IRAM headquarters in Grenoble (France) in April 2016. The unprecedented high angular resolution SOLIS observations of formamide in the region provided direct

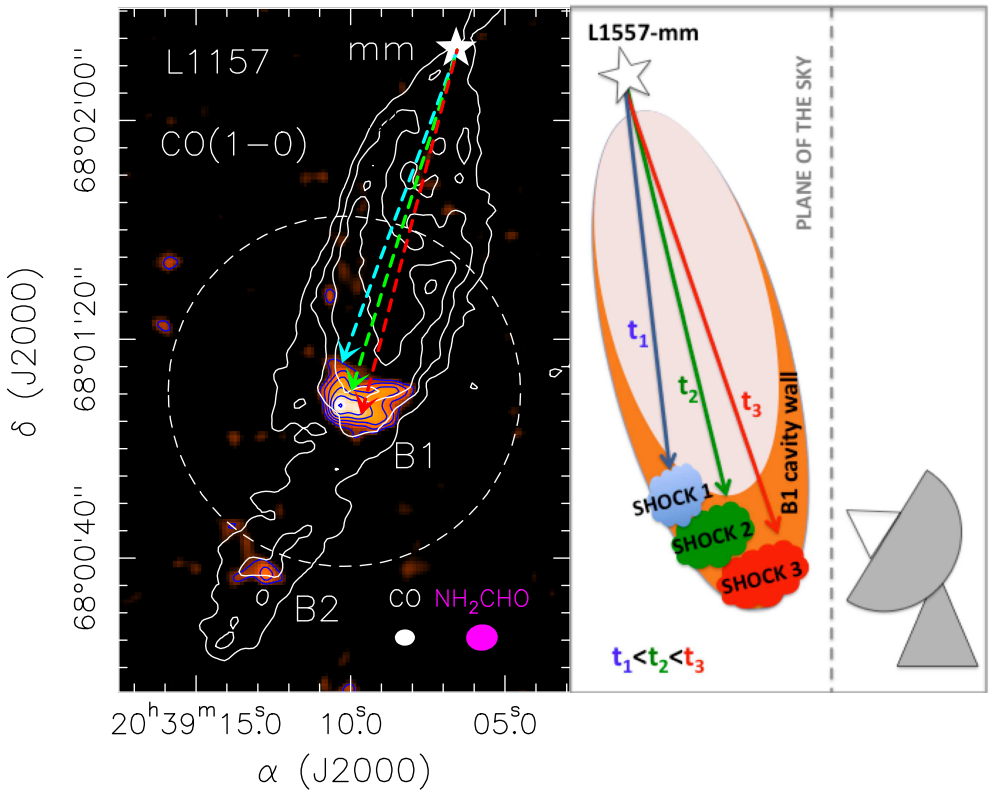

Figure 7.1: Figure from Codella et al. (2017). *Left panel:* The L1157 southern blueshifted lobe in CO (1–0) (white contours; Gueth et al. 1996). The precessing jet ejected by the central object L1157-mm (white star) excavated two cavities, with apices B1 and B2, respectively. The maps are centred at $\Delta\alpha$ = +25″ and $\Delta\delta$ = –63.″5 from L1157-mm. The emission map of the NH_2CHO ($4_{1,4}$–$3_{1,3}$) line is shown by the colour image. For the CO image, the first contour and step are 6σ (1σ = 0.5 Jy beam^{-1} km s^{-1}) and 4σ, respectively. The first contour and step of the NH_2CHO map correspond to 3σ (15 mJy beam^{-1} km s^{-1}) and 1σ, respectively. The dashed circle shows the primary beam of the NH_2CHO image (64″). The magenta and white ellipses depict the synthesised beams of the NH_2CHO (5.″79 × 4.″81, PA = –94°) and CO (3.″65 × 2.″96, PA=+88°) observations, respectively. The three dashed arrows indicate the directions (projected on the plane of the sky) of the episodic jet producing the shocks. *Right panel:* sketch of the L1157-B1 system, showing the three episodic shocks.

evidence of the formation in gas-phase of this fundamental iCOM (Codella et al. 2017). The first high spatial resolution NH_2CHO image in L1157-B1 has been reported and compared with the spatial distribution of other key species (see Fig. 7.2). In particular, Fig. 7.2 shows in the left panel that the formamide emission does not coincide with that from H_2CO and SiO, but only covers the southern portion of the B1 structure. Moreover, Fig. 7.2 (middle panel) shows the acetaldehyde (CH_3CHO; Codella et al. 2015) distribution which is mostly associated with the northern portion of B1. When considering in particular the distribution of these two species, three different zones can be identified: SHOCK 1 (the northern and youngest one, where only acetaldehyde emits); SHOCK 2 (an intermediate zone, where both formamide and acetaldehyde are present); SHOCK 3 (the southern and oldest region, where only formamide emits). The chemical modelling of the source (Codella et al. 2017) suggested that the formamide formation is dominated in L1157-B1 by gas-phase reactions involving species previously hydrogenated on the grain surfaces (Barone et al. 2015 and references therein). This also explains why the formamide abundance peaks where the acetaldehyde abundance has already started to decrease. These new observations togheter with the recent detection of iCOMs in cold objects (e.g. Vastel et al. 2014), challenge the pure grain-surface chemistry paradigm (e.g. Vasyunin & Herbst 2013) and add evidence that gas-phase chemistry plays an important role in the iCOMs formation. These results highlights the potentiality of SOLIS to improve dramatically our understanding of iCOMs formation and evolution, once the whole dataset will be analysed. After the PhD project, I will move to IPAG[1] to further work on the SOLIS data, starting from the exploitation of the SVS13-A observations.

[1] Institut de planétologie et d'astrophysique de Grenoble, France

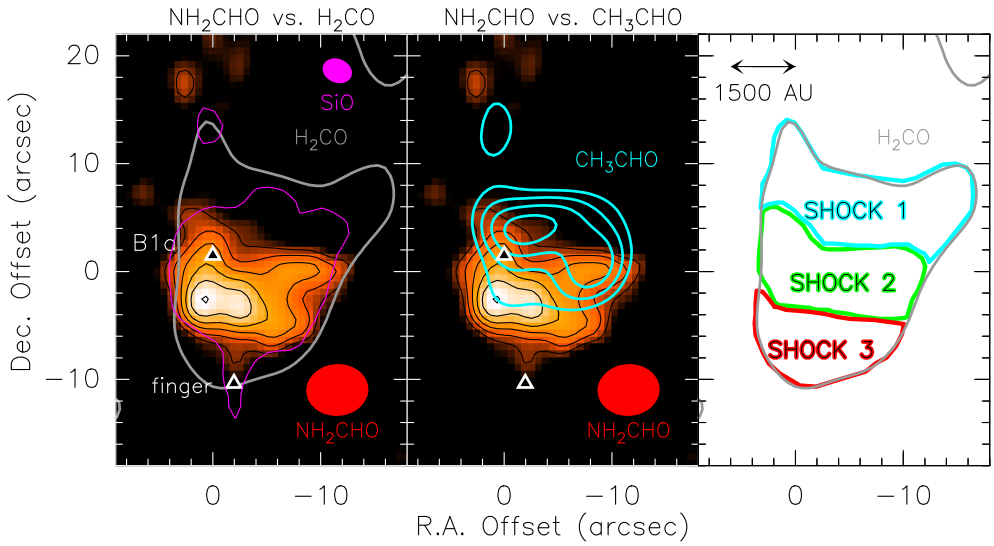

Figure 7.2: Figure from Codella et al. (2017) which shows the chemical segregation in L1157-B1. The maps are centred at: α(J2000) = $20^h\ 39^m\ 09\overset{s}{.}5$, δ(J2000) = +68° 01′ 10.″0. *Left panel:* p-H_2CO ($2_{0,2}$–$1_{0,1}$) integrated emission (grey), and SiO (2–1) (magenta) at low-velocity (less than –10 km s^{-1} with respect to v_{sys}) on top of the present NH_2CHO line emission map (colour image, black contours). For clarity, for the H_2CO and SiO images, only the 3σ (1σ = 3.3 mJy beam^{-1} km s^{-1} and 50 mJy beam^{-1} km s^{-1} for H_2CO and SiO, respectively) contour is reported to show the overall B1 structure. The northern triangle at "B1a" identifies the youngest position in B1, where the precessing jet driven by L1157-mm impacts the cavity wall while the southern triangle denotes the position of the oldest shock, which is identified by the so-called "finger" feature traced by SiO at low-velocity. The H_2CO image is smoothed to the same angular resolution (red ellipse) of the NH_2CHO ($4_{1,4}$–$3_{1,3}$) line data. The synthesised beam of the SiO is: 2.″8 × 2.″2, PA = 56°. *Middle panel:* Same as in the left panel for the CH_3CHO ($7_{0,7}$–$6_{0,6}$ E+A) velocity-integrated emission (cyan contours; also smoothed to the same beam of the NH_2CHO map; first contour and step correspond to 3σ, 4 mJy beam^{-1} km s^{-1}, and 1σ, respectively). *Right panel:* Sketch of the three zones identified from the spatial distribution of formamide and acetaldehyde: SHOCK 1 (blue), the northern region, where CH_3CHO (and not NH_2CHO) is detected; SHOCK 2 (green), where both CH_3CHO and NH_2CHO are detected; and SHOCK 3 (red), the southern region, where only NH_2CHO (and not CH_3CHO) is detected. Time increases and chemistry evolves going from SHOCK 1 to SHOCK 3 (see arrows in Fig. 7.1).

References

[**André et al. 2014**] P. André, J. Di Francesco, D. Ward-Thompson, S.-I. Inutsuka, R. E. Pudritz & J. E. Pineda, 'From Filamentary Networks to Dense Cores in Molecular Clouds: Toward a New Paradigm for Star Formation'. *Protostars and Planets VI*, 2014, pages 27–51, doi:10.2458/azu_uapress_9780816531240-ch002, 1312.6232.

[**André et al. 1993**] P. André, D. Ward-Thompson & M. Barsony, 'Submillimeter continuum observations of Rho Ophiuchi A - The candidate protostar VLA 1623 and prestellar clumps'. *ApJ*, March 1993, volume 406, 122–141, doi:10.1086/172425.

[**Anglada et al. 2000**] G. Anglada, L. F. Rodríguez & J. M. Torrelles, 'Discovery of a Subarcsecond Radio Binary Associated with the SVS 13 Star in the HH 7-11 Region'. *ApJLett*, October 2000, volume 542, L123–L126, doi:10.1086/312933.

[**Arce et al. 2008**] H. G. Arce, J. Santiago-García, J. K. Jørgensen, M. Tafalla & R. Bachiller, 'Complex Molecules in the L1157 Molecular Outflow'. *ApJLett*, July 2008, volume 681, L21, doi:10.1086/590110, 0805.2550.

[**Bachiller & Cernicharo 1986**] R. Bachiller & J. Cernicharo, 'The relation between carbon monoxide emission and visual extinction in the local Perseus dark clouds'. *A&A*, September 1986, volume 166, 283–290.

[**Bachiller et al. 1998**] R. Bachiller, S. Guilloteau, F. Gueth, M. Tafalla, A. Dutrey, C. Codella & A. Castets, 'A molecular jet from SVS 13B near HH 7-11'. *A&A*, November 1998, volume 339, L49–L52.

[**Bachiller et al. 2001**] R. Bachiller, M. Pérez Gutiérrez, M. S. N. Kumar & M. Tafalla, 'Chemically active outflow L 1157'. *A&A*, June 2001, volume 372, 899–912, doi:10.1051/0004-6361:20010519.

[**Bacmann et al. 2003**] A. Bacmann, B. Lefloch, C. Ceccarelli, J. Steinacker, A. Castets & L. Loinard, 'CO Depletion and Deuterium Fractionation in Prestellar Cores'. *ApJLett*, March 2003, volume 585, L55–L58, doi:10.1086/374263, astro-ph/0301651.

[**Bacmann et al. 2012**] A. Bacmann, V. Taquet, A. Faure, C. Kahane & C. Ceccarelli, 'Detection of complex organic molecules in a prestellar core: a new challenge for astrochemical models'. *A&A*, May 2012, volume 541, L12, doi:10.1051/0004-6361/201219207.

[**Bally et al. 2008**] J. Bally, J. Walawender, D. Johnstone, H. Kirk & A. Goodman, *The Perseus Cloud*, page 308 (2008).

[**Balucani et al. 2015**] N. Balucani, C. Ceccarelli & V. Taquet, 'Formation of complex organic molecules in cold objects: the role of gas-phase reactions'. *MNRAS*, April 2015, volume 449, L16–L20, doi:10.1093/mnrasl/slv009, 1501.03668.

[**Barone et al. 2015**] V. Barone, C. Latouche, D. Skouteris, F. Vazart, N. Balucani, C. Ceccarelli & B. Lefloch, 'Gas-phase formation of the prebiotic molecule formamide: insights from new quantum computations'. *MNRAS*, October 2015, volume 453, L31–L35, doi:10.1093/mnrasl/slv094, 1507.03741.

[**Belloche et al. 2016**] A. Belloche, H. S. P. Müller, R. T. Garrod & K. M. Menten, 'Exploring molecular complexity with ALMA (EMoCA): Deuterated complex organic molecules in Sagittarius B2(N2)'. *A&A*, March 2016, volume 587, A91, doi:10.1051/0004-6361/201527268, 1511.05721.

[**Bennett & Kaiser 2007**] C. J. Bennett & R. I. Kaiser, 'On the Formation of Glycolaldehyde ($HCOCH_2OH$) and Methyl Formate ($HCOOCH_3$) in Interstellar Ice Analogs'. *ApJ*, June 2007, volume 661, 899–909, doi:10.1086/516745.

[**Bergner et al. 2017**] J. B. Bergner, K. I. Öberg, R. T. Garrod & D. M. Graninger, 'Complex Organic Molecules toward Embedded Low-mass Protostars'. *ApJ*, June 2017, volume 841, 120, doi:10.3847/1538-4357/aa72f6, 1705.05338.

[**Bianchi et al. 2017a**] E. Bianchi, C. Codella, C. Ceccarelli, F. Fontani, L. Testi, R. Bachiller, B. Lefloch, L. Podio & V. Taquet, 'Decrease of the organic deuteration during the evolution of Sun-like protostars: the case of SVS13-A'. *MNRAS*, May 2017a, volume 467, 3011–3023, doi:10.1093/mnras/stx252, 1701.08656.

[**Bianchi et al. 2017b**] E. Bianchi, C. Codella, C. Ceccarelli, V. Taquet, S. Cabrit, F. Bacciotti, R. Bachiller, E. Chapillon, F. Gueth, A. Gusdorf, B. Lefloch, S. Leurini, L. Podio, K. L. J. Rygl, B. Tabone & M. Tafalla, 'Deuterated methanol on Solar System scale around the HH212 protostar'. *ArXiv e-prints*, September 2017b, 1709.04726.

[**Biver et al. 2015**] N. Biver, D. Bockelée-Morvan, R. Moreno, J. Crovisier, P. Colom, D. C. Lis, A. Sandqvist, J. Boissier, D. Despois & S. N. Milam, 'Ethyl alcohol and sugar in comet C/2014 Q2 (Lovejoy)'. *Science Advances*, October 2015, volume 1, 1500863, doi:10.1126/sciadv.1500863.

[**Bizzocchi et al. 2014**] L. Bizzocchi, P. Caselli, S. Spezzano & E. Leonardo, 'Deuterated methanol in the pre-stellar core L1544'. *A&A*, September 2014, volume 569, A27, doi:10.1051/0004-6361/201423858, 1408.2491.

[**Bottinelli et al. 2004**] S. Bottinelli, C. Ceccarelli, B. Lefloch, J. P. Williams, A. Castets, E. Caux, S. Cazaux, S. Maret, B. Parise & A. G. G. M. Tielens, 'Complex Molecules in the Hot Core of the Low-Mass Protostar NGC 1333 IRAS 4A'. *ApJ*, November 2004, volume 615, 354–358, doi:10.1086/423952, astro-ph/0407154.

[**Bottinelli et al. 2007**] S. Bottinelli, C. Ceccarelli, J. P. Williams & B. Lefloch, 'Hot corinos in NGC 1333-IRAS4B and IRAS2A'. *A&A*, February 2007, volume 463, 601–610, doi:10.1051/0004-6361:20065139, astro-ph/0611480.

[**Brouillet et al. 2013**] N. Brouillet, D. Despois, A. Baudry, T.-C. Peng, C. Favre, A. Wootten, A. J. Remijan, T. L. Wilson, F. Combes & G. Wlodarczak, 'CH_3OCH_3 in Orion-KL: a striking similarity with $HCOOCH_3$'. *A&A*, February 2013, volume 550, A46, doi:10.1051/0004-6361/201219983, 1212.4531.

[**Brown et al. 1975**] R. D. Brown, J. G. Crofts, P. D. Godfrey, F. F. Gardner, B. J. Robinson & J. B. Whiteoak, 'Discovery of interstellar methyl formate'. *ApJLett*, April 1975, volume 197, L29–L31, doi:10.1086/181769.

[**Burke & Brown 2010**] D. J. Burke & W. A. Brown, 'Ice in space: surface science investigations of the thermal desorption of model interstellar ices on dust grain analogue surfaces'. *Physical Chemistry Chemical Physics (Incorporating Faraday Transactions)*, 2010, volume 12, 5947, doi:10.1039/b917005g.

[**Cabrit et al. 2012**] S. Cabrit, C. Codella, F. Gueth & A. Gusdorf, 'High SiO abundance in the HH212 protostellar jet'. *A&A*, December 2012, volume 548, L2, doi:10.1051/0004-6361/201219784, 1211.1258.

[**Cabrit et al. 2007**] S. Cabrit, C. Codella, F. Gueth, B. Nisini, A. Gusdorf, C. Dougados & F. Bacciotti, 'PdBI sub-arcsecond study of the SiO microjet in HH212. Origin and collimation of class 0 jets'. *A&A*, June 2007, volume 468, L29–L32, doi:10.1051/0004-6361:20077387, 0704.2685.

[**Caselli & Ceccarelli 2012**] P. Caselli & C. Ceccarelli, 'Our astrochemical heritage'. *A&A Rev.*, October 2012, volume 20, 56, doi:10.1007/s00159-012-0056-x, 1210.6368.

[**Caselli et al. 1999**] P. Caselli, C. M. Walmsley, M. Tafalla, L. Dore & P. C. Myers, 'CO Depletion in the Starless Cloud Core L1544'. *ApJLett*, October 1999, volume 523, L165–L169, doi:10.1086/312280.

[**Caselli et al. 2002**] P. Caselli, C. M. Walmsley, A. Zucconi, M. Tafalla, L. Dore & P. C. Myers, 'Molecular Ions in L1544. I. Kinematics'. *ApJ*, January 2002, volume 565, 331–343, doi:10.1086/324301, astro-ph/0109021.

[**Caux et al. 2011**] E. Caux, C. Kahane, A. Castets, A. Coutens, C. Ceccarelli, A. Bacmann, S. Bisschop, S. Bottinelli, C. Comito, F. P. Helmich, B. Lefloch, B. Parise, P. Schilke, A. G. G. M. Tielens, E. van Dishoeck, C. Vastel, V. Wakelam & A. Walters, 'TIMASSS: the IRAS 16293-2422 millimeter and submillimeter spectral survey. I. Observations, calibration, and analysis of the line kinematics'. *A&A*, August 2011, volume 532, A23, doi:10.1051/0004-6361/201015399, 1103.5347.

[**Cazaux et al. 2003**] S. Cazaux, A. G. G. M. Tielens, C. Ceccarelli, A. Castets, V. Wakelam, E. Caux, B. Parise & D. Teyssier, 'The Hot Core around the Low-mass Protostar IRAS 16293-2422: Scoundrels Rule!' *ApJLett*, August 2003, volume 593, L51–L55, doi:10.1086/378038.

[**Ceccarelli et al. 2014**] C. Ceccarelli, P. Caselli, D. Bockelée-Morvan, O. Mousis, S. Pizzarello, F. Robert & D. Semenov, 'Deuterium Fractionation: The Ariadne's Thread from the Precollapse Phase to Meteorites and Comets Today'. *Protostars and Planets VI*, 2014, pages 859–882, doi:10.2458/azu_uapress_9780816531240-ch037, 1403.7143.

[**Ceccarelli et al. 2007**] C. Ceccarelli, P. Caselli, E. Herbst, A. G. G. M. Tielens & E. Caux, 'Extreme Deuteration and Hot Corinos: The Earliest Chemical Signatures of Low-Mass Star Formation'. *Protostars and Planets V*, 2007, pages 47–62, astro-ph/0603018.

[**Ceccarelli et al. 1998**] C. Ceccarelli, A. Castets, L. Loinard, E. Caux & A. G. G. M. Tielens, 'Detection of doubly deuterated formaldehyde towards the low-luminosity protostar IRAS 16293-2422'. *A&A*, October 1998, volume 338, L43–L46.

[**Ceccarelli et al. 2001**] C. Ceccarelli, L. Loinard, A. Castets, A. G. G. M. Tielens, E. Caux, B. Lefloch & C. Vastel, 'Extended D_2CO emission: The smoking gun of grain surface-chemistry'. *A&A*, June 2001, volume 372, 998–1004, doi:10.1051/0004-6361:20010559.

[**Ceccarelli et al. 2003**] C. Ceccarelli, S. Maret, A. G. G. M. Tielens, A. Castets & E. Caux, 'Theoretical H_2CO emission from protostellar envelopes'. *A&A*, November 2003, volume 410, 587–595, doi:10.1051/0004-6361:20031243, astro-ph/0506144.

[**Cernicharo et al. 2012**] J. Cernicharo, N. Marcelino, E. Roueff, M. Gerin, A. Jiménez-Escobar & G. M. Muñoz Caro, 'Discovery of the Methoxy Radical, CH_3O, toward B1: Dust Grain and Gas-phase Chemistry in Cold Dark Clouds'. *ApJLett*, November 2012, volume 759, L43, doi:10.1088/2041-8205/759/2/L43.

[**Charnley et al. 1992**] S. B. Charnley, A. G. G. M. Tielens & T. J. Millar, 'On the molecular complexity of the hot cores in Orion A - Grain surface chemistry as 'The last refuge of the scoundrel''. *ApJLett*, November 1992, volume 399, L71–L74, doi:10.1086/186609.

[**Charnley et al. 1997**] S. B. Charnley, A. G. G. M. Tielens & S. D. Rodgers, 'Deuterated Methanol in the Orion Compact Ridge'. *ApJLett*, June 1997, volume 482, L203–L206, doi:10.1086/310697.

[**Chen et al. 2009**] X. Chen, R. Launhardt & T. Henning, 'IRAM-PdBI Observations of Binary Protostars. I. The Hierarchical System SVS 13 in NGC 1333'. *ApJ*, February 2009, volume 691, 1729–1737, doi:10.1088/0004-637X/691/2/1729, 0810.1712.

[**Chini et al. 1997**] R. Chini, B. Reipurth, A. Sievers, D. Ward-Thompson, C. G. T. Haslam, E. Kreysa & R. Lemke, 'Cold dust around Herbig-Haro energy sources: morphology and new protostellar candidates.' *A&A*, September 1997, volume 325, 542–550.

[**Claussen et al. 1998**] M. J. Claussen, K. B. Marvel, A. Wootten & B. A. Wilking, 'Distribution and Motion of the Water Masers near IRAS 05413-0104'. *ApJLett*, November 1998, volume 507, L79–L82, doi:10.1086/311669.

[**Codella et al. 1999**] C. Codella, R. Bachiller & B. Reipurth, 'Low and high velocity SiO emission around young stellar objects'. *A&A*, March 1999, volume 343, 585–598.

[**Codella et al. 2007**] C. Codella, S. Cabrit, F. Gueth, R. Cesaroni, F. Bacciotti, B. Lefloch & M. J. McCaughrean, 'A highly-collimated SiO jet in the HH212 protostellar outflow'. *A&A*, February 2007, volume 462, L53–L56, doi:10.1051/0004-6361:20066800, astro-ph/0612482.

[**Codella et al. 2014**] C. Codella, S. Cabrit, F. Gueth, L. Podio, S. Leurini, R. Bachiller, A. Gusdorf, B. Lefloch, B. Nisini, M. Tafalla & W. Yvart, 'The ALMA view of the protostellar

system HH212. The wind, the cavity, and the disk'. *A&A*, August 2014, volume 568, L5, doi:10.1051/0004-6361/201424103, 1407.6229.

[**Codella et al. 2016a**] C. Codella, C. Ceccarelli, E. Bianchi, L. Podio, R. Bachiller, B. Lefloch, F. Fontani, V. Taquet & L. Testi, 'Hot and dense water in the inner 25 au of SVS13-A'. *MNRAS*, October 2016a, volume 462, L75–L79, doi:10.1093/mnrasl/slw127, 1606.06847.

[**Codella et al. 2016b**] C. Codella, C. Ceccarelli, S. Cabrit, F. Gueth, L. Podio, R. Bachiller, F. Fontani, A. Gusdorf, B. Lefloch, S. Leurini & M. Tafalla, 'Water and acetaldehyde in HH212: The first hot corino in Orion'. *A&A*, February 2016b, volume 586, L3, doi:10.1051/0004-6361/201527424, 1601.00539.

[**Codella et al. 2017**] C. Codella, C. Ceccarelli, P. Caselli, N. Balucani, V. Barone, F. Fontani, B. Lefloch, L. Podio, S. Viti, S. Feng, R. Bachiller, E. Bianchi, F. Dulieu, I. Jiménez-Serra, J. Holdship et al., 'Seeds of Life in Space (SOLIS). II. Formamide in protostellar shocks: Evidence for gas-phase formation'. *A&A*, September 2017, volume 605, L3, doi:10.1051/0004-6361/201731249, 1708.04663.

[**Codella et al. 2012**] C. Codella, C. Ceccarelli, B. Lefloch, F. Fontani, G. Busquet, P. Caselli, C. Kahane, D. Lis, V. Taquet, M. Vasta, S. Viti & L. Wiesenfeld, 'The Herschel and IRAM CHESS Spectral Surveys of the Protostellar Shock L1157-B1: Fossil Deuteration'. *ApJLett*, September 2012, volume 757, L9, doi:10.1088/2041-8205/757/1/L9.

[**Codella et al. 2015**] C. Codella, F. Fontani, C. Ceccarelli, L. Podio, S. Viti, R. Bachiller, M. Benedettini & B. Lefloch, 'Astrochemistry at work in the L1157-B1 shock: acetaldehyde formation'. *MNRAS*, April 2015, volume 449, L11–L15, doi:10.1093/mnrasl/slu204, 1412.8318.

[**Codella et al. 2010**] C. Codella, B. Lefloch, C. Ceccarelli, J. Cernicharo, E. Caux, A. Lorenzani, S. Viti, P. Hily-Blant, B. Parise, S. Maret, B. Nisini, P. Caselli, S. Cabrit, L. Pagani, M. Benedettini et al., 'The CHESS spectral survey of star forming regions: Peering into the protostellar shock L1157-B1. I. Shock chemical complexity'. *A&A*, July 2010, volume 518, L112, doi:10.1051/0004-6361/201014582, 1006.1864.

[**Davis et al. 2000**] C. J. Davis, A. Berndsen, M. D. Smith, A. Chrysostomou & J. Hobson, 'High-resolution near-infrared observations of Herbig-Haro flows - II. Echelle spectroscopy'. *MNRAS*, May 2000, volume 314, 241–255, doi:10.1046/j.1365-8711.2000.03305.x.

[**De Simone et al. 2017**] M. De Simone, C. Codella, L. Testi, A. Belloche, A. J. Maury, S. Anderl, P. André, S. Maret & L. Podio, 'Glycolaldehyde in Perseus young solar analogs'. *A&A*, March 2017, volume 599, A121, doi:10.1051/0004-6361/201630049, 1701.00724.

[**Despois et al. 2005**] D. Despois, N. Biver, D. Bockelée-Morvan & J. Crovisier, 'Observations of Molecules in Comets'. In D. C. Lis, G. A. Blake & E. Herbst, editors, *Astrochemistry: Recent Successes and Current Challenges*, volume 231 of *IAU Symposium* (2005) pages 469–478, doi:10.1017/S1743921306007484.

[**Dubernet et al. 2013**] M.-L. Dubernet, M. H. Alexander, Y. A. Ba, N. Balakrishnan, C. Balança, C. Ceccarelli, J. Cernicharo, F. Daniel, F. Dayou, M. Doronin, F. Dumouchel, A. Faure,

N. Feautrier, D. R. Flower, A. Grosjean et al., 'BASECOL2012: A collisional database repository and web service within the Virtual Atomic and Molecular Data Centre (VAMDC)'. *A&A*, May 2013, volume 553, A50, doi:10.1051/0004-6361/201220630.

[**Ehrenfreund & Charnley 2000**] P. Ehrenfreund & S. B. Charnley, 'Organic Molecules in the Interstellar Medium, Comets, and Meteorites: A Voyage from Dark Clouds to the Early Earth'. *ARA&A*, 2000, volume 38, 427–483, doi:10.1146/annurev.astro.38.1.427.

[**Enrique-Romero et al. 2016**] J. Enrique-Romero, A. Rimola, C. Ceccarelli & N. Balucani, 'The (impossible?) formation of acetaldehyde on the grain surfaces: insights from quantum chemical calculations'. *MNRAS*, June 2016, volume 459, L6–L10, doi:10.1093/mnrasl/slw031, 1603.09096.

[**Evans et al. 2009**] N. J. Evans, II, M. M. Dunham, J. K. Jørgensen, M. L. Enoch, B. Merín, E. F. van Dishoeck, J. M. Alcalá, P. C. Myers, K. R. Stapelfeldt, T. L. Huard, L. E. Allen, P. M. Harvey, T. van Kempen, G. A. Blake, D. W. Koerner, L. G. Mundy, D. L. Padgett & A. I. Sargent, 'The Spitzer c2d Legacy Results: Star-Formation Rates and Efficiencies; Evolution and Lifetimes'. *ApJS*, April 2009, volume 181, 321-350, doi:10.1088/0067-0049/181/2/321, 0811.1059.

[**Faure et al. 2012**] A. Faure, L. Wiesenfeld, Y. Scribano & C. Ceccarelli, 'Rotational excitation of mono- and doubly-deuterated water by hydrogen molecules'. *MNRAS*, February 2012, volume 420, 699–704, doi:10.1111/j.1365-2966.2011.20081.x.

[**Ferreira et al. 2006**] J. Ferreira, C. Dougados & S. Cabrit, 'Which jet launching mechanism(s) in T Tauri stars?' *A&A*, July 2006, volume 453, 785–796, doi:10.1051/0004-6361:20054231, astro-ph/0604053.

[**Flower et al. 2006**] D. R. Flower, G. Pineau Des Forêts & C. M. Walmsley, 'The importance of the ortho:para H_2 ratio for the deuteration of molecules during pre-protostellar collapse'. *A&A*, April 2006, volume 449, 621–629, doi:10.1051/0004-6361:20054246, astro-ph/0601429.

[**Fontani et al. 2017**] F. Fontani, C. Ceccarelli, C. Favre, P. Caselli, R. Neri, I. R. Sims, C. Kahane, F. O. Alves, N. Balucani, E. Bianchi, E. Caux, A. Jaber Al-Edhari, A. Lopez-Sepulcre, J. E. Pineda, R. Bachiller et al., 'Seeds of Life in Space (SOLIS). I. Carbon-chain growth in the Solar-type protocluster OMC2-FIR4'. *A&A*, September 2017, volume 605, A57, doi:10.1051/0004-6361/201730527, 1707.01384.

[**Fontani et al. 2014**] F. Fontani, C. Codella, C. Ceccarelli, B. Lefloch, S. Viti & M. Benedettini, 'The L1157-B1 Astrochemical Laboratory: Measuring the True Formaldehyde Deuteration on Grain Mantles'. *ApJLett*, June 2014, volume 788, L43, doi:10.1088/2041-8205/788/2/L43.

[**Frank et al. 2014**] A. Frank, T. P. Ray, S. Cabrit, P. Hartigan, H. G. Arce, F. Bacciotti, J. Bally, M. Benisty, J. Eislöffel, M. Güdel, S. Lebedev, B. Nisini & A. Raga, 'Jets and Outflows from Star to Cloud: Observations Confront Theory'. *Protostars and Planets VI*, 2014, pages 451–474, doi:10.2458/azu_uapress_9780816531240-ch020, 1402.3553.

[**Fuente et al. 2014**] A. Fuente, J. Cernicharo, P. Caselli, C. McCoey, D. Johnstone, M. Fich, T. van Kempen, A. Palau, U. A. Yıldız, B. Tercero & A. López, 'The hot core towards the

intermediate-mass protostar NGC 7129 FIRS 2. Chemical similarities with Orion KL'. *A&A*, August 2014, volume 568, A65, doi:10.1051/0004-6361/201323074, 1405.4639.

[**Garrod & Herbst 2006**] R. T. Garrod & E. Herbst, 'Formation of methyl formate and other organic species in the warm-up phase of hot molecular cores'. *A&A*, October 2006, volume 457, 927–936, doi:10.1051/0004-6361:20065560, astro-ph/0607560.

[**Gerin et al. 2015**] M. Gerin, J. Pety, A. Fuente, J. Cernicharo, B. Commerçon & N. Marcelino, 'Nascent bipolar outflows associated with the first hydrostatic core candidates Barnard 1b-N and 1b-S'. *A&A*, May 2015, volume 577, L2, doi:10.1051/0004-6361/201525777, 1504.06648.

[**Goldsmith & Langer 1999**] P. F. Goldsmith & W. D. Langer, 'Population Diagram Analysis of Molecular Line Emission'. *ApJ*, May 1999, volume 517, 209–225, doi:10.1086/307195.

[**Graninger et al. 2016**] D. M. Graninger, O. H. Wilkins & K. I. Öberg, 'Carbon Chains and Methanol toward Embedded Protostars'. *ApJ*, March 2016, volume 819, 140, doi:10.3847/0004-637X/819/2/140, 1602.01472.

[**Grossman et al. 1987**] E. N. Grossman, C. R. Masson, A. I. Sargent, N. Z. Scoville, S. Scott & D. P. Woody, 'A possible protostar near HH 7-11'. *ApJ*, September 1987, volume 320, 356–363, doi:10.1086/165549.

[**Gueth et al. 1996**] F. Gueth, S. Guilloteau & R. Bachiller, 'A precessing jet in the L1157 molecular outflow.' *A&A*, March 1996, volume 307, 891–897.

[**Guillet et al. 2011**] V. Guillet, G. Pineau Des Forêts & A. P. Jones, 'Shocks in dense clouds. III. Dust processing and feedback effects in C-type shocks'. *A&A*, March 2011, volume 527, A123, doi:10.1051/0004-6361/201015973.

[**Guilloteau et al. 2006**] S. Guilloteau, V. Piétu, A. Dutrey & M. Guélin, 'Deuterated molecules in DM Tauri: DCO^+, but no HDO'. *A&A*, March 2006, volume 448, L5–L8, doi:10.1051/0004-6361:200600005, astro-ph/0602396.

[**Gutermuth et al. 2008**] R. A. Gutermuth, P. C. Myers, S. T. Megeath, L. E. Allen, J. L. Pipher, J. Muzerolle, A. Porras, E. Winston & G. Fazio, 'Spitzer Observations of NGC 1333: A Study of Structure and Evolution in a Nearby Embedded Cluster'. *ApJ*, February 2008, volume 674, 336-356, doi:10.1086/524722, 0710.1860.

[**Hasegawa & Herbst 1993**] T. I. Hasegawa & E. Herbst, 'Three-Phase Chemical Models of Dense Interstellar Clouds - Gas Dust Particle Mantles and Dust Particle Surfaces'. *MNRAS*, August 1993, volume 263, 589, doi:10.1093/mnras/263.3.589.

[**Herbst & van Dishoeck 2009**] E. Herbst & E. F. van Dishoeck, 'Complex Organic Interstellar Molecules'. *ARA&A*, September 2009, volume 47, 427–480, doi:10.1146/annurev-astro-082708-101654.

[**Hirota et al. 2008**] T. Hirota, T. Bushimata, Y. K. Choi, M. Honma, H. Imai, K. Iwadate, T. Jike, O. Kameya, R. Kamohara, Y. Kan-Ya, N. Kawaguchi, M. Kijima, H. Kobayashi, S. Kuji, T. Kurayama, S. Manabe, T. Miyaji, T. Nagayama, A. Nakagawa, C. S. Oh, T. Omodaka, T. Oyama, S. Sakai, T. Sasao, K. Sato, K. M. Shibata, Y. Tamura & K. Yamashita, 'Astrometry

of H_2O Masers in Nearby Star-Forming Regions with VERA. II. SVS13 in NGC1333'. *PASJ*, February 2008, volume 60, 37–44, doi:10.1093/pasj/60.1.37, 0709.1626.

[**Hollis et al. 2001**] J. M. Hollis, S. N. Vogel, L. E. Snyder, P. R. Jewell & F. J. Lovas, 'The Spatial Scale of Glycolaldehyde in the Galactic Center'. *ApJLett*, June 2001, volume 554, L81–L85, doi:10.1086/320930.

[**Hudson & Loeffler 2013**] R. L. Hudson & M. J. Loeffler, 'Ketene Formation in Interstellar Ices: A Laboratory Study'. *ApJ*, August 2013, volume 773, 109, doi:10.1088/0004-637X/773/2/109.

[**Imai et al. 2016**] M. Imai, N. Sakai, Y. Oya, A. López-Sepulcre, Y. Watanabe, C. Ceccarelli, B. Lefloch, E. Caux, C. Vastel, C. Kahane, T. Sakai, T. Hirota, Y. Aikawa & S. Yamamoto, 'Discovery of a Hot Corino in the Bok Globule B335'. *ApJLett*, October 2016, volume 830, L37, doi:10.3847/2041-8205/830/2/L37, 1610.03942.

[**Jaber et al. 2014**] A. A. Jaber, C. Ceccarelli, C. Kahane & E. Caux, 'The Census of Complex Organic Molecules in the Solar-type Protostar IRAS16293-2422'. *ApJ*, August 2014, volume 791, 29, doi:10.1088/0004-637X/791/1/29, 1406.7195.

[**Jiménez-Serra et al. 2016**] I. Jiménez-Serra, A. I. Vasyunin, P. Caselli, N. Marcelino, N. Billot, S. Viti, L. Testi, C. Vastel, B. Lefloch & R. Bachiller, 'The Spatial Distribution of Complex Organic Molecules in the L1544 Pre-stellar Core'. *ApJLett*, October 2016, volume 830, L6, doi:10.3847/2041-8205/830/1/L6, 1609.05045.

[**Jørgensen et al. 2012**] J. K. Jørgensen, C. Favre, S. E. Bisschop, T. L. Bourke, E. F. van Dishoeck & M. Schmalzl, 'Detection of the Simplest Sugar, Glycolaldehyde, in a Solar-type Protostar with ALMA'. *ApJLett*, September 2012, volume 757, L4, doi:10.1088/2041-8205/757/1/L4, 1208.5498.

[**Jørgensen et al. 2016**] J. K. Jørgensen, M. H. D. van der Wiel, A. Coutens, J. M. Lykke, H. S. P. Müller, E. F. van Dishoeck, H. Calcutt, P. Bjerkeli, T. L. Bourke, M. N. Drozdovskaya, C. Favre, E. C. Fayolle, R. T. Garrod, S. K. Jacobsen, K. I. Öberg, M. V. Persson & S. F. Wampfler, 'The ALMA Protostellar Interferometric Line Survey (PILS). First results from an unbiased submillimeter wavelength line survey of the Class 0 protostellar binary IRAS 16293-2422 with ALMA'. *A&A*, November 2016, volume 595, A117, doi:10.1051/0004-6361/201628648, 1607.08733.

[**Kahane et al. 2013**] C. Kahane, C. Ceccarelli, A. Faure & E. Caux, 'Detection of Formamide, the Simplest but Crucial Amide, in a Solar-type Protostar'. *ApJLett*, February 2013, volume 763, L38, doi:10.1088/2041-8205/763/2/L38.

[**Klessen & Glover 2016**] R. S. Klessen & S. C. O. Glover, 'Physical Processes in the Interstellar Medium'. *Star Formation in Galaxy Evolution: Connecting Numerical Models to Reality, Saas-Fee Advanced Course, Volume 43. ISBN 978-3-662-47889-9. Springer-Verlag Berlin Heidelberg, 2016, p. 85*, 2016, volume 43, 85, doi:10.1007/978-3-662-47890-5_2, 1412.5182.

[**Kounkel et al. 2017**] M. Kounkel, L. Hartmann, M. Mateo & J. I. Bailey, III, 'Kinematics of the Optically Visible YSOs toward the Orion B Molecular Cloud'. *ApJ*, August 2017, volume 844, 138, doi:10.3847/1538-4357/aa7dea, 1707.01115.

[**Laas et al. 2011**] J. C. Laas, R. T. Garrod, E. Herbst & S. L. Widicus Weaver, 'Contributions from Grain Surface and Gas Phase Chemistry to the Formation of Methyl Formate and Its Structural Isomers'. *ApJ*, February 2011, volume 728, 71, doi:10.1088/0004-637X/728/1/71.

[**Lada 1987**] C. J. Lada, 'Star formation - From OB associations to protostars'. In M. Peimbert & J. Jugaku, editors, *Star Forming Regions*, volume 115 of *IAU Symposium* (1987) pages 1–17.

[**Lee et al. 2014**] C.-F. Lee, N. Hirano, Q. Zhang, H. Shang, P. T. P. Ho & R. Krasnopolsky, 'ALMA Results of the Pseudodisk, Rotating Disk, and Jet in the Continuum and HCO^+ in the Protostellar System HH 212'. *ApJ*, May 2014, volume 786, 114, doi:10.1088/0004-637X/786/2/114, 1403.5853.

[**Lee et al. 2006**] C.-F. Lee, P. T. P. Ho, H. Beuther, T. L. Bourke, Q. Zhang, N. Hirano & H. Shang, 'Infall and Outflow around the HH 212 Protostellar System'. *ApJ*, March 2006, volume 639, 292–302, doi:10.1086/499297, astro-ph/0511059.

[**Lee et al. 2008**] C.-F. Lee, P. T. P. Ho, T. L. Bourke, N. Hirano, H. Shang & Q. Zhang, 'SiO Shocks of the Protostellar Jet HH 212: A Search for Jet Rotation'. *ApJ*, October 2008, volume 685, 1026-1032, doi:10.1086/591177.

[**Lee et al. 2007**] C.-F. Lee, P. T. P. Ho, N. Hirano, H. Beuther, T. L. Bourke, H. Shang & Q. Zhang, 'HH 212: Submillimeter Array Observations of a Remarkable Protostellar Jet'. *ApJ*, April 2007, volume 659, 499–511, doi:10.1086/512540, astro-ph/0701284.

[**Lee et al. 2017a**] C.-F. Lee, P. T. P. Ho, Z.-Y. Li, N. Hirano, Q. Zhang & H. Shang, 'A rotating protostellar jet launched from the innermost disk of HH 212'. *Nature Astronomy*, July 2017a, volume 1, 0152, doi:10.1038/s41550-017-0152, 1706.06343.

[**Lee et al. 2017b**] C.-F. Lee, Z.-Y. Li, P. T. P. Ho, N. Hirano, Q. Zhang & H. Shang, 'First detection of equatorial dark dust lane in a protostellar disk at submillimeter wavelength'. *Science Advances*, April 2017b, volume 3, e1602935, doi:10.1126/sciadv.1602935, 1704.08962.

[**Lee et al. 2017c**] C.-F. Lee, Z.-Y. Li, P. T. P. Ho, N. Hirano, Q. Zhang & H. Shang, 'Formation and Atmosphere of Complex Organic Molecules of the HH 212 Protostellar Disk'. *ApJ*, July 2017c, volume 843, 27, doi:10.3847/1538-4357/aa7757, 1706.06041.

[**Lefloch et al. 1998a**] B. Lefloch, A. Castets, J. Cernicharo, W. D. Langer & R. Zylka, 'Cores and cavities in NGC 1333'. *A&A*, June 1998a, volume 334, 269–279.

[**Lefloch et al. 1998b**] B. Lefloch, A. Castets, J. Cernicharo & L. Loinard, 'Widespread SiO Emission in NGC 1333'. *ApJLett*, September 1998b, volume 504, L109–L112, doi:10.1086/311581.

[**Lefloch et al. 2017**] B. Lefloch, C. Ceccarelli, C. Codella, C. Favre, L. Podio, C. Vastel, S. Viti & R. Bachiller, 'L1157-B1, a factory of complex organic molecules in a solar-type star-forming region'. *MNRAS*, July 2017, volume 469, L73–L77, doi:10.1093/mnrasl/slx050, 1704.04646.

[**Leurini et al. 2016**] S. Leurini, C. Codella, S. Cabrit, F. Gueth, A. Giannetti, F. Bacciotti, R. Bachiller, C. Ceccarelli, A. Gusdorf, B. Lefloch, L. Podio & M. Tafalla, 'Hot methanol from the inner region of the HH 212 protostellar system'. *A&A*, October 2016, volume 595, L4, doi:10.1051/0004-6361/201629460, 1610.05322.

[**Linsky 2007**] J. L. Linsky, 'D/H and Nearby Interstellar Cloud Structures'. *Space Sci. Rev.*, June 2007, volume 130, 367–375, doi:10.1007/s11214-007-9160-z.

[**Loinard et al. 2001**] L. Loinard, A. Castets, C. Ceccarelli, E. Caux & A. G. G. M. Tielens, 'Doubly Deuterated Molecular Species in Protostellar Environments'. *ApJLett*, May 2001, volume 552, L163–L166, doi:10.1086/320331.

[**Loinard et al. 2002**] L. Loinard, A. Castets, C. Ceccarelli, B. Lefloch, J.-J. Benayoun, E. Caux, C. Vastel, E. Dartois & A. G. G. M. Tielens, 'Doubly deuterated formaldehyde in star-forming regions: an observational approach'. *Planet. Space Sci.*, October 2002, volume 50, 1205–1213, doi:10.1016/S0032-0633(02)00084-3.

[**Loinard et al. 2008**] L. Loinard, R. M. Torres, A. J. Mioduszewski & L. F. Rodríguez, 'A Preliminary VLBA Distance to the Core of Ophiuchus, with an Accuracy of 4%'. *ApJLett*, March 2008, volume 675, L29, doi:10.1086/529548, 0801.2192.

[**Lombardi et al. 2014**] M. Lombardi, H. Bouy, J. Alves & C. J. Lada, 'Herschel-Planck dust optical-depth and column-density maps. I. Method description and results for Orion'. *A&A*, June 2014, volume 566, A45, doi:10.1051/0004-6361/201323293, 1404.0032.

[**Looney et al. 2000**] L. W. Looney, L. G. Mundy & W. J. Welch, 'Unveiling the Circumstellar Envelope and Disk: A Subarcsecond Survey of Circumstellar Structures'. *ApJ*, January 2000, volume 529, 477–498, doi:10.1086/308239, astro-ph/9908301.

[**Looney et al. 2007**] L. W. Looney, J. J. Tobin & W. Kwon, 'A Flattened Protostellar Envelope in Absorption around L1157'. *ApJLett*, December 2007, volume 670, L131–L134, doi:10.1086/524361, 0710.2314.

[**López-Sepulcre et al. 2015**] A. López-Sepulcre, A. A. Jaber, E. Mendoza, B. Lefloch, C. Ceccarelli, C. Vastel, R. Bachiller, J. Cernicharo, C. Codella, C. Kahane, M. Kama & M. Tafalla, 'Shedding light on the formation of the pre-biotic molecule formamide with ASAI'. *MNRAS*, May 2015, volume 449, 2438–2458, doi:10.1093/mnras/stv377, 1502.05762.

[**Maret et al. 2005**] S. Maret, C. Ceccarelli, A. G. G. M. Tielens, E. Caux, B. Lefloch, A. Faure, A. Castets & D. R. Flower, 'CH3OH abundance in low mass protostars'. *A&A*, November 2005, volume 442, 527–538, doi:10.1051/0004-6361:20052899, astro-ph/0507172.

[**Maret et al. 2011**] S. Maret, P. Hily-Blant, J. Pety, S. Bardeau & E. Reynier, 'Weeds: a CLASS extension for the analysis of millimeter and sub-millimeter spectral surveys'. *A&A*, February 2011, volume 526, A47, doi:10.1051/0004-6361/201015487, 1012.1747.

[**Marois et al. 2010**] C. Marois, B. Zuckerman, Q. M. Konopacky, B. Macintosh & T. Barman, 'Images of a fourth planet orbiting HR 8799'. *Nature*, December 2010, volume 468, 1080–1083, doi:10.1038/nature09684, 1011.4918.

[**Mendoza et al. 2014**] E. Mendoza, B. Lefloch, A. López-Sepulcre, C. Ceccarelli, C. Codella, H. M. Boechat-Roberty & R. Bachiller, 'Molecules with a peptide link in protostellar shocks: a comprehensive study of L1157'. *MNRAS*, November 2014, volume 445, 151–161, doi:10.1093/mnras/stu1718, 1408.4857.

[**Milam et al. 2005**] S. N. Milam, C. Savage, M. A. Brewster, L. M. Ziurys & S. Wyckoff, 'The $^{12}C/^{13}C$ Isotope Gradient Derived from Millimeter Transitions of CN: The Case for Galactic Chemical Evolution'. *ApJ*, December 2005, volume 634, 1126–1132, doi:10.1086/497123.

[**Müller et al. 2005**] H. S. P. Müller, F. Schlöder, J. Stutzki & G. Winnewisser, 'The Cologne Database for Molecular Spectroscopy, CDMS: a useful tool for astronomers and spectroscopists'. *Journal of Molecular Structure*, May 2005, volume 742, 215–227, doi:10.1016/j.molstruc.2005.01.027.

[**Müller et al. 2001**] H. S. P. Müller, S. Thorwirth, D. A. Roth & G. Winnewisser, 'The Cologne Database for Molecular Spectroscopy, CDMS'. *A&A*, April 2001, volume 370, L49–L52, doi:10.1051/0004-6361:20010367.

[**Myers & Ladd 1993**] P. C. Myers & E. F. Ladd, 'Bolometric temperatures of young stellar objects'. *ApJLett*, August 1993, volume 413, L47–L50, doi:10.1086/186956.

[**Myers & Bright Wilson 1960**] R. J. Myers & E. Bright Wilson, Jr., 'Application of Symmetry Principles to the Rotation-Internal Torsion Levels of Molecules with Two Equivalent Methyl Groups'. *J. Chem. Phys.*, July 1960, volume 33, 186–191, doi:10.1063/1.1731075.

[**Napier 1999**] P. J. Napier, 'The Primary Antenna Elements'. In G. B. Taylor, C. L. Carilli & R. A. Perley, editors, *Synthesis Imaging in Radio Astronomy II*, volume 180 of *Astronomical Society of the Pacific Conference Series* (1999) page 37.

[**Neill et al. 2012**] J. L. Neill, M. T. Muckle, D. P. Zaleski, A. L. Steber, B. H. Pate, V. Lattanzi, S. Spezzano, M. C. McCarthy & A. J. Remijan, 'Laboratory and Tentative Interstellar Detection of Trans-Methyl Formate Using the Publicly Available Green Bank Telescope Primos Survey'. *ApJ*, August 2012, volume 755, 153, doi:10.1088/0004-637X/755/2/153, 1206.6021.

[**Öberg et al. 2009**] K. I. Öberg, R. T. Garrod, E. F. van Dishoeck & H. Linnartz, 'Formation rates of complex organics in UV irradiated CH_3OH-rich ices. I. Experiments'. *A&A*, September 2009, volume 504, 891–913, doi:10.1051/0004-6361/200912559, 0908.1169.

[**Öberg et al. 2014**] K. I. Öberg, T. Lauck & D. Graninger, 'Complex Organic Molecules during Low-mass Star Formation: Pilot Survey Results'. *ApJ*, June 2014, volume 788, 68, doi:10.1088/0004-637X/788/1/68, 1406.1542.

[**Öberg et al. 2012**] K. I. Öberg, C. Qi, D. J. Wilner & M. R. Hogerheijde, 'Evidence for Multiple Pathways to Deuterium Enhancements in Protoplanetary Disks'. *ApJ*, April 2012, volume 749, 162, doi:10.1088/0004-637X/749/2/162, 1202.3992.

[**Öberg et al. 2011**] K. I. Öberg, N. van der Marel, L. E. Kristensen & E. F. van Dishoeck, 'Complex Molecules toward Low-mass Protostars: The Serpens Core'. *ApJ*, October 2011, volume 740, 14, doi:10.1088/0004-637X/740/1/14, 1107.5824.

[**Ohishi et al. 1991**] M. Ohishi, K. Kawaguchi, N. Kaifu, W. M. Irvine, Y. C. Minh, S. Yamamoto & S. Saito, 'The Ortho to Para Ratio for Ketene in TMC-1'. In A. D. Haschick & P. T. P. Ho, editors, *Atoms, Ions and Molecules: New Results in Spectral Line Astrophysics*, volume 16 of *Astronomical Society of the Pacific Conference Series* (1991) page 387.

[**Osamura et al. 2004**] Y. Osamura, H. Roberts & E. Herbst, 'On the possible interconversion between pairs of deuterated isotopomers of methanol, its ion, and its protonated ion in star-forming regions'. *A&A*, July 2004, volume 421, 1101–1111, doi:10.1051/0004-6361:20035762.

[**Ossenkopf & Henning 1994**] V. Ossenkopf & T. Henning, 'Dust opacities for protostellar cores'. *A&A*, November 1994, volume 291, 943–959.

[**Oya et al. 2016**] Y. Oya, N. Sakai, A. López-Sepulcre, Y. Watanabe, C. Ceccarelli, B. Lefloch, C. Favre & S. Yamamoto, 'Infalling-Rotating Motion and Associated Chemical Change in the Envelope of IRAS 16293-2422 Source A Studied with ALMA'. *ApJ*, June 2016, volume 824, 88, doi:10.3847/0004-637X/824/2/88, 1605.00340.

[**Oya et al. 2017**] Y. Oya, N. Sakai, Y. Watanabe, A. E. Higuchi, T. Hirota, A. López-Sepulcre, T. Sakai, Y. Aikawa, C. Ceccarelli, B. Lefloch, E. Caux, C. Vastel, C. Kahane & S. Yamamoto, 'L483: Warm Carbon-chain Chemistry Source Harboring Hot Corino Activity'. *ApJ*, March 2017, volume 837, 174, doi:10.3847/1538-4357/aa6300, 1703.03653.

[**Parise 2004**] B. Parise, *Deuteration in low-mass protostars*. Ph.D. thesis, Centre d'Étude Spatiale des Rayonnements, September 2004.

[**Parise et al. 2004**] B. Parise, A. Castets, E. Herbst, E. Caux, C. Ceccarelli, I. Mukhopadhyay & A. G. G. M. Tielens, 'First detection of triply-deuterated methanol'. *A&A*, March 2004, volume 416, 159–163, doi:10.1051/0004-6361:20034490, astro-ph/0311038.

[**Parise et al. 2006**] B. Parise, C. Ceccarelli, A. G. G. M. Tielens, A. Castets, E. Caux, B. Lefloch & S. Maret, 'Testing grain surface chemistry: a survey of deuterated formaldehyde and methanol in low-mass class 0 protostars'. *A&A*, July 2006, volume 453, 949–958, doi:10.1051/0004-6361:20054476, astro-ph/0603135.

[**Parise et al. 2002**] B. Parise, C. Ceccarelli, A. G. G. M. Tielens, E. Herbst, B. Lefloch, E. Caux, A. Castets, I. Mukhopadhyay, L. Pagani & L. Loinard, 'Detection of doubly-deuterated methanol in the solar-type protostar IRAS 16293-2422'. *A&A*, October 2002, volume 393, L49–L53, doi:10.1051/0004-6361:20021131, astro-ph/0207577.

[**Peng et al. 2012**] T.-C. Peng, D. Despois, N. Brouillet, B. Parise & A. Baudry, 'Deuterated methanol in Orion BN/KL'. *A&A*, July 2012, volume 543, A152, doi:10.1051/0004-6361/201118310, 1206.2140.

[**Persson 2014**] M. V. Persson, 'SEDs of the different protostellar evolutionary stages'. 8 2014, doi:10.6084/m9.figshare.1121574.v2, URL https://figshare.com/articles/SEDs_of_the_different_protostellar_evolutionary_stages/1121574.

[**Pezzuto et al. 2012**] S. Pezzuto, D. Elia, E. Schisano, F. Strafella, J. Di Francesco, S. Sadavoy, P. André, M. Benedettini, J. P. Bernard, A. M. di Giorgio, A. Facchini, M. Hennemann,

T. Hill, V. Könyves, S. Molinari, F. Motte, Q. Nguyen-Luong, N. Peretto, M. Pestalozzi, D. Polychroni, K. L. J. Rygl, P. Saraceno, N. Schneider, L. Spinoglio, L. Testi, D. Ward-Thompson & G. J. White, 'Herschel observations of B1-bS and B1-bN: two first hydrostatic core candidates in the Perseus star-forming cloud'. *A&A*, November 2012, volume 547, A54, doi:10.1051/0004-6361/201219501, 1209.5290.

[**Pickett et al. 1998**] H. M. Pickett, R. L. Poynter, E. A. Cohen, M. L. Delitsky, J. C. Pearson & H. S. P. Müller, 'Submillimeter, millimeter and microwave spectral line catalog.' *J. Quant. Spectrosc. Radiat. Trans.*, November 1998, volume 60, 883–890, doi:10.1016/S0022-4073(98)00091-0.

[**Pineau des Forets et al. 1993**] G. Pineau des Forets, E. Roueff, P. Schilke & D. R. Flower, 'Sulphur-bearing molecules as tracers of shocks in interstellar clouds'. *MNRAS*, June 1993, volume 262, 915–928, doi:10.1093/mnras/262.4.915.

[**Plunkett et al. 2013**] A. L. Plunkett, H. G. Arce, S. A. Corder, D. Mardones, A. I. Sargent & S. L. Schnee, 'CARMA Observations of Protostellar Outflows in NGC 1333'. *ApJ*, September 2013, volume 774, 22, doi:10.1088/0004-637X/774/1/22, 1307.3558.

[**Podio et al. 2015**] L. Podio, C. Codella, F. Gueth, S. Cabrit, R. Bachiller, A. Gusdorf, C.-F. Lee, B. Lefloch, S. Leurini, B. Nisini & M. Tafalla, 'The jet and the disk of the HH 212 low-mass protostar imaged by ALMA: SO and SO_2 emission'. *A&A*, September 2015, volume 581, A85, doi:10.1051/0004-6361/201525778, 1505.05919.

[**Podio et al. 2016**] L. Podio, C. Codella, F. Gueth, S. Cabrit, A. Maury, B. Tabone, C. Lefèvre, S. Anderl, P. André, A. Belloche, S. Bontemps, P. Hennebelle, B. Lefloch, S. Maret & L. Testi, 'First image of the L1157 molecular jet by the CALYPSO IRAM-PdBI survey'. *A&A*, September 2016, volume 593, L4, doi:10.1051/0004-6361/201628876, 1608.05026.

[**Ratajczak et al. 2011**] A. Ratajczak, V. Taquet, C. Kahane, C. Ceccarelli, A. Faure & E. Quirico, 'The puzzling deuteration of methanol in low- to high-mass protostars'. *A&A*, April 2011, volume 528, L13, doi:10.1051/0004-6361/201016402.

[**Reipurth et al. 1993**] B. Reipurth, R. Chini, E. Krugel, E. Kreysa & A. Sievers, 'Cold Dust around Herbig-Haro Energy Sources - a 1300-MICRON Survey'. *A&A*, June 1993, volume 273, 221.

[**Roberts & Millar 2000**] H. Roberts & T. J. Millar, 'Gas-phase formation of doubly-deuterated species'. *A&A*, December 2000, volume 364, 780–784.

[**Roberts & Millar 2007**] H. Roberts & T. J. Millar, 'A survey of [D2CO] /[H2CO] and [N2Dˆ+] /[N2Hˆ+] ratios towards protostellar cores'. *A&A*, September 2007, volume 471, 849–863, doi:10.1051/0004-6361:20066608.

[**Rodríguez et al. 1997**] L. F. Rodríguez, G. Anglada & S. Curiel, 'Is SVS 13 the Exciting Source of the HH 7-11 Flow?' *ApJLett*, May 1997, volume 480, L125–L128, doi:10.1086/310636.

[**Rodríguez et al. 1999**] L. F. Rodríguez, G. Anglada & S. Curiel, 'The Nature of the Radio Continuum Sources Embedded in the HH 7-11 Region and Its Surroundings'. *ApJS*, December 1999, volume 125, 427–438, doi:10.1086/313283.

[**Rubin et al. 1971**] R. H. Rubin, G. W. Swenson, Jr., R. C. Benson, H. L. Tigelaar & W. H. Flygare, 'Microwave Detection of Interstellar Formamide'. *ApJLett*, October 1971, volume 169, L39, doi:10.1086/180810.

[**Sakai et al. 2017**] N. Sakai, Y. Oya, A. E. Higuchi, Y. Aikawa, T. Hanawa, C. Ceccarelli, B. Lefloch, A. López-Sepulcre, Y. Watanabe, T. Sakai, T. Hirota, E. Caux, C. Vastel, C. Kahane & S. Yamamoto, 'Vertical structure of the transition zone from infalling rotating envelope to disc in the Class 0 protostar, IRAS 04368+2557'. *MNRAS*, May 2017, volume 467, L76–L80, doi:10.1093/mnrasl/slx002.

[**Sakai et al. 2016**] N. Sakai, Y. Oya, A. López-Sepulcre, Y. Watanabe, T. Sakai, T. Hirota, Y. Aikawa, C. Ceccarelli, B. Lefloch, E. Caux, C. Vastel, C. Kahane & S. Yamamoto, 'Sub-arcsecond Analysis of the Infalling-Rotating Envelope around the Class I Protostar IRAS 04365+2535'. *ApJLett*, April 2016, volume 820, L34, doi:10.3847/2041-8205/820/2/L34, 1603.08608.

[**Sakai et al. 2014a**] N. Sakai, Y. Oya, T. Sakai, Y. Watanabe, T. Hirota, C. Ceccarelli, C. Kahane, A. Lopez-Sepulcre, B. Lefloch, C. Vastel, S. Bottinelli, E. Caux, A. Coutens, Y. Aikawa, S. Takakuwa, N. Ohashi, H.-W. Yen & S. Yamamoto, 'A Chemical View of Protostellar-disk Formation in L1527'. *ApJLett*, August 2014a, volume 791, L38, doi:10.1088/2041-8205/791/2/L38.

[**Sakai et al. 2009**] N. Sakai, T. Sakai, T. Hirota, M. Burton & S. Yamamoto, 'Discovery of the Second Warm Carbon-Chain-Chemistry Source, IRAS15398 - 3359 in Lupus'. *ApJ*, May 2009, volume 697, 769–786, doi:10.1088/0004-637X/697/1/769.

[**Sakai et al. 2014b**] N. Sakai, T. Sakai, T. Hirota, Y. Watanabe, C. Ceccarelli, C. Kahane, S. Bottinelli, E. Caux, K. Demyk, C. Vastel, A. Coutens, V. Taquet, N. Ohashi, S. Takakuwa, H.-W. Yen, Y. Aikawa & S. Yamamoto, 'Change in the chemical composition of infalling gas forming a disk around a protostar'. *Nature*, March 2014b, volume 507, 78–80, doi:10.1038/nature13000.

[**Sakai et al. 2008**] N. Sakai, T. Sakai, T. Hirota & S. Yamamoto, 'Abundant Carbon-Chain Molecules toward the Low-Mass Protostar IRAS 04368+2557 in L1527'. *ApJ*, January 2008, volume 672, 371-381, doi:10.1086/523635.

[**Sakai et al. 2010**] N. Sakai, T. Sakai, T. Hirota & S. Yamamoto, 'Distributions of Carbon-chain Molecules in L1527'. *ApJ*, October 2010, volume 722, 1633–1643, doi:10.1088/0004-637X/722/2/1633.

[**Sakai & Yamamoto 2011**] N. Sakai & S. Yamamoto, 'Observations of Complex Molecules in Low-Mass Protostars'. In J. Cernicharo & R. Bachiller, editors, *The Molecular Universe*, volume 280 of *IAU Symposium* (2011) pages 43–52, doi:10.1017/S1743921311024859.

[**Sakai & Yamamoto 2013**] N. Sakai & S. Yamamoto, 'Warm Carbon-Chain Chemistry'. *Chemical Reviews*, December 2013, volume 113, 8981–9015, doi:10.1021/cr4001308.

[**Saladino et al. 2012**] R. Saladino, G. Botta, S. Pino, G. Costanzo & E. Di Mauro, 'Genetics first or metabolism first? The formamide clue'. *Chem. Soc. Rev.*, 2012, volume 41, 5526–5565, doi:10.1039/C2CS35066A, URL http://dx.doi.org/10.1039/C2CS35066A.

[**Sandell et al. 1991**] G. Sandell, C. Aspin, W. D. Duncan, A. P. G. Russell & E. I. Robson, 'NGC 1333 IRAS 4 - A very young, low-luminosity binary system'. *ApJLett*, July 1991, volume 376, L17–L20, doi:10.1086/186092.

[**Shang 2007**] H. Shang, 'Jets and molecular outflows from Herbig-Haro objects'. *Ap&SS*, October 2007, volume 311, 25–34, doi:10.1007/s10509-007-9587-4.

[**Shu 1977**] F. H. Shu, 'Self-similar collapse of isothermal spheres and star formation'. *ApJ*, June 1977, volume 214, 488–497, doi:10.1086/155274.

[**Sipilä et al. 2013**] O. Sipilä, P. Caselli & J. Harju, 'HD depletion in starless cores'. *A&A*, June 2013, volume 554, A92, doi:10.1051/0004-6361/201220922, 1304.4031.

[**Snyder et al. 1974**] L. E. Snyder, D. Buhl, P. R. Schwartz, F. O. Clark, D. R. Johnson, F. J. Lovas & P. T. Giguere, 'Radio Detection of Interstellar Dimethyl Ether'. *ApJLett*, July 1974, volume 191, L79, doi:10.1086/181554.

[**Tabone et al. 2017**] B. Tabone, S. Cabrit, E. Bianchi, J. Ferreira, G. Pineau des Forêts, C. Codella, A. Gusdorf, F. Gueth, L. Podio & E. Chapillon, 'ALMA discovery of a rotating SO/SO_2 flow in HH212. A possible MHD disk wind?' *ArXiv e-prints*, October 2017, 1710.01401.

[**Takano et al. 2011**] S. Takano, Y. Aikawa, V. Chen, N. Hirano, M. Hiramatsu, T. Hirota, K. Kamegai, K. Kobayashi, K. Kohno, Y. J. Kuan, S. Y. Liu, T. Nakajima, H. Nomura, N. Ohashi, M. Ohishi, H. Ozeki, N. Sakai, T. Sakai, S. Shiba, Y. N. Su, M. Sugimura, S. Takakuwa, T. Umemoto, K. Wang, M. Yamada, T. Yamaguchi, S. Yamamoto & Q. Z. Zhang, 'Nobeyama 45 m telescope legacy project: Line survey'. In J. Cernicharo & R. Bachiller, editors, *The Molecular Universe*, volume 280 of *IAU Symposium* (2011) .

[**Taquet et al. 2012a**] V. Taquet, C. Ceccarelli & C. Kahane, 'Formaldehyde and Methanol Deuteration in Protostars: Fossils from a Past Fast High-density Pre-collapse Phase'. *ApJLett*, March 2012a, volume 748, L3, doi:10.1088/2041-8205/748/1/L3, 1202.3073.

[**Taquet et al. 2012b**] V. Taquet, C. Ceccarelli & C. Kahane, 'Multilayer modeling of porous grain surface chemistry. I. The GRAINOBLE model'. *A&A*, February 2012b, volume 538, A42, doi:10.1051/0004-6361/201117802, 1111.4165.

[**Taquet et al. 2014**] V. Taquet, S. B. Charnley & O. Sipilä, 'Multilayer Formation and Evaporation of Deuterated Ices in Prestellar and Protostellar Cores'. *ApJ*, August 2014, volume 791, 1, doi:10.1088/0004-637X/791/1/1, 1405.3268.

[**Taquet et al. 2015**] V. Taquet, A. López-Sepulcre, C. Ceccarelli, R. Neri, C. Kahane & S. B. Charnley, 'Constraining the Abundances of Complex Organics in the Inner Regions of Solar-type Protostars'. *ApJ*, May 2015, volume 804, 81, doi:10.1088/0004-637X/804/2/81, 1502.06427.

[**Taquet et al. 2013**] V. Taquet, P. S. Peters, C. Kahane, C. Ceccarelli, A. López-Sepulcre, C. Toubin, D. Duflot & L. Wiesenfeld, 'Water ice deuteration: a tracer of the chemical history of protostars'. *A&A*, February 2013, volume 550, A127, doi:10.1051/0004-6361/201220084, 1211.0514.

[**Taquet et al. 2017**] V. Taquet, E. Wirström, S. B. Charnley, A. Faure, A. López-Sepulcre & C. M. Persson, 'Chemical complexity induced by efficient ice evaporation in the Barnard 5 molecular cloud'. *ArXiv e-prints*, June 2017, 1706.01368.

[**Tielens 1983**] A. G. G. M. Tielens, 'Surface chemistry of deuterated molecules'. *A&A*, March 1983, volume 119, 177–184.

[**Tobin et al. 2016**] J. J. Tobin, L. W. Looney, Z.-Y. Li, C. J. Chandler, M. M. Dunham, D. Segura-Cox, S. I. Sadavoy, C. Melis, R. J. Harris, K. Kratter & L. Perez, 'The VLA Nascent Disk and Multiplicity Survey of Perseus Protostars (VANDAM). II. Multiplicity of Protostars in the Perseus Molecular Cloud'. *ApJ*, February 2016, volume 818, 73, doi:10.3847/0004-637X/818/1/73, 1601.00692.

[**Troscompt et al. 2009a**] N. Troscompt, A. Faure, S. Maret, C. Ceccarelli, P. Hily-Blant & L. Wiesenfeld, 'Constraining the ortho-to-para ratio of H_2 with anomalous H_2CO absorption'. *A&A*, November 2009a, volume 506, 1243–1247, doi:10.1051/0004-6361/200912770.

[**Troscompt et al. 2009b**] N. Troscompt, A. Faure, L. Wiesenfeld, C. Ceccarelli & P. Valiron, 'Rotational excitation of formaldehyde by hydrogen molecules: ortho-H_2CO at low temperature'. *A&A*, January 2009b, volume 493, 687–696, doi:10.1051/0004-6361:200810712.

[**Turner 1977**] B. E. Turner, 'Microwave detection of interstellar ketene'. *ApJLett*, April 1977, volume 213, L75–L79, doi:10.1086/182413.

[**Turner 1991**] B. E. Turner, 'A molecular line survey of Sagittarius B2 and Orion-KL from 70 to 115 GHz. II - Analysis of the data.' *ApJS*, June 1991, volume 76, 617–686, doi:10.1086/191577.

[**van Dishoeck & Blake 1998**] E. F. van Dishoeck & G. A. Blake, 'Chemical Evolution of Star-Forming Regions'. *ARA&A*, 1998, volume 36, 317–368, doi:10.1146/annurev.astro.36.1.317.

[**van Dishoeck et al. 2003**] E. F. van Dishoeck, W.-F. Thi & G.-J. van Zadelhoff, 'Detection of DCO^+ in a circumstellar disk'. *A&A*, March 2003, volume 400, L1–L4, doi:10.1051/0004-6361:20030091, astro-ph/0301571.

[**Vastel et al. 2014**] C. Vastel, C. Ceccarelli, B. Lefloch & R. Bachiller, 'The Origin of Complex Organic Molecules in Prestellar Cores'. *ApJLett*, November 2014, volume 795, L2, doi:10.1088/2041-8205/795/1/L2, 1409.6565.

[**Vasyunin & Herbst 2013**] A. I. Vasyunin & E. Herbst, 'Reactive Desorption and Radiative Association as Possible Drivers of Complex Molecule Formation in the Cold Interstellar Medium'. *ApJ*, May 2013, volume 769, 34, doi:10.1088/0004-637X/769/1/34, 1303.7266.

[**Vazart et al. 2016**] F. Vazart, D. Calderini, C. Puzzarini, D. Skouteris & V. Barone, 'State-of-the-Art Thermochemical and Kinetic Computations for Astrochemical Complex Organic Molecules: Formamide Formation in Cold Interstellar Clouds as a Case Study'. *Journal of Chemical Theory and Computation*, 2016, volume 12(11), 5385–5397, doi:10.1021/acs.jctc.6b00379, pMID: 27689448, http://dx.doi.org/10.1021/acs.jctc.6b00379, URL http://dx.doi.org/10.1021/acs.jctc.6b00379.

[**Visser et al. 2009**] R. Visser, E. F. van Dishoeck & J. H. Black, 'The photodissociation and chemistry of CO isotopologues: applications to interstellar clouds and circumstellar disks'. *A&A*, August 2009, volume 503, 323–343, doi:10.1051/0004-6361/200912129, 0906.3699.

[**Wakelam et al. 2012**] V. Wakelam, E. Herbst, J.-C. Loison, I. W. M. Smith, V. Chandrasekaran, B. Pavone, N. G. Adams, M.-C. Bacchus-Montabonel, A. Bergeat, K. Béroff, V. M. Bierbaum, M. Chabot, A. Dalgarno, E. F. van Dishoeck, A. Faure et al., 'A KInetic Database for Astrochemistry (KIDA)'. *ApJS*, March 2012, volume 199, 21, doi:10.1088/0067-0049/199/1/21, 1201.5887.

[**Walawender et al. 2008**] J. Walawender, J. Bally, J. D. Francesco, J. Jørgensen & K. . Getman, *NGC 1333: A Nearby Burst of Star Formation*, page 346 (2008).

[**Watanabe et al. 2012**] Y. Watanabe, N. Sakai, J. E. Lindberg, J. K. Jørgensen, S. E. Bisschop & S. Yamamoto, 'An Unbiased Spectral Line Survey toward R CrA IRS7B in the 345 GHz Window with ASTE'. *ApJ*, February 2012, volume 745, 126, doi:10.1088/0004-637X/745/2/126, 1110.2226.

[**Wilson 2009**] T. L. Wilson, 'Introduction to Millimeter/Sub-Millimeter Astronomy'. *ArXiv e-prints*, March 2009, 0903.0562.

[**Wilson et al. 2013**] T. L. Wilson, K. Rohlfs & S. Hüttemeister, *Tools of Radio Astronomy* (2013), doi:10.1007/978-3-642-39950-3.

[**Wiseman et al. 2001**] J. Wiseman, A. Wootten, H. Zinnecker & M. McCaughrean, 'The Flattened, Rotating Molecular Gas Core of Protostellar Jet HH 212'. *ApJLett*, March 2001, volume 550, L87–L90, doi:10.1086/319474, astro-ph/0103385.

[**Yamaguchi et al. 2012**] T. Yamaguchi, S. Takano, Y. Watanabe, N. Sakai, T. Sakai, S.-Y. Liu, Y.-N. Su, N. Hirano, S. Takakuwa, Y. Aikawa, H. Nomura & S. Yamamoto, 'The 3 mm Spectral Line Survey toward the Lynds 1157 B1 Shocked Region. I. Data'. *PASJ*, October 2012, volume 64, 105, doi:10.1093/pasj/64.5.105.

[**Yamamoto 2017**] S. Yamamoto, *Introduction to Astrochemistry: Chemical Evolution from Interstellar Clouds to Star and Planet Formation* (2017), doi:10.1007/978-4-431-54171-4.

[**Zari et al. 2016**] E. Zari, M. Lombardi, J. Alves, C. J. Lada & H. Bouy, 'Herschel-Planck dust optical depth and column density maps. II. Perseus'. *A&A*, March 2016, volume 587, A106, doi:10.1051/0004-6361/201526597, 1511.08503.

[**Zinnecker et al. 1998**] H. Zinnecker, M. J. McCaughrean & J. T. Rayner, 'A symmetrically pulsed jet of gas from an invisible protostar in Orion'. *Nature*, August 1998, volume 394, 862–865, doi:10.1038/29716.